TAMPEREEN TEKNILLINEN YLIOPISTO
TAMPERE UNIVERSITY OF TECHNOLOGY

Matti Lindroos

Experimental and Numerical Studies on the Abrasive and Impact Behavior of Wear Resistant Steels

Julkaisu 1416 • Publication 1416

Tampere 2016

Tampereen teknillinen yliopisto. Julkaisu 1416
Tampere University of Technology. Publication 1416

Matti Lindroos

Experimental and Numerical Studies on the Abrasive and Impact Behavior of Wear Resistant Steels

Thesis for the degree of Doctor of Science in Technology to be presented with due permission for public examination and criticism in Konetalo Building, Auditorium K1702, at Tampere University of Technology, on the 4th of November 2016, at 12 noon.

Tampereen teknillinen yliopisto - Tampere University of Technology
Tampere 2016

ISBN 978-952-15-3814-8 (printed)
ISBN 978-952-15-3828-5 (PDF)
ISSN 1459-2045

Abstract

The demand for more wear resistant materials originates from modern applications of many industries, such as mining, automotive, aerospace and civil structures. The motivation to develop more efficient engineering structures and components can be seen beneficial in both economically and environmentally. Lighter, higher strength and more wear resistant solutions can be attractive, for example because of savings in energy consumption (e.g., petrol and running costs), higher load bearing capability per material thickness/volume, and increased component lifespan. Steels remain still today very competitive materials for various wear applications because of their relatively good wear resistance in many conditions arising from their excellet mechanical properties, and because of the reasonable cost of manufacturing and processing of the components.

The steels exposed to high stress abrasive and impact wear conditions, for example in the equipment used in mining, are required to withstand heavy static and dynamic loadings for long periods of time. The evaluation of the performance of different steels in these type of conditions is often performed with experimental setups imitating the real loading conditions and material characterizations done afterwards, giving an insight into the material's wear behavior in a particular tribosystem.

This work concentrates on the characterization of the mechanical behavior of wear resistant steels subjected to abrasive and impact loadings by hard particles. The mechanical behavior of the steels was first characterized at a wide range of strain rates from 10^{-3} to 4000 s^{-1}. Although the increase in the flow stress with the increasing the strain rate is well established, limited information is available of the behavior of these steels in the dynamic range. For example, the localization phenomena, such as adiabatic shear banding, have an important role in the failure behavior of the martensitic steels. On the other hand, the strain hardening behavior of austenitic manganese steels that evolves with strain and strain rate is affected largely by the twinning phenomenon. Two in-service cases including sample materials from a jaw crusher and from a cutting edge of a bucket loader were also characterized and analyzed. The observations made on the deformed microstructures of the laboratory and in-service samples formed the basis for the simulation approaches developed in this work.

High stress abrasion experiments were performed and further developed for the testing of wear resistant steels to study their capabilities to surface harden and to withstand wear. The results show that the surface hardening of the steels has a substantial effect on their wear rates. The common single scratch experiments, however, were shown to be insufficient to reveal all important aspects related for example to the surface hardening of the studied materials, and therefore different types of multi-scratch experiments were also applied. The characterization also showed that the martensitic steels generate two types of tribolayers depending on the prevailing contact conditions.

High velocity impact testing was conducted with a novel high velocity particle impactor device. The steels showed dependence on several external factors and conditions, such as impact energy, impact angle, and incident impulse. It was shown that the wear characteristics depended on the deformation mechanisms such as ploughing or cutting in addition to some more special mechanisms such as shear banding, which becomes active only at higher impact energies and/or higher strain rates. The strain hardening had both positive and negative effects on the material's resistance against impacts depending on the loading conditions.

Two numerical crystal plasticity models were implemented to assist the development of the understanding of the deformation behavior at micro-scale. First a phenomenological model including dislocation slip and twinning was formulated to describe the micromechanical phenomena occurring in austenitic manganese steels. The model was found capable of representing the material behavior with a satisfactory accuracy in the studied deformation conditions, starting from the single crystal behavior and extending to the polycrystal level. A multi-scale method linking the application and microstructural scales was also demonstrated using a jaw crusher as an example. Implementation of a crystal plasticity method for BCC microstructure in the large deformation framework was also carried out. The model was extended to include a phenomenological description of the shear banding phenomenon in the microscale. The extension was demonstrated with simulations on single crystals with four different initial orientations. The results indicated that shear banding is a heavily orientation dependent phenomenon, but its relevance for the performance of polycrystalline microstructures still requires further examinations.

Preface

This work was mainly carried out at Tampere Wear Center (TWC) at the Department of Materials Science of Tampere University of Technology. A part of the work was also carried out at Centre des Matériaux (CDM) of MINES ParisTech located at Évry in the Paris region, between October 2014 and March 2015.

This research was initiated during the industry related research programmes Demanding Applications (DEMAPP) and finalized in Breakthrough Steels and Applications (BSA) within the Finnish Metals and Engineering Competence Cluster (FIMECC). These research programmes, funded by the Finnish Funding Agency for Technology and Innovations (TEKES) and the participating companies and research institutions, provided the basic funding for the work as well as for the research visit to CDM. The test materials used in the work were kindly provided by Metso Minerals Oy and SSAB Europe Oy (formerly Ruukki Metals Oy).

I wish to express my gratitude to my supervisor Professor Veli-Tapani Kuokkala for his guidance, encouraging attitude and support, and enthusiasm towards my research. I am grateful to all the former and present staff at the Department of Materials Science and especially at the Tampere Wear Center for their help over the years and for the always so excellent working atmosphere. A special thanks is in place for Lic.Tech. Kati Valtonen, Dr. Marian Apostol, Dr. Vilma Ratia, M.Sc. Vuokko Heino, M.Sc. Niko Ojala, M.Sc. Juuso Terva and M.Sc. Kauko Östman for the great time spent at TWC laboratories, their sincere help, and for the valuable discussions concerning wear research. I also wish to express my thanks to M.Sc. Anssi Laukkanen for never exhausting help and tips with numerical approaches.

I owe much gratitude to Professor Georges Cailletaud for his valuable help and for sharing his vast knowledge that greatly aided me with my research. I want to thank Dr. Vladislav Yastrebov for the nice conversations, guidance and new insights. I thank all the people I came across at the CDM for hosting me during the research visit, and most essentially for the friendly atmosphere and making me feel welcome.

The support from my friends and family has been an infinite and tremendously appreciated resource. I address deep gratitude to my parents Jukka and Pirkko, as well as to my brother Vesa for their encouragement in everything and the never-ending support during my life. A thousand thanks to my beloved Elina for being by my side and for providing the much needed counterbalance and care.

Tampere, September 2016

Matti Lindroos

Author's contribution

The author planned and executed the mechanical testing of the materials with the aid of the personnel of the Department of Materials Science (DMS) at Tampere University of Technology (TUT). He also planned and carried out the abrasion and impact experiments for the test materials, excluding the execution of the normal direction impact tests, which were performed by Dr. Vilma Ratia. All of the material characterization was performed by the author, except for the scanning electron microscopy based measurements that were performed by M.Sc. Kauko Östman according to the instructions given by the author. The final data processing and analyses were carried out by the author. The author designed and implemented the material constitutive models in the finite element software and performed all of the simulations presented in this thesis. Some aspects related to the material models and their implementation were commented by Prof. Georges Cailletaud.

This thesis has been written by the author and it is the author's original work. The thesis manuscript was commented by the thesis supervisor Prof. Veli-Tapani Kuokkala. The author wrote all of the related publications mentioned in the thesis, and the publication manuscripts were commented and partially contributed by the co-authors.

Contents

Acronyms

ASB	Adiabatic shear band
CPOD	Crushing pin-on-disc
DASB	Deformed adiabatic shear band
DD	Dislocation dynamics
DOF	Degree of freedom
DQ	Direct Quench
DRX	Dynamic recrystallization
EBSD	Electron backscatter diffraction
FE	Finite element
FEM	Finite element method
GP	Gauss point
HSB	Hopkinson Split Bar
H-P	Hall-Petch
HVPI	High velocity particle impactor
HVx	Vickers hardness value, x denotes the weight used in the measurements
IPF	Inverse pole figure
MaSB	Macroscopic shear band
MiSB	Microscopic shear band
NSRS	Negative strain rate sensitivity
PSRS	Positive strain rate sensitivity
RVE	Representative volume element or aggregate
SEM	Scanning electron microscope
SFE	Stacking fault energy
TASB	Transformed adiabatic shear band
XFEM	Extended finite element method
Zébulon	Commercial finite element solver
Z-set	Commercial finite element software package

Nomenclature

Latin alphabet

a^{su}	Interaction matrix characterizing hardening from dislocation density of slip system s to u
A_b	Cross-sectional area of the HSB bar
A_s	Cross-sectional area of a test sample
b	Coefficient of slip hardening saturation
b_c	Magnitude of Burgers vector
b_{ta}	Normalization time in ASB
b_t	Exponent characterizing twin-twin interaction
b_χ	Coefficient of shear band self-hardening saturation
c	Kinematic hardening parameter
c_p	Specific heat capacity
C_0	Reference/initial configuration of material
C_{0s}	Speed of sound in the bar material
$\underline{C}^e$	Right hand Cauchy-Green tensor
C_T	Actual/current configuration
$\bar{C}_T$	Intermediate/relaxed configuration
d	Kinematic hardening parameter, or an exponent related to slip-twin interaction
d_0	Initial diameter of a mechanical test sample
D	Fitting variable related to β-method
e_i	i^{th} principal direction vector
E	Young's modulus
$\underline{E}$	Elastic part of the deformation gradient tensor
$\underline{\dot{E}}$	Rate tensor of elastic deformation
E_d	Dissipated energy during an impact
$\underline{E}_{gl}$	Green-Lagrange strain
E^{Mises}	Von Mises strain
$\underline{E}_p$	Macroscopic plastic strain tensor
f_{max}	Maximum volume fraction possible to twin
f^β_{max}	Maximum allowed twin volume fraction in a system β
f^β	Twin volume fraction of twin system β
$\dot{f}^\beta$	Twinning rate of a twin system β
F_{comp}	Compressive force in impact experiments
$\underline{F}^E$	Elastic part of the deformation gradient tensor
F_{max}	Maximum resultant force during an impact
$\underline{F}^P$	Plastic part of the deformation gradient tensor
F_x	Force perpendicular to the sliding direction of the impacting particle

F_y	Force parallel to the sliding direction of the impacting particle
ΔG_0	Activation energy for dislocation motion
g	Exponent characterizing coplanar twin-twin interaction
G_c	Parameter related to the dislocation annihilation process
h_0	Initial hardening rate
$h_{\alpha\beta}$	Hardening moduli characterizing hardening between α and β
H_χ	Parameter characterizing the magnitude of shear band self-hardening
H_{sbnd}	Parameter characterizing the magnitude of hardening from the interaction between shear bands
H_{rs}	Interaction matrix characterizing hardening from slip system r to s
H_{sl}^{tw}	Parameter characterizing the magnitude of hardening from slip to twinning
H_{slsb}	Parameter characterizing the magnitude of hardening from slip to shear bands
H_{nc}^{tw}	Hardening parameter characterizing non-coplanar interaction of twins
H_{cp}^{tw}	Hardening parameter characterizing coplanar interaction of twins and self-hardening of a twin system
$H^{tw\to sl}$	Hardening coefficient characterizing strength of twin-slip interaction
$\underline{I}$	Identity tensor, rank 2
$\underline{\underline{I}}$	Identity tensor, rank 4
$\underline{\underline{J}}_e$	Jacobian operator (elastic)
k_B	Boltzmann constant
k_c	Parameter controlling twin intensity
K	Nominator in Norton flow rule characterizing viscocity for slip systems
K_b	Nominator in Norton flow rule characterizing viscocity for shear band systems
K_o	Parameter related to probability of immobilizing a dislocation
K_t	Nominator in Norton flow rule characterizing viscocity for twin systems
l_{tw}	Average twin spacing
L_0	Initial length of a mechanical test sample
$\underline{\underline{L}}^n$	Elastic stiffness tensor for a grain or phase
$\underline{L}$	Total velocity gradient tensor
$\underline{L}^e$	Elastic velocity gradient tensor
$\underline{L}^p$	Plastic velocity gradient tensor
L_s	Gauge length of a test sample
L^{sm}	Mean free path for mobile dislocations before facing an immobilizing obstacle
m	Strain rate sensitivity factor
m_p	Mass of a projectile
$\mathbf{m}^s$	Vector defining slip direction of a slip system s
$\underline{m}^s$	Slip orientation tensor of a slip system s
$\underline{m}^{s_{tw}}$	Slip orientation tensor of a slip system s inside twin system β
$\underline{m}^t$	Twin orientation tensor of a twin system β
$\underline{M}$	Mandel stress tensor
$\underline{m}^\chi$	Orientation tensor for shear band system χ
n	Hardening or viscoplastic exponent
$\mathbf{n}^s$	Vector defining slip plane normal of a slip system s
$\mathbf{n}^\beta$	Vector defining twin plane normal of a twin system β
$\underline{N}^s$	Orientation tensor of a slip system s
$\underline{P}$	Plastic part of the deformation gradient tensor
P_c	Contact pressure
q	Hardening coefficient characterizing self and latent hardening
Q	Hardening coefficient for slip interaction

$\underline{Q}^{\beta}$	Transformation tensor for twin system β
r_s	Isotropic slip resistance of a slip system s
$r^{sl \to sl}$	Hardening from slip-slip interaction
$\dot{r}^{sl \to tw}$	Rate of hardening caused by slip to twinning
r^{χ}	Total resistance against shear banding of a system χ
r^{χ}_{ext}	Hardening against shear banding from external sources
r^{χ}_{t}	Hardening against shear banding
$r^{tw \to sl}$	Hardening from twin-slip interaction
r^{β}_{tw}	Hardening of a twin system β
R_{α}	Ratio between the maximum depth of the impact crater and the highest point of the pile-up region
$\underline{s}$	Deviatoric part of stress tensor
Δs	Distance traveled by a projectile in time Δt
$\underline{S}^{e}$	Second Piola-Kirchoff stress tensor
Δt	Increment of time
T	Temperature
$\bar{v}$	Average glide velocity of in a slip system
v	General expression of velocity
v_{0p}	Imposed driving particle velocity in ASB
ΔV^{*}	Activation volume
v_D	Debye frequence
v_{exit}	Exit velocity
v_{init}	Initial velocity
V_{neg}	Volume below zero-level (negative)
V_{pos}	Volume above zero-level (positive)
v^{r}	Accumulated slip in slip system r
$\mathbf{x}$	Current material coordinates
$\mathbf{X}$	Reference material coordinates
x^{s}	Kinematic hardening term of a slip system s

Greek alphabet

α_s	Average strength of an obstacle in front of a mobile dislocation, or kinematic hardening variable
$\dot{\alpha}^{s}$	Rate of the kinematic hardening variable
$\underline{\beta}$	Elasto-plastic tensor related to homogenization schemes
β_{α}	Coefficient characterizing the fraction of energy converted to heat
$\dot{\chi}^{r}$	Rate of accumulated shear in shear band system r
δ	Fitting variable related to β-method
ϵ	General expression of strain
$\underline{\epsilon}$	Strain tensor
$\dot{\epsilon}$	Total strain rate
$\dot{\epsilon}^{eqv}_{p}$	Equivalent plastic strain rate
$\underline{\dot{\epsilon}}^{sl}_{p}$	Contribution to plastic strain rate from slip
$\underline{\dot{\epsilon}}^{tw}_{p}$	Contribution to plastic strain rate from twinning
$\|\|\dot{\epsilon}^{m}\|\|$	Total strain rate in the matrix
$\dot{\epsilon}_{p}$	Plastic strain rate
$\dot{\epsilon}^{n,Mises}_{p}$	Von Mises plastic strain rate in a grain or phase
ϵ_E	Engineering strain

$\underline{\epsilon}_p$	Plastic strain
$\underline{\epsilon}_p^n$	Local plastic strain tensor of a grain or phase
ϵ_R	Reflected stress pulse
ϵ_T	True logatrihmic strain
ϵ_{TR}	Transmitted bar stress pulse
γ_c	Mean distance controlling annihilation process
γ_{sfe}	Stacking fault energy
γ^{tw}	Chacteristic twin shear
$\dot{\gamma}_0$	Reference shear strain rate
$\dot{\gamma}$	Shear strain rate
$\dot{\gamma}^s$	Shear strain rate of a slip system s
$\dot{\gamma}^\chi$	Shear banding rate of a shear band system χ
κ	Thermal diffusivity
λ	Thermal softening parameter in ASB
$\underline{\underline{\Lambda}}$	Elastic stiffness tensor
$\underline{\underline{\Lambda}}^\beta$	Elastic stiffness tensor in twin orientation
μ	Shear modulus, or micron (10^{-6} m)
μ_f	Coefficient of friction
$\dot{\nu}^s$	Rate of absolute value of slip of a slip system s
ϕ_{cp}	Cutting-to-ploughing ratio
ρ	Density of a material
ρ_m^s	Density of mobile dislocations
ρ_r	Dislocation density of a slip system r
ρ^s	Dislocation density of a slip system s
ρ^u	Dislocation density of a slip system u
σ_0	Yield strenght
$\underline{\sigma}$	Cauchy stress tensor
σ_g	General expression of stress
σ_E	Engineering stress
σ^{Mises}	Von Mises stress
$\underline{\sigma}^n$	Local stress tensor of a grain or phase
σ_T	True stress
$\underline{\sigma}^\beta$	Stress related to twin system β
$\underline{\Sigma}$	Macroscopic stress tensor
τ_0	Initial (critical) resolved shear stress
τ_0^χ	Initial resistance against shear banding
τ^s	Resolved shear stress in a slip system s
τ^{*s}	Thermally activated portion of stress in a slip system s
τ_μ^s	Critical stress to overcome long-range obstacles in a slip system s
τ_c^s	Critical resolved shear stress of a slip system s
τ_s^s	Saturation stress of a slip system s
τ_y	Initial resolved shear resistance of a slip system s

1 Introduction

The demand for more wear resistant materials originates from modern applications of many industries, such as mining, automotive, aerospace, and civil structures. The motivation to develop more efficient engineering structures and components can be seen beneficial in both economically and environmentally. Lighter, higher strength, and more wear resistant solutions can be attractive, for example, because of savings in energy consumption (e.g., petrol and running costs), higher load bearing capability per material thickness/volume, and increased component lifespan. The longer lifespans of engineering components can reduce stress on environment by increasing the service time of a component and thus reducing the need to replace it frequently. Another beneficial aspect of increased wear resistance and lifespan is that the downtime of production, which usually equals to zero production rates, can be reduced by some amount when better materials are available. The use of coatings, composites, and hybrids has proven useful in many cases reducing the weight of components and improving material and wear properties, e.g., strength and corrosion resistance. However, in heavy loading conditions that apply to mining, the aforementioned materials may not be able to withstand such conditions for long. Consequently, steels (and other metals) are still the most widely favored choice for wear resistant components due to their versatile mechanical properties, reasonable manufacturing costs and ease of joining of the components (e.g,. by welding). The motivation of this thesis is driven by the needs of the mining and earth construction industry to further develop the modern wear resistant steels, and hence the discussion here is focused on heavy loading conditions and large deformations.

The material loss, understood commonly as wear, of a material in a tribosystem is a complex phenomenon due to its dependence on the prevailing conditions. The wear resistance of a material is not a property but rather a measure of its performance in certain type of conditions. The external loading and environmental conditions are in the essential role, as well as the internal response of the material to these boundary conditions. The complex phenomena taking place during the deformation of a material require characterization at many different levels to evaluate the performance of the materials. The characterization is a step-by-step process including experimental testing, microstructure characterization, and numerical simulations, which all provide different types of information piecewise adding to the knowledge.

The performance of steels can be quantified in many different ways depending on the practical application. One way, for example, is to look at the capability of the material to absorb and reflect impact energy, which generally benefits from the micromechanical phenomena leading to high strength, high strain hardening capability, and good ductility. However, classically for steels, the inverse dependence between strength and ductility leads to a compromise between the properties. Advances in metallurgical engineering aim to reduce such trade-offs with the use of heterogeneous complex microstructures that

enable different micromechanical phenomena to take place. Dual phase (DP) steels have been used to take advantage of the soft ferrite phase combined with the hard martensite phase to generate reasonably high strength without reducing ductility drastically even in impact conditions, as well as to maintain the good workability. Transformation Induced Plasticity (TRIP) steels, which may already have quite complex initial microstructure with a mixture of ferrite, bainite, martensite and retained austenite, rely on the martensitic phase transformation of the softer metastable retained austenitic phase during deformation to facilitate noticeable increase in the strain hardening rate combined with good elongation properties. An alternative to DP and TRIP steels are the Twinning Induced Plasticity (TWIP) steels. The TWIP steels usually do not have very high initial yield strength, but during deformation the twinning of the crystal planes strengthens the grains by interfering with the dislocation motion, and the strain hardening capability is markedly good up to high elongations. This is due to the stable austenitic microstructure at room temperature, achieved usually by high alloying with manganese, which retains ductility even at high strains. These steels are especially preferred in automotive industry due to their superior behavior over conventional structural steel grades.

Further development of low alloy and microalloyed steels aims to increase the yield and ultimate strengths reaching above 1000 MPa, or even above 2000 MPa for steels with either close to fully martensitic microstructure with some bainite and retained austenite, or through the carbide reinforcing effect, for example. This increase in flow stress, or hardness, can be beneficial for resistance against hard particles in abrasive wear. However, the ductility of the initially hard microstructures suffer from their restricted capability to accomodate strain energy, e.g., due to the absence of softer phases and dominance of fragile carbides. What can follow, for example, is that the onset of localized plastic flow may trigger a sudden failure. However, the novel thermomechanical processing [205] during manufacturing in combination with microalloying of the martensitic wear resistant steels aim to enhance the steel properties by facilitating heterogeneous microstructures, which are initially hard but can macroscopically accommodate strain in a more homogeneous way retarding the localization effects.

As the composition and microstructures of the steels can differ considerably depending on how the microstructure is engineered, it is common for all different steel grades that when the heterogeneity of the microstructure increases, the more complex are the resulting deformation mechanisms at a microstructural scale. Furthermore, the deformation of crystalline microstructures is influenced by both strain rate and temperature throught the thermally activated dislocation motion. At very high strain rates, i.e., above $1000s^{-1}$, where even less time is available for deformation to take place, the deformation by dislocation motion becomes also affected by various dislocation drag mechanisms, which can increase the strength substantially. If deformation twinning, for example, coexists as a deformation mechanism with dislocation slip, it may at high strain rates become increasingly important changing the deformation behavior. At the same time, the effect of temperature further adds the complexity since, for example, the stacking fault energy, which is understood as a major concept affecting twinning, is dependent on temperature. Similarly metastable phases, such as austenite at room temperature, may no longer be stable at low or elevated temperatures. Additionally, as different deformation and hardening/softening mechanisms can be active at the same time depending on the temperature and loading conditions, the prior deformation of the material may become important, including the strain rate history of the material [104]. It then becomes more and more important to separately study the loading conditions in order to understand the fundamental reasons behind the wear behavior of materials.

When focusing on the mineral processing industry, the high stress conditions create a challenging environment for the wear protection steels. Great amounts of highly abrasive rocks are being processed and transported in earth construction, excavation, mining and mineral processing, inducing heavy abrasion, gouging, and impact wear. Materials are required to withstand repeated cycles of high stress loading causing scratching, denting, impacting, and mineral crushing without premature failure or critical reduction in the service life. The loading subjected to the surface poses both high strains and high strain rate to the material. Regardless that usually the processes are not operating at elevated temperatures, the effects of increased temperature can be observed locally because of the adiabatic heating in the above-mentioned conditions. At the microstructural scale, the accommodation of plastic deformation and related strain hardening can generate textures or other types of microstructural features on the material surface. In these regions, often referred to as tribolayers, which are to be distinguished from any oil layers, the wear behavior can change drastically from that of the bulk microstructure, which exemplifies the compound effects of the microscopic deformation mechanisms and their relationship to the prevailing loading conditions.

Experimental testing and material characterization aim to study the loading conditions and evaluate their relationship to the deformation and wear behavior. This is performed commonly on multiple levels, where the different scales or levels of physical simulation focus on increasing understanding of the prevailing phenomena. However, the closer the conditions are to practical applications, the more complex they tend to be. It follows that the individual characteristics may mask the other, which makes identification of the deformation or wear mechanisms rather challenging. The simplification of the conditions to more controlled environments inversely alienates the test conditions from the practical case. The level-by-level approach then offers a link between the application and the simplified experimental setups, which can be exemplified as follows: i) large scale wear experiments offers overall benchmarking of materials in the chosen conditions (e.g., impact-erosion wear tests with multiple rocks in contact) usually under complex loads, ii) simplified contact-to-contact conditions that simulate the effect of single contacts over a certain period of time in somewhat reduced loading conditions (e.g., a single grit contact), and iii) uniaxial mechanical testing that provides information of the mechanical behavior at low or high strain rates with specially designed test methods, which represent often satisfactory control over deformation conditions. The magnification from a larger scale to a more sophisticated scale aids the characterization process, the ultimate aim of which is to reveal the microstructure-properties-performance relationships in the material in question.

The measuring and monitoring techniques combined with prior and post test characterization is a valid and popular method for research and development of materials. In past decades, however, the use of numerical simulations has increased exponentially. Although several reasons motivate for the use of numerical approaches, perhaps one of the key factors is that the simulations usually are able to study the stress/strain state of the material throughout the entire time history of an incident in almost any desired condition. To some extent, the in-situ experimental and characterization studies offer the same possibility, but they often are challenging and expensive to do. The most common goals of simulations can be divided into two categories: i) the simulation is aimed to provide more detailed information about a specific case and material behavior (interpolating or cohesive method), ii) the models are utilized to predict certain material behavior in chosen conditions (extrapolating or predictive method). It is, however, extremely important particularly in the latter case, that the numerical models can be verified with experimental

tests. Another important aspect of simulations is the choice of scale, mainly of space and time, as illustrated in Fig. 1.1. If a more general level of information is sufficient, macroscopic level models can be used and long periods of time may be simulated (e.g., with Finite Elements or Discrete methods). Reducing the size and time can, however, provide much more detailed information, for example at the microstructural level. Meso-scale is usually used as a term for "between the macro and macro levels", which would include crystal plasticity and microstructure models (e.g., Crystal Plasticity Finite Elements CPFEM). Even finer analyses are performed whenever more fundamental information is needed, using dislocation dynamics (discrete dislocation dynamics) or atomistic level simulations (Molecular Dynamics or ab initio). This thesis focuses on the macro- and microscopic levels.

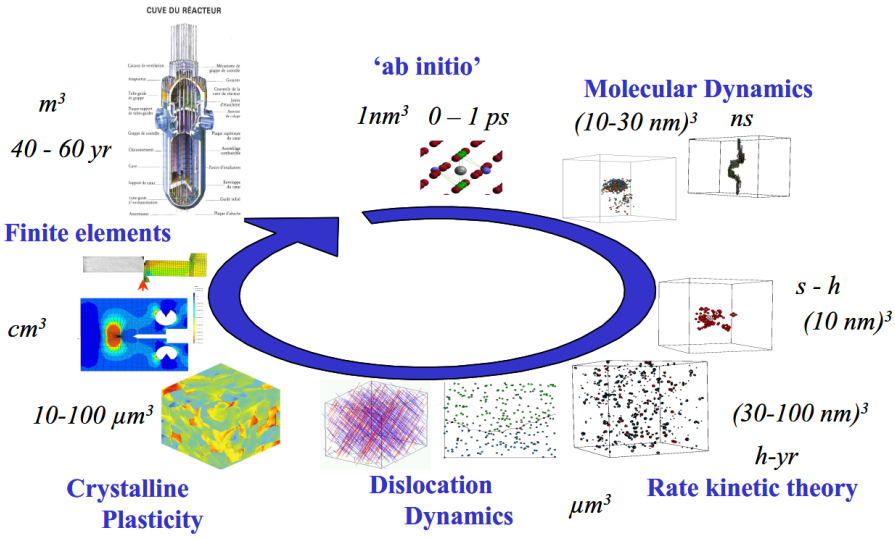

Figure 1.1: Multiscale modeling approach identifying different levels of simulations and scales for material research in nuclear reactors [145].

1.1 Aim and scope of the work

The main objective of this study is to gather information about the wear behavior of materials in abrasive and impact conditions and to provide simulation tools for future use in the investigation of the micro-scale behavior of the wear resistant steels. The work aims to increase the knowledge by focusing on the scale of individual contacts to elaborate the interactions between single hard particles and steel surface in abrasion, and to elucidate the dynamics of impact contacts. The characterizations performed for both wear situations as well as on the in-service samples used in the field (mineral crushing and mining) have a significant role in the understanding of the hardening/softening and failure behavior of the steels. More information about the deformation behavior is obtained with a mechanical testing program performed at quasi-static and dynamic conditions, after which microstructural characterization are used to reveal the main characteristics of the deformation mechanisms important also in the wear conditions. In order to gain more insight into the local material behavior at the microstructural level, two crystal plasticity models are developed and utilized. These modeling tools will be required

especially in the future studies when investigating the kinetics of the wear phenomena at the microstructural level during varying loading sequences. The modeling can also be used to benefit material development, e.g., for tailoring and optimizing wear resistant microstructures by minimizing the stress concentrations in the microstructure.

The research questions of this thesis are the following:

1. How can the high stress abrasion and impact conditions be best simulated for wear resistant steels in controlled laboratory testing environments and how well can these testing methods simulate realistic wear conditions?
2. What are the accuracy and the limits of the phenomenological FCC crystal plasticity material model including dislocation slip and twinning in describing the complex deformation and hardening behavior of single and polycrystalline Hadfield steels?
3. What is the performance of the BCC crystal plasticity model in describing the deformation behavior of martensitic wear resistant steels, and how can the shear banding phenomenon be integrated into the model to describe the localization of deformation in the martensitic microstructures?
4. What are the main deformation mechanisms and characteristics of wear resistant steels in high stress abrasion and high velocity impacts, what is the effect of loading conditions, and what are the most important factors causing hardening and failure in these materials?

The research questions 1 and 4 are addressed in the material characterization and experimental parts of the thesis in Chapters 4 - 6. The simulation part of the thesis in Chapters 7 and 8 focuses on the research questions 2 and 3. The relevant observations and findings are summarized in Chapter 9 along with the final conclusions.

The scientific novelty and contributions of this thesis can be summarized as follows:

- The thesis describes novel laboratory scale testing methods for studying the material behavior in high stress abrasion and impact conditions. The developed testing procedures were found suitable for studying the deformation and wear behavior of wear resistant steels with different initial microstructures.
- The wear testing results and material characterizations revealed many important phenomena related to the wear and failure behavior of the steels, such as the significance of strain hardening through several different mechanisms and their interactions, including shear localization. Many of these phenomena were also observed in the in-service samples examined in this work, showing that the utilized test methods can imitate realistic wear conditions quite well. In addition, the conducted high strain rate mechanical tests gave important new insight into the effects of strain rate on the material behavior of wear resistant steels, which has received less attention in the literature.
- A phenomenological FCC crystal plasticity model was formulated to describe the complex deformation and hardening behavior of austenitic manganese steels exhibiting deformation by both dislocation slip and twinning. The model was implemented in the finite element code, which widens its applicability for studying also realistic microstructures. It was shown that the model can quite well reproduce

the single crystal and polycrystal stress-strain and twinning behavior of Hadfield steels. Instead of only focusing on the stress-strain response of the material model, the model was also used to study the deformation behavior of polycrystal aggregates imitating the real grain structures of Hadfield steels. In addition, a method to transfer the loading history from the application level to the micro scale was suggested and demonstrated, providing a direct link between the microstructure and application level phenomena.

- Implementation of a phenomenological BCC crystal plasticity model was performed in the large deformation framework within a finite element code. The first results show that the model can describe the stress-strain behavior of BCC materials with satisfactory accuracy. A model extension including the shear band phenomenon was also implemented with simulations showing that shear banding has a marked orientation dependent effect on the stress-strain response of BCC single crystals with a martensitic microstructure.

2 Background of wear and deformation

2.1 Concept of abrasive wear and experimental setups

The material removal, or wear, from the material surface is a result of various factors, such as the material's internal properties and external conditions. In a wide sense, for example, material's microstructure, texture, and strain hardening capability including the corresponding mechanisms of hardening could be considered as internal material properties. In contrast, variables such as the type of contacting bodies and their properties, contact kinetics and environmental factors could be considered as external conditions. The two former variables typify the shape, size, and mechanical properties of the bodies subjecting loading and wear to the material, while the latter two include the type of loading and the amount of cycles, rate of deformation, friction, temperature and media surrounding the material. This means that the whole tribosystem contributes to the wear of a material denoting that wear resistance is not a material property *per se* but rather an observation of its behavior in a certain condition by complex interactions. Hence, the division to separate internal and external variables is quite crude, but to gain fundamental understanding of the affecting variables, one often makes this type of selective categorizations. Another classical way to to define wear is simply to express wear as the progressive loss of material from the surface of a solid body due to mechanical action together with possible thermal and chemical contributions [246]. To be more precise about the mechanical action or thermochemical conditions facilitating wear, often characterization of the type of wear is made, for example, as abrasive wear, impact wear, surface fatigue, or corrosion [115]. Of these categories, the first two are investigated in this work to elucidate the behavior of selected high and ultra high strength steels in these triboconditions.

2.1.1 Aspects of high stress abrasion in wear resistant steels

Mining and earth construction are typical industries that use high and ultra high strength wear resistant steels. Highly abrasive conditions including impacts create a demanding environment generally for any wear resistant material, and can be considered easily as the source of economical losses by wear. The intensity of abrasion depends on the individual application, whether it is an excavator, a mineral crusher, or a truck transporting minerals. All of these cases can be considered to be under high stress abrasion because of the magnitude of loading caused by the abrasives to the surfaces. One classification of high stress abrasion defines that the stress in the abrasive exceeds its mechanical failure limit and the abrasive is fractured in the process, generating fresh sharp abrasives capable of subjecting high contact pressures. Low stress abrasion, in turn, refers to a case where

the contact loads do not cause extremely high stresses in the abrasive or on the counter-surface. The exact classification is usually quite difficult, as the prevailing conditions in the tribosystem can easily change. Another way of classification is to widen the concept of high stress abrasion to consider mechanical response of the material facing abrasion. Gates et al. [78] conducted a detailed study of various testing methods including characteristics of high stress abrasion. They pointed out that if an abrasive is sufficiently strong to transfer the load to a wear resistant material, the features of high stress abrasion are already met when microcracking is observed in the material, either by fracturing of the hardening carbides or by the cracks in the microstructure. Gates et al. [78] also noted that by defining high wear rate as part of the characteristics of high stress abrasion, the criteria can already be met at moderate contact forces with high sliding velocities, which in many cases are known to promote wear.

As a consequence of these additional considerations, it can follow that by changing the material in an application a transition from low to high stress abrasion can occur even if the loading conditions and abrasives remain nominally the same. To explain this behavior, the severity of wear and the consequent wear rate can further be investigated by distinguishing different abrasive modes, such as microploughing, microcutting, microcracking and microfatigue, of which the most severe tends to be microcutting [246]. Therefore, the tendency to any single or a combination of micromechanisms depends on the material properties or behavior, such as ductile or brittle behavior. Again from the engineering perspective, the transition from mild to moderate to severe wear is controlled by many variables, which can be understood to a certain extent by establishing wear maps [130], which can be quite useful in design of components.

The effects of high stress abrasion on the behavior of wear resistant steels and their resistance against abrasion may be presented with a simplified schematic of a relatively sharp abrasive sliding on a steel surface, as shown in Figure 2.1.

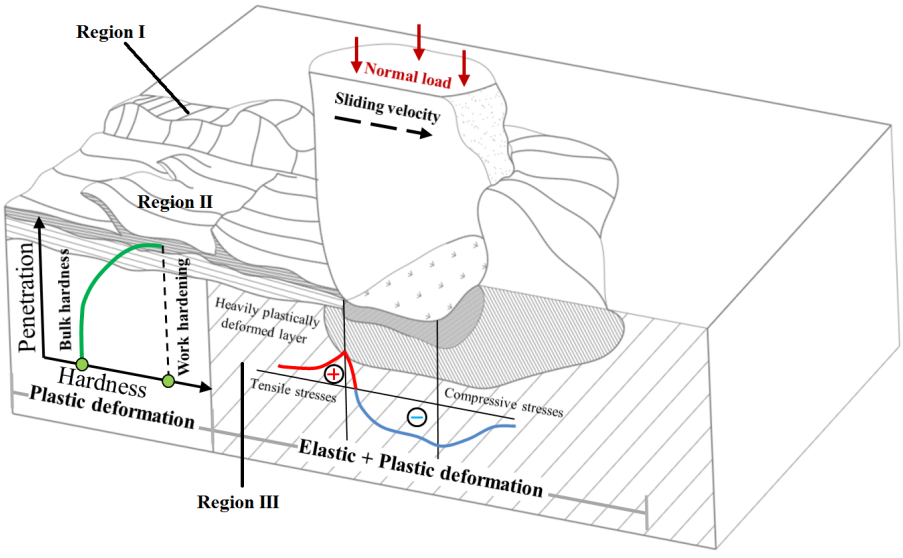

Figure 2.1: Illustration of a single macro-asperity sliding on a deformable surface representing high stress abrasive wear conditions [135].

The most apparent sign of intense wear on the surface is revealed by the propensity to

shear damage around the groove (region I) and at the bottom of the groove (region II), as the removal of material occurs mainly in these two areas. The shear in region I depends greatly on the ductility of the steel, but on the other hand, also hardness plays an essential role in the formation of the ploughed regions. If hardness is low, the penetration depth of the indenting particle can become large [95]. It follows that when the particle moves on the surface, it is ploughing material aside and in front of it. Hence, the ability of the steel to plastically deform dictates how easily the material is sheared off from the surface in the process. In contrast, when the penetration depth of the particle is low, i.e., when the hardness of the resisting surface is high, the energy is easily consumed in more cutting related deformation when the particle is moving on the surface. This, in turn, may increase the wear rate, especially when the steel's ductility is decreased by the increasing hardness. The ability of the material to withstand the subsequent deformation of the ploughed regions by the particles moving on the surface in arbitrary directions (not in the same path as the scratch groove) becomes important because the easier the previously deformed regions are removed, the higher the wear rate contribution of region I will increase.

Both the initial hardness and the surface hardening during deformation contribute to the steel's ability to resist the penetration of particles. The hardening can change the wear mechanism by directly affecting the ploughing/cutting behavior of the contact. Hence, the local deformation behavior defines the susceptibility of the material to damage, e.g., cracking. For example, if the material reaches its mechanical limit in the deformation process, tensile stresses can easily nucleate cracking from the surface, which can penetrate deep into the material and finally release even sizeable wear particles. The deformed regions in the vicinity of the surface can be understood as deformation based tribolayers, which in this context refer to distinct changes in the microstructure in comparison to the bulk microstructure. These changes can be produced, for example, by recrystallization of the microstructure, or be identified simply by visible shearing of the microstructure (elongation of the grains). The effects of the tribolayer on the wear rate may be beneficial (resisting) or degrading (accelerating) depending on its behavior in the contact, which ultimately depends on the material and the contact conditions.

The subsurface damage (region III) is not always easily detected because it is not visible on the surface of the material. The cracks may arise from the shear stresses caused by the contact, dependent or independent of the tribolayer. In the former case, wear particles may be generated by several effective mechanisms, such as fatigue that makes a subsurface crack grow up to the surface. In the presence of a tribolayer, the damage may follow from an interaction with the tribolayer, for example at the interface between the bulk and the tribolayer. In such a case, the cracks can grow along the interface causing failure of the tribolayer and detachment of even substantial layers of material and exposing less deformed material.

2.1.2 Common testing methods of abrasion

A large number of testing methods exists for abrasion. One of the most popular methods is the ASTM G-65 rubber wheel dry sand abrasion test. In this test, quartz is fed between a rubber wheel and the test material as a third body component. Ideally the contact conditions should be designed to correspond to realistic in-service conditions, but the rubber wheel test in most cases lacks this feature. However, since a great amount of data is available for this standardized test, it is possible to benchmark new experimental materials to the existing ones. Alternatively it is possible to design specialized testing

methods that include more application related conditions. For example, an extension to the conventional pin against disc configuration abrasion test can be made by insert gravel in the contact between the pin and the disc, e.g., a crushing pin-on-disc setup [211]. In this case, the pin material as well as the counter-surface contacting the rock may be more easily related to the application materials. Also, modifiable systems allow better detailing of the abrasive conditions, e.g., prescribing the movement/sliding velocity of the abrasive on the surface. For example, the rubber wheel experiment forces the majority of the movement to happen only in one direction, whereas the crushing pin-on-disc experiment allows the arbitrary movement of the rocks against the pin (test material). Modifications of course can also be made to the standardized rubber wheel test, for example by replacing the rubber wheel by a steel wheel, but the same testing principle still remains.

Other methods that include specific loading and environmental conditions, such as impact loading and presence of media (e.g., water), can be used to study the combined effects of abrasion and other external conditions. For example, the impeller-tumbler test [181] subjects impacts to the surface of the test material, while the particles abrade the surface by a sliding process. Slurry type of experiments [167], in turn, cause similar contact conditions but the samples may be submerged in the abrasive medium. More detailed analyses can be performed with scratch test experiments, where the sample surface is abraded with a single indenter. This approach can yield more specific information about the contact, but as a trade-off the situation can become more distant from the actual in-service conditions because of the simplifications made. Nevertheless, the benefit of these tests is that information can be gathered from the effects of loading, friction etc., which can also be obtained at elevated and sub-zero temperatures.

The essential aspect in the precise choosing of right testing method(s) is the type of information required of the material behavior. In the best scenario, field experiments down-scaled to laboratory multi-contact experiments and single contact conditions can be combined to produce good data in multiple lenght scales.

2.2 Impact wear by hard particles and experimental setups

Impact wear occurring due to the deformation and material detachment caused by impacting solid particles is distinguishable as its own form of wear. The nature of the incidents is different from 'normal' abrasion, as usually the time for the deformation to take place is fairly short depending on the impact energy and impulse of the incident. It is known that impacts may also take place without any wear by simple collisions of objects on the surface, causing only elastic and plastic deformation. The capability of the material, or specifically its microstructure, to *absorb the impact energy* is essential in order to avoid high wear rates due to cracking and shearing of the material. From a different point of view, the materials capability to *reflect impact energy* is significant as well, since the surface may be able to reflect impact projectiles away absorbing only a small proportion of the projectile' kinetic energy in the contact.

2.2.1 Surface deformation and wear under impacts

The deformation and wear caused by hard particle impact/erosion can be investigated in simplified conditions by controlling as many variables as possible, such as presented by Lindroos et al. [133] in the examination of single impact conditions (see also Chapter 6). A simplified schematic of a hard spherical particle impacting a ductile steel surface

is presented in Figure 2.2. The illustration shows some of the regions essential to the characterization of the impact-related deformation, wear, and damage behavior.

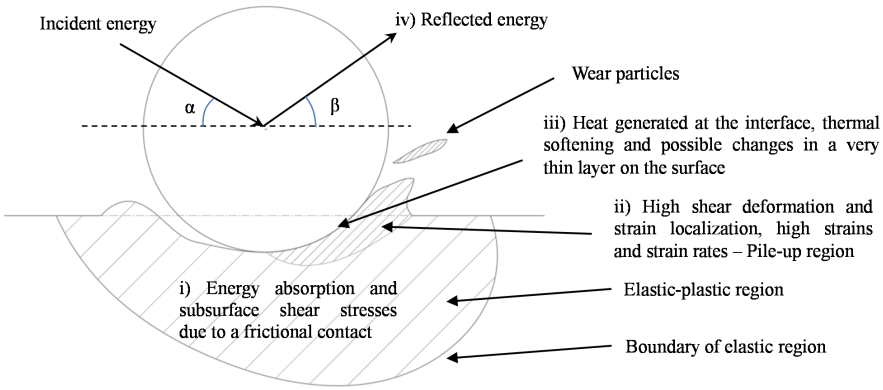

Figure 2.2: Illustration of an impact incident of a hard spherical particle on a ductile steel surface [133].

The impact resistance of a steel can be assessed by its aforementioned ability to absorb energy. Effectively, the impact resistance depends on several parameters such as the strenght, the material's ability to resist deformation in dynamic conditions, and ductility. The extent of the volume undergoing elastic-plastic deformation (region I) is not clearly defined in Figure 2.2, but it characterizes the material's ability to absorb energy in certain impact conditions and how easily cracks are formed in the subsurface microstructure. A more specific large deformation region II, or the pile-up region, is often distinguished in an oblique angle impact. This region is subjected to significant shear deformation and is hence susceptible to deformation localization phenomena, while the probability for shear localization depends on the impact angle. Among others, Hutchings and Winter reported shear banding and fracture in this pile-up region after impacting spherical [99] and angular [223] particles on the sample material. Some early studies consider the pile-up region as already lost material based on the fact that it can contain a considerable amount of damage, such as small cracks.

In the surface region III, the friction between the particle and the steel surface has an effect on the subsurface stress state and on how the ploughed regions are formed. Sundararajan and Shewmon [207], and Sundararajan [206] studied the surface deformation and friction behavior using a numerical approach and analytical models. They found that the best fit resulted when friction included both sliding (adhesion) and ploughing terms. They also concluded that friction is a strong function of the impact velocity and incident angle α.

Another aspect of the frictional contact between a sliding particle and the surface is that the heat generated in the contact may become significant in terms of the plastic behavior of the steels. The rate of the frictional energy generated in a sliding contact may be written as $\dot{Q} = \mu_f P_c v$, where μ_f, P_c and v are the coefficient of friction, contact pressure, and sliding velocity, respectively. At high impact velocities and high surface pressures combined with moderate friction, the heat generated in the contact can also affect the formation of tribolayers. The same situation holds for high stress abrasion with particles sliding at rather high velocities.

The wear in impact conditions is often presented by the weight loss caused by one kilogram of impact particles, which can be used to benchmark different materials. Another way

to assess the material performance is to look at the material loss per used energy (i.e., $[mm^3/J]$), since material loss is a result of the material's capability to absorb energy or reflect it away. The use of this type of a definition for the wear rate can reveal specific characteristics of the incident, e.g., changes in the deformation and wear behavior. Although it is not necessarily clear where the energy is consumed, it is obvious that the initial and residual kinetic energies in the form of 'in-out' energy can be used for example to verify the simulation results. Alternatively, the volume loss inflicted by the initial kinetic energy of a particle could be useful design-wise for example by constructing wear models based on the initial kinetic energies of the particles impacting the surface, because such information is often more easily available than the actual amount of energy consumed in the contact.

2.2.2 Testing methods of high velocity impacts

The solid particle erosion/impact-abrasion at normal or oblique angles is often experimentally studied with various multiple impact test rigs. Such erosion tests are aimed to imitate realistic operation conditions and they thus can provide useful information about the material's wear resistance. The laboratory scale experiments are, however, in many cases restricted to low impact energies due to small particle sizes (often below 500 μm) and/or relatively low impact velocities (often below 10 m/s). The effects of small particles can be challenging to characterize by the microstructural observations, since the impact crater sizes are rather small.

To gain more control over the individual contacts, different types of single particle impact test setups including high impact velocities have been presented. For example, Hutchings and Winter [100] developed a 16 mm barrel gas gun that fires smaller particles, such as 3 mm steel balls using sabots. In their early setup, the velocity of the sabot was measured instead of the velocity of the particle(s) without any knowledge of the particle's exit velocity. Sundararajan and Shewmon [206, 207] studied oblique impacts on ductile materials using also gas propelled 4.76 mm particles. In their slightly more advanced setup, they measured the initial velocity of the particles with a timer and the exit velocity and exit angle using an aluminium foil system. Recently, Cenna et al. [41, 42] used a piston-tube setup to accelerate projectiles towards target materials. However, the projectile sizes were still small steel and zirconia balls with diameters of 500 μm and 150 μm. This caused the crater size to be very small, which required the use of electron microscope in the characterization. In addition, Cenna et al. [41, 42] did not measure the exit velocity, and thus the dissipated energy during the contact could not be determined. Wang and Shi [218] studied foreign object damage to aerospace components with a helium gas powered pressure tube. The projectile size was larger, 6.35 mm, which allowed easy characterization by optical microscope. More importantly, their experiments were aimed to provide data for numerical simulations with finite element methods in order to calibrate a damage model. This highlights the fact that well controlled single impact experiments can be used to provide verification data for simulations which then, hopefully, can be utilized in the application level studies to reduce the cap between laboratory and larger scale events.

2.3 Role of shear banding

In many engineering applications such as machining and cutting, mining, metal forming, and ballistic protection, the materials are subjected to high strains and high strain rates,

which can often lead to shear banding. The shear banding phenomenon can be identified as a highly localized shear deformation in relatively narrow regions in a specimen or a component. For example in wear conditions such localization of deformation may in some cases act as initiation sites for cracks and failure, thus promoting wear.

As several descriptions for the shear bands exist in the literature, it is good to make a distinction between the macroscopic and microscopic shear bands. In the macroscopic shear bands (MaSB), the shear localization exceeds the grain boundaries and forms meso- and macroscale deformation patterns (e.g., visible shear regions that stretch through the failed compression samples). In the microscopic shear bands (MiSB), shear localization happens mainly at the grain level, e.g., by starting from multiple slip activity leading to shear concentration in a single grain. It should be noted that shear banding is not always related to dislocation slip only, but it may be caused by a combination of several deformation mechanisms, for instance by accumulation of slip and twinning leading to a local deformation band. Also, the micro shear bands do not necessarily always widen to form macroscopic shear bands. In this work, MaSBs are identified and discussed in Chapter 6 in conjunction with the impact experiments. The concept of MiSBs is included in the crystal plasticity framework presented in Chapter 8, and in the characterization of the deformation mechanisms in Chapter 4.

2.3.1 Initiation of localized deformation

The initiation point of localized deformation is usually denoted as an instability point in the compression stress-strain behavior, ($\partial\sigma^g/\partial\epsilon = 0$), either seen in the macroscopic stress-strain curve or defined as the local response in the grain level. Prior to this point, metals generally exhibit strain hardening ($\partial\sigma^g/\partial\epsilon > 0$), i.e., increasing resistance against plastic flow. Beyond the instability point, given that such exists, ($\partial\sigma^g/\partial\epsilon < 0$), softening behavior[1] is evidenced as the transition from nominally homogeneous flow at the micro level to more inhomogeneous flow by shear localization. Figure 2.3 shows the competing effects of strain rate and temperature, where an increase in strain rate has a positive effect on strain hardening, while increase in temperature often results in softening. It is worthwhile to note that in tension the material usually exhibits apparent softening without any shear banding, when the material's strain hardening capability is exceeded by the stress increase due to the reducing cross-sectional area. The concept of shear banding is visualized for various scales in Figure 2.5.

[1] Zener and Hollomon [238] first described thermal softening behavior that overcomes strain hardening at high strain rate by adiabatic or quasi-adiabatic conditions.

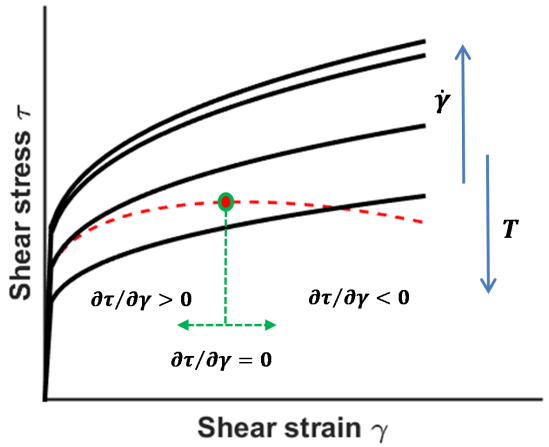

Figure 2.3: Illustration of the stress-strain behavior with strain hardening and softening schemes in compression, after [224].

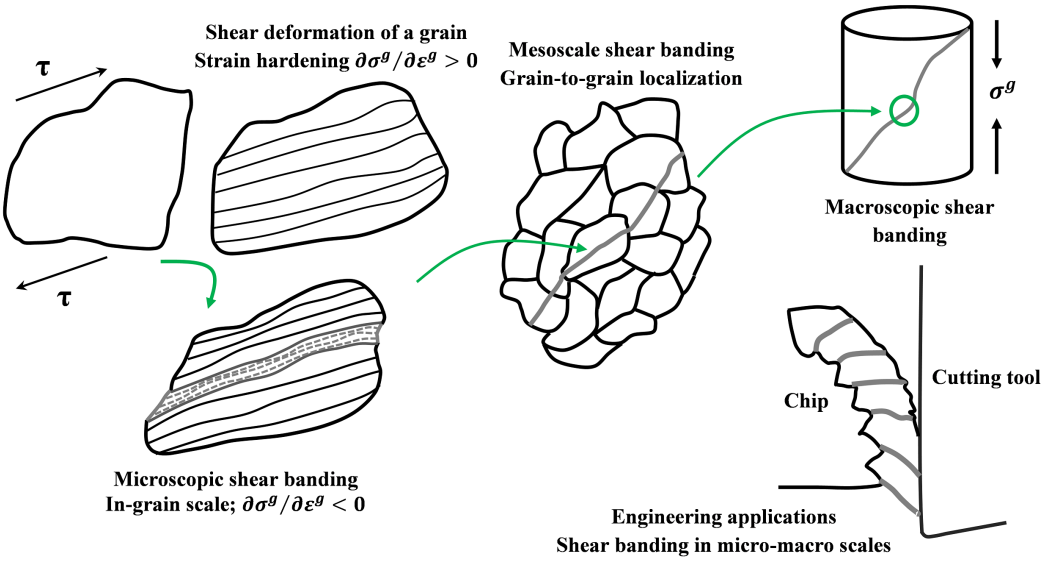

Figure 2.4: Idealized schematic of shear banding in a polycrystalline microstructure.

2.3.2 Adiabatic shear bands

A special case of shear banding are the adiabatic shear bands (ASB)s. The adiabatic shear bands have been under particular interest during the last decades due to some practical aspects of steel deformation under high strain rates [61, 224]). The formation of ASBs can take place, for example, when large strains are experienced by the material at high strain rates, leading to an increase of temperature. The term 'adiabatic' refers to a situation where the time available does not suffice for the heat to transfer away from the region of

interest, leading to approximately adiabatic conditions and large temperature gradients. In contrast, at low strain rates the conditions are mostly isothermal, meaning that heat is transferred away by conduction, convection and radiation. In such conditions the materials are not usually prone to any adiabatic shear banding, but instead deformation shear banding may occur. The increase in local temperature is facilitated by the intense shear localization, where only a small part of the mechanical energy is stored in the microstructure, for example in dislocations, while rest of it goes to heat. A simplified initiation criterion (e.g., $\partial\sigma^g/\partial\epsilon < 0$) can be more easily met when the *strain hardening* is overcome by the *strain softening*, enabling local instabilities that could lead to shear banding.

The increase of temperature due to adiabatic heating in an arbitrary material volume is often expressed as

$$\Delta T = \frac{1}{\rho c_p} \int_0^{\epsilon^p} \beta_a \sigma^g \partial\epsilon_p \tag{2.1}$$

where c_p is the heat capacity and ρ is the density of the material.

The coefficient β_a expressing the amount of energy dissipated as heat is frequently taken as 0.9. Of course, it should be noted that the value of β may not always be constant during deformation but can depend on the strain rate, strain, and the material in question [69, 93, 184]. However, this simplification is often made and found in many cases reasonable [112]. Also, the boundary conditions have an effect on the heat transfer. For example, in high strain rate compression tests it can happen that the average temperature of the whole sample increases fairly rapidly during deformation, but if shear bands are formed, the local temperature may still be significantly higher than the average temperature.

The adiabatic shear bands can be classified into two separate types [61]. The deformed adiabatic shear bands (DASB) refer to shear localization that can be identified from the microstructure easily by fibering and texture of the material in the shear direction. The transformed adiabatic shear bands (TASB), or white shear bands, are distinguished from the DASBs by their white appearance when etched. The term transformed stems from the assumption that the material volume inside the shear band undergoes phase transformation and/or related recrystallization process. However, it is still under debate how the TASBs are formed, as will be discussed below. According to Dodd and Bai [61], the basic difference between the two types of shear bands is that the heavily deformed DASB's are precursors to the more brittle TASB's. Figure 2.5 presents an etched micrograph of an ultra high strength steel subjected to a high strain rate impact, showing homogeneously of deformed bulk microstructure, deformed adiabatic shear bands, as well as transformed adiabatic shear bands.

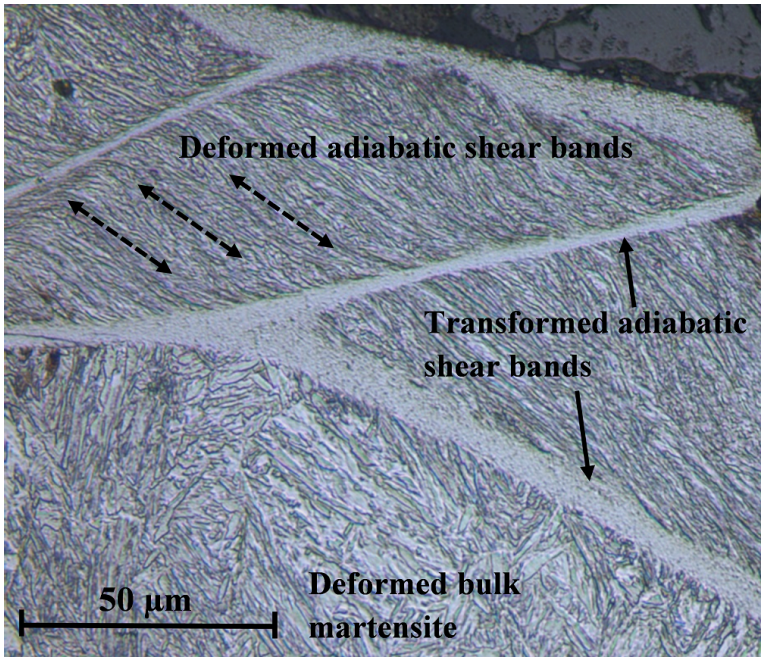

Figure 2.5: Ultra high strength steel deformed by an impact, showing deformed adiabatic shear bands (dashed arrows aligned with the apparent shear direction), transformed adiabatic shear bands (appearing white), and deformed bulk martensitic microstructure bounded by the transformed band.

2.3.3 Microstructure, formation and failure of shear bands

Increasing interest in the microstructure inside and at the boundaries of the shear bands is motivated by the complexity of failure initiation in the shear bands. Many experimental and characterization results (e.g., [63, 121, 136, 150, 175, 234]) report of fine grained microstructures inside the shear band region, tending to get even finer towards the centers of the bands. Depending on the material under investigation, both highly elongated and equiaxed grains or mixtures of the two, have been reported. However, as pointed out above, no consensus about their formation prevails. Furthermore, the difference between the microstructures inside the DASBs and TASBs can be distinctive. For instance, Duan et al. [64] studied adiabatic shear banding in AISI 1045 and reported highly elongated grains inside the DASB's originating mainly from large deformations with high dislocation densities, while the grains inside the TASBs were equiaxed with low inherent dislocation density after being generated partly by other mechanisms (e.g., the recrystallization process). Linz et al. [136] characterized the adiabatic shear bands (mainly transformed) in IF-steel with EBSD, and found that the equiaxed grains form generally closer to the middle of the band, while elongated grains remain closer to the boundaries of the shear band. Figure 2.6 shows their observations in an Orientation Imaging Microscope map together with a quality map of the measurement to clarify this. Outside the apparent shear band boundaries the microstructure appeared elongated with deformation texture following the shear direction. Linz et al. [136] also reported increased number of deformation twins accommodating strains in these regions. Hence, this observation indicates that the regions next to the shear bands is are also of interest, as

other deformation mechanisms tend to be activated as well. In fact, it is unclear whether the twins preceeded the formation of shear bands, or whether they appear due to the deformation and increased temperature in the shear region. The texture information from the shear bands is of major importance in revealing the formation of the microstructure, but the challenging factor in the characterization of the shear band regions with EBSD is the resolution of the SEM, when the grain size is below 0.2 μm, as frequently observed for the shear bands [153, 230, 231].

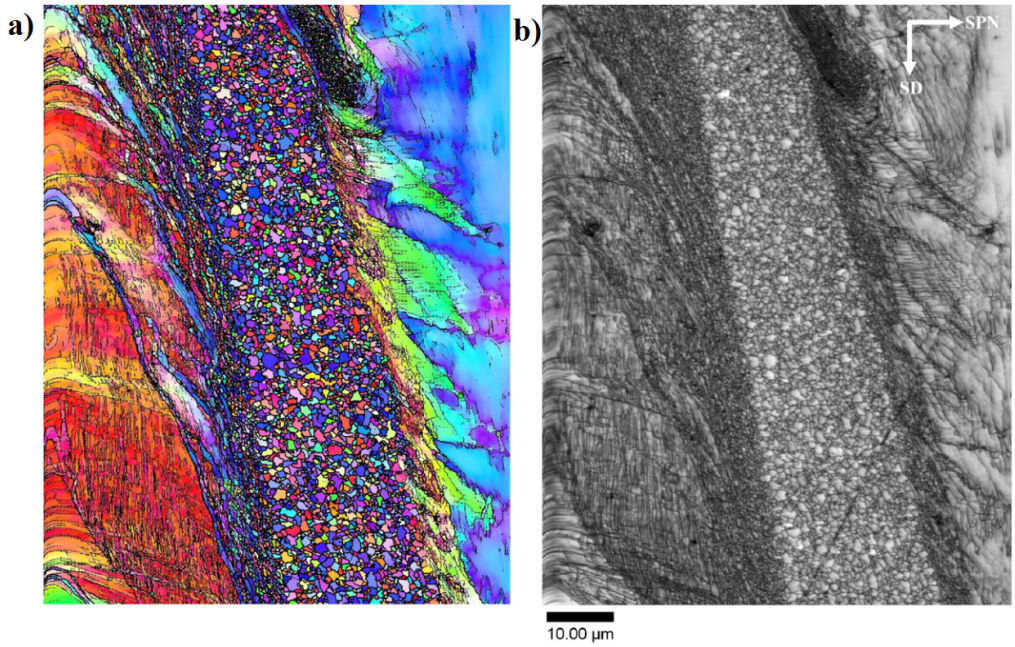

Figure 2.6: a) OIM colored map of a transformed shear band in IF-steel showing misorientations between recrystallized grains, and b) the quality map of the same area [136].

Some studies [47, 208] support the ASB formation theory based on the austenization and rapid quenching leading to a hard small-grained microstructure. Diffusion based kinetics of austenization has been criticized unlikely since the time available for the conventional diffusion controlled transformation is far too short, at least by many magnitudes. Instead of diffusion, an alternative theory of a *displacive* martensite-to-austenite reversion has been suggested by some authors [123, 161, 162] to account for the extremely rapid heating taking place during shear band formation. However, it is challenging to experimentally verify this due to the short temporal scale of the phenomenon.

The present belief according to a great number of studies, e.g., [9, 152, 153] and a recent review [194], is that the dynamic recrystallization (DRX) process is responsible for the grain refinement inside the shear bands in many metals and alloys. The recrystallization is considered dynamic because the observations support that the process is effective *during* the deformation of the shear band region and not afterwards. However, due to the high temperatures reached inside the band, for example Hines and Vecchio [89] suggested that recrystallization occurs only during cooling of the deformed microstructure, giving the ASB formation more static recrystallization characteristics. Regardless of the interpretation of the dynamics of the ASB formation, more important is that the process

leads to a grain structure refinement. In many cases it is accepted that the DRX in ASBs is a *thermally driven* process as a part of high strain rate deformation in adiabatic conditions. However, Rittel et al. [188] studied shear banding in Ti6Al4V with high strain rate experiments by loading the samples to the failure strain and to half of this value (interrupted test). DRX based grain refinement was observed in both cases, but Rittel et al. [188] did not classify the DRX observed in the interrupted test as a adiabatic shear band, leading to a conclusion that DRX may also preceed shear banding by this interpretation. A very similar finding was made by Hines and Vecchio [89] in the tests performed at high strain rates in liquid nitrogen for copper, where it was observed that it is possible for DRX to occur before shear banding, demonstrating the complexity of the process. On the other hand, it is also possible that prior strain could affect the formation of ASBs. However, Rittel et al. [187] observed that in Ti6Al4V quasi-static pre-straining does not affect the failure strain of the material or much the ASB formation, either. Recently, however, Peirs et al. [175] observed that the nanocrystalline microstructure in Ti6Al4V caused by DRX took place only after shear band formation, which indicates dependence on the loading conditions, since they used almost twice the strain rate of Rittel et al. [188].

An explanation for the dynamic recrystallization has been suggested by Hines and Vecchio [89] and by Meyers et al. [151]. They analyzed the classical mechanisms of high-angle boundary migration and subgrain coalescence in the recrystallization based on the time and temperature inside the ASBs. It was noted that the kinetics of these phenomena are inadequate to produce the observed grain sizes during the deformation and cooling of the ASBs. Hence, they concluded that also other mechanisms must contribute to the process. The most common explanation for the DRX process is based on a dislocation dynamics controlled mechanism arising from dislocation interactions, cell formation, and rotational sub-grain formation. The concepts such as 'mechanically-driven subgrain rotation' [89], 'rotational dynamic recrystallization' [150], or 'progressive subgrain misorientation' [136] have slight differences in their definitions, but the mechanisms suggested in them are essentially the same: i) first uniformly distributed dislocations account for the deformation and form cell structures, ii) the cells elongate with deformation, generating elongated sub-grains by a recovery process (dynamic rearrangement of dislocations), iii) increasing deformation break-up the dislocation cells, and iv) recrystallized grains with high angle boundaries are formed. In this process, the geometrically necessary dislocations (GND) take care of the strain incompatibility [68, 185]. Meyers et al. [151] and Nesterenko et al. [165] suggested the visualization, presented in Figure 2.7, of the DRX process by dislocation interactions. Additionally, successful but quite complex modeling approaches of this process have been presented by Hines et al. [90] based on crystal plasticity model, and by Rittel and Osovski [185] based on the dislocation dynamics model.

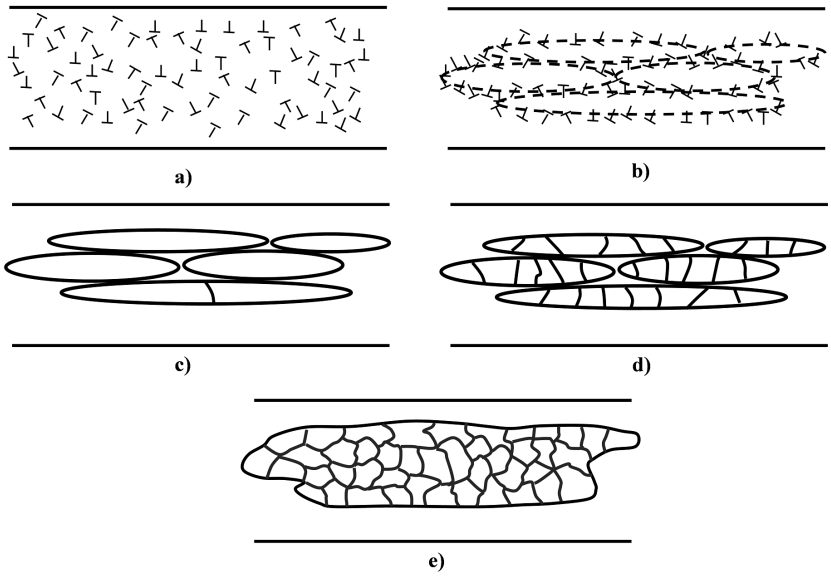

Figure 2.7: Microstructure evolution inside an adiabatic shear band: a) Uniform dislocation distribution, b) elongated dislocation cells c) elongated sub-grains with high density dislocation walls d) sub-grain break-up, and e) dynamically recrystallized grains by rotational formation. After [151, 165]

Dodd and Bai [61] suggested an equation to describe the half width of the ASB based on the governing thermomechanical equations of a uniform heat source (the ASB is assumed insulated and heat diffusion is stationary from the heat source).

$$\delta_{asb} \approx \sqrt{\frac{\rho c \kappa T}{\beta \tau \dot{\gamma}}} \tag{2.2}$$

where ρ is the density, c_p is the specific heat, κ is the thermal diffusion coefficient, β_α is the fraction of mechanical energy converted to heat, and is the $\dot{\gamma}$ shear strain rate inside of the ASB.

Wright [224] pointed out that Equation 2.2 is more related to the thermal thickness of the ASB, because it is based on the solution of thermal balance, and hence an alternative form was suggested in Equation 2.3 that defining the "mechanical length scale". The mechanical lenght refers to the changes in velocity within the ASB [220].

$$\delta_{asb} = \left(\frac{1-m}{m} \frac{\lambda \sigma_0 b_{ta}^m}{k} \right)^{-1/(1-m)} v_{0p}^{-(1+m)/(1-m)} \tag{2.3}$$

where m is the strain sensitivity parameter, λ a thermal softening parameter evaluated in isothermal conditions, σ_0 is the yield strength, b_{ta} is the normalized time, and v_{0p} is the model driving velocity defined by the strain rate and sample thickness ($\dot{\epsilon} d_s$).

Wei et al. [220] measured and calculated the thickness of the ASB with the Equations 2.2 and 2.3 an ultra fine grained iron. The results were roughly 15 μm from the experiments,

14 μm from Equation 2.2, and 2 μm from Equation 2.3. This shows that the Dodd and Bai Equation 2.2 works better at least in this particular case. Wei et al. [220] suggested that the discrepancy between the analytical results may come from the fact that the Wrigth's equation does not account for any transformation inside the band (e.g., DRX) and assumes a sharp drop of strain rate at the boundary of the apparent shear band. Based on the discussion above, the elongated grains near the shear band edges, both inside and outside, suggest that the strain rate and the temperature field are not strictly bounded to the apparent edge of the calculated shear band width. Hence, Equation 2.2 gives a more reasonable estimation in this particular case, as it is more related to the thermal diffusion from the heat source to its vicinity with less limitations from sharp 'boundaries'. Batra and Kim [21] showed, as could be reasonably expected, that the thermal properties of the material have a nonlinear effect on the ASB width. However, in their study the thermal conductivity was not proportional to the square-root, as in Equation 2.2, which means that the estimation could be too simplified. In addition, Batra and Chen [20] showed that the choice of the constitutive visco-plastic model has a marked effect on the band width and growth rate. Chen and Batra [44] pointed out that the mean spacing of the shear bands is a strong function of the strain hardening exponent, strain rate and the characteristic length of the sample and the microstructure [45].

The failure has been often observed to take place inside the transformed shear band rather than in the boundary region. It could be that if the temperature field softens the region outside the shear band, it behaves in a more ductile manner, while the inside of the newly formed microstructure is more susceptible to initiate failure [61]. For example, Bassim and Odeshi [19] identified and suggested a five step process of the failure inside the adiabatic shear bands in high strength martensitic steels, as shown in Figure 2.8: a) small microvoids are formed inside the ASB, b) the voids form clusters, which elongate parallel to the shear bands, c) microcracks are formed at the ends of the void clusters, d) the microcracks and void clusters become interconnected along the shear band (inside it, not at the boundary of the ASB), e) the growth and propagation of the microcracks lead to failure inside the ASB regions. According to their observations, the failure showed initiation in both the middle section of the band region with equiaxed grains as well as in the elongated grain zone. It is quite likely that the failure process occurs already during the deformation and propagation of the shear bands, and thus complete separation of these phenomena is not physically justified, although it makes the fundamental understanding of the process more simple.

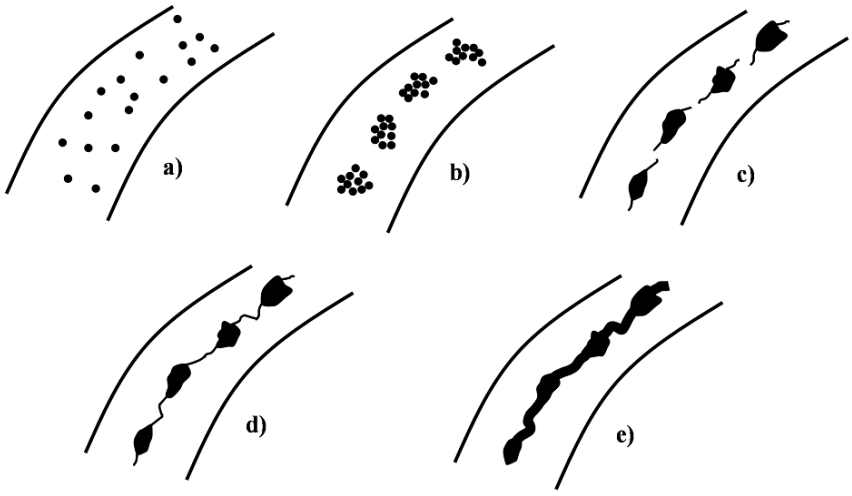

Figure 2.8: The process of failure nucleation and development inside an adiabatic shear band, after [19]

2.3.4 Numerical modeling of shear band activity

The models of shear bands may be roughly divided into two categories: analytical models and numerical models. The analytical models aim to derive the exact solution of the adiabatic shear band formation and propagation. This, however, often includes simplifications and the solutions are derived for example in one dimension only [224]. Multidimensional analyses can quickly become complex, for instance in the case a mode II shear analysis [241]. The loading conditions and geometries in engineering components usually are multidimensional in nature and therefore the use of numerical models may be more attractive. This is because the numerical models can be applied to arbitrary geometries and loading conditions when discretization methods, such as finite elements, are used. The constitutive relations are an essential part of both analytical and numerical models; they for example dictate when the shear band criteria are met and the band formation initiates, as well as how the shear band propagation evolves. It has been suggested that in the simulation of shear banding it is a good idea to divide the phenomena into two stages, i.e., the *formation* (e.g., depending on the critical shear strain, strain softening, etc.) and the *propagation* (e.g., thermally coupled visco-plastic relationship with evolution laws) [20, 44, 45, 148].

In this context, the *formation* of ASB's is, as mentioned above, a local occurrence of deformation instability, which is a relatively slow process due to the uniform deformation at first stage and more dependent on the nominal strain rate. For example, the strain rate at the center of the shear band has been estimated to be three times the nominal strain rate of the surrounding material [224]. On the other hand, the following *propagation* is a much faster dynamic process and dependent on the local strain rates due to extreme growth velocities [83], where the shear band could be considered as a phase transition region (as the grain size is much smaller than in the matrix). This region propagates in the matrix characterized by a shear band tip (e.g., when simplified it is somewhat similar to a crack tip field damaging the material), which is then a different phenomenon by its growth mechanism than the ASB formation. A third stage could be introduced to this

type of phenomenological separation as the failure process (a fracture model), because shear banding does not necessarily lead to immediate failure, depending on the material behavior and ductility. The failure could be embedded in the constitutive description of the propagation process by directly utilizing damage mechanics, or be described as its own evolution process with fracture mechanics. Therefore it actually would lead to a third stage in a sense that when the damage or fracture criterion is met, the evolution of failure would occur separately from the actual propagation of the band, i.e., the shear band can grow independently while the cracks evolve only in some parts of the shear band.

The actual choice of the constitutive model for shear banding is dictated by the modeled problem and used numerical solver, such as a mechanical or a thermo-mechanical solver. The model is generally required to be viscoplastic to accommodate the effects of strain rate, but on the other hand, it is beneficial to be coupled with temperature. This way the model can describe strain hardening and/or possible softening related to strain rate and temperature. Furthermore, the computational framework must be suitable for large strains, as the localized deformation is essentially a result of large shear strains. Some of the well known material models have also been applied to shear band studies, at least to some extent. Johnson and Cook [109] proposed an empirical model including strain and strain rate dependence as well as thermal effects. The model has been adapted to various conditions due to its fairly simple use and reasonable agreement with experimental results. The models of Follansbee and Kocks [70] and Zerilli and Armstrong [239] with origins in the dislocation dynamics of different crystalline microstructures are more physically based.

Finite elements has been a popular choice to implement a constitutive model for shear bands and to simulate their evolution in a variety of conditions, such as simple experimental shear and torsion tests [62, 148], machining and manufacturing [6, 193], impacts and perforation [22, 57, 242]. The most challenging characteristic of the shear band activity in FE models is their spurious mesh dependency. This is commonly seen for example when the mesh is refined and it follows that the shear band width is also reduced. In contrast, coarse meshes yield too wide shear band regions, while fine meshes may overestimate shear localization by stress concentrations arising from the mesh itself (e.g., fine mesh with sharp 'corners' provoking singularities). For example, Ambati et al. [6] noticed a fairly strong mesh dependency in the simulation of orthogonal cutting that included shear banding. The mesh size directly affected the shape of the chips, which is one of the primary prediction aims of the simulation. If the shape is incorrectly predicted by the simulations, the usability of the results is quite limited, as the optimization of the cutting tool geometry or process parameters depends on the correct chip formation. Ambati et al. [6] also noticed that it is possible to suppress the mesh dependency partly by using a non-local damage model. The dependency, however, persisted especially with highly thermally dependent material models. Li et al. [126–128] and Medyanik et al. [148] employed so-called mesh-free or meshless[2] methods to investigate adiabatic shear bands. The main outcome of these studies was that the meshless methods can describe the occurrence of adiabatic shear bands in a far less mesh-sensitive manner, i.e., i) refinement in mesh/density of particles affects notably less the shear band size, ii) the direction of the shear band propagation and its curvature appear more realistic because the propagation

[2]In meshless methods, the material is treated as particles and their region of influence (interpolation), a background mesh is often only used for integration and hence the mesh sensitivity is less pronounced as material points are not directly bound to the mesh. The reader may refer to the books describing these methods [125, 138].

does not tend to align with mesh edges. Also, mesh distortions that may take place inside the shear band region due to a stress collapse are relieved with the meshless technique. However, although the meshless techniques seem an attractive choice for shear band studies, their implementation in computation codes is not yet widely available and the cost of computations may be much higher. Alternatively, Areis and Belytschko [12] utilized the extended finite element method (XFEM), which is generally used for crack growth, and showed that this method can represent shear band activity reasonably well but still requires modifications for more precise solution (e.g., enrichment of the elements inside the shear band region in addition to the shear band tip).

Another way to increase the understanding of the effects of microstructure on shear banding is to focus on a smaller microstructure level aiming to capture the intragrain and intergrain interactions, and hence the growth of microscopic shear bands to macroscopic shear bands. This differs from the above described approach by taking into account the actual or representative microstructure of the material in the discretization (i.e., grains and their orientations are actually included). The constitutive relations also differ since the microscopic deformation is required to be presented by dislocations, twinning, etc. Therefore, a convenient way to include microscopic deformation mechanisms is to use crystal plasticity models (see section 2.5), in which, for example, the dislocation motion is presented with crystallographic slip planes and directions. Hines et al. [90] focused on the details of DRX occurring inside the ASBs by studying the slip based crystal rotations and the resulting misorientations between the grains in BCC bicrystals. In their model, they observed the progressive subgrain misorientation as a cause for the mechanically driven DRX process. However, in this approach the model concentrated in a rather small scale on the formation of MiSB's and their intragrain evolution (ASBs in this case), while the intergrain level was mostly omitted as the model was intended only to show this particular misorientation feature. The most likely reason for limited implementations of the shear banding in the crystal plasticity environment is that the connection between deformation mechanisms and their interactions, softening and hardening behavior, and microstructural features is difficult to maintain both physically and numerically. For example, Forest and Cailletaud [73] studied the effects of multiple slip localization with interfaces and material flaws showing that softening causes localized flow which can also propagate to hardened regions. Furthermore, a more complex crystal plasticity model was used by Forest [72] to reveal the effect of lattice curvature on shear localization. Forest realized that the effect is more pronounced in kink bands, which could in some cases be considered precursors for shear banding, than in other types of slip bands pointing out the complex relationship of deformation mechanisms. It is also uncertain what is the direct effect of grain boundaries on the propagation of shear bands, as the movement of dislocations in the modelling approach of Ma et al. [140, 141] over the grain boundaries showed dependence on the geometric (orientations) properties of the grains and is a thermally activated process in nature. This means that in more accurate models it would be required to take into account the attempts of the dislocations to move over the grain boundaries, where its success depends on various variables, such as on the critical stress's Schmid factors of the incoming and outgoing slip systems in neighboring grains [140]. The incoming here refers to the active slip system in one grain, and the outgoing to the slip system having the highest probability to activate in the neighboring grain.

An alternative framework that can be considered as a meso-scale model was suggested by Anand and Su [8] to study shear banding in amorphous material, where the shear bands could extend through the whole simulated structure. In this framework, an additional virtual deformation mechanism to account for the shear bands was introduced being closely

analogous to dislocation slip in the crystalline structure although actual slip systems do not exist. The model is driven by the 'slip planes' constructed from the principal stresses, as the shear banding could be expected to initiate in the stress concentrations generated by these stresses. It follows that the virtual slip planes constructed in this way do not necessarily correspond the common slip planes and directions of crystalline structures, and hence the term non-crystallographic is adopted. Later, Wei et al. [221] used this framework to study the failure of grain boundaries in nano-crystalline FCC microstructures. The results showed reasonable agreement with the experiments but did not provide grain-to-grain propagation, as the model was only implemented for the failure of the amorphous grain boundaries. Jia et al. [105–108] added the non-crystallographic virtual shear banding to slip and twinning in FCC crystals to produce an alternative additional form of deformation. Their model reproduced the experimental results quite well in terms of the generation of shear bands as well as the development of texture. The activation of the potential shear band systems was taken to follow the Schmid type resolved shear stress activation, i.e., there exists a resistance against shear banding with a threshold stress, which somewhat differs from the above mentioned common constitutive formulation of macroscopic models. It was, however, noted that a minor shortcoming in the model was the absence of any hardening related to shear banding and its interaction with slip or twinning, which can lead to an over-pronounced effect of shear band softening.

2.4 Deformation twinning

According to the classical definition of deformation twinning, it is required that the twin and the surrounding matrix lattices are related either by reflection across some plane (the twin plane), or by a rotation of 180 degrees about an axis (the twin axis). The term *deformation* twin refers to a condition, where simple homogeneous shear of the matrix lattice forms a deformation twin, at least in principle. For example, in the FCC structure this takes place on the $\{111\}$ planes in the $< 112 >$ directions, whereas the slip can be taken occur on the $\{111\}$ planes in $< 110 >$ directions. This process is considered different from the dislocation slip by its more co-ordinated individual atom displacement in contrast to the apparently chaotic generation and growth of slip bands. Another distinct characteristic of deformation twinning is that it is polarized, which is different from slip deformation. It means that shear by twinning can only take place in the predefined direction and it cannot be reversed in the same way, i.e., twinning occurs only in the 'positive' directions ($+ < 112 >$), whereas slip can occur in both positive and negative directions ($\pm < 110 >$). Finally, a difference between deformation twinning (or mechanical twinning) and transformation twinning is due to their formation. The latter is usually formed as a result of some type of martensitic transformation, which follows the crystallographic theories of martensite. [48]. In the scope of this work, the deformation twinning is more relevant and some of its aspects are briefly discussed in this section.

2.4.1 Mechanisms of the initiation and growth of twins

The fundamental mechanism(s) of deformation twinning has been under debate in literature. The reason for different observations and theories may be partly due to the studies performed on different materials, varying compositions, and simply in different loading conditions. It can also be challenging to distinguish twin initiation and growth from each other during deformation, and to understand the role of interaction between dislocation slip and twinning. The most classical mechanisms are explained based on the characteristics of the dissociation of a perfect $b = a/2 < 110 >$ dislocation and interaction

with other dislocations [48]. Three mechanisms are most commonly used to describe the phenomenon: the pole mechanisms based on original work of Cottrell and Bilby [49] and Venables [214, 215], the deviation mechanisms (e.g., the Miura-Takamura-Narita (MTN) model [154]), and the three-layer stacking fault mechanism suggested by Mahajan and Chin [142]. These mechanisms are frequently reviewed with the focus on the twin initiation and growth, as for example in [103, 204].

The actual mechanisms responsible for twin initiation and growth are still under debate, as many authors claim that one or the other mechanism is responsible for twinning based on their experiments and characterization. For example in quite recent studies on FCC materials, both the MTN and three layer stacking fault models have received support from both experimental and modeling perspectives. Idrissi et al. [103] and Karaman et al. [114] suggest that the MTN or its modification best describes the twinning phenomena in Hadfield type steels. Bracke et al., [30], Steinmetz et al. [204] and Kibey et al. [117] found evidence that supports the three-layer stacking fault type twin nucleation mechanism. It is highly likely that the twin mechanisms can vary in different circumstances (e.g., loading conditions, rate of deformation, compositions) and therefore no sole mechanism can always apply [48]. Generally, however, a common feature in all nucleation models is that the existence of multiple slip and stress concentrations is required to trigger twinning.

The initiation and growth of twins is often formulated in an analogous way with the slip by critical resolved shear stress, which is based on the Schmid law. This choice simplifies the complex nucleation mechanisms and dislocation scale interactions so that twinning can be treated in a phenomenological sense alongside with slip, especially in the modeling approaches (e.g., [203] compared to a different approach in ref. [43]). However, in some cases a large scatter in the experimental results is observed even in the same material, rendering the verification of the models challenging. This can partly be explained by the strong competition between dislocation slip and twinning, and also by the high sensitivity to orientation, intragrain stress concentrations, and grain boundary emission of dislocations [87]. Beyerlain et al. [28, 29] observed that the activated twin variant is not always with the highest Schmid factor. However, when multiple twin variants were active, the highest Schmid factor did contribute the most to the total twinned volume, while decreasing Schmid value lead to a decreasing volume contribution [28]. Additionally, the twin systems with lower Schmid factor appeared thinner. Both of these observations lead the authors to suggest that twin initiation and growth can be expressed by using a Schmid type resolved shear stress, at least in the case magnesium. Also in general, a reasonable correlation with the onset and growth of twins has been found with Schmid factors, yet occasionally with some deviations, for example as reported quite recently in refs [31, 79, 86, 170].

2.4.2 Properties and conditions affecting twinning

A great interest exists to understand the effect of internal properties and external conditions on twinning. This is driven by the motivation to optimize steel behavior in selected conditions and to achieve the best possible performance in the engineering applications. In automotive applications the TWIP steels are used in the chassis, and hence the effect of strain rate can be one of the most important factors in crash safety. Alternatively, in some wear applications facing a lot of abrasion, strong surface strain hardening may be desired combined with reasonable ductility to avoid fracturing of large wear particles from the surface. The performance can be improved by alloying and understanding its effects on strain hardening, elongation and fracture properties [46].

Numerous studies have been performed to identify the effects of stacking fault energy, temperature and strain rate, grain size, and alloying on the twinning propensity, of which some most important aspects are summarized below:

- **Stacking fault energy:** It is well known that stacking fault energy(SFE) is one of the most important factors affecting twinning. Low to moderate stacking fault energy, i.e., 20-40 mJ/m^2, has a preferential effect on deformation twinning. For example Frommeyer et al. [76] reported that in TWIP steels the critical value lies around 25 mJ/m^2. The main reason for this is that lower stacking fault energy leads to wider stacking faults as the separation of partial dislocations becomes easier, increasing also the twinning propensity. In the aforementioned region of SFE, mechanical twinning can work together with ordinary dislocation slip as a deformation and strain hardening mechanism. If the stacking fault energy is high enough, the separation of partial dislocations is not energetically favorable, leading to deformation mainly by dislocation slip. On the other hand, very low of stacking fault energy ($<$ 15-16 mJ/m^2 [76]) usually leads to a higher probability of martensitic transformation in austenitic microstructures. However, in some cases with a suitable SFE, concurrent dislocation slip, twinning and martensitic transformation can occur [5]. The stacking fault energy is affected by temperature, which is one reason for the changes in the propensity of twinning at different temperatures. Also alternative views exists about the importance of SFE in twinning. For example, El-Danaf et al. [66] proposed that the dislocation density and homogeneous slip distance, which depends on the grain size, affects more the twinning stress than SFE.

- **Temperature and strain rate:** Temperature and strain rate are known to affect the twinning propensity, increasing it when temperature is decreased and strain rate is increased, which implies some analogy to the thermal activation process [48]. For dislocation slip, if a strong sensitivity to temperature exists, usually also a quite strong sensitivity to strain rate is observed. For twinning, similar effect is not always clear, which may be due to the competition between slip and twinning that may hinder the direct effects of temperature or strain rate on twinning. However, at low temperatures some observations suggest that the twinning stress is less affected than the critical stress for slip by the reduction of temperature, hence promoting twinning. The effect of high strain rates is generally more distinct, for example under shock loads many crystal structures deform mainly by twinning [48]. Hokka [94], Curtze [51], and Frommeyer et al. [76] studied TWIP steels at moderately high strain rates, i.e., from 10^3 to $10^4 s^{-1}$, and also noticed that twin propensity is increased with increasing strain rate. However, they also reported that low temperatures lead to less extensive twin formation than expected, as twins appeared only in the most favorable orientations. Hence, the contradictory results on the effect of temperature on twinning are not yet fully understood. This may partially be explained by the strong link between twinning and SFE and its connection to the favorable range for twinning. On the other hand, an indirect contribution to the stacking fault energy may also arise from the adiabatic heating at high strain rates [50, 178].

- **Grain size:** Decrease in grain size has been observed to have a negative effect on twinning [48, 51]. The general explanation is that the twinning stress increases with decreasing grain size through a similar Hall-Petch type relationship as for the dislocation slip, but it has a higher effect on twinning [66, 87]. At sub-micron grain sizes, however, an inverse effect has been observed. The twinning stress first

increases but when the grain size becomes small enough, it starts to decrease again [229, 243].

- **Chemical composition:** Changes to the chemical compositions are often made to improve some properties of the material or to get rid of some other properties, such as to stabilize austenite, improve elongation or toughness, add corrosion resistance, or alter the strain hardening capability [38, 39, 46, 82, 222]. The use of alloying elements may also affect the material's propensity of twinning, changing the balance between different deformation mechanism. Very often this happens via changes in the SFE.

The preceding summary is not exhaustive, but it points out that depending on the conditions prevailing in the applications, careful design of the alloys is very important. Other factors and local kinetics, such as the competition between slip and twinning, can easily hinder the underlying micromechanism and only the apparent effect of conditions is observed.

2.5 Crystal plasticity micromechanical modeling

The plastic deformation of crystalline materials at microscale is usually accommodated by dislocation glide, possibly together with some additional deformation mechanisms such as deformation twinning or martensitic transformation. The mechanical response of crystalline materials is anisotropic and usually also time-dependent in nature. In a single crystal level this means that the crystal orientation has an effect on the outcome of deformation, for example in the activation of different deformation mechanisms. Another aspect is that the distribution of orientations and defects affects the material response differently at different lenght and time scales. [190]. For example, lattice defects cause internal friction for mobile dislocations at nano-scale, which may then accumulate to stress concentrations at micro-scale due to dislocation interactions, and finally manifest themselves as cracks at the meso-scale. An illustration of this division of scales is presented in Figure 2.9.

Crystal plasticity aims to provide means to describe the material behavior based on the physical aspects of dislocation motion, their interactions, and related strain hardening and/or softening mechanisms, and to implement single crystal behavior to polycrystal microstructures to investigate their behavior under various loading conditions and environments. From the modeling point of view, models representing these phenomena may be categorized into three main groups based on the context of the equations of evolution: phenomenological models, quasi-physical models, and dislocation-dynamics based models (DD). All of the model types represent the deformation at varying levels, including either a single phenomenon or a set of phenomena occurring during deformation, such a generation of three-layer stacking faults that initiate twinning, and hardening due to different types of dislocation interactions. Of the three model types, the phenomenological and quasi-physical models are closely connected, and in many occasions no direct separation is made due to their similar contents. The main difference is that DD based models often use very discrete relations of individual phenomena (e.g., inspired even from *ab initio* calculations), such as dislocation movement and interaction, while phenomenological descriptions also include the interactive behavior but in a more average sense. Nevertheless, it should be noted that it does not directly mean that phenomenological models would be any less meaningful than the fine detailed DD models, regardless that the former

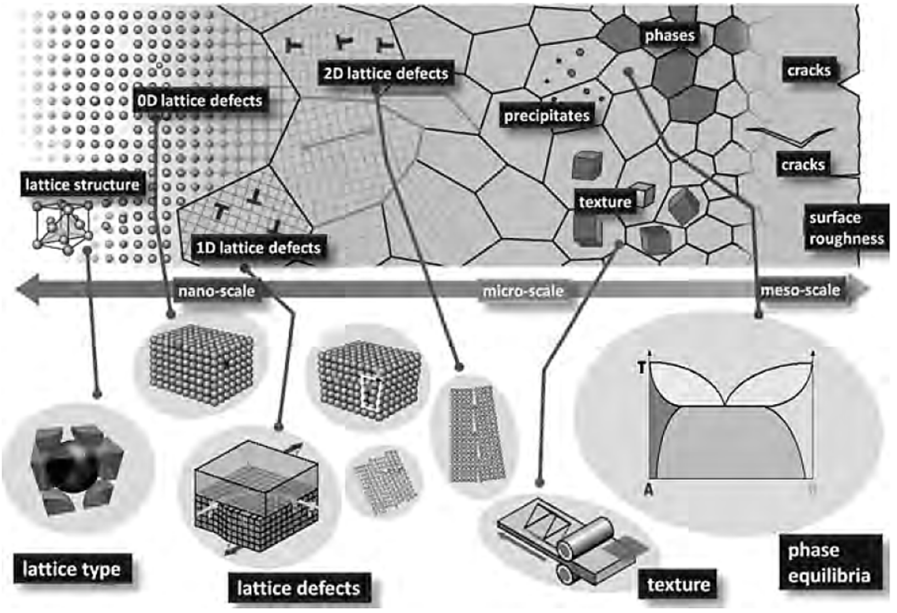

Figure 2.9: Presentation of some of the important scales in material behavior, reprinted from [190]

models generally use quite simplified expressions in the equations. On the contrary, the phenomenological models may perform better than the very complex DD models if only little information is available from the material's physical behavior, or the model parameters are poorly chosen. Generally, it appears that increasing the details describing the deformation behavior increases the amount of model variables, which may lead to difficulties in parameter identification. Often it also increases the computational time, e.g., due to slower convergence. In addition, the complexity of the deformation behavior (including twinning or martensitic transformation) requires more complex descriptions in the models, which will essentially lead to the same situation. In the end, the models normally can provide only an estimate of the material behavior, and thus the complex relations are still only approximations and the slightly simplified mathematical equations can easily provide the same results. Examples of the different model types are briefly given in the following.

2.5.1 Phenomenological and quasi-physical models

Quite many studies use the phenomenological modeling of the dislocation mechanisms. A general idea is that a set of equations describe the flow of dislocations in the microstructure, including their interactions with self and latent hardening models. The hardening models usually adopt a suitable mathematical equation, such as exponential hardening [34] or secant hardening functions [18], to present the shape of the strain hardening curves in single crystals. The choice is justified by the fact that often the models including interactions can describe the shape of the hardening curve quite accurately, including for example single and multple slip systems and multistage hardening [14, 18, 174]. Mechanisms that appear in some materials can be adapted to the models quite widely, such as the Bauschinger

effect by introducing a kinematic hardening part to the models. The transition to quasi-physical models from "purely" phenomenological models is fairly easy to make because the quasi-physical models in many occasions only modify the hardening type and consider the flow rule still unchanged, e.g, by introducing a dislocation density type of a hardening rule [92].

The phenomenological models usually consider the critical resolved shear stress as a state variable, which evolves according to the hardening rules. The relationship between the resolved shear stress and the shear strain rate can be approximated with viscoplastic flow rules, which at the same time dictate the material's strain rate sensitivity. In their review of crystal plasticity models Roters et al. [191] note that the phenomenological models rely on the evolution of the critical resolved shear stress (initial + hardening contributions) instead of directly using the lattice defect population as a variable. The latter aspect may become relevant when the model is aimed to provide information also about path- and size-dependence, which can for example be presented with geometrically necessary dislocations. However, the phenomenological models are able to represent the stress-strain behavior of a variety of materials quite well. A typical phenomenological flow model for FCC still frequently in use was suggested by Hutchinson et al. [102]. The same type of flow rule was applied successfully later for example by Peirce et al. [174] and Bassani and Wu [18]. The shear strain rate is given as:

$$\dot{\gamma}^s = \dot{\gamma}_0 \left| \frac{\tau^s}{\tau_c^s} \right|^n sign(\tau^s) \tag{2.4}$$

where $\dot{\gamma}_0$ is the reference shear rate, τ^s is the resolved shear stress of a slip system and τ_c^s is the critical resolved shear stress or the slip resistance as it evolves with hardening. Exponent n characterizes the material's strain rate sensitivity of slip. Sometimes the form $1/m$ is used as well, where the rate independent limit is $m \to 0$. The sign function provides the direction of the flow as given by the sign of the resolved shear stress directions. Alternatively, Teodosiu [210] suggested a flow rule including a threshold based on the theory of thermally activated dislocation motion. Starting from the Orowan relation:

$$\dot{\gamma}^s = \rho_m^s b_c \bar{v} \tag{2.5}$$

where ρ_m^s is the dislocation density of mobile dislocations, b_c the Burgers vector, and $\bar{v}$ the average glide velocity of this system. When considering the time to overcome the obstacles negligible compared to the time consumed in front of the obstacle before overcoming it, the average velocity can be expressed as:

$$\bar{v} = \frac{b_c v_D}{exp\left(\frac{\Delta G_0}{kT}\right)\left[2sinh\left(\frac{\tau^{*s}\Delta V^*}{k_B T}\right)\right]^{-1}} \tag{2.6}$$

where v_D is Debye frequency, b_c Burgers vector, ΔG_0 activation energy, ΔV^* activation volume, k_B Boltzmann constant, T temperature, and τ^{*s} the thermally activated portion of stress of a system s. If a separation of the components of the critical flow stress needed to make the dislocation mobile is assumed, the contribution of long range obstacles, such as grain boundaries and precipitates, to the critical shear stress is τ_μ^s. The additional part required to overcome short range obstacles with some atomic spacings, such mobile dislocations crossing dislocations in another slip system, i.e., the forest dislocations, is τ^{*s}.

The latter component relies partly on thermal energy and hence is *thermally activated*, whereas the former component is *athermal* with necligible dependence on temperature. Therefore, the critical shear stress required to activate a system s is $\tau_c^s = \tau_\mu^s + \tau^{*s}$. After combining Equations 2.5 and 2.6 and performing simplifying approximations, i.e., replacing τ^{*s} with $\tau_\mu^s - \tau^s$ and developing a Taylor series approximate, Fivel and Forest [139] presented the slip rate equation in a more convenient form to be used in numerical models:

$$\dot{\gamma}^s = \rho_m^s b^2 v_D exp\left(\frac{\Delta G_0}{kT}\right)\left|\frac{\tau^s}{\tau_c^s}\right|^{\frac{\tau_c^s \Delta V^s}{kT}} \tag{2.7}$$

given that the reference strain rate $\dot{\gamma}_0$ and strain rate exponent n can be written as:

$$\dot{\gamma}_0 = \rho_m^s b^2 v_D exp\left(\frac{\Delta G_0}{kT}\right) \;\; and \;\; n = \frac{\tau_c^s \Delta V^s}{kT} \tag{2.8}$$

Finally the equation would end up in the classical form presented in Equation 2.4 by pointing out that the phenomenological parameters $\dot{\gamma}_0$ and n have a physical basis by depending on τ^{*s}, ΔG_0, and ΔV. The phenomenological parameters are usually identified from the experimental data generated at various strain rates and occasionally coupled with temperature.

The rate of hardening, i.e., the increase of the critical resolved shear stress, above its initial value τ_0, can be given for example as formulated by Peirce et al. [174]:

$$\dot{\tau}_c^s = \sum_\beta h_{\alpha\beta}|\dot{\gamma}^\beta| \;\; with \;\; h_{\alpha\beta} = qh + (1-q)h\delta_{\alpha\beta} \tag{2.9}$$

The hardening moduli $h_{\alpha\beta}$ characterize the self ($\alpha\alpha$) and latent hardening terms ($\alpha\beta$). The parameter q, defining the level of latent hardening usually varies between 1 and 1.4 and can be experimentally determined. In the equation h is the hardening coefficient. Alternatively, the hardening moduli can be expressed with a secant hardening model as a function of cumulative shear strain in a slip system:

$$h(\gamma) = h_0 sech^2\left(\frac{h_0\gamma}{\tau_s^s - \tau_0}\right) \tag{2.10}$$

where τ_s^s is the saturation strength, τ_0 is the initial resolved shear stress, and h_0 represents the initial hardening rate. In a similar manner, Bassani and Wu [18] and Wu et al. [172] used the secant hardening model with saturation to describe the three stages of hardening in single crystals. Cailletaud [34], Méric and Cailletaud [157] proposed a phenomenological viscoplastic model that describes the micromechanical behavior of single crystals and the anisotropy occurring in complex loading paths:

$$\dot{\gamma^s} = \left\langle \frac{|\tau^s - x^s| - r^s}{K} \right\rangle^n sign(\tau^s - x^s) \tag{2.11}$$

In this model, the slip flow is strain rate sensitive characterized with a Norton type flow rule, where K and n and characterize the strain rate sensitivity. The term $|\tau^s - x^s|$,

describing the effective resolved shear stress, includes the effect of kinematic hardening e.g., the Bauschinger effect. The isotropic slip resistance r_s is composed of additive components describing the slip resistance strength including the initial resolved shear stress and a component from hardening, which can be explicitly given as an internal variable:

$$r^s = \tau_0 + Q \sum_r H_{rs}\{1 - exp(-bv^r)\} \ ; \ v^r = \int_0^t |\dot{\gamma}^r| \tag{2.12}$$

where H_{rs} represents the dislocation interactions. Hence, the slip resistance evolves depending on the activity of slip systems, while Q and b characterize the magnitude of hardening and its saturation, respectively. The slip does not occur if $|\tau^s - x^s| < r^s$. The directionality is again described by the sign function. This model is used in this work with more details given in Chapter 7.

Extensions to the phenomenological models for the inclusion of detailed physical aspects are frequently suggested. For example, the Tabourot-Teodosiu model [209] utilizes the flow expression in Equation 2.4 but extends the effective slip resistance with a dislocation density driven hardening model, based on the estimate of Mecking and Kocks [147] ($\tau_c^s = \alpha\mu\sqrt{\rho_u}$), which was further modified by Franciosi [74] and Tabourot et al. [209] into a more general form:

$$\tau_c^s = \alpha_s \mu b_c \sqrt{a^{su}\rho^u} \tag{2.13}$$

where α_s is a parameter describing the average strength of the obstacles encountered by mobile dislocations and hence is basically a function of strain rate and temperature due to the nature of thermally activated dislocation motion. However, α_s is frequently used as a constant because its value does not change drastically [119]. Parameters μ and b_c are the shear modulus and magnitude of the Burgers vector, respectively. This form accounts for the dislocation interaction by the interaction matrix a^{su}, and an implicit summation is carried over index u with ρ^u as the dislocation density of a slip system u. Hence, the difference to the more common forms of phenomenological hardening rules is the introduction of an internal variable, the dislocation density in this case. One of the most common forms for the rate of the dislocation density is derived from the Orowan relation consisting of two terms: dislocation storage and dislocation annihilation [147], as presented in the following equation:

$$\dot{\rho}^s = \frac{1}{b}\left(\frac{1}{L^{sm}} - G_c\rho^s\right)|\dot{\gamma}^s| \tag{2.14}$$

where G_c is a parameter proportional to the characteristic length associated with the annihilation of dislocation dipoles. Parameter G_c is related to the mean distance γ_c controlling the annihilation process, as $G_c = 2\gamma_c$. In the storage term $1/L^{sm}$, L^{sm} is the mean free path of a mobile dislocation before it faces an immobilizing obstacle, which may be expressed as the square root of the forest dislocation density [147, 209].

$$L^s = K_o \frac{1}{\sqrt{\sum_{u \neq s} \rho^u}} \tag{2.15}$$

where K_o is a material parameter interpreted as the number of obstacles passed by a dislocation before being immobilized. Use of the L^s relation leads to the final form of the Teodosiu-Tabouret model for FCC single crystals, which therefore has a quasi-physical or dislocation based content:

$$\dot{\rho}^s = \frac{1}{b_c}\left(\frac{\sqrt{\sum_{u\neq s}\rho^u}}{K_o} - 2\gamma_c\rho^s\right)|\dot{\gamma}^s| \tag{2.16}$$

A similar model has also been successfully adapted for BCC crystals under complex loading paths with some modifications by Hoc and Forest [91], and Hoc et al. [92]. Hence the introduction of internal variables makes the models quasi-physical instead of purely phenomenological, and they also could be considered to have a close relationship to the dislocation dynamics based models explained in the following.

2.5.2 Dislocation dynamics based models

The dislocation dynamics based models aim to include the length and size dependencies to crystal plasticity in more detail, and not only to represent the stress-strain curve but also to identify the underlaying dislocation structures responsible for the behavior [13, 190]. As already pointed out, the critical resolved shear stress can be expressed as a function of the lattice defect population. Identification of the actual small scale phenomena occuring in a metallic material dictates the ingredients of the models, such as the formation of dislocation cells and walls [68, 173], shear bands [185], twinning [113, 204], etc. In these models, it has become more and more relevant to include direct relationships to temperature and strain rate effects, including also viscous drag on dislocations at very high strain rates and dynamic recrystallization occurring at elevated temperatures at high strains.

The detailed contents of this type of models is not reviewed in this thesis except for mentioning that they all have their distinctive features. For example, Roters et al. [189] suggested a model for the strain hardening behavior of polycrystalline materials including three internal variables: mobile and immobile dislocations acting in both dislocation cell walls and cell interiors, and linking the effect of precipitates and ripening of second phases to the mobile dislocations by the influence of the mean free path of mobile dislocations. The modeling approach of Steinmetz et al.[204] to twinning in TWIP type steels shared the basic ingredients of this model. They based their twinning model on the three-layer stacking fault initiation, showing quite good agreement with experimental findings in a wide range of temperatures. Ma et al. [140, 141] used the distinction between geometrically necessary dislocations (GND) and statistically stored dislocations (SSD) to study the strain gradients and to investigate the importance of grain boundaries and dislocation transmission between the grains. The former aspect rendered the model size dependent, while the latter tried to elucidate the effect of grain structure and texture. When including both effects, the experimental findings were reproduced reasonably well. Similarly, for example Li et al. [124] included the effects of GNDs and SSDs in their modeling of martensitic steels with precipitates and length-scale relationship to laths. They found a strong dependence between dislocation mean free path and the morphology of the sub-micron structure, showing that coarsening of both precipitates and the lath structure caused softening. All of the previous modeling approaches aim to investigate single or multiple mechanisms affecting the deformation behavior of the materials by

recognizing the most important effects at fine scales. On the other hand, the cost of this knowledge becomes higher since very detailed and complex models require large amounts of characterization in order to establish the relationships required at very small scales, and also supporting smaller scale simulations are often needed to identify the interactions (e.g., discrete dislocation dynamics or atomistic scale simulations).

2.5.3 Crystal plasticity finite elements

One of the most common discretization schemes and solvers for crystal plasticity problems is finite elements, generally referred to as Crystal Plasticity Finite Elements (CPFEM). Reasonably recent overviews and descriptions of the solution procedures of CPFEM are given for example in refs. [27, 190, 191] and are not reviewed here in detail. The CPFEM methods are based on the variational solution of the weak form of the principle of virtual work with the equilibrium of the forces, while maintaining the compatibility of displacements in a predetermined finite volume element [190]. Hence, it makes the use of finite elements very attractive because many scales, shapes, or types of applications or microstructures can be discretized with ease. Also the constitutive models, including complex material behavior, may be easily applied to investigate the interdepencies of the material performance, properties, microstructures, and processing routes. A top-down multi-scale simulation is often favored when operating in application-material performance level solved with finite elements. Many scales may be considered, but one way is to first investigate the component of interest as a whole part, then focus on a certain region of interest, and finally study the behavior of the material in these regions under different loading conditions. Figure 2.10 exemplifies the application-to-microstructure approach performed in two different ways: a direct implementation of representative microstructural aggregates in the application, or a solution where different scales are implemented under the concept of crystal plasticity [191] operating within single gauss points.

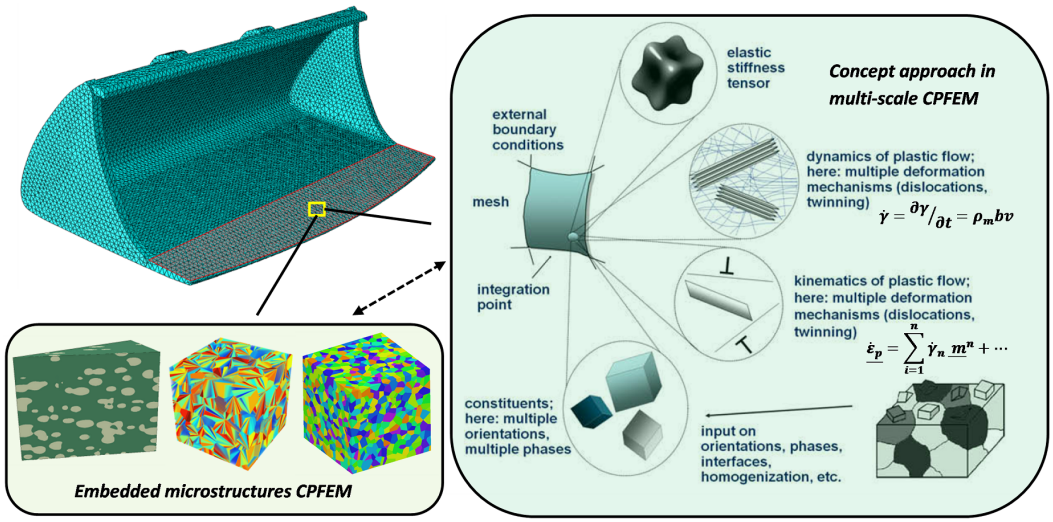

Figure 2.10: Two approaches in multi-scale modelling linking the application and microstructure levels, the right-hand side concept modified from ref. [191]

The direct implementation of the microstructure into the application requires correct

scaling of the microstructure size and mesh compatibilities, but it can provide accurate information about the microstructure behavior under complex boundary conditions, such as contacts of small regions. Larger regions of interest would require representation of the total geometry with the microstructural features (e.g., grains), which can quickly turn out a non-efficient way from the computational point of view. Alternatively, gauss points of a mesh can include a crystal plasticity loop, where no direct discretization of the microstructure necessarily exists in the application level. In this loop, the material model is driven by the multiphysics aspect of many scales. The solution of the deformation behavior can then be obtained by first supplying a material behavior model, then giving the texture (one or many orientations per gauss point), and finally solving the homogenization constituents and translating the deformation and micromechanics to the application level. Another way is to use a hybrid concept where the boundary conditions from the mesh constraint the deformation conditions of a microstructure aggregate, which supplies small scale information of the deformation, damage and failure mechanisms in the microstructure depending on the details (grains, phases, grain boundaries etc.) and methods (damage evolution, fracture models, etc.) included in the models.

2.6 Microstructure informed modeling of deformation

Microstructurally informed modeling usually proceeds in two main steps. The first step is a 'loop' where the material parameters are identified for the constitutive model. The extent of the identification process depends on the dimensionality of the material model and its environment of implementation. The dimensionality, here, refers to the conditions where the material model is designed to be descriptive, such as the ranges of strain rate and temperature, type of loading and its path (monotonic, cyclic, complex deformation), etc. The environment of its implementation directly affects the consistence of the model, as some models only operate at room temperature but at various strain rates, whereas others require direct dependence on temperature. The second step after the identification of the model parameters is equally important because the actual microstructure of the material must be introduced. The microstructure can be introduced already in the first step either virtually by including texture and phases (orientation and phase distributions) with homogenization rules or by using a simplified finite element mesh, but the second step actually includes the *representative microstructure* with realistic type grain morphologies, as exemplified in Figure 2.11.

On the other hand, the benefit of using the homogenization rules is that no actual structure or mesh is required in the computations. Every material point has its own stress and strain tensors and the homogenization is performed over a number of grains in the 'structure' including a distribution of different orientations and phases. However, most often a large number of grains/orientations is used to achieve a better approximation, and hence the used distribution is more or less random. Characteristic to the identification process is that a large number of iterations is performed to optimize the parameter set, and therefore the process is beneficial to be automatized to reduce the required manual effort. Sometimes, when such implementation does not exist or it is incompatible with the model framework (e.g., small deformation vs. large deformation theories), the material parameter identification can be performed with simplified meshes, which is the case in this work. Similarly to the homogenization models, these meshes/elements are assigned to different orientations and can consist of various phases to reproduce grains, which together generate a representative volume element (RVE) of the microstructure without any unnecessary geometrical features of the grains. This is a quite drastic simplification,

but already a relatively reasonable number of elements can often suffice to describe the macroscopic stress-strain behavior (see Chapter 7). This type of identification process usually is less automated, but it is possible to create an optimization loop to identify the parameters even with the mesh based RVEs.

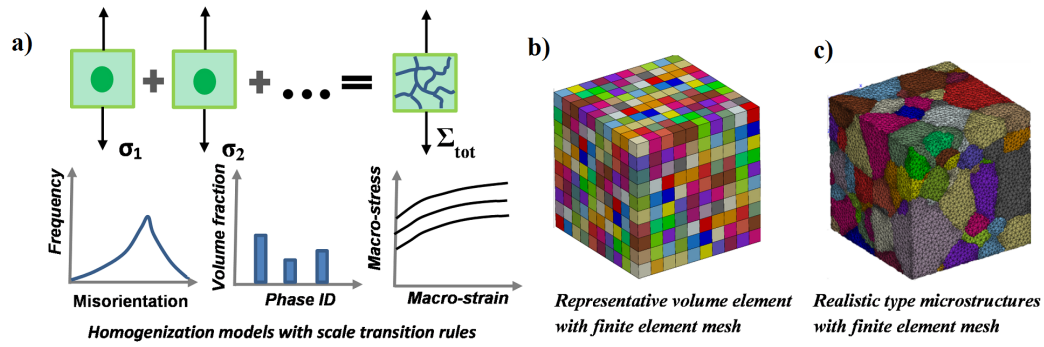

Figure 2.11: a) Expression of the homogenization of several grains/phases producing a macroscopic stress-strain behavior. b) A simplified FE discretized mesh for parameter identification with a number of grains (colors represent different grains), and c) a realistic type synthetic microstructure aggregate with grain morphologies.

There are several homogenization models available, most of them including scale transition rules, where single crystal behavior is transformed to the homogenized behavior of the polycrystalline microstructure. The behavior of individual grains and their interaction with the whole aggregate is identified by a procedure that expresses the local and global mechanical response [80]. Two common methods have been presented by Berveiller and Zaoui (BZ-model) [24] and Pilvin and Cailletaud [35] (Beta-model). The BZ-model is a self-consistent model based on the Hill elasto-plastic solution with a spherical inclusion in an isotropic elasto-plastic matrix modifying the Kröner's approximation to reduce the stress concentrations. The model is intended for monotonic or radial loadings, and the localization relations are written as:

$$\underline{\sigma}^n = \underline{\Sigma} + 2\mu(1-\beta)\alpha(\underline{\mathbf{E}}_p - \underline{\epsilon}_p^n), \tag{2.17}$$
$$with\ \beta = \frac{2(4-5v)}{15(1-v)},\ and\ \frac{1}{\alpha} = 1 + \frac{3}{2}\mu\frac{E^{Mises}}{\Sigma^{Mises}}$$

$$where, \begin{cases} \epsilon^{Mises} = \sqrt{\frac{2}{3}\underline{\epsilon} : \underline{\epsilon}}, & \text{for strain.} \\ \sigma^{Mises} = \sqrt{\frac{3}{2}\underline{s} : \underline{s}}, & \text{for stress.} \end{cases} \tag{2.18}$$

where $\underline{s}$ is the deviatoric stress $\underline{s} = \underline{\sigma} - \frac{1}{3}tr(\underline{\sigma}) \cdot \underline{I}$.

Another model was introduced by Pilvin and Cailletaud, e.g., ref [35], known as the Beta-method/rule. In this model, the elastoplastic tensor $\underline{\beta}$ is introduced to describe the interphase or intergranular constraints, or more precisely, the effect of other phases or grains. The module $\underline{\underline{L}}$ can be chosen, for example, to be Kröner's approximation, Eshelby's inclusion, or simply equal to the shear modulus of the material.

$$\underline{\sigma}^n = \underline{\Sigma} + \underline{\underline{L}}^n : (\underline{\beta} - \underline{\beta}^n) \tag{2.19}$$

The evolution of tensor $\underline{\beta}$ can be written as:

$$\dot{\underline{\beta}} = \dot{\underline{\epsilon}}_p^n - D^n \left(\dot{\epsilon}_p^{n,Mises} \left(\underline{\beta}^n - \delta^n \underline{\epsilon}_p^n \right) \right) \tag{2.20}$$

where two scale transition variables D and δ are introduced. These variables are searched using a fitting procedure, and they can be different for each phase, such as austenite, ferrite, etc. More detailed descriptions can be found in the references presented above, but the ultimate aim of both methods is to establish the macroscopic behavior from a number of orientations and phases in the structure. The methods are more effective in providing parameter fitting that utilizing a discretized finite element representation of the microstructure because of their computational efficiency and often automated implementations.

After the parameters of the models correspond to the experimentally measured macroscopic behavior of the material, the simulations may be performed on a more realistic type of microstructure. Figure 2.12 demonstrates the translation of the characterization of microstructure to representative microstructural aggregates for austenite (a), martensite/bainite (b), and a composite (c).

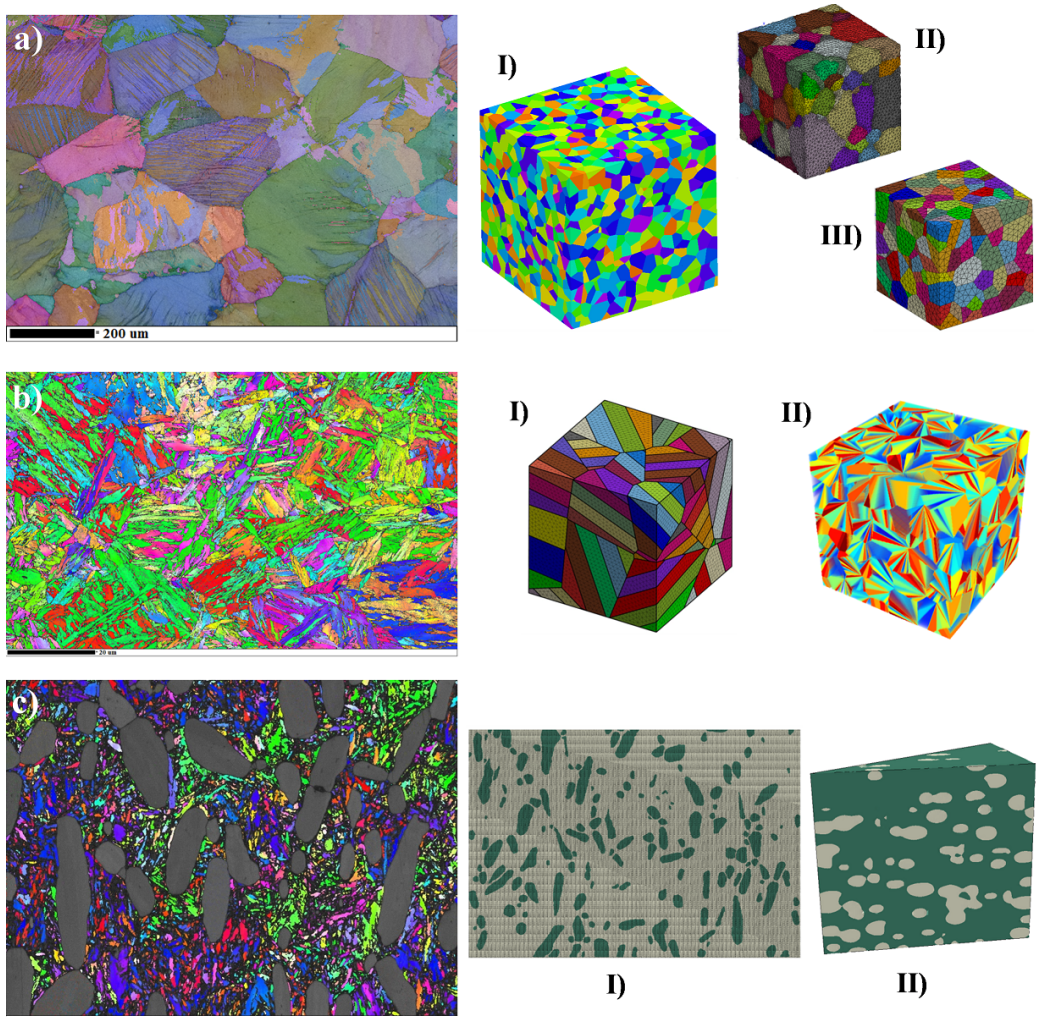

Figure 2.12: Different microstructures transformed to computational representative aggregates, a) austenitic steel, b) martensitic/bainitic steel, c) matrix-carbide composite.

The austenitic microstructures are often convenient to represent because of their rather large grain size and relatively simple grain morphology. However, the more details are included in the microstructural representation, such as explicit definition of meshable grain boundaries in the austenitic microstructure, the more specific information may be extracted from the computations. Similarly, if the microstructure contains a significant amount of fine subset structures, as in lath martensite, the level of simplifications comes to an essential role. The reduction of fine topological features leads to higher computational efficiency desired in many cases for more practical use, but at the same time details of the microstucture are lost. The details, however, can be in a very significant role in the assessment of the factors affecting material performance, e.g., when identifying the probability for cleavage fracture in BCC structures arising from the microstructure. On the other hand, sometimes it is possible to reduce the details of some microstructural

features, for example by separating the matrix and the carbides from each other and by choosing some simple material behaviors for both of them, such as elastic-plastic matrix and elastic carbides. By this approach, the stress and strain concentrations taking place in the composite microstructure may be recognized. Thus, this can be used as a design type of method to investigate the effect of some microstructural variables, such as the volume content, shape and distribution of carbides. The material tailoring method for other microstructures, such as austenite, depends essentially on which factors can be modified in the manufacturing process, including for example the grain size. The knowledge gathered by several performance indicators can be translated to product development, for example by using the common manufacturing-structure-properties-performance ideology.

3 Materials and methods

This chapter presents the materials and their common uses in applications studied in this work. This is followed by the presentation of the used experimental setups, including both high and low strain rate mechanical tests, and abrasion and impact wear experiments. The last two sections discuss the characterization techniques used to analyze the results and the simulations software and techniques applied in the work.

3.1 Materials

This chapter introduces the materials used in this study. The material properties and common applications are briefly discussed to explain the loading conditions related to abrasion and impact wear and the relevance of the current experimental setups.

3.1.1 High manganese austenitic steel

The austenitic wear resistant steel used in this study was a high manganese Hadfield-type steel having a metastable austenitic microstructure at room temperature. The manganese content was 16.5-wt with 1.15-wt of carbon, which differs from standard ASTM-A128 Hadfield grades by higher manganese content. In addition, the steel was alloyed with 1.8-wt of chromium, 0.2-wt of nickel, 0.13-wt of molybdenum, 0.50-wt of silicon, and small amount $<$ 0.05-wt of aluminium. The steel was cast as a crusher jaw, and then water quenched followed by annealing at 1100 °C. The cast structure contains some amounts of imperfections, and its grain size varies depending on the section thickness from $200-800\mu m$, or occasionally even larger. The as-cast hardness of the steel was 250-300 HV5. Figure 3.1 presents the microstructure of the steel.

The high manganese austenitic steel is often used as wear resistant jaws/plates in mineral crushers. This is due to the material's high work hardening capability, which retains its ductility better than the initially hard martensitic microstructures. The work hardening capability, however, depends on the composition, deformation mechanisms (dislocation slip, twinning or martensitic transformation) and the type of deformation. High stress abrasion increases the surface hardness by deforming the surface layer, while impacts can additionally alter the deformation mechanisms through the increase in the strain rate and local temperatures (adiabatic effects). In such high strain rate cases, for example twinning may be promoted, which effectively increases obstacles to dislocation slip and thus the flow stress (hardness) of the steel. Therefore,it is important to understand the hardening and deformation behavior of the steel both in low and high strain rate conditions.

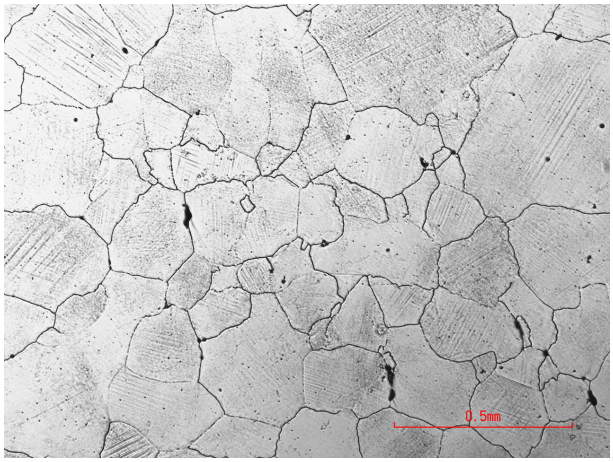

Figure 3.1: Microstructure of high manganese austenitic steel

3.1.2 Martensitic wear steels

Three martensitic wear resistant steels were studied in this work. The steels were manufactured by thermomechanical rolling and a direct quenching (DQ) process, described for example in ref. [205]. The steels were alloyed slightly differently to affect the properties such as strength, strain hardening capability and ductility, and initial hardness, which are important for the abrasion and impact wear resistance of the material. In the DQ process, the steels undergo auto-tempering, which leads to a microstructure containing a combination of tempered martensite and hard untempered martensite. The microstructures of the studied steels are shown in Figure 3.2. The steels have a slightly different lath martensite morphology, prior austenite grain size, and packet and block sizes. Figure 3.3 visualizes the martensite morphology relevant to the studied ultra high strength steels.

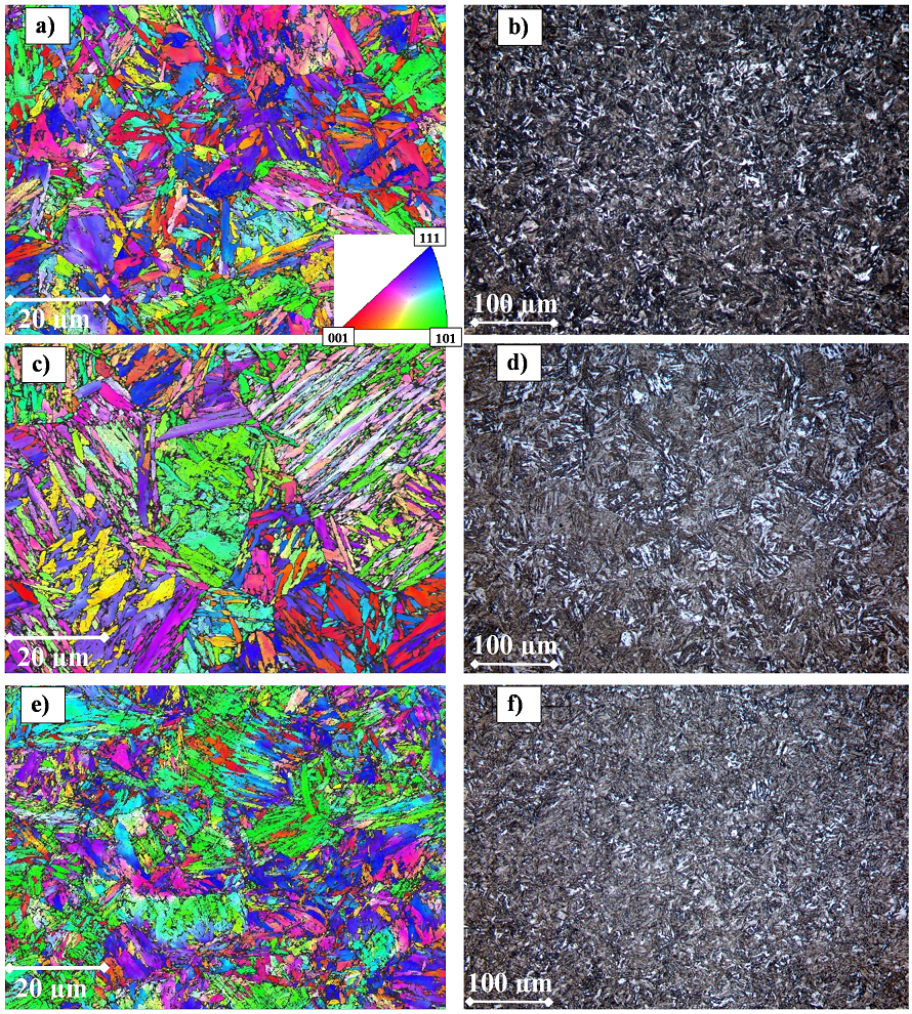

Figure 3.2: Microstructures of the studied martensitic steels. a,c and e are inverse pole figures (IPF) with a coloring scheme shown in (a). b,d, and f are etched microstructures of the materials.

The nominal compositions and initial hardness values are listed in Table 3.1.

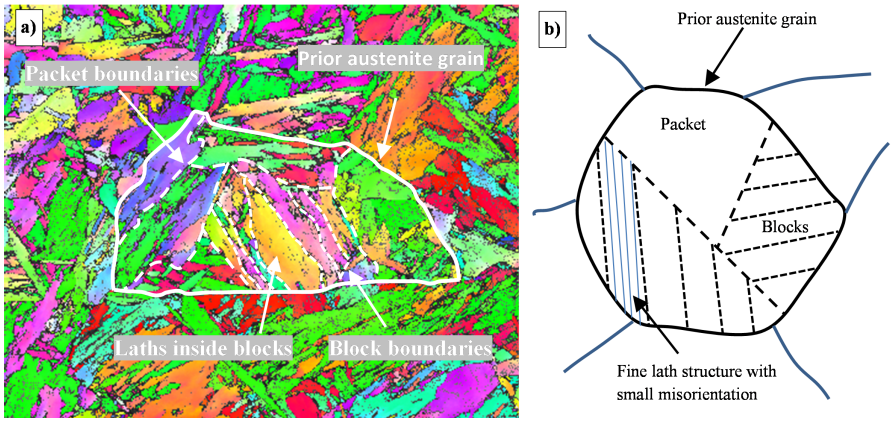

Figure 3.3: a) Morphological features of martensite redrawn on a IPF coloured microstructure of lath martensite presenting one grain and its subsets, b) a schematic of the martensite morphology

Table 3.1: Nominal compositions and hardness values of the studied martensitic steels

Material	HV500A	HV500B	HV550
Initial hardness [HV10]	500-510	490-515	540-564
C [%]	0.30	0.32	0.36
Si [%]	0.80	0.70	0.60
Mn [%]	1.70	1.50	1.00
P [%]	0.025	0.015	0.015
S [%]	0.015	0.005	0.005
Cr [%]	1.50	1.00	1.50
Ni [%]	-	2.00	2.50
Mo [%]	0.50	0.70	0.80
B [%]	0.005	0.005	0.005

The martensitic wear resistant steels are often used as protective plates in mining, mineral handling and earth construction applications, such as gravel beds of a lorry or in the cutting edge of a bucket loader. The harsh conditions related to the interaction with natural rocks cause heavy abrasion and impacts to the steel surfaces. Therefore the initial hardness, ductility and work hardening capability of the steel grades are in an essential role in providing sufficient wear resistance. Similar type DQ-steels manufactured in the laboratory scale by the rolling and DQ processes have shown quite good abrasive wear resistance [118].

3.1.3 Carbide-reinforced wear steel

The experimental grade carbide reinforced steel studied in this work contained nominally 2-wt % of carbon and 20-wt % of chromium. The steel was manufactured by casting followed by tempering. The high chromium content causes precipitation of chromium carbides (Cr_7C_3) in the microstructure, while the matrix is tempered lath martensite. Some amounts of retained austenite exist in the matrix, estimated between to be 5-10 % by preliminary Xray diffraction measurements. However, the amounts are close to low end limit of the measurement reliability so that the precise can be difficult to extract

from the data reliably. Figure 3.4 shows the microstructure, where the matrix is colored with IPF coloring to reveal the lath structure. The gray areas represent the carbides. The average initial hardness of the steel is 750 HV.

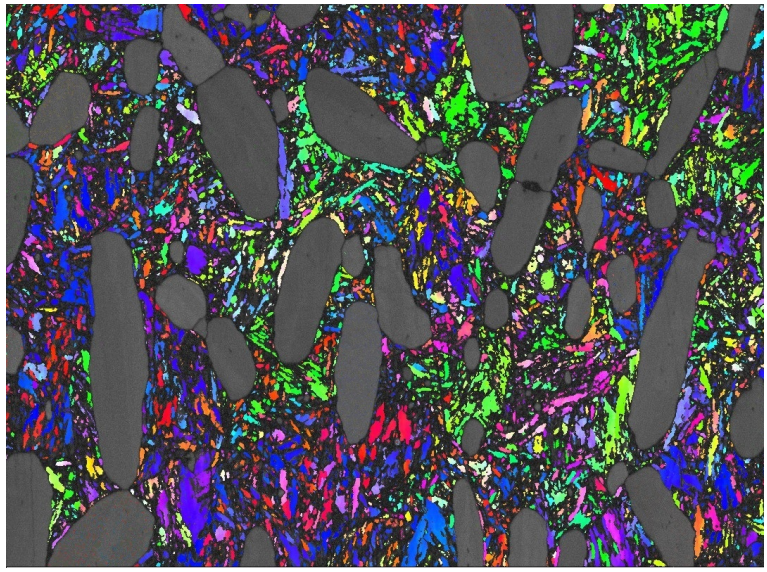

Figure 3.4: Microstructure of the carbide reinforced steel, IPF colouring showing the lath martensite matrix and the gray areas the chromium carbides

The high initial hardness of the steel suggests that the material can be used in abrasive conditions. On the other hand, the microstructure including both hard carbides and martensite suggests that impacts may be deleterious in terms of wear resistance. Therefore, the steel was investigated in both abrasive and impact conditions and its performance was evaluated based on these results.

3.2 Mechanical testing

This section presents the testing methods used to determine the mechanical properties and behavior of the studied steels.

Quasi-static compression tests

The mechanical testing was performed at room temperature with an Instron 8800 servo-hydraulic materials testing machine at quasi-static strain rates. The strain rate ranged from 10^{-3} to 1 s^{-1}. Tungsten carbide hard metal compression platens were used with a thin layer of MoS_2 (Molycote) at the interface to reduce friction. The hot-rolled and quenched martensitic steels were tested normal to the rolling plane of the plate, because this surface is subjected to the loading in the applications. Since the high manganese austenitic steel (Hadfield) and the carbide reinforced steel were manufactured by casting, the samples were prepared in a typical manner with no special orientation dependence. The selection of the sample diameter was based on the strength of the materials and on the capacity of the testing machines. The length-to-diameter ratios of the samples are presented in Table 3.2. The same sample sizes were also used in the dynamic compression tests with the Hopkinson Split Bar (HSB).

Table 3.2: Compression sample sizes for cylindrical samples in mechanical testing

Material	Microstructure	Sample size in mechanical testing
HV500A	Tempered martensite (Hot rolled)	d = 6 mm, L0 = 5 mm, L0/d = 0.83
HV500B	Tempered martensite (Hot rolled)	d = 6 mm, L0 = 7 mm, L0/d = 1.17
HV550	Tempered martensite (Hot rolled)	d = 6 mm, L0 = 6 mm, L0/d = 1.0
HV750	Cr_7C_3 carbides and martensitic matrix	d = 5 mm, L0 = 6 mm, L0/d = 1.2
Hadfield	Austenitic	d = 8 mm, L0 = 6 mm, L0/d = 0.75

Compression Hopkinson Split Bar

The dynamic properties of the test materials were determined with the compressive Hopkinson Split Bar technique. The strain rates ranged from 700 to 3600 1/s depending on the test materials. The HSB test device of the Department of Materials Science (DMS) at TUT is described for example in ref. [10]. In the current tests, the set-up consisted of 22 mm diameter maraging incident, transmitted and striker bars. Three millimeter thick high strength steel inserts were placed between the bars and the cylindrical sample to avoid any plastic deformation and damage to the incident and reflected bars due to the high strength of the test materials. A thin layer of MoS_2 was used between the inserts and the sample to reduce friction and minimize the possibility of barreling of the deforming samples. Very thin copper pulse shapers were placed between the striker and the incident bar to smoothen and shape the incident pulse. The stress, strain and strain rate were calculated in the usual manner from three measured pulses (i.e., incident, reflected and transmitted pulses), as shown in Equation 3.1.

$$\sigma_E(t) = \frac{A_b E \epsilon_{TR}(t)}{A_s},\ \epsilon_E(t) = \frac{2C_0 s}{L_s}\int_0^t \epsilon_R(t)dt,\ \dot{\epsilon}(t) = \frac{2C_0 s \epsilon_R(t)}{L_s} \tag{3.1}$$

where, $A_b, E, C_0 s$ are the cross-sectional area, Young's modulus, and the speed of sound in the bar material, A_s, L_s are the cross-sectional area and the gauge length of the sample. ϵ_{TR} and ϵ_R are the transmitted and reflected stress pulses, and t is time. Here, dynamic equilibrium of the stress in the specimen was assumed (strain being much larger than 0.05), and the calculations were based on the reflected and transmitted pulses only, as seen in Equation 3.1. The common logarithmic equations were used to obtain the true stress and true strain, as presented in Equation 3.2

$$\sigma_T = \sigma_E(1+\epsilon_E),\ \epsilon_T = ln(1+\epsilon_E) \tag{3.2}$$

3.3 Abrasion wear experiments

This section describes the abrasive wear testing methods used in this work.

3.3.1 Scratch tests

The high stress two-body abrasion experiments were conducted in a controlled environment with a CETR UMT-2 tribotester at room temperature. Both single and multiple overlapping scratch tests were performed with a standard Rockwell-C tip having a 200 μm $\pm$ 10 radius. The number of scratches was 1, 2, 5, and 10. The tests were force controlled so that four normal loads were used, 20, 40, 60, and 80N. The used force sensor was limited

to maximum of a 200 N with the resolution of 10 mN. The sliding velocity was chosen as a constant 0.1 mm/s in all tests. A circular scratching track was found best to reduce any effects related to rolling direction of the hot rolled martensitic steels, and to easily test the high manganese austenitic steel cylindrical samples that had been pre-strained in compression. The surfaces facing the loading were similar to those that would carry the load in the application; the rolling plane in the martensitic steels, the pre-compressed surface of the high manganese austenitic steel, and an arbitrary surface of the carbide reinforced steel (no direction dependence). All samples were mounted in resin to ensure proper fixing and to allow polishing of the surface prior to the experiments. After the experiments, from the nominally flat wear groove produced by the Rockwell-C tip, it was possible to measure the hardness of the bottom of the scratch with a microhardness tester.

Some preliminary experiments were performed with natural rock granite and quartz tips to compare the coefficient of friction and to justify the use of a rigid Rockwell-C tip instead of the fragile rock tips. The rocks were screened from actual batches of abrasives obtained from the quarries. The hardness of the granite and quartz were roughly 750 HV and 1100 HV, respectively. Only single scratches were made with the rock tips. In this work, however, further rock tests were not done because of the irregular rock geometries and due to the failure of the sharp rock tips during the tests.

3.3.2 Crushing Pin-On-Disc

The multiple contact abrasion experiments were performed with a crushing pin-on-disc setup, described in detail for example in ref. [211]. A bed of gravel was placed between the sample pin and the counter-surface disc. The rotation speed of the disc was 28 rpm, and the normal force used in the experiments was 235 N. One contact cycle comprises 5 seconds of contact time with the gravel and 2.5 seconds during which the pin is lifted above gravel bed. The total test time was 30 minutes, of which the contact time was 20. The mass loss was determined by weighting the ethanol rinsed sample every 7.5 minutes. The samples were pre-worn for 15 minutes with 2-4 mm sized granite to reach the steady state of wear before starting the actual test. Four abrasives were used in the experiments: granite, tonalite, quartz, and basalt. The bottom disc used in the experiments was made of tool steel with a hardness of 600 HV.

3.4 High velocity particle impactor - development and procedure

High velocity impacts were performed with the High Velocity Particle Impactor (HVPI) test equipment [11]. A schematic of the HVPI setup is shown in Figure 3.5. The equipment comprises a pressure reservoir and a smooth bore barrel that accelerates projectiles onto the target. All operations of the device are computer controlled to maintain accuracy of timing and positioning of the impacts.

The incident velocity of the projectile is measured with a chronograph placed in front of the target assembly. The target is usually set 1 m away from the barrel in the target assembly. The target can be tilted to oblique angles, generally between 10-90°. A trap wall captures the exiting particle after the impact, which can also be used to measure the exit angle. The impact event is recorded with a high speed camera (NAC Memrecam fx K5, NAC Image Technology) to analyze the material behavior in-situ and to define the

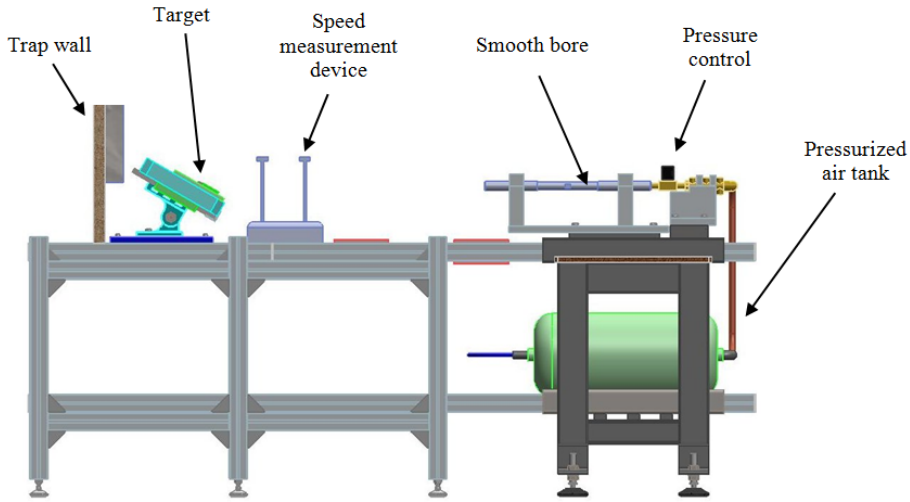

Figure 3.5: High Velocity Particle Impactor test setup [11].

exit velocity of the particle. Two sizes of projectiles can be used in the current setup with diameters of 9 mm and 6.35 mm, and although round projectiles are generally used due to their steady flight, also other shapes are possible, such as cylindrical projectiles. The high speed videos were recorded at a constant frame rate varying between 20000-40000 frames per second depending on the impact velocity of the particle. The forces acting on the sample during the impact incident can be recorded with a piezo-electric 3D force sensor placed below the sample. The HVPI setup has been used for studying various materials. For example, Lindroos et al. [132−134] performed experiments on ultra high strength steels focusing on the deformation and wear behavior, while Waudby et al. [219] studied the failure behavior of thick thermally sprayed coatings. Molnar et al. [155] studied the deformation response of rubbers and used the results to verify an impact simulation model. In their work, since the deformation of rubbers cannot be studied afterwards due to their mainly elastic behavior, the high speed images were used to determine the penetration depth of the projectile during the impact incident. Sarlin et al. [198, 199], in turn, studied the effects of impact conditions on the damage behavior of steel/rubber/composites. Figure 3.6 shows typical high speed images of impact events on four different materials: a wear resistant steel (a), thermally sprayed thick coating (b), fiber reinforced rubber (c), and steel/rubber/composite (d).

In the current study, the effects of the impact angle, impact velocity, number of impacts, and prior deformation were investigated. Three impact angles of 15°±1°, 30°±1°, and 60°±1°were used to test the impact properties of martensitic and carbide reinforced steels at low, intermediate and high impact angles, while the austenitic manganese steel was tested only at the 30°±1°impact angle. The normal direction impacts at 90°were not conducted due to the rebound of the particle that could cause damage to the device. Tungsten carbide ($94\% - WC, 6\% - Co$, 1800 HV10, 5.69 g in weight) balls with a diameter of 9 mm were used as projectiles due to their higher rigidity in comparison to steel balls. In order to study the effect of shorter contact times at a constant impact energy, the same size but lower weight hard ceramic projectiles were shot at higher speeds. The projectiles were made of zirconia oxide (ZrO_2, 2.22 g in weight) and silicon nitride (Si_3N_4, 1.24 g in weight), with hardnesses of 1240 and ca. 1600 HV10, respectively. The air launching

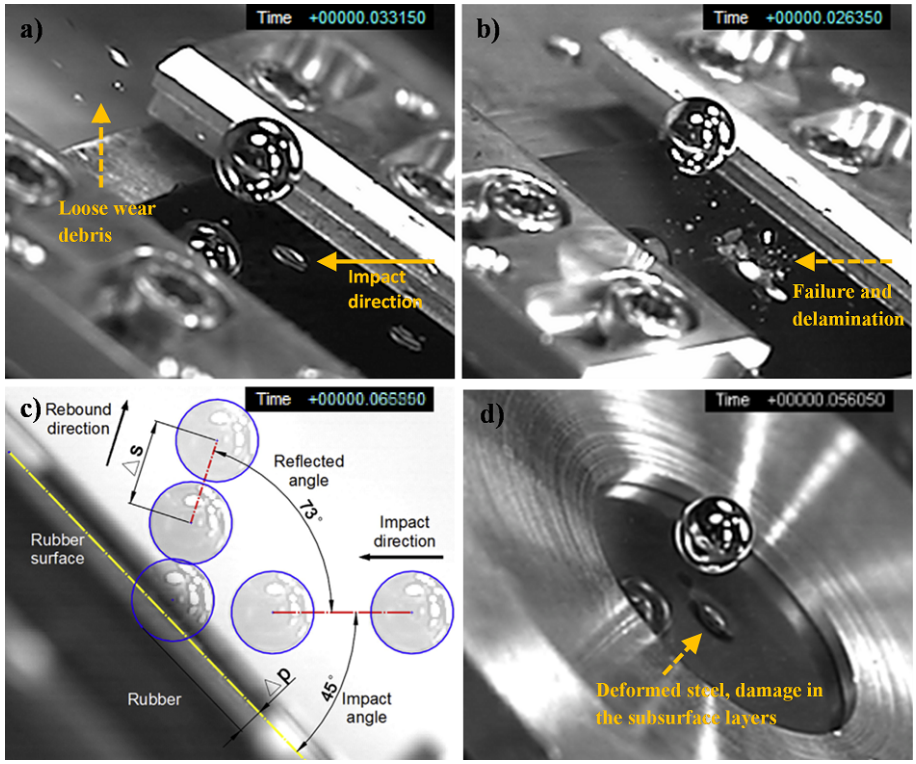

Figure 3.6: Typical high speed images of the impact incident on four materials, a) a wear resistant steel [132−134], b) thermally sprayed coating on steel substrate [219], c) rubber [155], d) steel/rubber/composite [198, 199]

pressure ranged from 2 to 14 bars depending on the aimed impact velocity, which varied from ca. 40 to 115 m/s, from 72 to 123 m/s, and from 96 to 165 m/s for the $WC-Co$, ZrO_2, and Si_3N_4 balls, respectively.

The sample size was 40 mm x 40 mm for the martensitic and carbide reinforced steels, but the thickness varied depending on the sample material from 5 to 8 mm. The samples were clamped from the edges to the specimen holder table. The high manganese steel samples were initially 8 mm diameter cylindrical compression samples, but since the effect of prior deformation was one of the studied factors, the diameter of the impact samples varied depending on the applied pre-strain. These samples were mounted in resin to properly hold the samples during the impacts from the edges. The pre-straining was performed in compression at a constant strain rate of 0.1 s^{-1}. All samples were ground and then polished with a 1 μm diamond suspension and cloth to ensure smooth surface and ease the determination of the undeformed zero-level in profilometry.

The initial kinetic energy was calculated from the velocity v_{init} of the projectile measured with the chronograph in front of the target assembly. The exit velocity of the projectiles v_{exit} was determined from the high speed images, as shown in Figure 3.7. The dissipated energy E_d was calculated using Equation 3.3, where Δs is the distance and Δt the time consumed for this displacement to take place, and m_p is the mass of the projectile.

$$E_d = \frac{1}{2} m_p \left[v_{init}^2 - \left(\frac{\Delta s}{\Delta t} \right)^2 \right] \tag{3.3}$$

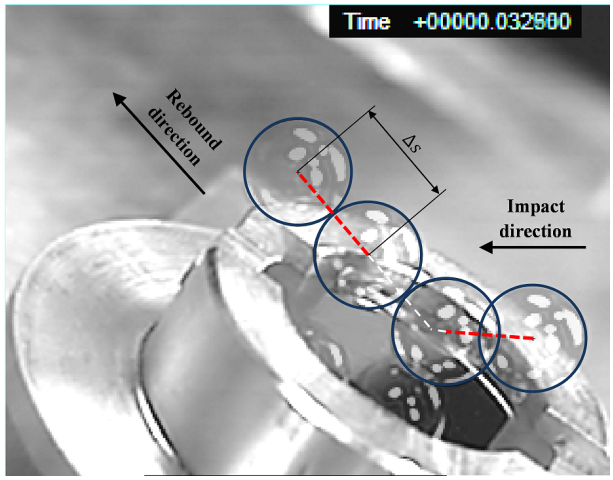

Figure 3.7: Iimpact of a WC-Co ball on a high manganese austenitic steel sample at a 30 angle recorded with a high-speed camera [132]. The outlines of the projectile are shown for clarity.

A small error may be involved in the measurements due to a slightly angular position of the camera observing the impact incident. It, however, has a negligible influence on the accuracy of the results and therefore it was omitted. Similarly, the rotational kinetic energy of the projectile was not included in the calculation because in the preliminary testing a pattern painted on the projectile revealed that the ball did not essentially rotate during its flight. Also, Hutchings et al. [101] showed that in the case of spherical projectiles the rotational energy is negligible. The mass of the rigid projectiles was also considered unchanged, since no noticeable signs of wear or increase in the mass because of adhesion was observed in the weighting of the projectile balls before and after the impacts.

3.5 Characterization techniques

This section describes the characterization techniques used to analyze the deformation and wear behavior of the materials studied in this work.

3.5.1 Hardness testing

The macroscopic hardness of the samples was measured with Struers Duramin-A300 as HV5 and HV10. Matsuzawa MMT-7X was used for microhardness measurements. The microhardness values obtained from the bottom of the scratch test grooves were measured as HV0.2. The cross-section hardness profile measurements, indentations in the white etch surface layers, and shear band hardness measurements were done using a very small weight (HV0.025) to retain the effective indent area within the very narrow region of interest, for example in the adiabatic shear bands.

3.5.2 Microscopy

Before microscopic investigations, conventional sample preparation techniques were used. The samples were first cut to suitable sample sizes, followed by grinding with SiC grinding paper from P80 down to P4000. The martensitic steel samples were ground sufficiently with a coarse P80 paper or a P80 diamond grinding counter surface to remove the decarburized layer that can be present in the samples due to the thermomechanical rolling manufacturing. The samples were polished with diamond suspension down to 1 μm, and the scanning electron microscope Electron Back-Scatter Diffraction (EBSD) samples were further fine polished with colloidal silica. The cross-sectional samples were cut from the original samples and then mounted in resin followed by the grinding/polishing sequences. A stereo microscope was used to analyze the wear marks (scratches and impact craters) and the cross-sections. In some cases 4% Nital etchant was used to reveal the microstructure including shear bands. The samples that were used for mechanical testing underwent only light grinding on the compression surfaces to flatten the surface and to reduce friction between the compression platens.

The EBSD measurements were performed with a field emission gun scanning electron microscope (FEG-SEM) Zeiss ULTRAplus equipped with a Nordlys F400 detector. The data acquisition package HKL channel 5 was used to handle and analyze the data. The EBSD measurements on the martensitic steels were performed normals to the rolling plane, in the transverse direction, and in the longitudal transverse direction. On the carbide-reinforced samples, the measurements were performed only in one direction, since the steel is manufactured by casting and does not pose such orientation dependence as the hot rolled steels. The high manganese austenitic steel samples used in the mechanical testing were observed in the compression direction and in the cross-sectional direction as well. Generally, 7-9 bands were used to identify the crystal structure from the Kikuchi patterns. To estimate the twinned volume content, the HKL software used the 60°$\pm$ 5°misorientation with respect to the base crystal orientation and highlighted such boundaries with colors in the back-scatter image to identify the twins, followed by an image analysis to approximate the content of the twinned volume.

3.5.3 Profilometry

The surface topologies of the scratch grooves and impact craters were analyzed using a Plμ confocal imaging profilometer at the VTT Research Center of Finland and a Wyko NT-1100 optical profilometer at Tampere Wear Center. A special Matlab code was developed to analyze the volume loss and other parameters from the 2D/3D profiles. The volume loss was determined as a sum of positive V_{pos} and negative V_{neg} volumes, where the undeformed zero-level is used as a reference surface. A quarter of an impact crater is shown in Figure 3.8 as an example.

The cutting-to-ploughing ratio ϕ_{cp}, which defines the ratio between the material being cut off from the surface profile and being ploughed aside is defined as

$$\phi_{cp} = \frac{||V_{pos}| - |V_{neg}||}{|V_{neg}|} \tag{3.4}$$

The values of ϕ_{cp} range from 0 to 1, 1 meaning that all displaced material has been cut away, while 0 denotes ideal plastic flow without any measurable material loss. The ratio therefore expresses whether the material experiences more severe cutting or ductile plastic displacement/deformation during the wear process.

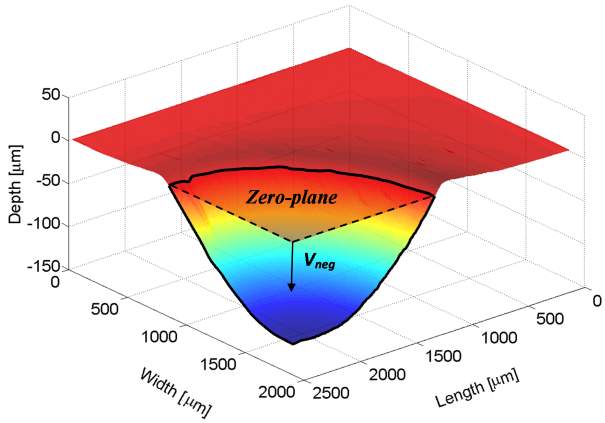

Figure 3.8: Quarter of a 3D profile of an impact crater [132].

3.6 Simulation procedures

The numerical simulations included in this work were performed with finite element code Zebulon (Z-set). The interface of the FE software allows wide implementation of user modified material models and analysis techniques. The crystal plasticity models presented in Chapters 7 and 8 were implemented using object oriented C++/Zebulon coding. In those chapters, also some of the most important details will be given concerning the finite strain formalism and the material models. The models make use of the routines and computation libraries available in Zebulon, such as the the existing numerical integration methods embedded in the libraries. Modern and robust parallel computing is possible in many FE codes, making the usefulness of the developed codes greater also in industrial applications. All of the computational examples presented in this thesis were, however, performed with a personal computer with parallel computing instead of using large scale computational clusters.

4 Material characterization results

This section presents the characterization results and observations of each of the steels investigated in this work. The characterization comprises studying the mechanical behavior of the steels at various strain rates, their hardening behavior, and failure mechanisms. To further study the behavior of the selected steels under their common loading conditions, samples from two industrial applications were further characterized. The first application was a jaw crusher, where Hadfield types of steels are frequently used. The second application, the cutting edge of a bucket loader, is also related to the mining industry where various types of ultra high strength steels are employed. Some of the results have been published earlier in refs. [132–134].

4.1 Deformation and hardening in austenitic high manganese steel

In the following, the results of the mechanical tests on the high manganese austenitic steel (alloyed Hadfield steel) at various strain rates are presented. The deformation mechanisms are characterized and analyzed to provide the necessary details for crystal plasticity modeling presented later in Chapter 7, and to elucidate factors in the steel's strain hardening behavior that have importance in abrasive and impact wear conditions. A brief investigation is performed also on an in-service sample taken from a mineral jaw crusher in order to compare the characteristics of deformation found in the laboratory and in-service samples.

4.1.1 Mechanical behavior

Figure 4.1 shows the compressive stress-strain behavior of the as-cast Hadfield steel in a wide range of strain rates at room temperature. The material has a positive strain rate dependence resulting in increasing yield strength, increasing from about 480 MPa at $10^{-3}s^{-1}$ to about 800 MPa at 4000 s^{-1}. The effect of strain rate on the strain hardening rate θ is more complex, as illustrated in Figure 4.1b. A positive and rather linear dependence of the strain hardening rate on strain rate is observed at quasi-static strain rates below 1 s^{-1}. When the strain rate is increased to 1 s^{-1}, a notable drop is observed in the strain hardening rate, and at the strain rate of 4000 s^{-1}, the strain hardening rate is more or less the same as at the lowest strain rate of 10^{-3} s^{-1}. The poor thermal conductivity of austenitic steels can change the conditions close to adiabatic already at 1 s^{-1}, which leads to an increase in the material temperature during testing, reducing the thermal component $\tau*$ of the flow stress. For example, the reduced hardening rate can be seen in the curves of 0.1 and 1 s^{-1}, that intersect already at 12 % of plastic strain. At higher strain rates, the dislocation motion can change from thermally activated

dislocation glide to include also dislocation drag effects. This increases the flow stress considerably, but the strain hardening rates still remain lower than at the quasi-static range.

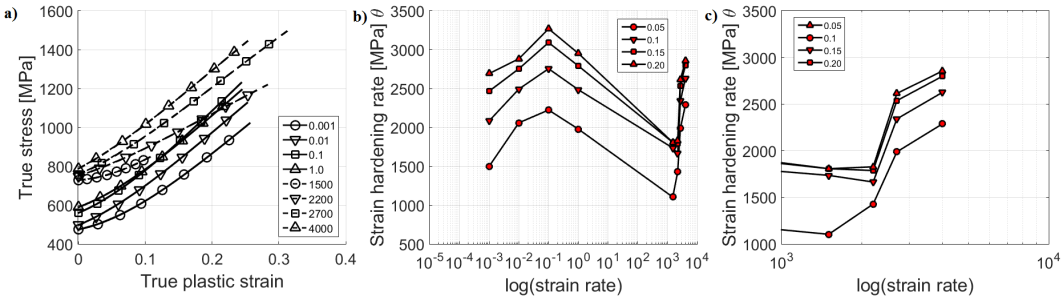

Figure 4.1: a) Stress-strain behavior of the high manganese austenitic steel at various strain rates in compression, b) the strain hardening rate ($\theta = \Delta\sigma/\Delta\epsilon_p$) as a function of strain rate at constant plastic strains, and c) magnification on the high strain rate regime of (b). [132]

The strong upward curvature of the stress-strain curves reflects the typical effect of twinning on the material behavior. The increased strain hardening at the two highest dynamic strain rates indicates that twinning is an effective strain hardening mechanism in spite of the more or less fully adiabatic conditions. The stacking fault energy of the TWIP steels is affected by temperature [50], the increase of which has been established to reduce the twinning propensity by favoring perfect dislocations instead of their dissociation to partials, which triggers twinning. The strain rate itself can also affect the twinning related behavior of austenitic steels. For example Liu et al. [137] observed increased elongation with increasing strain rate, which was partially attributed to increased twinning. Twinning can be thought to affect the flow stress in two different ways. On one hand, it could decrease the flow stress by providing an additional and partly competing deformation mechanism to dislocation slip. On the other hand, twins can act as barriers to dislocation motion and further twinning, thus increasing the flow stress and causing the observed upward curvature in the stress-strain curve.

The comparison of tensile and compressive loading directions in Figure 4.2 shows the asymmetric behavior exhibited by the Hadfield steel at 0.1 s^{-1} strain rate. The asymmetric stress-strain behavior is not unexpected for materials exhibiting deformation twinning because of the asymmetric nature of twinning. The extent of twinning, however, has to be notable for the upward curvature in the stress-strain curve to take place. For example, Hadfield grades alloyed with aluminium [39] and silicon [222] did not show an upward curvature because twinning was largely suppressed by the alloying favoring conventional dislocation slip or formation of epsilon martensite. In the present tests, also the failed tensile samples showed decent amounts of twin-like bands after etching. However, no precise volume fractions of twins were determined from the tensile samples, mainly because of the quite small sample size leading to a small number of grains in the sample cross-section as a consequence of the large initial grain size. Therefore the difference in the twin propensity cannot be confirmed by the current results.

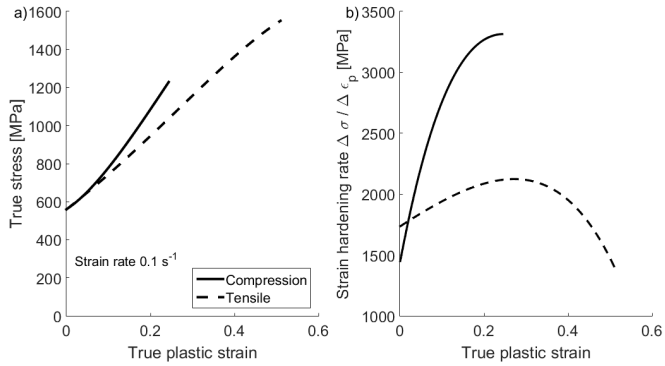

Figure 4.2: a) Comparison of the stress-strain behavior of the Hadfield steel at the constant strain rate of 0.1 in tensile and compression tests, b) the strain hardening rate of the two tests.

4.1.2 Microstructure analysis of the deformation behavior

Figure 4.3 shows the microstructures deformed at 0.1 s^{-1} as EBSD quality and IPF maps from the compression direction (a) and from the cross-sectional direction (b). A reasonable amount of deformation bands including both twins and slip bands can be seen from both directions. The current resolution of the EBSD cannot easily detect very thin twins or slip bands (or dislocation cells). However, the growth of twinned regions allows recognition of the twin bundles, which consist of a mixture of multiple thinner twins and the matrix. The slip bands, on the other hand, show themselves essentially only when the misorientation is noticeable, by constructing both thin and wide zones. Hence, even though the narrower slip bands are not easily seen in this measurement data, they exist in the microstructure. Another proof for the high slip activity may be found from the poorer indexing quality of the EBSD in some regions, especially in the vicinity of twins, where a reasonably high dislocation density or densely populated twins and nanotwins lead to a more distorted crystal structure (e.g., as seen in the cross-section).

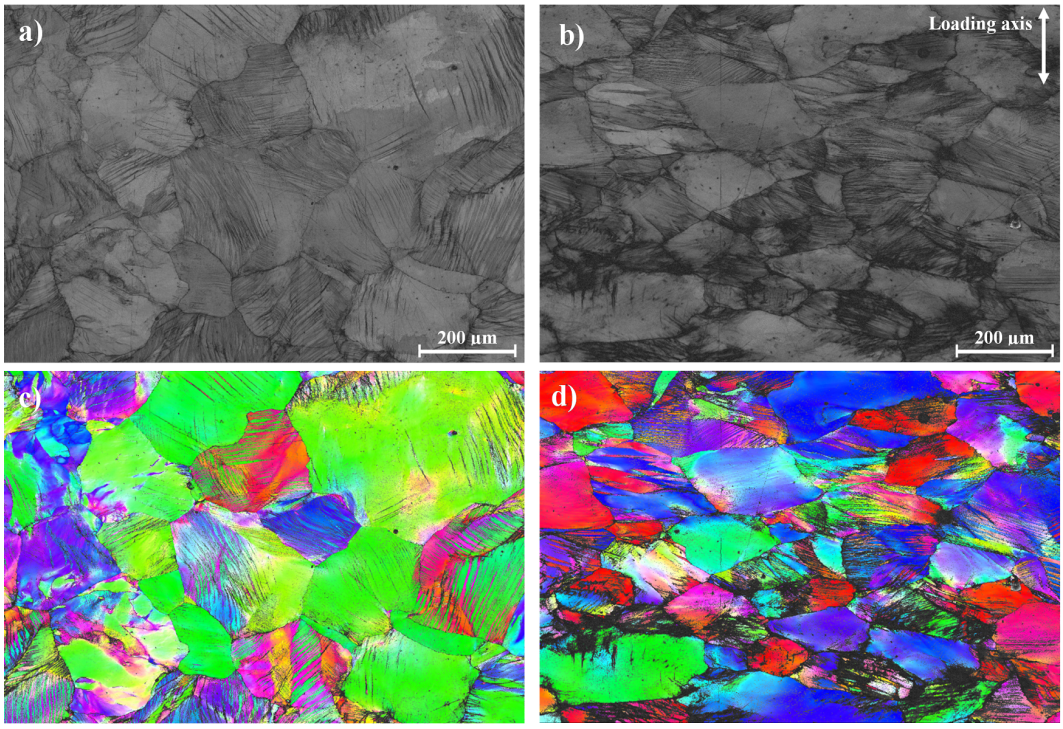

Figure 4.3: SEM band contrast images (quality maps of the EBSD measurement) of the Hadfield steel microstructures deformed to 26 % plastic strain at 0.1 s^{-1}, a) in the compression direction, and b) in the cross-section direction, and the corresponding IPF-maps c) and d). Dark/black areas have lower amount of recognized data points. Measurement step size was 0.7 μm with 9 bands used for indexing.

Based on the analysis of samples deformed to plastic strains ranging from 5% to 40 %, the twins and slip bands appear in multiple directions inside the grains depending on the amount of strain and the grain size. Smaller grains (e.g., around 100-200 μm) contained frequently twins in one direction only, i.e., predominantly in the primary twin system, while increasing plastic strain induced also other non-parallel twins. Large grains, on the other hand, showed a varying number of twins. Apart from the smaller grains, most of the grains exhibited mainly two twin variants at small strains, but continued straining led both to the growth of the existing twins and to the initiation of new variants.

The formation of wider slip bands, which can be detected by EBSD as an orientation difference, was observed in both small and large grains. However, visually it could be seen that moderate and large grain sizes tend to have a higher probability to form larger slip band regions (see Figure 4.4a and b) with clear orientation difference to the parent grain. Figure 4.4 illustrates grains with a different type of deformation mechanism active in each grain. The wide slip bands control the deformation in Figures 4.4a and b, suppressing any notable twin activity in this particular grain. The twins may appear as thinner regions in the grain, or as fairly wide bundles, over 25 μm thick, as shown in Figures 4.4c and d. The twins can form various curvatures instead of the thin needle-like structures due to their relatively large size. Thus, it is likely that the twins grow to the favorable areas in the grain with less resistance, while the slip activity around the twins and dislocations

penetrating the twins may cause irregularities in their shape.

The twin-twin interactions showed different features in the twin dominated grains. Heavy activity in two twin systems in the same grain can cause a 'bitwinned'-type of a grain, as shown in Figure 4.4e, which was observed more frequently than could probably be expected. The large grain size can have an effect on this behavior, as the two variants may grow independently until they intersect, or alternatively the parent grain may already have an annealing twin in the region of the intersection dividing the initial grain. The growth of the two deformation twins was observed to cease in these cases. The twins observed in Figure 4.4f show a stronger growth over each other, even through they are fairly wide. In these cases, the transferred/intersecting twins form second order twins [159], i.e., new twin variants inside an existing twin. Generally, it appeared that the twins are often coplanar at low strains, while higher strains lead more easily to the initiation of non-coplanar twins, which will start to interact with the existing ones.

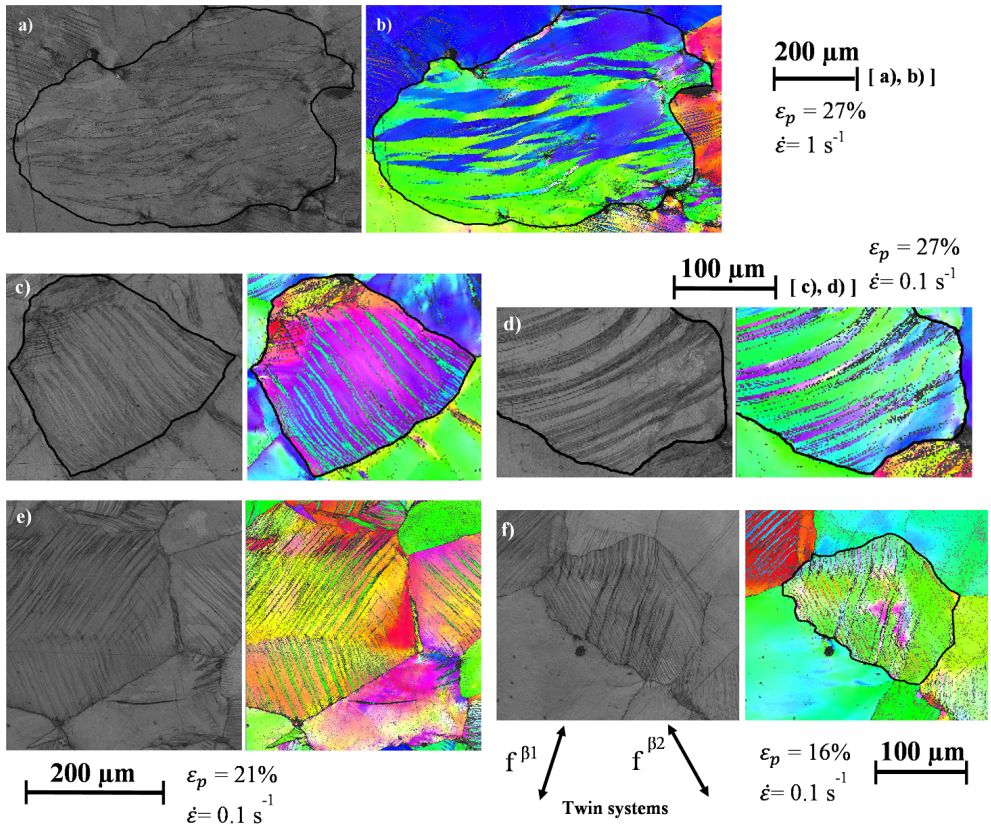

Figure 4.4: Different microscopic deformation and twinning mechanisms in the compression samples, a) and b) slip/microshear bands with large misorientations to the apparent parent grain, c) thin twin bundles in a grain, d) thick twin bundles, e) 'bitwinned' region having a misorientation of 7-10 degrees inside the apparent grain, and f) at least two active overlapping twin systems inside a grain. Apparent grain boundaries are highlighted with black color. The indicated strains are macroscopic plastic strains of the compression samples.

Figures 4.5a and b present band contrast images showing the recognized twins at two different plastic strains levels. From the images it is evident that increasing strain increases

the probability of twinning. Twinning occurs mainly by two mechanisms, the growth of existing twins and initiation of new twins at other nucleation sites.

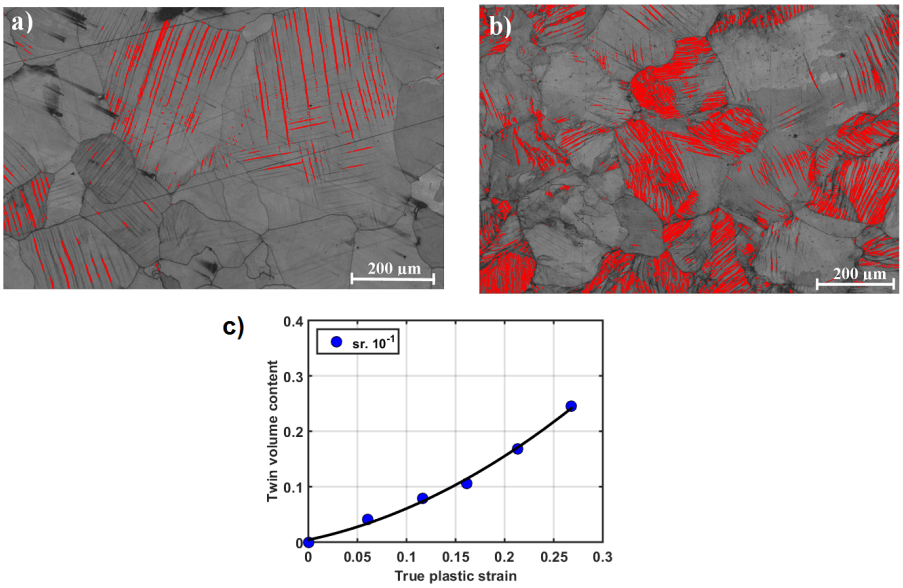

Figure 4.5: SEM band contrast images of microstructures deformed to, a) 6 % and b) 27 % of plastic strain. The red overlain areas are recognized twinned regions with a 60 degree misorientation to the {111} plane, c) the identified twin volume content at different macroscopic strains in the compression samples deformed at a constant strain rate of 0.1 s^{-1}.

The average twin volume fraction increases as a function of macroscopic strain in the samples as shown in Figure 4.5c. The initial twin volume fraction is considered to be zero, since the as-cast samples did not show any recognizable thermal twins. On the other hand, the indexing of higher strained samples (e.g., 40 %) lead to poor results, making the identification process of twins unreliable due to too many missing datapoints in the vicinity of the assumed twins and slip bands. Therefore, it is inconclusive where the possible twin saturation would happen. For the same reason, direct comparison of the twinning propensity at different strain rates was not possible, as suggested by Figure 4.6, which shows IPF colored microstructures of two samples deformed to the same plastic strain using two quite different strain rates. However, the visual inspection of etched samples suggests that the high strain rate samples tend to contain more localized bundles of twins and slip bands.

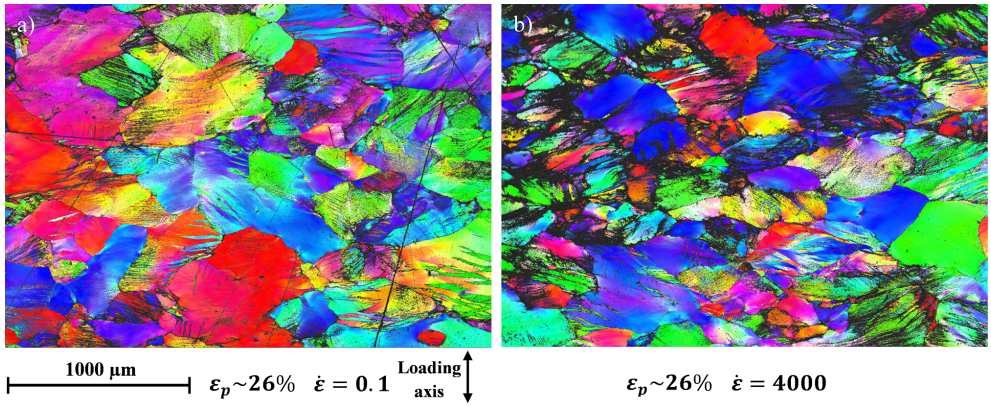

Figure 4.6: Deformed microstructures after compression to 26% of macroscopic plastic strain with IPF coloring, a) strain rate of 0.1 s^{-1} , and b) 4000 s^{-1}

The dislocation slip and twinning interactions can be examined from Figure 4.7. The misorientation profiles of a highly twinned grain in 4.7a show a wide slip band crossing the grain with an effect on the twin behavior. The slip band has a misorientation of around 15 degrees to the matrix (lines A and B in Figure 4.7b). The smooth transition in the misorientation from the matrix to the slip band suggests that the observed band actually is a slip band and not a grain boundary in a conventional sense, as the grain boundaries show a high misorientation angle with a step type transition similar to twins seen in the profiles. It is worth noting that the misorientations inside the grains of the as-cast material were very small even within the largest grains.

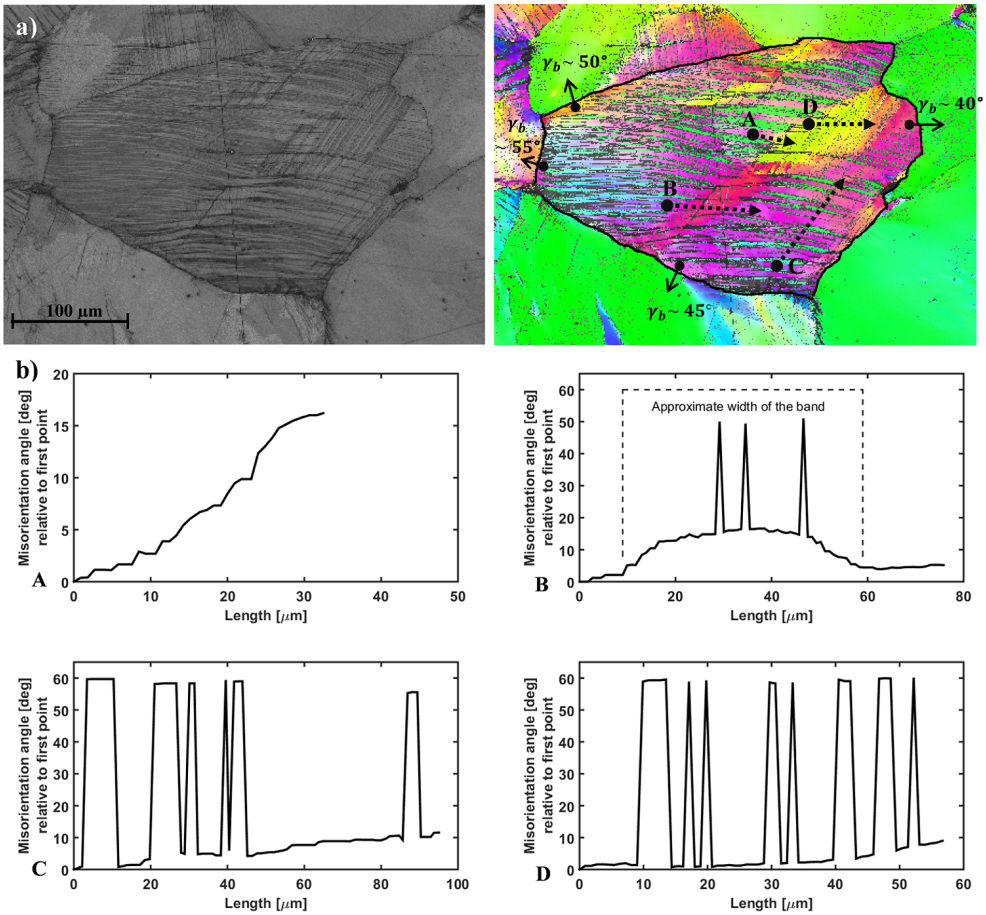

Figure 4.7: a) A heavily twinned grain with a deformation band inside. The macroscopic plastic strain of the sample is 21%. b) The misorientation profiles A to D are indicated in a) with arrows, dots mark the starting points, while the triangles are the end points of the profiles.

4.1.3 Evolution of hardness

The surface hardness evolution of the studied Hadfield steel is presented in Figure 4.8 as a function of plastic deformation. The highest hardness value was measured from the in-service sample in the direction of the loading. The degree of plastic deformation at the surface of the in-service sample is estimated by comparing the flow stress and hardness data in Figure 4.8. The exact amount of plastic deformation in the in-service sample, however, is impossible to determine due to complex cyclic and dynamic loading conditions, but this simplification is adopted to be used in the analyses presented in Chapters 5 and 6.

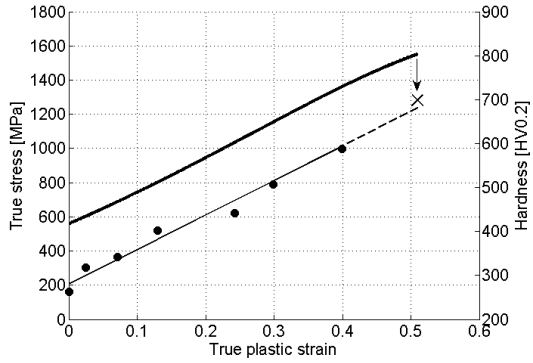

Figure 4.8: a) The tensile stress-strain behavior of the Hadfield steel at the strain rate of 0.1 s^{-1} (thick solid line). The hardness values of the samples compressed to different amounts of plastic deformation are indicated with dots, and the hardness of the failed sample measured near the failed region is marked with 'x'.

The microhardness depends on the local grain scale response of the steel, as show in Figure 4.9a. The measurements were performed on the grains that showed high amounts of twins and on the grains that showed none or very few twins (4.9b). The hardness difference is notable throughout the macroscopic average deformation range, revealing the strong strengthening effect of the twins.

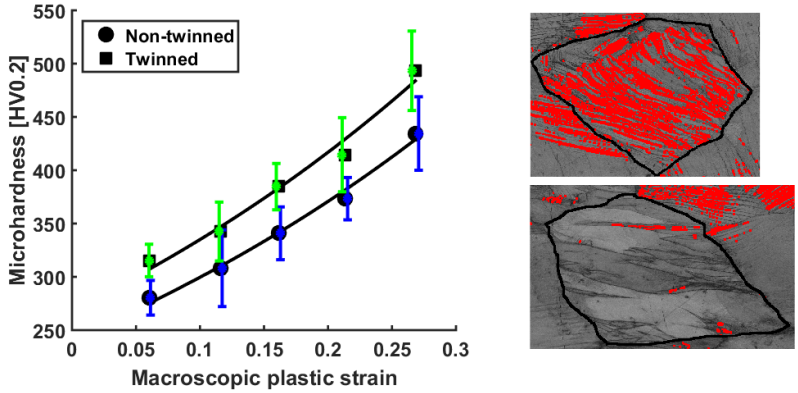

Figure 4.9: a) Average microhardness values at various pre-strains measured from the twinned and non- or low twinned grains. The error bars indicate the standard error. b) a twinned grain (upper), where the twinned regions appear red, and a non-twinned grain (lower). The black lines indicate the austenite grain boundaries.

The rather large variations in the measured hardness values arise from the fact that some of the twinned grains had far less twins than the others. Nevertheless, in most of the cases the grains showing high twin volume fractions showed also the highest hardness values. On the other hand, the grains considered non-twinned could also contain marked amounts of wide slip bands, which can also increase the strength of these particular grains. Both the twin density and the slip band density increased towards higher strains, increasing also the hardness deviation trend.

4.1.4 Deformation and hardening of the in-service jaw crusher sample

A common type of a jaw crusher is presented in Figure 4.10a, showing the wear plates crushing the rocks in green color. The contact conditions that prevail at the steel-rock interface depend on the setup of the jaw crusher. The jaws may be pivoted to favor either compression type loading or to cause more sliding. The choice is done according to the type of rock used in the crusher, and the optimization between the wear performance of the crusher and the quality of the end product. The wear of the jaw material is affected by several factors, such as the characteristics and topologies of the minerals, the environmental conditions such as moisture, and the running parameters of the crusher. Therefore, no universal solution exists for optimizing the operating parameters of the crushers or to choose the best performing materials against all wear inducing conditions.

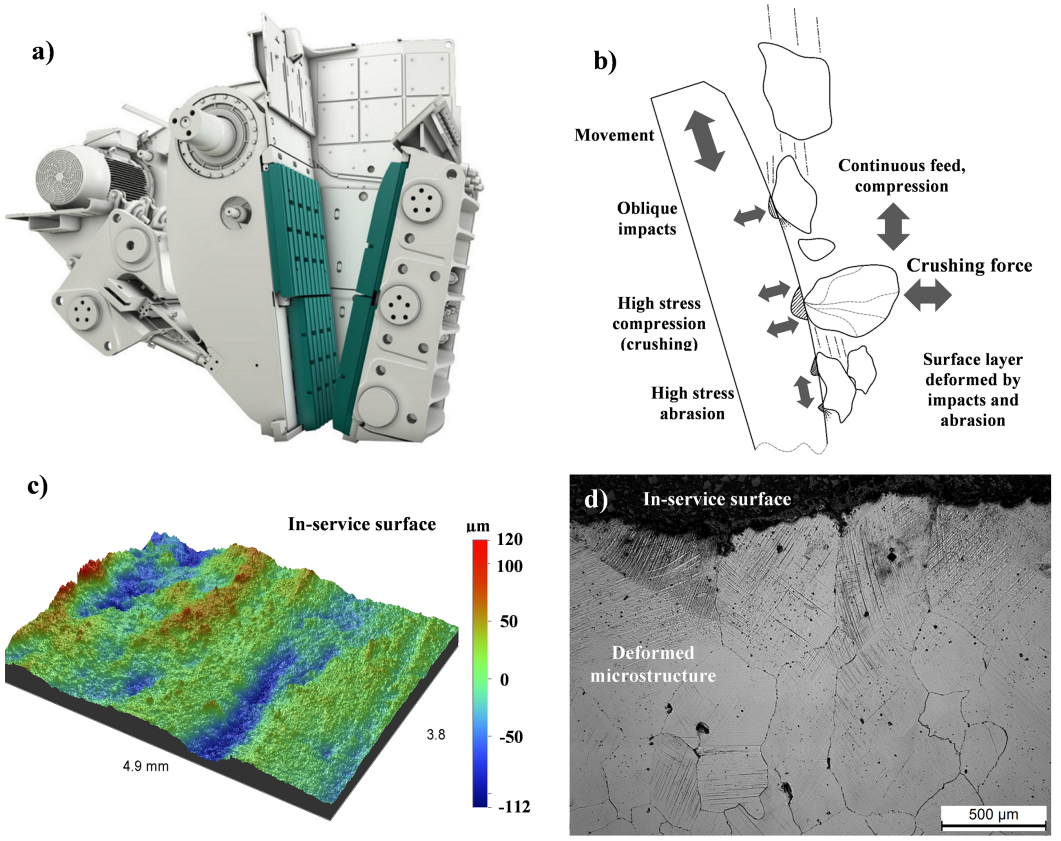

Figure 4.10: a) A typical jaw crusher assembly (Nordberg series C [149]) with wear jaws shown in green, b) simplified schematic of the loading conditions on the surface of a single jaw, c) 3D profile of a worn in-service sample showing wear marks from abrasion and impacts, d) a cross-section microstructure of the worn in-service sample.

Figure 4.10b idealizes some of the loading conditions present on the steel surface during the crushing process. While the jaw is moving during the crushing sequence, the rocks are impacted onto the surface from the supply funnel causing oblique angle erosion wear. However, again depending on the crusher setup, the supply funnel may be continuously

filled so that the rocks themselves absorb part of the impacts when they collide during the feed process. In the main event, cyclic crushing forces are subjected to the jaws when the rock comminuting is executed. The forces can reach very high values depending on the mechanical strength of the rocks. This phase is followed by sliding of the rocks on the surface causing abrasion, which can be considered as high stress abrasion because of the continued refinement of the rocks during this stage. Finally, the effect of different rock species on the wear rate is not clear; some rock types can be very aggressive such as quartzite, as they tend to fracture into sharp bits that cause severe cutting type abrasion to the surface [182]. As a summary of the process, the Hadfield steel used in the jaws is required to withstand impacts, high stress abrasion, cyclic loadings, added effect from corrosion, and relatively high strain rates appearing in the process.

Figure 4.10c shows a surface profile of an in-service sample that has experienced field conditions in a jaw crusher. The overall surface shows dents and abrasive cutting scratches that have been formed during crushing. Both impacts and abrasive deformation have considerably hardened the surface, as the hardness profile shows. The surface topology can be also seen in the cross-section of the in-service surface presented in Figure 4.10d. The etched micrograph reveals a high number of slip lines/bands and twins in the vicinity of the surface. The band contrast image in Figure 4.11a similarly shows grains with a high number of twins. However, the indexing of the surface region is poor because of the heavy deformation, which restricts reliable identification of the twins and slip bands. The hardness profile confirms that the strongest hardening is observed only in a relatively thin layer of ca. 1 mm, which in the coarse grained material corresponds to only about 1-3 grain diameters. The hardness variations deeper in the material seem to depend on the amount of twins/slip bands in the grains, as was already observed in the microhardness measurements (Figure 4.9). The maximum hardness of the investigated material in the in-service condition was around 680-720 HV, which is close to three times the hardness of the bulk material (250-300 HV).

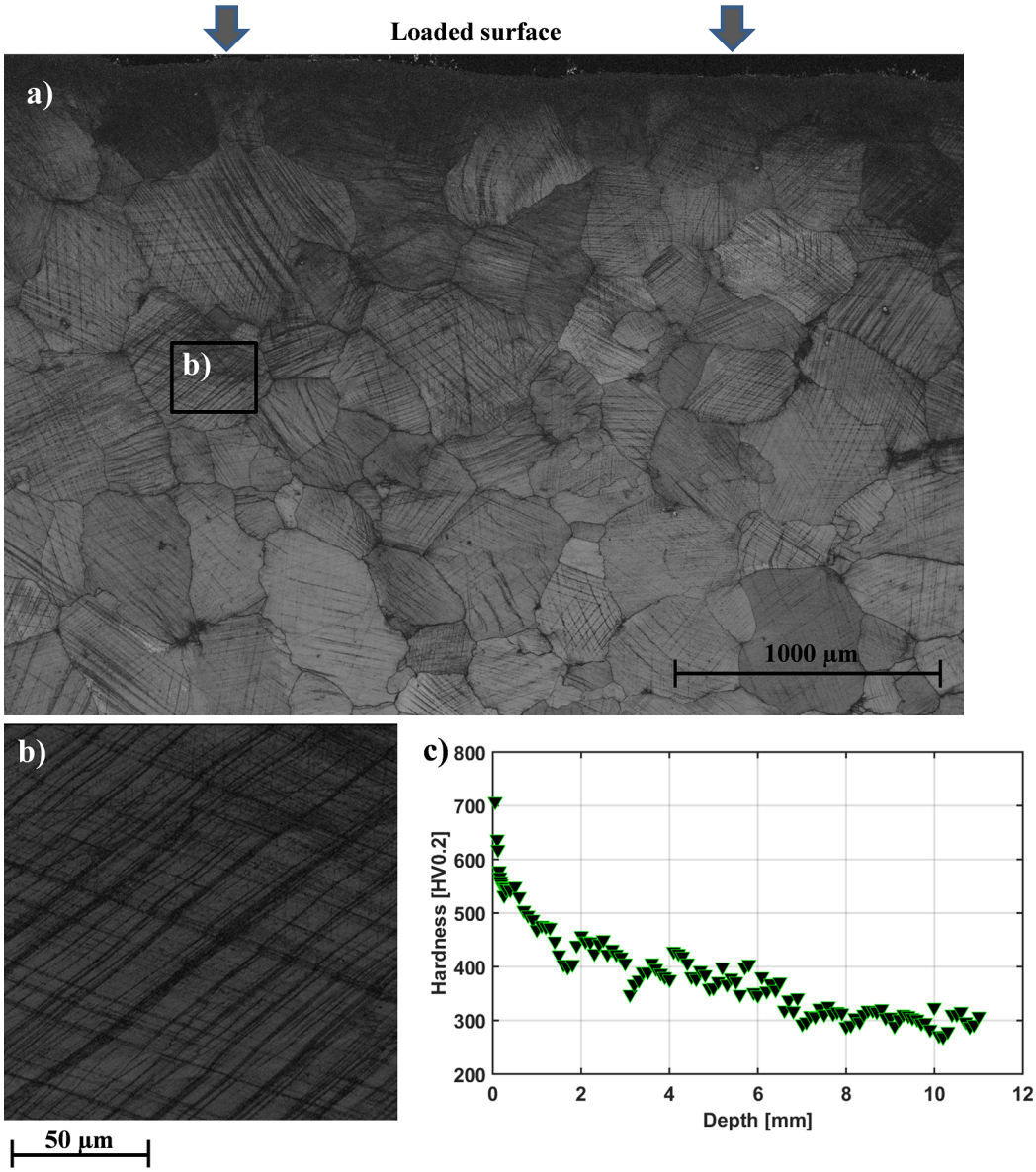

Figure 4.11: a) Band contrast map of a cross-section of the in-service sample, b) enlargement of a heavily twinned grain with multiple twin systems activated with a 60 degree misorientation to the parent grain, c) hardness profile of the surface.

The intensity of twins/slip bands decreases deeper in the material, which is also seen in the hardness profile. However, for example at the depth of 2 mm, where the hardness is still notably increased, the grains show similar behavior as the surface grains with multiple twin bands crossing and interacting. The interaction is also evident in Figure 4.11b, where some of the twin intersections show second order twins. From this micrograph it is not possible to determine which ones of the interacting twins are primary or secondary, since no in-situ information is available. The EBSD data showed exactly the same

characteristics as observed with the pre-strained samples discussed in the previous section; twins interact with twins and both thin and wide twins are present, wide slip bands appear in the microstructure and they have an effect on the twin behavior, and twins can promote twinning in the adjacent grains, which appear 'continuous' in the neighbouring grains.

4.1.5 Discussion

The deformation mechanisms responsible for the abrasive and impact wear behavior of Hadfield type steels has been of considerable interest and the topic of a large number of publications, e.g., [1, 40, 103, 113, 114, 131, 132, 169, 176, 233]. However, the dynamic range of the stress-strain behavior of these steels has not been so widely and precisely characterized, and therefore it is not quite clear which deformation mechanisms contribute to the hardening of the material at each strain rate range. The presently studied steel showed an increase of yield strength from about 480 MPa to 785 MPa, when the strain rate increased from 10^{-3} to 4000 s^{-1} at room temperature. As a comparison, recently Wen et al. [222] alloyed a Hadfield steel with silicon, which decreased the yield strength of the conventional Hadfield steel by 30 % to around 350 MPa. However, their alloying provided notably stronger strain hardening, increasing the flow stress to 1100 MPa already at 0.2 of plastic strain. Similar flow stress values are observed with the conventional grade only above 0.25 of plastic strain. In contrast, the currently tested grade showed flow stresses of ca. 950 MPa at 0.25, which are much lower than the normal values. On the other hand, the elongation before failure in the tensile test is markedly higher than that of the conventional or especially of the silicon alloyed Hadfield steel. Hence, with a good balance between the strain hardening capability and the ductility required in jaw crusher applications, the currently investigated grade could provide better resistance against impact and fatigue wear.

The strain rate dependence of the Hadfield steels is not straightforward. Some studies [23, 40, 56] on conventional Hadfield steel report both positive and negative strain rate dependence in the quasi-static strain rate range depending on the strain rate. For example, Canadinc et al. [40] observed negative strain rate dependence when comparing strain rates 10^{-2} and 10^{-4}, but again in the comparison of 10^{-1} and 10^{-4}, the material showed a positive strain rate dependence. The negative strain rate dependence is often explained by the dynamic strain aging (DSA), causing jerky flow attributed to the enhanced carbon diffusion affecting mobile dislocations [169]. On the other hand, the strong strain hardening of the Hadfield steels is believed to stem from the compound effect of deformation twinning, twin-slip interactions, and slip interactions with Mn-C atom pairs. Deformation twinning, for example, cannot alone provide high strain hardening, which has been pointed out by some fundamental studies on Hadfield steels [56, 244].

Most of the studies restrict only to quasi-static strain rates leaving the dynamic range unresolved in terms of deformation behavior. Lee and Chen [122] found a positive strain rate dependence in the dynamic range in tension, e.g., above $2 \cdot 10^3$, which is consistent with the findings of the present study, implying that the Hadfield steels do not exhibit negative strain rate dependence at high strain rates. At increasing strain rates Canadinc et al. [40] considered that the shorter waiting time of dislocations in front of the obstacles allows less time for the diffusing carbon atoms to interfere with the dislocation motion, affecting the competition between diffusivity of carbon and the aging of the immobile dislocations. The present results suggest that it is possible for the forest hardening to overcome the effect of DSA at higher strain rates. It is also possible that the higher

manganese content of the presently studied Hadfield steel has an effect on the DSA mechanism.

The characterization results demonstrate the importance of the interactions between the different deformation micromechanisms. Deformation twinning on its own causes very little strain hardening [114], but when it is combined with active dislocation slip, excellent strain hardening is observed. Also, the twin-twin interactions have some characteristics similar to the twin-slip interaction. Twins can act as barriers to the propagation of other twins, causing sometimes penetration by the generation of second order twins, or they may fully arrest the growth of each other, such as in the 'bitwinned' grains in Figure 4.4. The probability for twin-twin interactions grows with increasing macroscopic strain and twin volume fraction, as well as the due to activation of non-coplanar twins. Considering that the twin intersections do not fully restrict the growth of either primary or secondary twins [65], the material's strain hardening capability and ductility can be improved. This can be explained by noting that twin growth provides an alternative deformation mechanism to dislocation slip, possibly *increasing* the ductility of the material. On the other hand, the increasing volume fraction of twins intensifies the barrier effect to dislocation slip, *increasing* the strain hardening capability of the material.

It is worth noting that the twin volume fraction is only a scalar representing the microstructure on average. The size, length and spacing of the twins may vary, for example depending on the temperature and strain rate, as presented by Toker et al. [213]. They studied the conventional Hadfield steel in impact conditions and noted that high temperatures inhibited twinning in some cases, while low temperatures usually lead to higher twin propensity. However, the direct effect of strain rate was not reported in their work, as they had no control over it in their experiments. In the present experiments, the increase of temperature using the theoretical assumption of adiabatic conditions (Equation 2.1) can be approximately 75 °C in the 4000 s^{-1} test, if 95 % of the strain energy was converted to heat. In fact, for TWIP steels such a temperature increase may already cause an increase in the SFE by as much as 10-25 $mJ^{-1}m^2$ [50]. The experimental observations on the microstructure, however, show very notable amount of twins also in these conditions, even to such extent that it is equally plausible that high strain rate favors twinning, at least when the initial temperature of the sample is at room temperature. Unfortunately the EBSD data available at the moment is not sufficiently accurate to confirm this.

Finally, it can be concluded that the deformation behavior observed in the in-service and pre-strained samples shared the same characteristics. The in-service samples show that twinning is required to reach high hardness values at the surface of the steel, and the pre-strained samples point out that the twinned grains pose much higher grain level hardness values. In neither case, the substantial hardening of these grains did not seem to increase the probability to in-grain failure, so that the material retained its ductility. The similar features of the deformation mechanisms and microstructures in laboratory and field samples suggest that the applied laboratory tests characterize the in-service deformation behavior of this material fairly well. However, the exact comparison of the laboratory experiments and the field samples is difficult because of the unknown loading conditions of the in-service samples. Numerical simulations hopefully can provide more detailed information about the relationship between the assumed loading history and the deformation behavior of the material in real applications.

4.2 Deformation and hardening in martensitic wear steels

This section presents characterization results of martensitic wear resistant steels. The mechanical behavior of the steels is first investigated at low and high strain rates. The strain hardening and failure characteristics of the steels were studied to shed light on their impact behavior. An examination was also performed on an in-service sample extracted from a cutting edge of a bucket loader used in mining conditions.

4.2.1 Mechanical behavior

Figures 4.12a-c show the stress-strain behavior of the steels in compression performed at room temperature. The strain rate range covers the quasi-static range from $10^{-3} - 10^{0}$ s^{-1} to dynamic range of 700-3600 s^{-1}. The curves were smoothed with a second order polynomial that was fitted to the plastic strain region of the raw data to obtain the yield points by backward extrapolation, as presented in [133]. The yield points of the HV500B and HV550 steels show about 10 % and 15 % higher values that of the HV500A grade, respectively. The positive strain rate dependence of the yield strengths in Figure 4.12d shows the desired characteristics for impact conditions.

The strain hardening rates clearly show that the present martensitic steel grades first undergo moderate strain hardening, after which the hardening rate reduces or even softening occurs in some cases. It is evident that the strain hardening rate at quasi-static strain rates shows a fairly strong increase, but as the strain rate increases, the hardening rate decreases for all steel grades. This can be seen, for example, from the low strain rate curves of $10^{-3}s^{-1}$ exceeding the dynamic strain rate curves of 3600 s^{-1} at higher plastic strains.

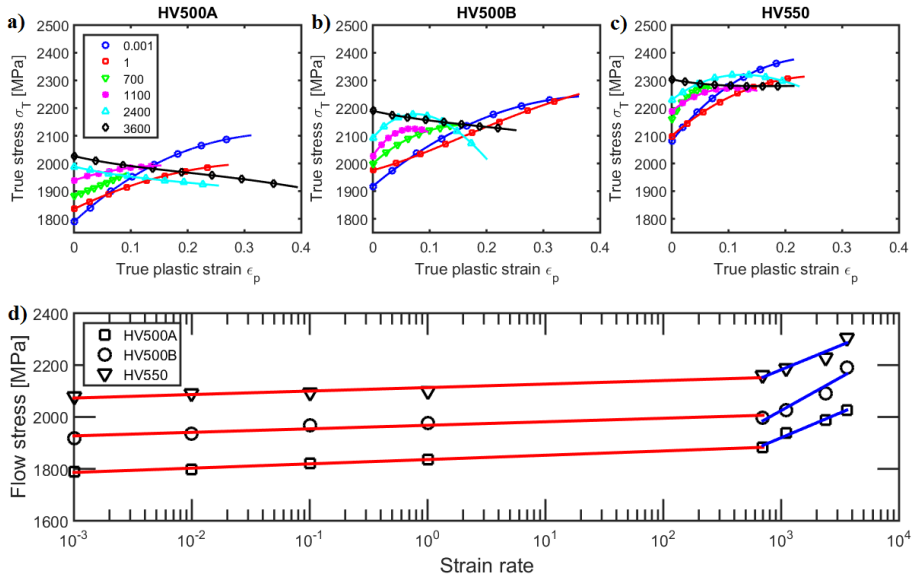

Figure 4.12: The stress-strain behavior at various strain rates in compression for the martensitic steels a) HV500A, b) HV500B, c) HV550, and d) the yield stresses as a function of strain rate.

The rapid change in the strain hardening rate from positive to negative values observed for all studied steel grades at 3600 s^{-1} was caused mainly by adiabatic shear banding

that was spreading throughout the test samples. At lower strain rates, notable formation of shear bands could not be observed from the etched microstructures. It is still possible that shear localization appeared in the form of deformed shear bands through localized slip. The macroscopic temperature of the high strain rate samples increased during the experiments due to the strongly adiabatic conditions. For example HV500B deformed at the strain rate of 3600 s^{-1} underwent a theoretical temperature increase of about 150 $°C$. This value, however, is not very high and it is unlikely that it alone can cause such marked softening. On the other hand, the strain concentrations at the local scale can lead to much higher temperatures due to adiabatic conditions, which eventually can lead to the formation of adiabatic shear bands. The additional tests performed at the strain rate of 4200 s^{-1} also resulted in softening and shear banding, which suggests that increase in the strain rate increases the probability for localization.

4.2.2 Adiabatic shear banding and failure

Figure 4.13 show the cross-sections of the compression samples failed in the tests at 3600 s^{-1}. The images were taken approximately in middle of the sample on the x_1-x_3 plane, where the compression direction is denoted by x_3. A schematic presentation of the incident is shown in Figure 4.13d.

The steels exhibited a typical shear failure into two or more pieces. The main failure occurred usually at ca. 39-45° angle in respect to the loading direction. The main crack propagated parallel to the adiabatic shear bands that appeared white in the micrographs, typifying them as transformed adiabatic shear bands. The comparison of the two halves clearly shows that the cracks propagated inside the shear band region instead of the interface of the shear band and the matrix, as both halves contained visible white etch regions. Similarly, if the samples failed to multiple pieces, the failure propagated mainly along the transformed shear bands. In contrast, the quasi-static samples did not show failure or formation of such bands even at high strains. For example, even up to ca. 35 % of plastic strain the samples remained in one piece, whereas the dynamically loaded samples could break already after 20 % of plastic strain.

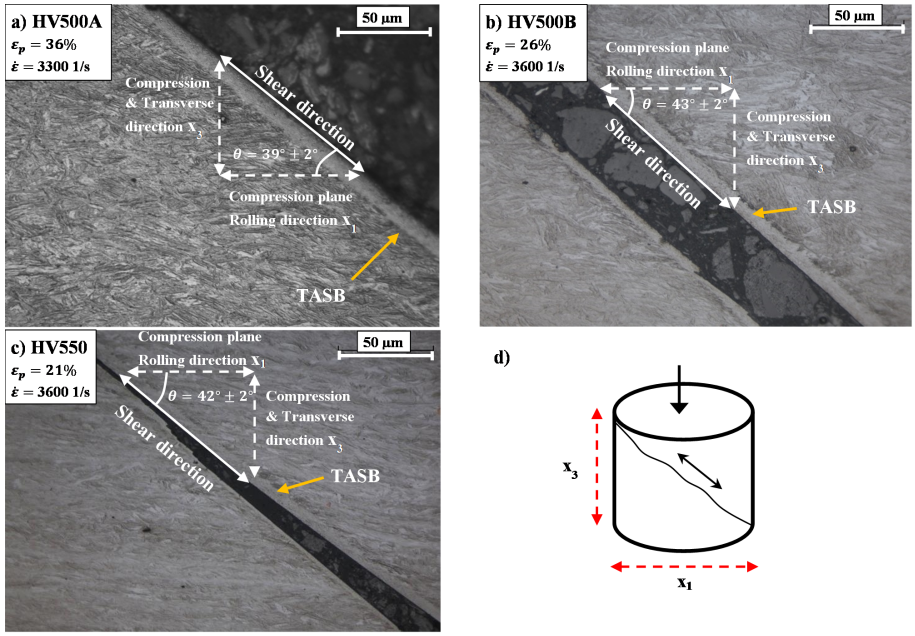

Figure 4.13: Shear failures along transformed adiabatic shear bands in the compression samples of the martensitic test materials tested at high strain rates [133].

The highest probability for the formation of adiabatic shear bands was observed for HV550, leading to highest number of failed samples, while HV500A failed most rarely. This result suggests that the initially hardest and finest microstructure was the most susceptible for shear banding in the present tests. Table 4.1 presents the microhardness values measured from the failed high strain rate samples in the deformed and undeformed matrix, and inside the shear bands.

The most shear band resistant steel of the studied grades was HV500A, which showed the lowest strain hardening with ca. 19 % increase in the matrix. The high initial hardness of HV550 provided the highest deformed hardness of the matrix, while the highest increase from the bulk hardness was observed for HV500B. In all cases, the hardness of the shear band regions was notably higher than that of the deformed matrix. The EBSD measurements performed on the deformed matrix showed that the grains tend to orient towards the shear direction near the shear band regions. The current findings also suggest that the adiabatic shear bands had underwent dynamic recrystallization process, as they showed significantly higher hardness values and notably smaller equiaxed grain size, which both are typical for the transformed shear bands. As a conclusions, the observed failure

Table 4.1: Microhardness (HV0.025) values of the samples deformed and fractured in the high strain rate tests.

Material	Underformed steel	Deformed steel	Adiabatic shear band
HV500A ($\epsilon_p = 36\%$)	511 ±8	600 ±12 (19%)	741 ±5 (43%)
HV500B ($\epsilon_p = 26\%$)	517 ±9	707 ±8 (37%)	796 ±14 (54%)
HV550 ($\epsilon_p = 21\%$)	542 ±7	724 ±10 (34%)	824 ±8 (52%)

process showed similar characteristics inside the transformed adiabatic shear bands as suggested in Figure 2.8.

4.2.3 Cutting edge of a bucket loader field sample

Wear parts of mining equipment are a typical application for the currently investigated ultra high strength martensitic steels. A simplified schematic of the cutting edge of a bucket loader is presented in Figure 4.14a. The cutting edge is subjected to harsh loading conditions when transporting minerals in a mine. Figure 4.14b exemplifies some contact characteristics taking place between the gravel and the steel. The cutting edge is subjected to high stresses when the bucket collides with a pile of minerals. In more detail, the underside of the cutting edge faces heavy abrasion with high surface pressures and high coefficients of friction in the contact with minerals that are entrapped between the steel and soil. The upper side of the cutting edge usually faces somewhat milder loadings because the rocks are able to move on the surface more freely. However, during the loading sequence, the upper side may be subjected to rather heavy loads when the bucket is plounged into the rock pile.

It has been widely established that the sliding velocity affects the wear process, and therefore the sliding velocity of the particles in the loading process is important. Even though the operating velocities of the bucket loader equipment in mines and quarries are limited, the surface sliding velocities of the rock-wear plate pair may reach several meters per second at the underside of the bucket. For example, by estimating the occasional operating velocity of the loader to be 10-12 km/h, the sliding velocity of a rigid surface point relative to another would result in around 3 m/s. This sliding velocity can be considered dynamic abrasion, and some added effects from frictional heating are very likely. The actual intensity of wear is influenced by many variables in the mine, such as the wear plate material and the characteristics of the abrasives being handled. Recently Keltamäki and Ylitolva [116] performed a survey on the in-service cutting edge in an underground mine and found that already during 928 operating hours the ultra high strength steel (HV500A of this work) had lost around 27 % of its original weight. This material loss was sufficient to remove it from active use. Their optical profiling showed that the most material had been lost from the underside of the cutting edge, while the upper side had worn much less.

Figure 4.14c present the worn surface on the underside of the cutting edge showing a number of abrasive marks. The three-body nature of the abrasion between the steel surface, hard soil, and rocks generate a number of parallel and non-parallel scratches on the surface with varying depths and different amounts of ploughed material at the edges of the wear scratches. Figure 4.14d presents a cross-section of the worn underside surface. The etched image shows a special tribolayer formed on the surface appearing white, denoted commonly as the 'white layer'. The layer is present only in some parts in the cross-sections, indicating that it only forms in special conditions. The other parts of the surface without the white layer showed more typical plastic deformation. The thickness of the white layers varied from thin 10-20 μm even up to 150 μm thick layers. The underside and the tip region of the cutting edge were most prone to the formation of the white layers, while on the topside such surface layers were not observed, which is consistent with the considerations of the severity of the contacts.

A more detailed image of the in-service surface wear and a comparable image of the scratch test surface (see Chapter 5) are shown in Figure 4.15. The plastic deformations of the scratches resemble each other well. Regardless that the scratch tests were performed

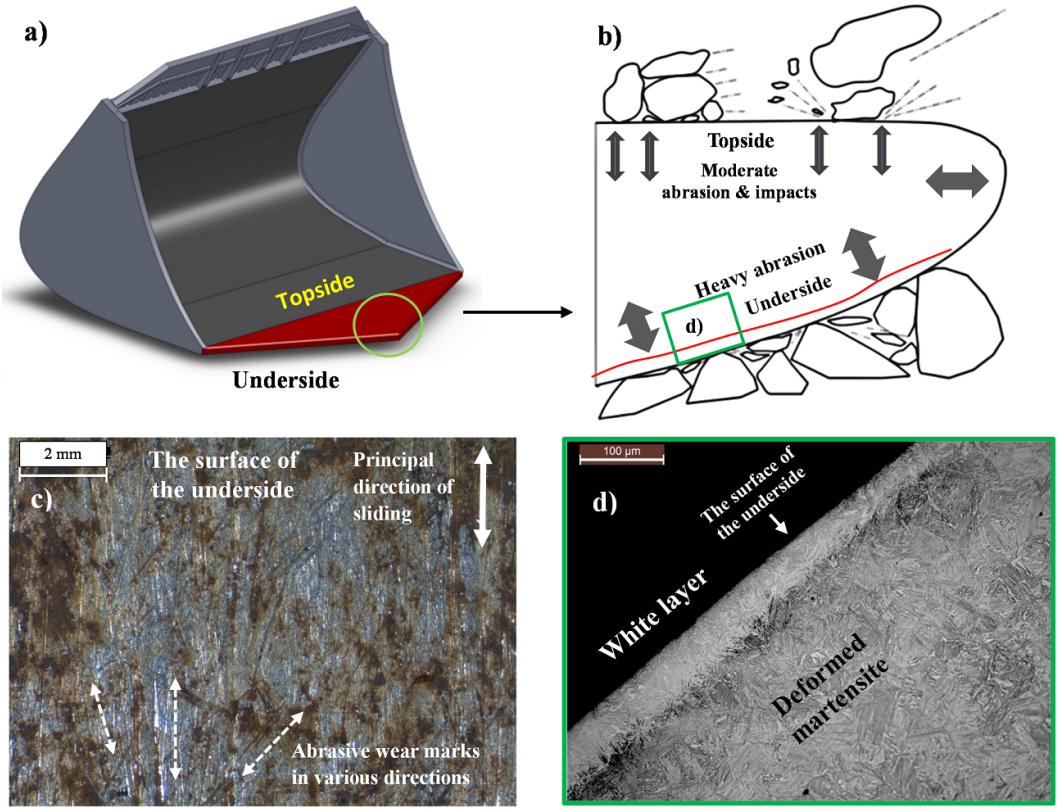

Figure 4.14: a) Typical geometry of a bucket loader cutting edge, b) schematic of some loading conditions in the cutting edge of a bucket loader, c) worn surface from the underside of a cutting edge (the surface facing ground and gravel, photo by Kati Valtonen), d) etched cross-section from a worn cutting edge with a white layer on the underside.

on polished surfaces, the scratched surface reaches similar wear characteristics as the in-service samples already after 5-10 loading cycles. In both in-service and laboratory experiments, the edges of the scratch show almost detached wear particles that would likely be removed in any subsequent loading especially if that happens in some other direction. This is also evident from the surface of the in-service sample, where several plastically deformed lips are observed, but which are mostly rounded with the sharper wear platelets being effectively removed.

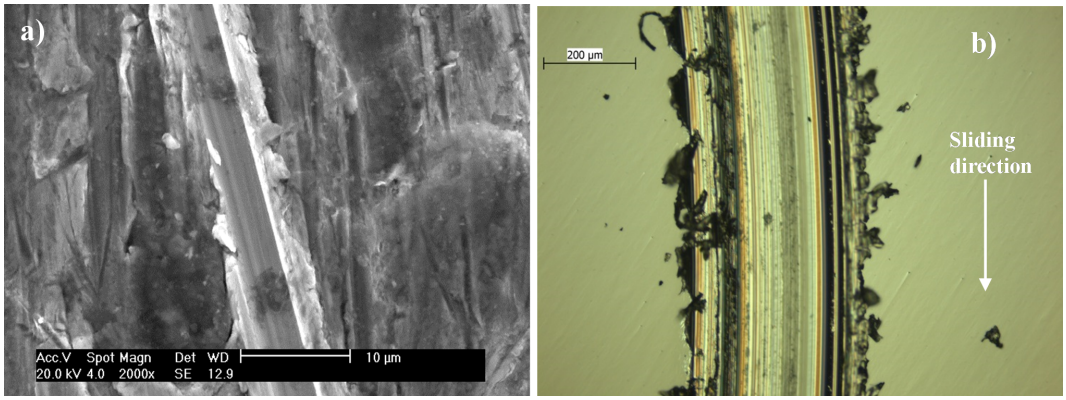

Figure 4.15: a) Abrasive marks on the surface of the in-service sample (Photo by Kati Valtonen), b) scratch test surface after ten overlapping passes on a polished surface at a normal load of 80 N. Material is HV500A in both cases.

Characterization of the microstructure of the white surface layers reveals a gradient type refinement of the grain structure, as shown in Figure 4.16a. A very fine grain size exists near the abraded surface, coarsening towards to interior of the material. A more detailed EBSD measurement confirms that the grains in the immediate vicinity of the surface are generally equiaxed and the grain size appears to gradually increase deeper in the material, still retaining the rounded shape. The size of the small equiaxed grains at the surface is only a fraction of a micron, suggesting a process very similar to the dynamic recrystallization near the surface, which would also explain the more etch resistant nature of the white layers compared to the bulk microstructure.

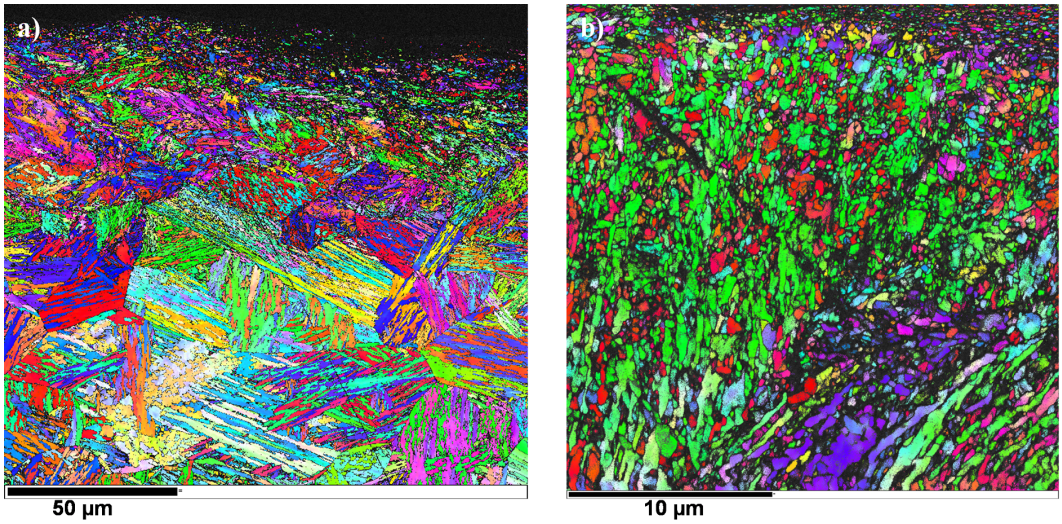

Figure 4.16: Band contrast image with IPF coloring of a) the white layer and bulk microstructure, and b) the microstructure of the white layer at the surface.

Figure 4.17 presents hardness contours with and without white layers and hardness profiles measured from regions of the surface. The hardness of the white layers appears

higher than that of the deformed surface without white layers. There exist hardness variations between the different regions of the white layers, which is a results of different microstructures of the layers at different locations in the in-service sample. The hardness gradient from the white layer to the bulk microstucture is significant, since the hardness easily decreases by over 50 %. The transition zone that comprises of a mixture of new rounded grains and needle type sharp grains, results in a roughly 20-30 % higher hardness than the bulk. The hardness profile of the deformed surface without a white layer has a smoother transition from the hardened microstucture to the bulk, but the hardness is still notably higher than that of the bulk microstructure.

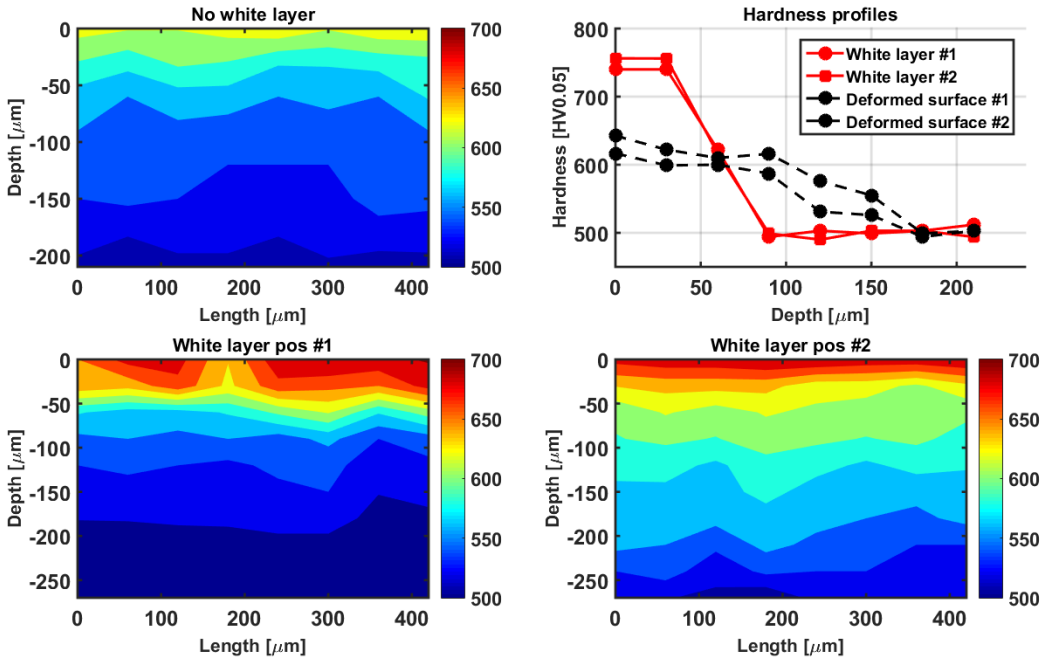

Figure 4.17: a) Hardness contour of the deformed in-service sample's sub-surface with no white layer, b) hardness profiles showing two measurements on the white layers and two on the deformed layers without an apparent white layer, c) and d) hardness contours of white surface layers.

4.2.4 Discussion

The strain hardening behavior of the studied three ultra high strength steel grades is quite good for hard martensitic microstructures. The hot-rolling processing of the steels allows autotempering of the steel during the process, increasing the ductility in comparison to untempered martensite. The high strain rate compression tests performed on the steels with quite similar hardness, however, showed that the steel grades are prone to adiabatic shear banding. Generally, none of the studied steel grades can be considered as highly strain rate sensitive, as is usual for BCC type of crystal structures. When comparing the yield stress of HV500B at 10^{-3} and 3600 s^{-1}, only about 15 % increase is observed. The adiabatic shear bands can cause local softening in the microstructure of the steels, but the observed strain softening has also many other reasons. For example, no visible shear band formation was observed in the tests of HV500A at 2400 s^{-1}, but still slight

softening is evident. Fairly recently for example Rittel et al. [186] found evidence that softening in pure Fe can be caused by $\alpha(BCC) \rightarrow \epsilon(HCP)$ transformation, when shear bands are not present or their effect is negligible.

The observation that the hardness of the matrix in the studied steels was lower than that of the shear bands is consistent with the results reported for example by Odeshi et al. [166] for AISI 4340 exhibiting shear banding in high rate deformation. Their results showed that the hardness of the shear bands was almost twice the bulk hardness. They also found that the surrounding matrix did not undergo severe strain hardening even when failure occurred in their tests, leaving the matrix hardness almost unchanged at the original bulk-level hardness. Although AISI 4340 is also considered a high strength steel, the present steel grades showed more significant increases in the hardnesses of the matrix, suggesting that their microstructures are capable of storing strain energy more uniformly. However, evidence was also found that with increasing hardening of the matrix and the shear band regions, the material had a higher probability to develop failure at lower macroscopic plastic strains.

The tribolayers generated in the in-service conditions show very similar characteristics to the adiabatic shear bands. Two types of deformed surfaces were observed, including transformed type of white surface layers and more conventional type of plastically deformed surface regions. The former, in fact, share the hardness increase and refined microstructure of the TASBs suggesting that they can be produced by the DRX process. Further support for this type of transformation may be considered from the frictional heating of the surface during sliding of the abrasive. The relatively high coefficient of friction of rocks against steel combined with the high surface pressure and high sliding velocity can increase the surface temperature dramatically by conversion of frictional energy to heat. At the same time, it can be regarded that the strain levels and the strain rates can provide the required conditions for the DRX. Although alternative explanations for the development of the microstructures of the tribolayer are suggested, such as martensite reversion [123, 161, 162] or diffusion based austenization and rapid quenching [47, 208], they do not considered the effects of high strains and high strain rates exhibited by the surface during the contact between the rocks and the steel. Hence, based on the present results and characteristics of the white tribolayers, it appears that they are likely products of the dynamic recrystallization process. At present, however, it is a bit uncertain what is the real effect of these layers on the wear behavior of the steels, i.e., whether they have a favorable effect (e.g., high hardness resisting abrasion) or a deteriorating effect (e.g., prone to crack formation due to reduced ductility as product of high hardness) on the final outcome.

4.3 Deformation of carbide-reinforced wear steel - results and discussion

Figure 4.18 presents the stress-strain behavior of the chromium carbide reinforced steel in compression in a wide range of strain rates at room temperature. The stress-strain curves are smoothed by fitting a second order polynomial to the raw data. The results show that the material is quite strain rate insensitive, as only about 10 % increase in the yield strength is observed when the strain rate is increased from 10^{-3} to 3600 s^{-1}. The samples failed generally already below 0.1 of plastic strain, which is typical for this kind of high strength matrix-carbide composite materials. The strain hardening, on the other hand, is surprisingly strong during the deformation, for example an increasing the flow

stress by ca. 600 MPa in the quasi-static test at 10^{-3} s^{-1}, which is notably more than observed for the martensitic steels studied in this work.

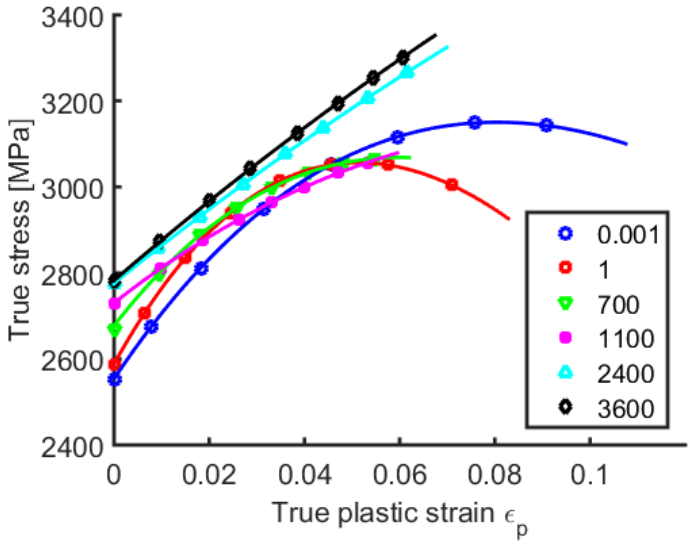

Figure 4.18: Stress-strain behavior of the carbide reinforced steel at various strain rates. All samples failed during the compression tests

Increase in the strain rate generally decreases in both the strain hardening rate and ductility of the carbide reinforced steel, as seen in Figure 4.18. However, a change in the behavior can be see at the two highest strain rates, where no marked decrease in the strain hardening rate before failure is visible. Microscopic observations on the cross-sections of fragments of the failed sample deformed at the strain rate of 10^{-3} s^{-1} revealed that the failure nucleates and propagates from multiple nuclei sites, as seen in Figure 4.19. The cracks propagated in the matrix along the carbide boundaries as well as across the carbides. It is probable that the carbides act as nucleation sites for the cracks since also a great number of cracked carbides were observed without any cracks in the matrix around them. The stress concentrations arising from the phase boundaries may also trigger failure of the interfaces, carbides, or the matrix, but their effect is rather difficult to estimate based on the experimental findings only. For more thorough investigation of these phenomena, numerical simulations and comparison of their results with the experimental data would be quite useful.

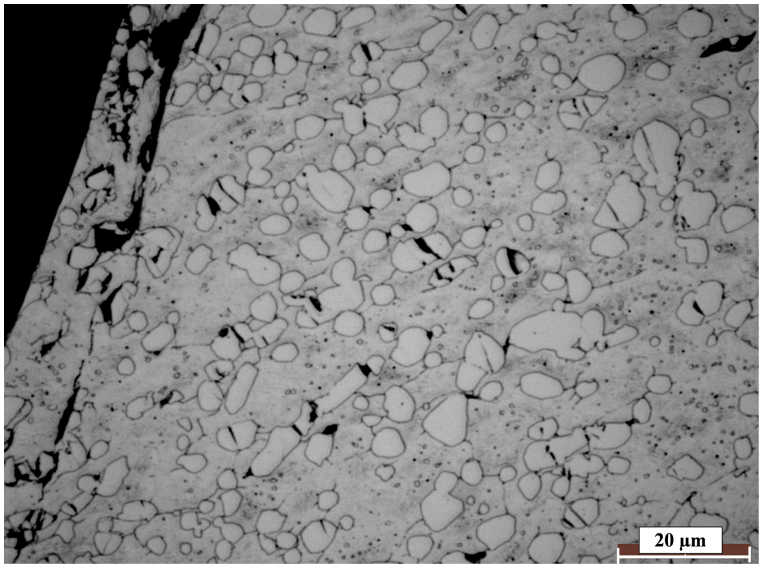

Figure 4.19: Microstructure of a failed sample fragment from a test at a low strain rate of $10^{-3}s^{-1}$.

The strain rate also had an effect on the failure characteristics of the material. At the low strain rates, the samples showed notably less fragmentation than especially at the two highest strain rates of the test range. The main reason for the increased fragmentation at the higher strain rates is evidently the higher probability of the formation of adiabatic shear bands. The matrix close to the main failure paths showed heavy deformation indicating either deformed or transformed shear bands in these areas. In the current material, the random size and shape distribution of the particles inhibit any strong orientation of the crack path with respect to the particles, which is consistent with the observations of Dai et al. [53].

The increase in the matrix hardness shows that its strain hardening capability is quite decent despite the quite low macroscopic strains applied to the samples. The low scatter of measured hardness values in the hardened state also indicates that the matrix strain hardens quite uniformly. The density of cracks inside the shear regions was too high to determine the hardness of these regions, but it could be expected that even higher values would have been obtained from there.

Table 4.2: Microhardness (HV0.025) values from a sample deformed and fractured in compression test conducted at the strain rate of 3600 s^{-1}

Material	Underformed steel	Deformed steel	Carbides
COMP ($\epsilon_p = 7\%$)	739 ±18	848 ±12 (15%)	1385 ±107

The strain hardening behavior of the metal matrix composite type of steel is a complex process comprising the strengthening effect of hard particles and supporting the strain rate sensitive matrix, which leads to different stress-strain behavior depeding on the conditions. Experimental and modeling approaches, e.g., [15, 32, 33, 180], have shown that the strain rate sensitivity and hardening rate of particle reinforced composites or metal matrix composites depend on the volume fraction of the reinforcing particles, their size and aspect ratio. Also, the failure behavior of the composites depends on strain rate through the connection between particle size and the propensity for adiabatic shear banding at high strain rates [52, 53].

The approximate volume fraction of chromium carbides in the current steel is about 0.20-0.25. Based on the simulation results presented by Cai et al. [32] for similarly reinforced materials, 0.20-0.25 particle volume fraction of reinforcing particles can easily lead to notable increase in the flow stress in dynamic region of the strain rate, which is consistent with the presently obtained results. The simulations of Cai et al. [32] also showed that irregular carbides with varying aspect ratios provide a better strain hardening capability especially at high strain rates. The currently examined microstructure consists of a great number of varying particle topologies, which were identified as the long needle type, an almost spherical, or a type mixture of these two. No directionality that would cause any pronounced anisotropic behavior exists at the macroscopic scale as a consequence of manufacturing by casting. In addition, the XRD measurements resulted in an approximation of the retained austenite content of ca. 8 %, which can have a positive effect on the strain hardening capability of otherwise martensitic microstructure [156]. Based on these aspects, it is quite expected that the present steel shows quite good strain hardening capability at both low and high strain rates. As a trade-off, it is not completely unexpected that the ductility of the material decreases towards higher strain rates for two reasons: i) small carbide size (5-15 μm here) effectively promotes shear banding [52], and ii) the high strain gradients act as a strong driving force for the formation of adiabatic shear bands [52].

4.4 Summary and partial conclusions

Characterization of the deformation behavior of selected wear resistant steels was performed to elucidate the key factors essential in abrasive and impact wear conditions. The mechanical behavior of the test materials was investigated in a wide range of strain rates including quasi-static and dynamic deformation conditions in compression at room temperature. The post-deformation characterization of the deformed samples revealed details of the dominating deformation mechanisms, such as the competing nature of dislocation slip and twinning. Also the localization of strain in the microstructures was investigated to increase understanding of the dynamic failure processes of ultra high strength steel grades. In addition, some typical applications where these materials are used were introduced. In-service samples were examined to compare the deformation and wear behavior of the studied steels in real applications and laboratory scale tests.

The high manganese austenitic steel grade (Hadfield type steel) deforms by both dislocation slip and twinning, which causes the typical upward strain hardening behavior of the material. The characterization of the material's micromechanical behavior led to the following observations and conclusions:

- The investigated Hadfield grade showed positive strain rate dependence at all studied strain rates, suggesting that dynamic strain aging does not have a significant effect

on the strain hardening behavior of this grade, at least in the studied strain rate range.

- The material's strain hardening rate is affected by strain rate through adiabatic heating and possible effects on the twinning propensity.
- The overall twin volume fraction increases with increasing macroscopic strain, the favorably oriented grains exhibiting intense twinning first.
- Slip-slip, twin-slip, twin-twin, and slip-twin interactions affect the local deformation behavior; wide slip bands are a manifestation of localized deformation, which may inhibit or promote twinning, i.e., twin boundaries can act as effective barriers to dislocation motion, twin-twin intersections can create obstacles for other twins, or second order twins can be formed at the intersections (twins inside twins). Twins promote local hardening of the grains, increasing their hardness in comparison to sparsely twinned grains.
- Characterization of the in-service jaw crusher material revealed very similar deformation characteristics as found in the laboratory scale experiments, showing that the used test methods are feasible for studying the material's deformation behavior.

The ultra high strength steels with autotempered martensitic microstructure showed reasonable strain hardening capability usually required in abrasion and impact conditions. The following conclusions based on the compression experiments and the post-test characterizations of the three studied steel grades can be made:

- The ultra high strength steels show relatively strong strain hardening at low strain rates, which gradually diminishes towards higher (dynamic) strain rates and finally leads to pure softening. The softening behavior may be attributed to general (bulk) softening as well as to local softening due to adiabatic shear banding, but also other mechanisms may exist.
- Adiabatic shear banding is a major failure mechanism in compression loading of the UHSS at high strain rates, where the crack initiates and propagates inside the shear band region instead of the interface with the matrix. The propensity of shear banding is dictated by the microstructure, being higher when the initial hardness of the steel is high and the ductility is low.
- The microstructures of the investigated steels are capable of absorbing reasonable amounts of strain energy, being thus usable also in applications involving dynamic loadings and impacts
- The most probable cause for the refined microstructure inside the transformed adiabatic shear bands is dynamic recrystallization occurring at high local strains and high strain rates leading to considerable adiabatic temperature increase. The hardness of the shear bands varied between 143-153 % of the undeformed bulk hardness.
- The white tribolayers at the surface of the in-service samples have the same small grain size and high hardness as the transformed shear bands, and these tribolayers are most likely also formed by the dynamic recrystallization process.

The strain hardening capability of the as-cast hard carbide reinforced steel was found reasonably good in a wide range of strain rates despite its limited ductility. The main findings can be listed as:

- The flow stress of the material reached over 3000 MPa in all tests, increasing with increasing strain rate, while the maximum axial strains before failure remained between 0.07 and 0.11. The reasonable ductility of the tempered martensite matrix combined with a wide spectrum in carbide shapes and suitable carbide volume content are responsible for the well-balanced properties of the steel. The strain hardening rate first decreases with increasing strain rate, but a rapid upturn occurs above 2400 s^{-1} likely because of changes in the deformation mechanisms.
- Crack initiation takes place inside the strengthening chromium carbides, at the interface between the matrix and the carbide, as well as in the matrix. The propagation of the cracks is not arrested by the carbides. Higher strain rates promote intense fragmentation of the test material, which originates from the multiple local fracture processes attributed partly to shear banding.

5 Experimental results and discussion of the abrasion tests and material behavior

This chapter presents the results of the experimental abrasion tests conducted on several wear resistant steels. First some general aspects of multiple contact abrasion are discussed, which is followed by a more detailed analysis of single grit contacts. The suitability of the test method, the wear behavior, and the related surface hardening of the test materials are then evaluated. Major part of the wear results has been published earlier by the author in refs. [131, 132, 135] with some additional discussions.

5.1 Preliminary abrasion testing with multiple and single contacts

Preliminary experiments were performed with the crushing pin-on-disc (CPOD) test setup, where multiple particles are simultaneously in contact with the sample surface. Figure 5.1 shows the mass loss results for three steel grades, the Hadfield steel and two additional martensitic grades, tested with three or four rock types. The composite hardness of the rocks vary between 500 HV and 1100 HV, and the abrasiveness of the rocks is dependent on the rock type. The results indicate that the rock hardness as such has only a limited increasing effect on wear. Rock abrasiveness, on the other hand, correlates well with the wear of the Hadfield steel, while the martensitic grades do not follow the same trend. The highest mass loss of the Hadfield steel was observed with tonalite, having high hardness combined with high abrasiveness. For the martensitic grades, the highest wear result was obtained with granite, which behaves differently from tonalite in the experiment. Tonalite rocks tend to round from the edges during the test and new failure surface is not easily revealed in a similar manner as for example with quartz. Granite rounds similarly on the edges, but it also forms new sharp corners more intensively, which probably explains the higher wear of the martensitic grades with granite compared to tonalite.

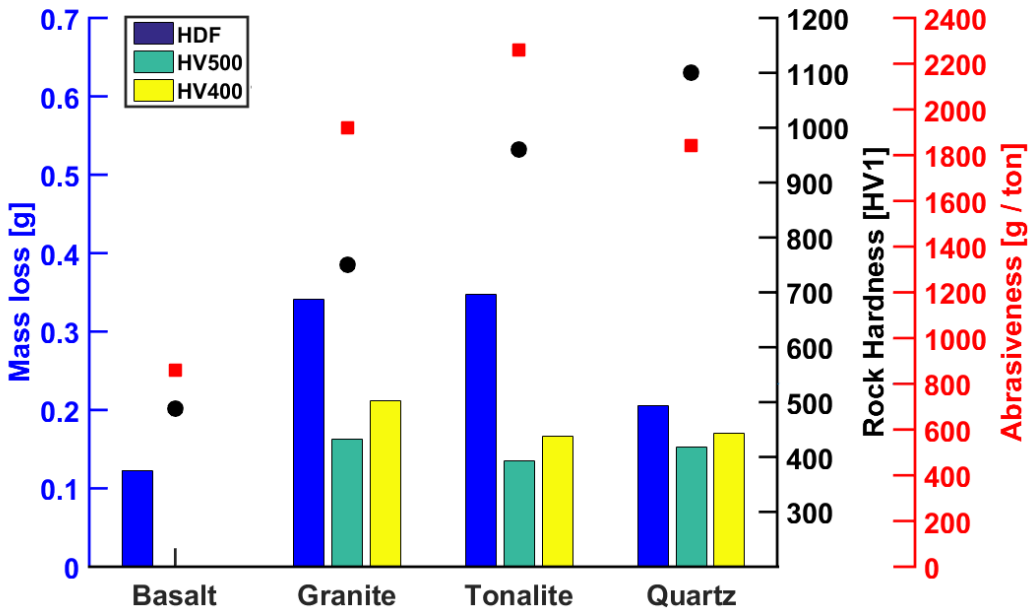

Figure 5.1: Multiple contact abrasion test (crushing pin-on-disc) results for three wear resistant steels tested with different rocks. The nominal hardness and crushability of the rocks are indicated with markers. The HDF-steel is the high manganese austenitic steel [132], while HV500 and HV400 are martensitic grades tested in ref. [182].

The CPOD method provides a good estimate for the behavior of materials facing different abrasives in a multicontact environment, and is a good method for evaluating the material performance relative to other steel grades, for example as shown by Ratia et al. [182]. However, the hardening capability and its relationship to the wear of the material may not be fully revealed by the test method, since only rather limited surface hardening has been reported [182]. This obviously is a result of the limited force used in the test setup, as demonstrated in Figure 5.2 for the Hadfield steel. As seen, the surface hardness does not reach as high values as measured from the in-service sample with any of the used abrasives. The figure also shows the hardness of a sample pre-strained to 40 % of plastic strain, and two different in-service samples for comparison. The in-service sample without polishing represents the surface directly from a mineral crusher, while in the polished sample some of the hardened layer on the surface has been removed.

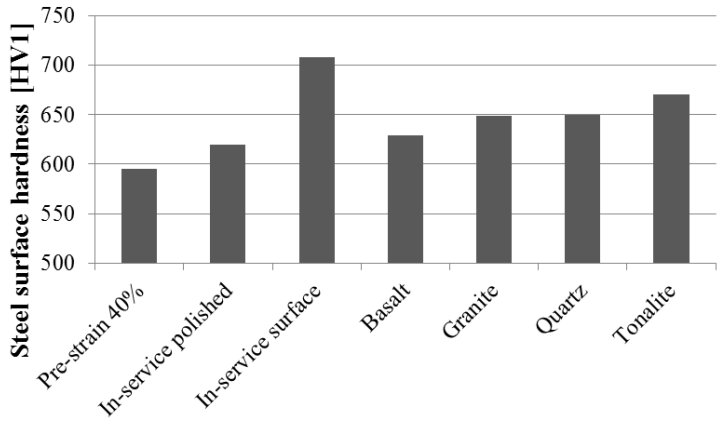

Figure 5.2: Hardness of Hadfield steel samples after the pin-on-disc crushing experiments with four rock types, after 40 % pre-straining, and hardness of in-service samples measured directly from the worn surface and after slight polishing. [132].

Figure 5.3a shows the true contact area between the abrasives and the pin sample measured with a pressure sensitive paper. The contact area remains fairly constant at the beginning of the test until ca. ten minutes of testing. The small decrease in the contact area after five minutes of testing obviously results from the fracturing of some of the bigger rocks, transferring the load to a smaller number of remaining large rocks before the actual comminution starts.

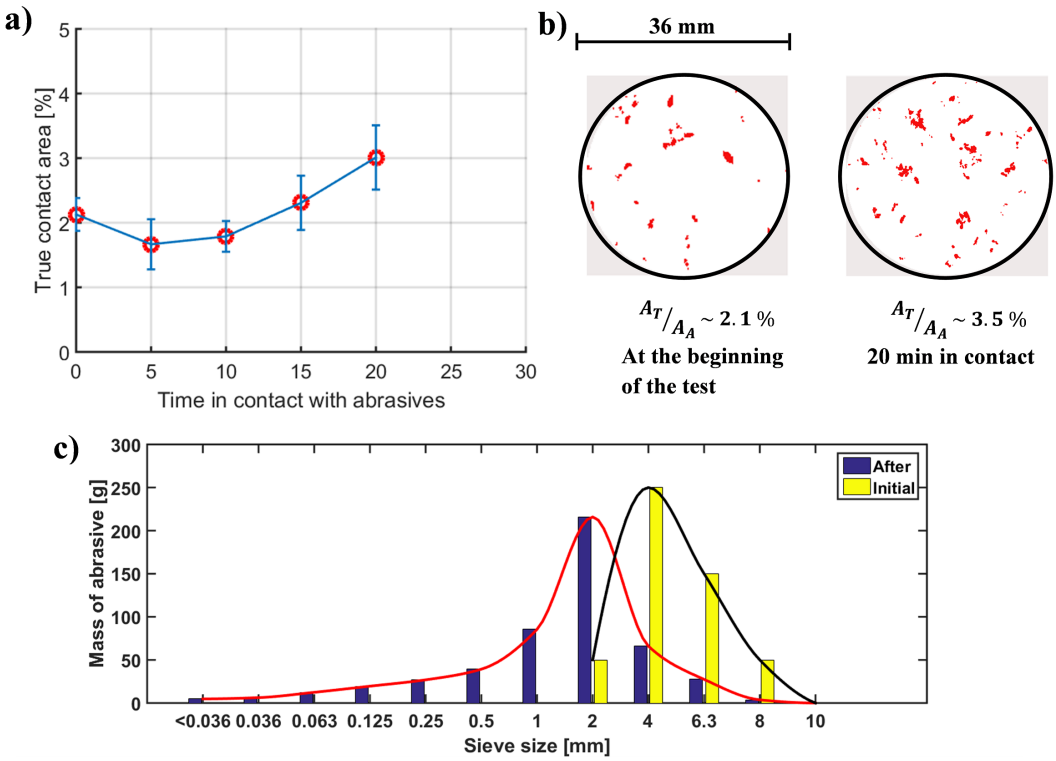

Figure 5.3: a) True contact area in a CPOD test, b) contact points recorded by pressure sensitive paper c) refinement of the abrasive during the experiment.

Because of the nature of the CPOD test with multiple simultaneous contacts, it is difficult to control or measure individual parameters or events. For example, the contact geometries evolve during the test and the number of contacts changes, which means that the surface pressure is not constant during the test. For this reason, single rocks were picked from a batch of abrasives and used as an indenting tip sliding on the steel surfaces.

Figure 5.4 shows the coefficient of friction during two experiments with a natural rock tip of granite (650-750 HV) and quartz (1050-1200 HV) on the HV500A steel. The sharp characteristics of the natural rocks led to fracturing of the rock tips during the tests, continuously changing the contact geometry. Figure 5.4a shows that the geometry at the end of the experiment is quite similar to the overlaid Rockwell-C tip geometry due to the rounding of the granite rock.

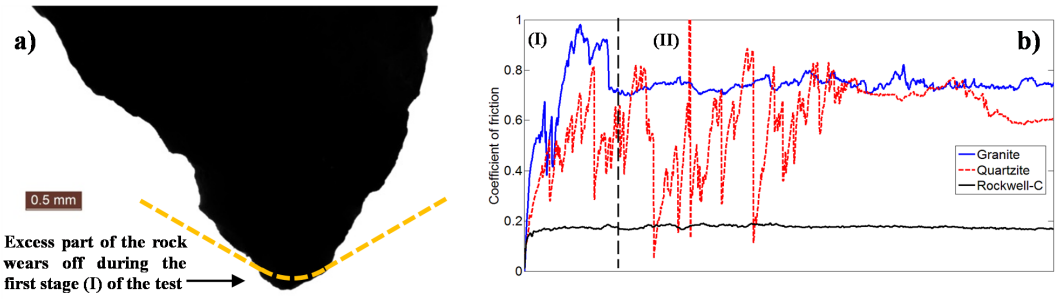

Figure 5.4: a) A typical 2D profile of a natural granite rock overlaid with the Rockwell-C geometry marked with a dashed line, b) single scratch tests with natural granite and quartzite rocks against the HV500A steel using a 40 N constant normal load [135].

Figure 5.4b shows that the granite rock tip evolves quite quickly towards a rather stable contact geometry. In contrast, the quartz rock continues to fracture, as seen from the sharp jumps in the coefficient of friction throughout the test. Terva et al. [212] also compared the wear response of rock-steel and diamond tip-steel contacts and noted that it is possible, although not very practical, to use granite rock indenters. The present results suggest that, in fact, the granite tips could perform fairly well in the experiments, but a large number of tests would be required to establish statistically reliable results of the wear behavior. It is especially challenging to find similarly shaped rocks for each individual test, and the accuracy and validity of this kind of a test may suffer from varying contact conditions. As a consequence, it was determined that the standard Rockwell-C tip is sufficiently representative of the contact and leads to more reliable comparison between the steels. Furthermore, the changes in the contact geometries easily restrict any further application of the results for example for simulation purposes, since the geometries cannot be in-situ tracked in the experiments, which is a problem that can mostly be avoided with diamond indenters.

5.2 Single grit wear and hardening in a scratch tests

Single scratch experiments were performed with a Rockwell-C indenter for various steel grades and OFHC copper (99,99 %) used as a simple reference. The HV400 steel is a laboratory grade test material studied only in the single scratch experiments. The details about the test parameters are given in Section 3.3.1. The current investigation aims to provide information about the single scratch test method for studying the wear and hardening behavior of wear resistant steels. All of the steels were either in the as-cast (Hadfield denoted with 0 % pre-strain, and carbide reinforced steel HV750) or in bulk hot-rolled condition before the tests, i.e., no prior deformation had been applied to cause hardening.

5.2.1 Wear rate in the single scratch experiment

The single scratch test results for the wear resistant steels are presented in Figure 5.5a at four constant normal loads. The wear rate is here defined in a simple manner by dividing the volume loss by the normal load multiplied by the sliding distance in the measured profile. Generally, a distinctive increase in the wear rate is seen with an increasing load. The increasing initial steel hardness is expected to have a decreasing effect on the wear

rate, since no prior hardening is affecting the behavior, which is evident in the results. The reference copper showed much higher wear rate values in most of the cases than the softest HV400 steel, ranging from roughly a magnitude higher values at 20 N. At 80 N, however, the difference was much smaller because of the extensive ploughing instead of direct material removal for both test materials. The wear rate of the HV400 steel, on the other hand, was much higher than that of the other martensitic grades and the carbide reinforced HV750. Because of the higher wear rate, the HV400 grade was omitted from the futher multiple scratch tests.

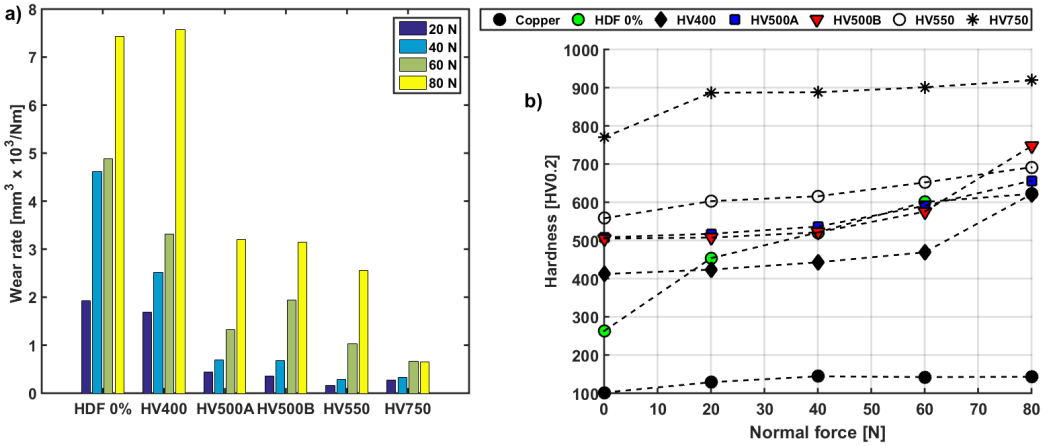

Figure 5.5: a) Wear rate of wear resistant steels of various hardness grades at different normal loads during a single scratch test, b) surface hardness values measured from the bottom of the wear grooves [135].

Figure 5.5b shows the microhardness measured from the bottoms of the scratches. Copper saturates to its maximum hardness at 40 N, while all of the martensitic grades, the HV750 carbide reinforced steel, and the Hadfield steel continue to harden throughout the studied normal force range. In Figure 5.6a, the effect of normal load can be seen as a change in the material removal mechanism. For example, the 40 N load increases ploughing in the HV500B and HV550 grades, whereas the HV400, HV500A, and HV750 steels exhibit more cutting at this load. However, again towards the 80 N load most of the steels show increasing ploughing because of increasing penetration of the scratch tip. However, the HV500B steel undergoes more cutting also in this region, mostly because of the shear damage occurring in the ridges around the scratch, which removes noticeable amounts of deformed material. For the less ductile carbide reinforced steel HV750 cutting is the main wear mechanism at all load levels. The initially high hardness of HV750 led to very shallow penetrations, only about 0.75 μm at 80 N, while in the martensitic grades the penetrations could be up to 10μm. [135].

The average friction behavior shown in Figure 5.6b also provides a link to the prevailing abrasion mechanism. Despite that the friction is measured for a steel-diamond tip pair instead of a steel-rock pair that would usually cause high friction in any case, the increase in the coefficient of friction with diamong-steel pair shows that the abrasion mechanism is either heavy ploughing or cutting. The low friction values for the HV750 steel, in turn, are a combined effect of the high initial hardness, low degree of penetration, and low adhesion between the hard carbides and the diamond tip. [135].

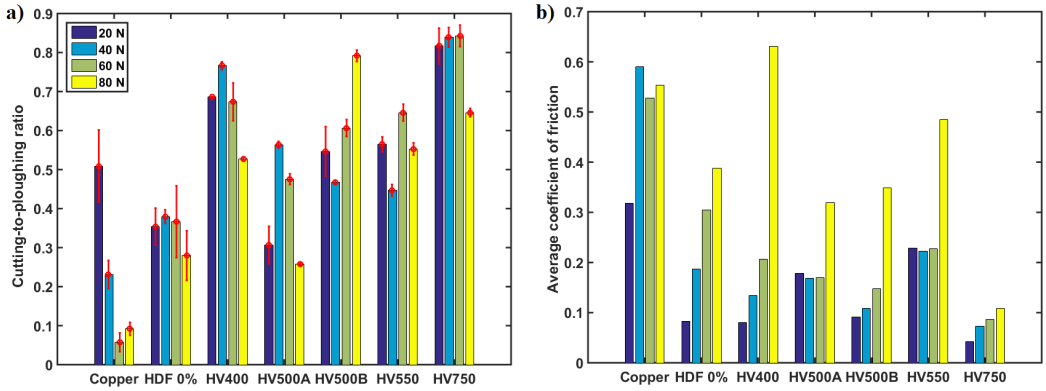

Figure 5.6: a) Cutting-to-ploughing ratio and b) average coefficient of friction at different normal loads [135].

A more detailed single scratch test program on the Hadfield steel pre-strained to different plastic strains was performed to investigate the relationship between strain hardening and wear rate, defined as the volume loss per sliding distance as shown in Figure 5.7. The increase of hardness associated with the increasing pre-strain decreases wear quite efficiently. The optical inspection of the scratches revealed that the samples with lower pre-strain and thus lower hardness exhibited more ploughing-type behavior as a function of the normal load, i.e., the material is pushed aside of the scratch. At the same time, however, the material was quite intensely removed because the ridges form fairly large chip-like wear particles. [132].

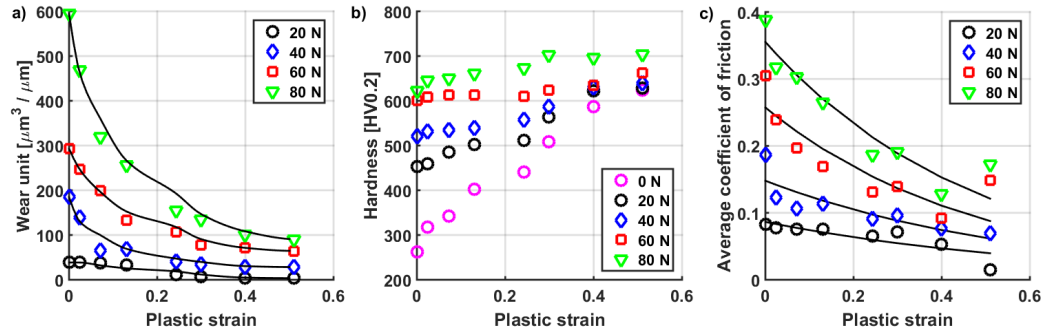

Figure 5.7: a) Volume loss per sliding distance at four normal loads for various pre-strains, b) surface hardness after scratching, and c) coefficients of frictions.

A clear increase in the cutting tendency was observed with larger pre-strains, although the depth and width of the wear tracks decreased. For example, in the samples pre-strained to 40 % as well as in the in-served samples, the notable increase in the cutting-to-ploughing ratio from 0.26 - 0.35 to 0.5 - 0.6 indicates that the material was more efficiently removed than just displaced. Figure 5.7b presents the hardness values after the scratch tests for different pre-strains. The measured hardness values of 650-750 HV after the high normal load experiments correlate well with the hardness of around 700 HV measured from the in-service samples and in the fractured tensile samples. The coefficient of friction

followed quite well the changes in the pre-strain hardness, reaching reasonably low friction values after larger pre-strains, as shown in Figure 5.7. As an exception, in the case of the in-service sample scratched at high loads, the surface was no longer able to deform and harden, which led to the formation of wear particles and increase in the coefficient of friction. However, it is worth noting that no distinct loss of ductility that would result in high wear rates was observed in the experiments. [132].

Although the single scratch tests aim to compensate for the unpredictability of multiple contact tests for many different materials, such as steels and coatings [95, 96, 179], the present results show that the single scratch tests do not properly represent the wear behavior of wear resistant steels. This arises mainly from the fact that the steels may harden up to 50 % from the bulk hardness already during a single scratch test. Hence, the initial conditions of the surface can change drastically before the next contact sequence, because the surface may have formed a tribolayer.

5.2.2 Effect of surface hardening to wear rate

The effects of surface hardening were studied with two HV500 grade steels using four increasing constant loads. Figure 5.8 presents the scratch test results showing that ten cycles is enough to saturate the hardness at the bottom of the scratch groove for both steel grades. It seems, however, that the steels exhibit slightly different hardening behavior due to their microstructure, e.g., differences in their martensite morphologies.

Figure 5.8 shows also the difference in the wear behavior between the two steel grades. Both steels show quite similar general behavior at lower loads, while at the higher loads the higher wear rates and the cutting-to-ploughing ratios of HV500B indicate more cutting.The examination of the scratches revealed that the more ductile HV500A grade showed mostly plastically deformed ridges around the scratch in comparison to the shearing off observed in the HV500B. Figures 5.9a and b present 2D and 3D profiles from the worn surface. The difference in the ploughed ridges between the steels is notable, as the HV500B shows much smaller and mostly cut off ridges. Both materials did, however, exhibit increased cutting after the second cycle when some parts of the ridges are removed, indicating that the ridges in HV500A are also susceptible to detach from the surface quite easily. [135].

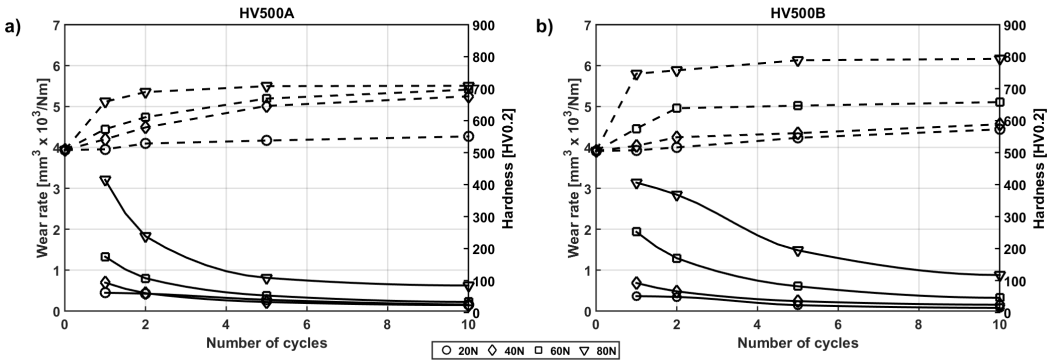

Figure 5.8: Surface hardness at the groove bottom and the wear rates of a) HV500A, b) HV500B in the cyclic scratch experiments [135].

To investigate how prone the HV500A and HV500B steel grades are to cutting of the ploughed regions, multipass experiments were performed by overlapping the ridges of the scratches. Altogether five scratches were done in the tests with 40 N and 80 N normal loads. Figure 5.9c shows the 3D and 2D profiles of the overlap test for HV500A at the 40 N constant normal load. The cutting-to-ploughing ratios remained at the same level as in the multipass experiments on the same groove, indicating that the steels do not exhibit any accelerated wear yet at this load level. At 80N, however, the more ductile HV500A sample showed in the overlapping multipass experiments two times higher cutting-to-ploughing ratios compared to the ordinary multiple cycle tests. This points out that the large ploughed ridges of this material are prone to removal by continued abrasion. In contrast, the HV500B exhibited two times smaller values in the cutting-to-ploughing ratio at 80 N in the overlap tests. This, on the other hand, suggests that the ridge areas of this steel grade are more resistant to abrasion than the groove itself, likely owing to the already flattened ridges with high hardness (unfortunately hardness could not be measured directly from the ridges).

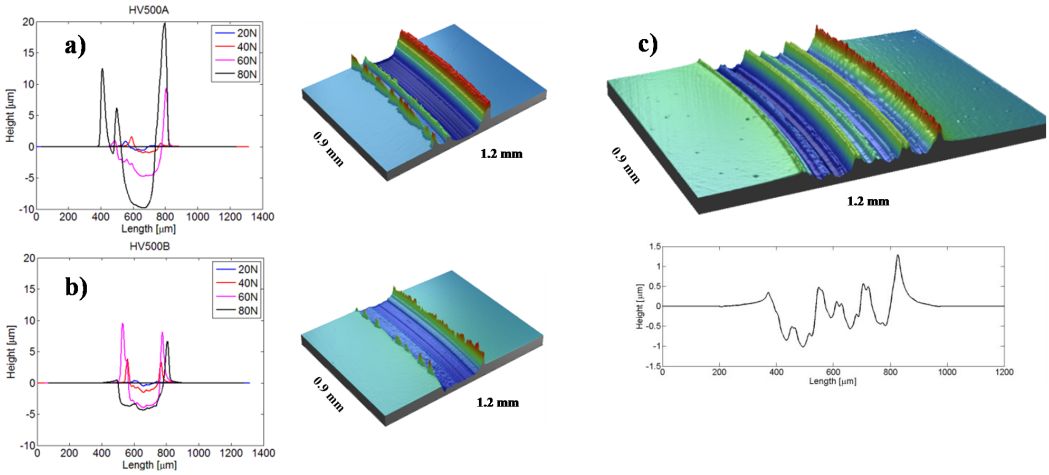

Figure 5.9: 2D profiles of a) HV500A and b) HV500B steels at four normal loads together with 3D profiles at 80 N after 10 cycles, c) 3D and line profiles of five scratches overlapping on the ploughed ridges in an HV500A sample at 40 N [135].

Figure 5.10 presents the surface hardening and wear rates for all of the studied steels in the moderate (40 N) and severe (80 N) wear regions in a similar manner as discussed above in detail for two of the steels.

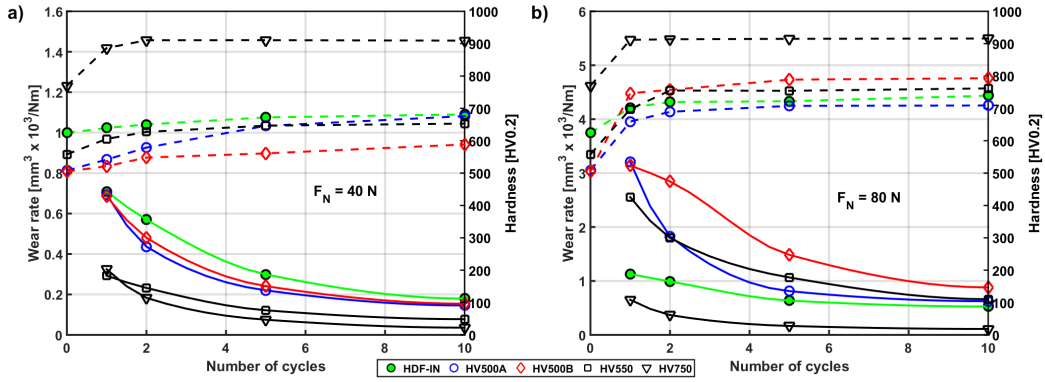

Figure 5.10: Surface hardening and wear rates of the studied steels in the multiple cycle scratching at a) moderate 40N and b) severe 80N loads [132, 135].

Some attempts of using wear and work hardening coefficients to describe the abrasive wear behavior of metals have been presented [3, 77, 246]. The models, however, are often limited by very little knowledge of the actual hardness of the work hardened surface due to abrasion. Occasionally, the models only consider the as-received hardness as a basis of the formulation, neglecting work hardening completely. It is obvious from the present results obtained from with multiple scratch tests that the models should take the surface hardening into account. Recently, a very similar experimental multipass approach with some modifications to the test method has been presented also by Xu et al. [228] for high strength steels. Although their approach focused on smaller loads, the main findings agree quite well with the present findings and those presented earlier by Lindroos et al. [135].

5.2.3 Wear surface and cross-sectional studies

Figure 5.11 illustrates the worn surfaces after ten cycles at two different normal loads. No severe damage is observed on the sides of the grooves at 40 N, but a distinct change in the wear mechanism is visible when the load is increased to 80 N. The images support the differences between the steel grades seen for example in Figures 5.8 - 5.10. The shear platelets in the HV500A grade can be interpreted as heavy deformation damage, whereas in HV500B as well as in HV550 the damage is more related to cutting and detachment of particles of varying sizes, even reaching down to the bottom of the grooves. The indenter has slid smoothly on the surface of HV750, but the microscopic inspection shows that some decohesion between the matrix and the carbides is present at the groove bottom surface. The cracks have propagated mainly in the matrix, but occasionally some secondary cracks were found also in the carbides. [135]. Also, the Hadfield steel shows quite smooth deformation at 40 N. The higher 80 N load, however, is capable of generating shear platelets in the ridges, and additionally some grain boundary cracking is found in the vicinity of the scratches.

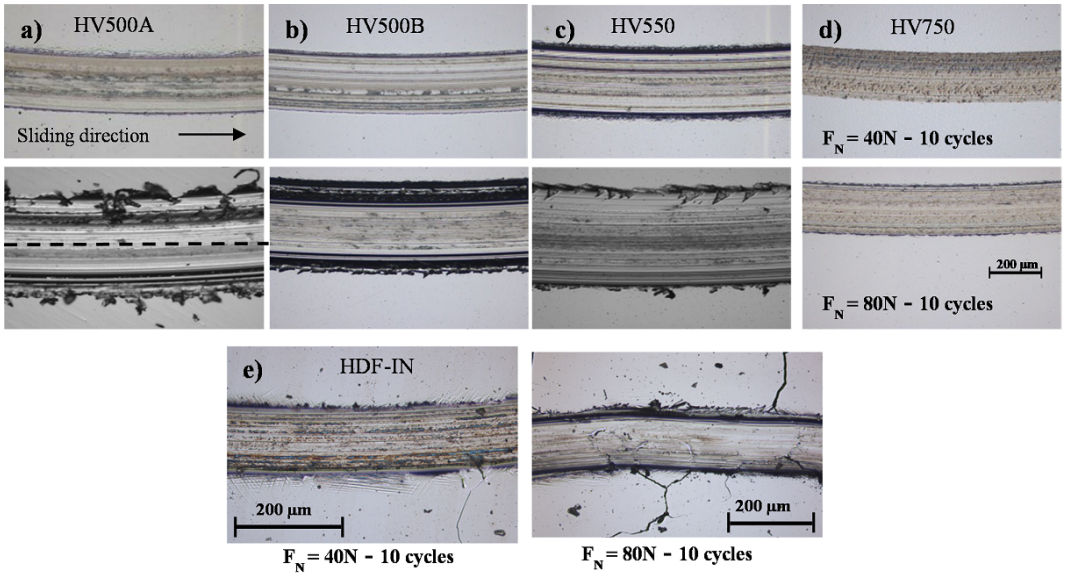

Figure 5.11: Worn surfaces after ten cycles at 40 N and 80 N normal loads. The dashed line marks the cutting plane for the cross-sectional samples. [135].

The cross-sectional studies, exemplified by Figure 5.12a for HV500A, exposed heavily deformed tribolayers and damage nucleating at the surfaces. The depth of the hardest layers was not very deep, only between 5-20 μm, as seen in the hardness profiles in Figure 5.12b. The hardening of the martensitic steels reached down to 100 - 150 μm before the bulk hardness was reached. The highest hardness values of 700-800 HV0.025 were measured from the tribolayers. The HV750, on the other hand, did not have such a distinct tribolayer, but the work hardening reached down to ca. 50 μm, as seen from the profile. However, as pointed out before, the surface hardness values measured from the bottoms of the scratches are the compound values from the vicinity of the deformed surface and the subsurface [195], and hence some differences may be observed between the cross-sectional and surface hardness values. It is worth noting that although the indenter depth is not very large with HV02 microindentations, in some cases when the layer is very thin the surface hardness measurement may still underestimate the value of the actual layer.

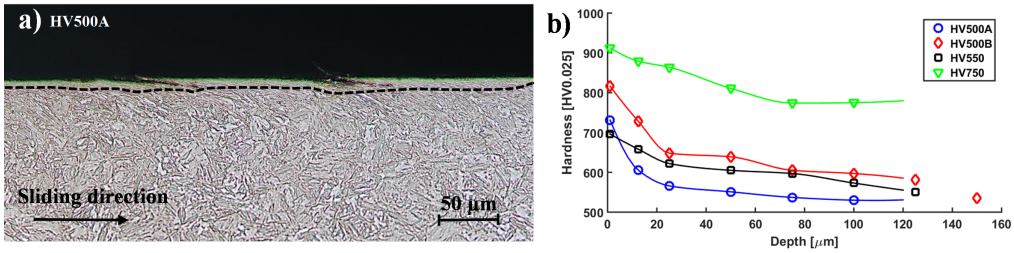

Figure 5.12: a) Cross-sectional view from the middle of the scratch groove in HV500A after ten cycles at 80 N. The dashed line shows the interface between the heavily deformed tribolayer and the more bulk-like microstructure, b) hardness profiles from the surface inwards. [135].

The largest shear platelets were found in the HV500A samples. The shear platelets formed at the bottom of the grooves of the martensitic grades propagated along the elongated grains/laths, but in most cases the cracks halted quite quickly after the interface between the tribolayer and the bulk microstructure. This could have accelerated the formation of wear particles as a result of contact fatigue. It has been reported for example by Venkataraman and Sundararajan [216] that the cracks beneath the deformed tribolayer can easily initiate at the interface and propagate laterally along the interface causing high wear rates, but the present results show quite the opposite at least for the relatively small number of load cycles. Although HV500B and HV550 showed somewhat higher wear rates due to the removal of parts of the ridge regions, the shear patters found in the cross-sections were smaller, which could indicate better long-term surface fatigue resistance. The martensitic matrix of HV750 contained some light shear band like deformation areas near the surface. However, the material loss in this steel occurs also by carbide detachment for example from the fractures at the carbide-matrix boundaries.

5.3 Summary and partial conclusions

Controlled experiments were performed to study the single grit - steel surface interaction, surface hardening, and wear behavior of wear resistant steels in scratch tests. Preliminary multiple contact experiments were carried out to elucidate the complex nature of high stress abrasion. The scratch experiments with a diamond indenter provided a more reliable comparison between steel grades with the initial hardness ranging from 250 to 750 HV, and allowed the detailed investigation of the contact situation. The following general conclusions can be made based on the results presented in this Chapter:

- Multiple contact abrasion tests provide information about the general wear behavior of a steel against selected abrasives, but individual characteristics of the contacts easily remain unrevealed. The wear behavior of high hardness steels in multiple crushing abrasion experiments cannot be explained solely by rock hardness, but also the rock crushability and the rock's ability to generate sharp or rounded geometries in the process are important. Single rock scratching adds realism to the scratch testing for example by creating realistic friction conditions between the surfaces, but the constantly changing geometric conditions in the contact would require a large number of tests to obtain reliable data about the rock-steel interactions and to facilitate the comparison of the wear response of different steel grades.

- A single scratch experiment with a diamond indenter is not suitable for studying the surface hardening and wear phenomena in steels with notable hardening capability, mostly due to insufficient hardening provided by the test method to the surface. However, it can offer important information about the wear behavior of the steel at a certain pre-strained condition. The multiple cycle scratch test, in which scratching is continued in the same scratch groove for several cycles, is more representative of the wear and hardening behavior of steels.

- The surface hardening saturates to a certain (maximum) level in the multiple scratch test, if the applied loading is sufficiently high. At lower loads, when the hardening is not necessarily saturated, the wear rates remain rather constant because of the lack of significant changes in the wear mechanism. In contrast, the saturation of strain hardening at high loads can reveal damage mechanisms that accelerate wear, depending on the microstructure especially for the martensitic steels.

- The high stress abrasive wear resistance of a steel should be evaluated by its capability to surface harden, resist shearing of ploughed regions, and by the behavior of possible tribolayers in terms of crack resistance.

6 Experimental results and discussion of the impact tests and material behavior

In this chapter, the impact behavior of the wear resistant materials is evaluated and characterized in various test conditions. The effects of impact energy, oblique impact angles, and strain rate (impulse) were investigated in single impact experiments with the high velocity particle impactor. The wear mechanisms are characterized and discussed to reveal the main features of the wear behavior in these conditions. A short test program was performed also in the normal impact direction including single and multiple impacts. Also, the effect of multiple impacts on the wear and damage behavior of some of the test materials was studied at a typical critical impact angle. Majority of the results has been published and discussed already in previous research papers by the author [132 – 134].

6.1 Single impact studies - results and discussion

The main characteristics of the single impact incident were schematically illustrated in Figure 2.2 and discussed in Section 2.2. This section presents the analysis of the deformation, wear, and damage subjected to the steel surfaces by a single impacting projectile.

6.1.1 Impact deformation and wear

The impact craters were characterized by optical profilometry to quantify the deformation and wear. For better understanding, Figures 6.1a and b illustrate typical 2D profiles of the deformation at different impact angles for the tested materials. However, it is obvious that with oblique angle impacts at different energies and impact angles the deformation and material removal can cause non-symmetric impact craters, making it more practical to utilize 3D data. Also, the type of energy dissipation depends on the impact conditions, as the energy is consumed primarily on either deformation or cutting. For example, Neilson and Gilchrist [163] used an analytical model to describe solid particle erosion by an additive decomposition of the wear components. Their approach includes one part that characterizes the energy consumed on the deformation and damage by the normal direction energy component. The second part accounts for the the kinetic energy parallel to the surface presumed to cause cutting of the material. The nature of the normal direction deformation would be compressive under the indenting particles. However, in terms of cutting, the deformation occurs first by ploughing of the material in front of the particles, which is followed by intense shearing of the material detaching loose wear

particles. The ratio between the maximum depth of the crater and the highest point of the pile-up region ($R_\alpha = d_{max}/h_{max}$) showed that an increase in the impact angle does not always cause a higher value of R_α, which would be expected simply by the increase in the normal direction energy component. For example, the HV500B steel exhibited ratios of $R_{15} = 1.9$, $R_{30} = 1.5$, and $R_{60} = 2.3$. The smallest value at the 30° impact angle indicates that a large pile-up is formed around the crater. [133].

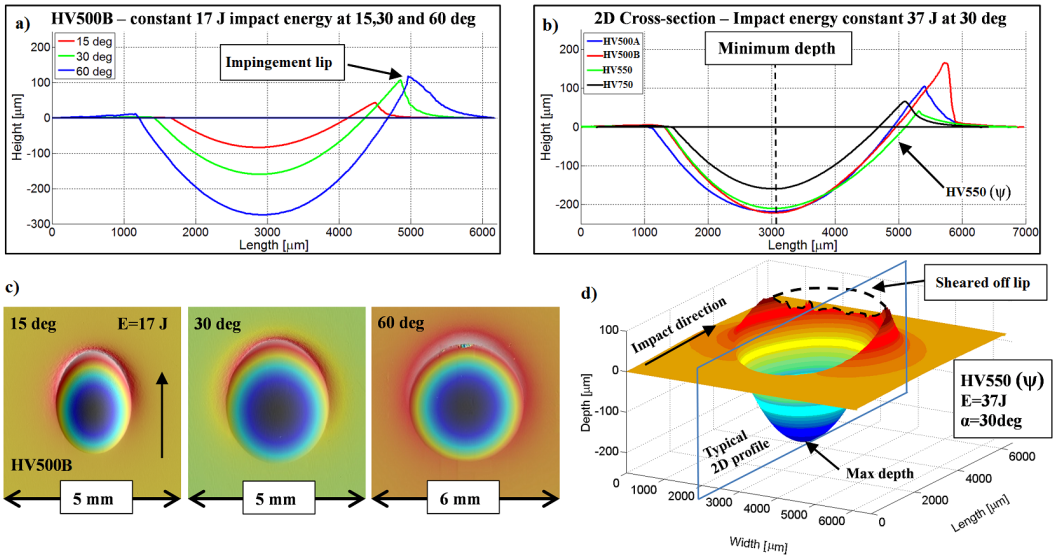

Figure 6.1: Deformation during a single particle impact [133].

The use of this type of ratios based on simple length-characteristics of the crater such as R_α, for example as discussed in ref [207], is not necessarily representative of the situation with the ultra high strenght steels since a part of the pile-up may also be cut off, as seen in a typical 3D profile in Figure 6.1. Hence, the effective amount of cutting is estimated from the value obtained from Equation 3.4. Similarly, the three-dimensional data is more suited for analyzing the overall deformation and wear of the craters because of the irregular shapes of the craters. Generally, as expected, the results showed that the depth of the crater has a strong dependence on the impact angle and also on the impact energy. The martensitic steel grades had very similar crater depths, but the carbide reinforced steel clearly had shallower craters owing to its higher strength. [133].

Figure 6.2 shows some of the wear characteristics of the studied steels at four impact angles and energies. All of the test materials show quite strong dependence on impact energy (Fig 6.2a). On the other hand, when the 'wear rate' is expressed as the volume loss per incident energy, the shape of the curves remains fairly flat at different impact velocities, especially at low impact angles. The highest impact angle of 60° has the greatest effect on the behavior of HV500 and HV750 steels, which is explainable by their increasingly high cutting ratios (Fig 6.2c). The lower wear rate, by the previous definition, of HV500B and HV550, in turn, results in the greater plastic deformation of these materials. [133].

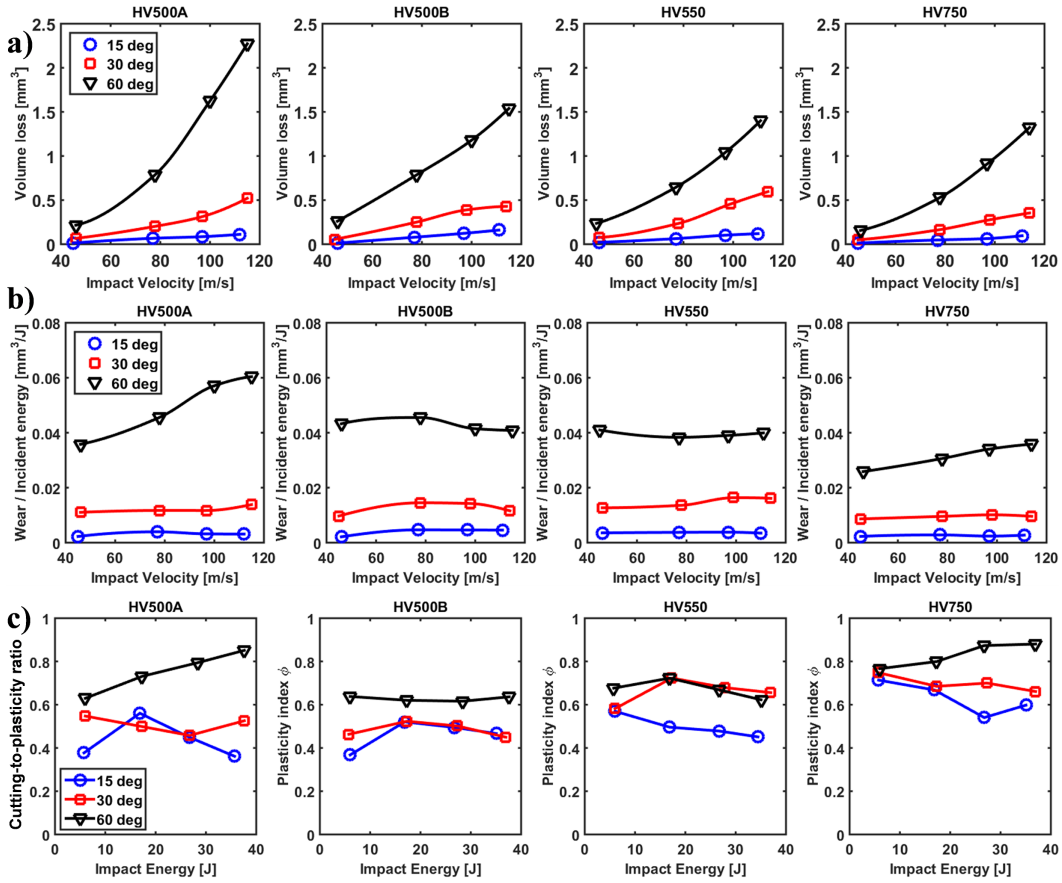

Figure 6.2: a) Material volume loss at different impact velocities, b) wear rate as volume loss per incident energy at different impact velocities, c) cutting-to-ploughing ratios at different angles [133].

The carbide reinforced steel HV750 exhibits the lowest volume loss at low impact angles throughout the tested impact energy range. It has the highest dynamic yield strength and is therefore capable of resisting plastic deformation better than the lower strenght materials. However, because the fracture strains in the dynamic range are quite limited even in compression, the microstructure cannot effectively accommodate increasing energy by plastic deformation, which leads to fracturing of the material at high impact angles. This result is expected for hard and relatively brittle metal matrix composites, which are not generally good against normal direction impacts. This was realized in the current tests as the HV750 steel showed a large subsurface crack network already with 17 J initial impact energy at 60° impact angle. [133].

Figure 6.3 presents the volume loss of the alloyed Hadfield steel with four pre-strains at two impact energies, i.e., the strain values represent the macroscopic plastic strain in the sample prior to the impact. The decreasing volume loss is attributed to the increased sample hardness (see Fig. 4.8 for comparison) until a certain threshold at around 0.25 of plastic strain. Beyond this critical strain the volume loss increases as a consequence of the heavily deformed microstructure limiting the capability of the material to absorb the

impact energy.

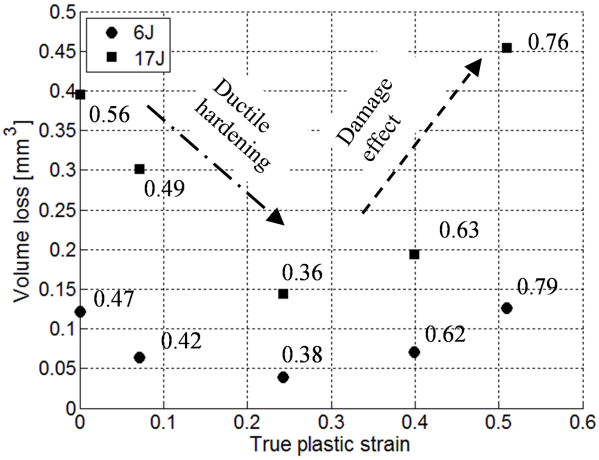

Figure 6.3: Volume losses in the Hadfield steel measured from the surface after 6 and 17 J single impacts for four pre-strains, and from the hardened in-service samples at a 30° impact angle. The numbers represent the cutting-to-ploughing ratios at each data point [132]

The change in the deformation mechanism is visible in the cutting-to-ploughing ratios, which start from a reasonably high value due to the soft bulk material deforming easily and material being cut off. The higher hardness restricts deformation and reduces the effective cutting by a mechanism denoted as 'ductile hardening', until higher macroscopic strain in the sample promotes cutting and material removal denoted here as 'damage effect'. Based on the two studied impact energies, the higher energy highlights these phenomena. The overall volume loss is in the similar range as with the martensitic steels. However, it can be seen that the volume loss at around 0.25 of plastic strain is notably lower, suggesting that the Hadfield type steel hardens significantly and in that way can resist the impacts.

6.1.2 Impact incident characteristics

The incident angle has a marked effect on the energy dissipation during the impact, while the initial impact energy has little effect on the percentage of the consumed energy. The ranges for the energy dissipation percentage for the martensitic steels and for the carbide reinforced steel were between 13-21 %, 33-44 %, and 80-82 % for the impacts at the 15, 30 and 60° angles, respectively. It is not surprising that the initially high strength steels show increasing wear and damage propensity when a large amount of energy is consumed during the impact at the 60° angle. The impacts performed on the Hadfield steel at 30 ° angle showed energy dissipation between 30-40 %, indicating that the steel type affects the energy dissipation.

The forces were recorded during the impacts on four steels using a force sensor placed below the sample. Figure 6.4 shows the contact forces as a function of time during a 30° impact at 114 m/s. The force sensor (Fig 6.4b) located directly below the impact crater recorded the highest forces F_{comp} in the compression direction. The vertical sliding force F_y, parallel to the sliding direction, did not reach very high values. As expected, the third orthogonal force F_x in the transverse direction was essentially zero throughout the

incident period. Hence, the maximum resultant force was calculated using Equation 6.1. [133].

$$F_{max} = \sqrt{F_{comp}^2 + F_y^2} \tag{6.1}$$

In the illustrated case, the greatest compression force spike lasts only about 50 μs, which was roughly confirmed from the high speed images to be the contact time. The maximum force values measured for the different steel grades are very similar for 15° and 30° impact angles. The 60° values may not be as reliable because the forces were close to the maximum limit of the sensor due to the increasing fraction of impact energy being absorbed during the contact. Therefore, at the highest impact energies, the 60° force values were extrapolated from the velocity data, as shown with the dashed lines in Figure 6.4c. The overall correlation between the maximum force and the impact energy seems to be quite linear. [133].

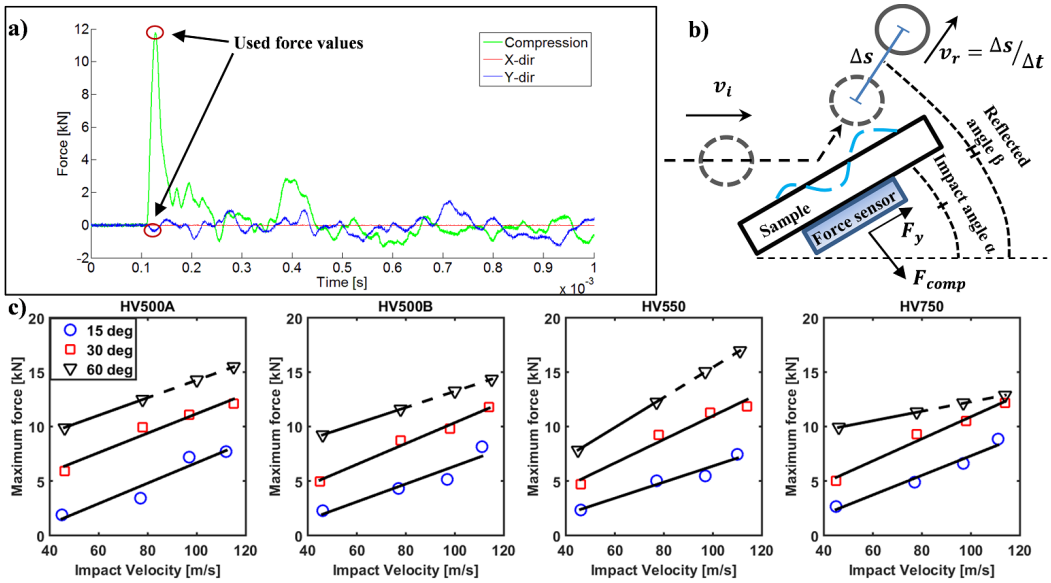

Figure 6.4: a) Force measurement during a 30° impact at 114 m/s, b) schematic presentation of the impact event and the definition of initial and reflected velocities used in the energy calculations, c) measured maximum force values with linear fits [133].

Figure 6.5 shows the measured reflected angles (defined in Fig 6.4b) as a function of impact velocity for the 15° and 30° impact angles. The reflected angle at the 60° impact angle was unmeasurable with the current test setup due to its reflected angle values close to 90° away from the sample surface. The reflected angle depends clearly on the material, as seen from the different values for each steel. For 15° and 30° impact angles, the reflected angles vary between 27-37° and 47-58°, respectively. The angle ratios in Figure 6.4b highlight the effect of velocity on the reflection event. For the studied steels, the differences between the grades as well as the velocity dependence on the reflected angle could be explained by the changes in the ratio of cutting and ploughing as a mechanism of material removal or displacement; when ploughing increases in the pile-up region (Fig 6.2c), the reflected angle becomes slightly larger as the projectile digs out from the sample surface. [133].

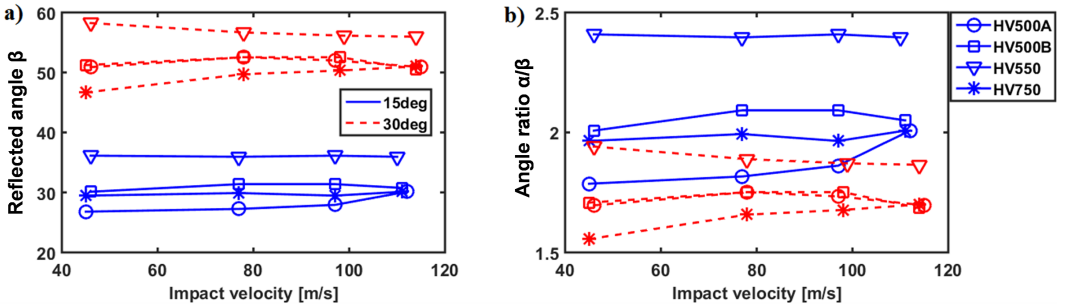

Figure 6.5: a) Measured reflected angles for 15 and 30° impacts and b) ratios between incident and reflected angles [133].

6.1.3 Damage characterization

Characterization was performed on the cross-sections of the impacted samples to reveal the main characteristics of the deformation and wear processes in the studied steels. Figure 6.6 demonstrates the damage mechanisms prevailing in the studied martensitic steels during oblique angle impacts. Several different mechanisms can be identified: 1) the crater bottoms show signs of adhesion and abrasion due to small particles being detached from the surface (the projectiles did not show high amounts of adhered material on their surfaces, though); 2) the most important region in terms of the wear resistance of ductile materials is the pile-up region, which exhibits heavy shear deformation and both deformed and white transformed adiabatic shear bands. In addition, a clearly visible white surface layer, roughly 10 μm in thickness is formed. 3) Subsurface cracks of varying lengths from tens to hundreds of micrometers are found at various depths.

The failure process in the adiabatic shear bands resembles the failure mechanism identified by Bassim and Odeshi [19] and described in Figure 2.8. The micro-voids initiating inside the shear bands form clusters that elongate parallel to the shear band. The clustered voids further lead to the formation of microcracks, which eventually interconnect to form larger fracture patterns leading to the fragmentation of the material along the shear band. This observation is consistent with the failures found in the high strain rate compression samples exhibiting adiabatic shear bands. The EBSD measurements performed on the shear bands indicate that the grain size is extremely small, but insufficient indexing resulting from the grain structure hindered the investigation. Slightly better data was obtained from the regions of deformed shear bands, which showed that the grain structure elongates with respect to the shear direction. It was also observed that cracks reach the surface from deeper in the material in the vicinity of deformed shear bands, which suggests that the deformed bands can also promote failure.

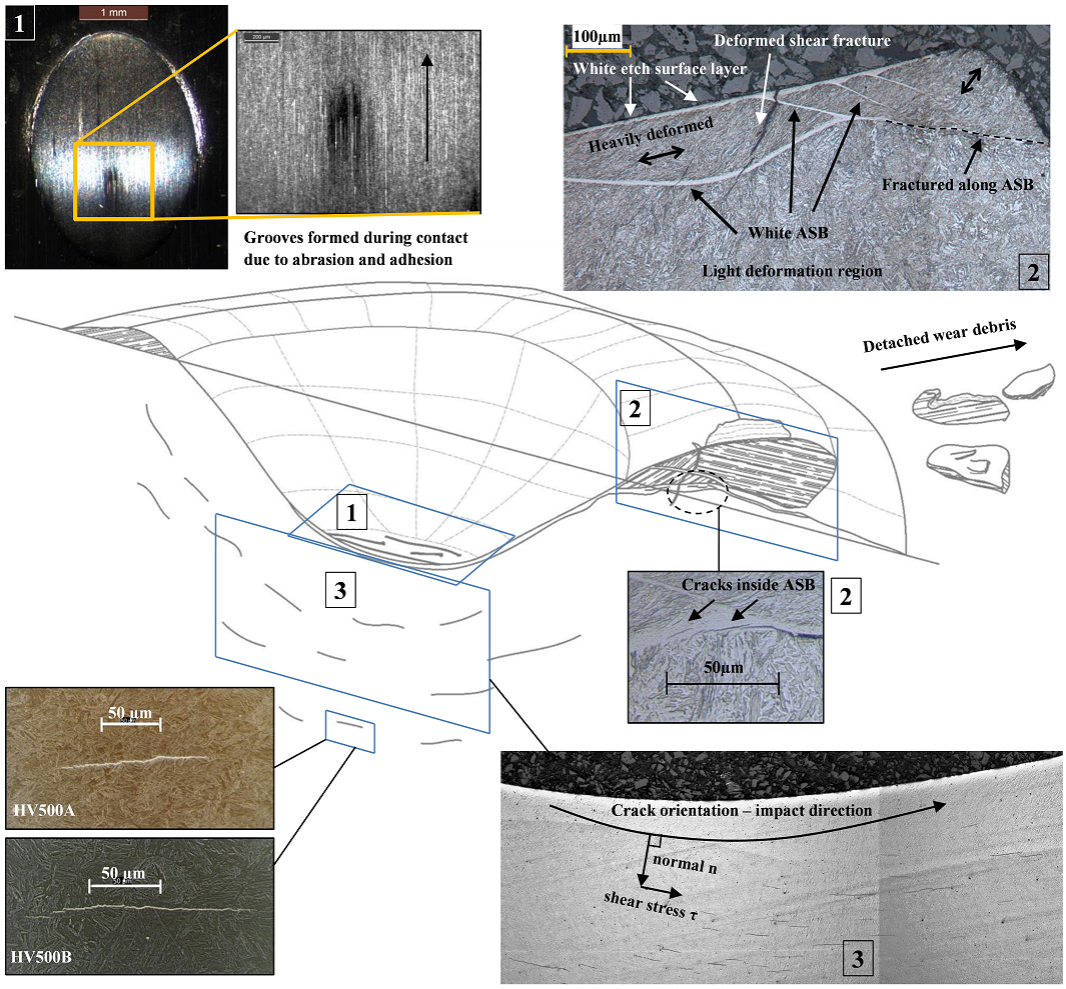

Figure 6.6: Schematic presentation of the impact damage, deformation and wear in martensitic wear resistant steels [133].

The microhardness measurements carried out on the cross-sections inside the white shear bands, deformed shear bands, white surface layers, and the less deformed bulk areas demonstrate the heterogeneous hardening. The measured depth profiles and average hardness values are presented in Figure 6.7 for the martensitic grades. The white surface layers have lower mean hardness than the subsurface white shear bands. The observed behavior could be due to some differences in the microstructures between these regions, which are products of different deformation conditions. For example, it is likely that heat is conducted away slower from the surface layer than from the shear band completely surrounded by the cold matrix metal. Also, the stress state of an internal white shear band is supposedly different because of the surrounding matrix compared to the free surface or contact with the projectile, depending where the layer is formed. The hardness values of the internal shear bands are in good agreement with the values measured from the high strain rate compression samples containing similar bands, or slightly higher. However, it is very likely that the strain rate is higher in the impact incident than during

the conducted Hopkinson Slip Bar tests on the materials. For example, Bassim and Odeshi [19] observed an increasing trend in the hardness values when the strain rate is increased in the dynamic region, which would also explain the present result. Based on these observations and previous discussions, such as the greatly refined grain structure, the differences in the hardness (and microstructures) can be reasonably explained by the DRX process, which is affected by the strain rate, stress state, and temperatures of the adiabatic shear bands and the surface layer, as pointed out in Section 2.3.

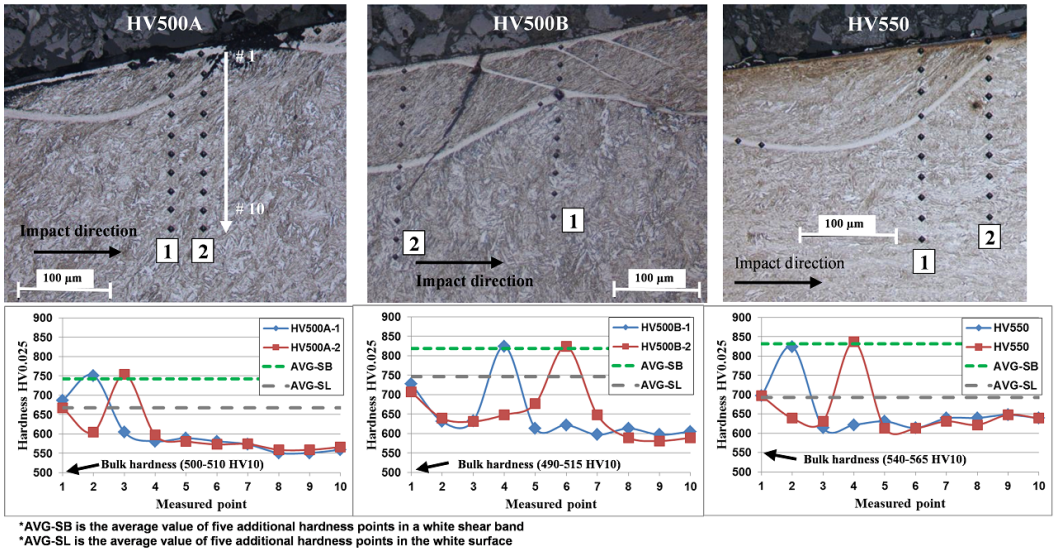

Figure 6.7: Cross-sectional microhardness profiles measured from the white surface layer, white shear bands, and deformed matrix produced in a single impact at a 30° angle on martensitic steels [133].

The wear characteristics of the carbide reinforced steel differ from the martensitic and Hadfield type steels. Figure 6.8 illustrates the damage and failure behavior of the HV750 steel under high velocity impacts at the 30° angle at the two highest impact energies, 27 and 37 J. Based on the mechanical test results, the steel showed reasonable strain hardening capability of the matrix, but the larger strains subjected to the material in the impact experiments exceeded the material limits. Besides the crack initiation in the matrix, cracks were found in many of the carbides even beyond the main fracture bands, indicating also that the larger cracks can originate from the carbides themselves.

One of the main damage types observed in the cross-sections of the impact craters were the subsurface lateral cracks (1). The bottoms of the craters revealed signs of adhesion and abrasion, most likely produced by the detaching carbides dragging along the surface. Small secondary fractures along the carbide-matrix interfaces were detected right on the surface, which explains the detachment of the carbides during the frictional contact between the impacting projectile and the steel surface. Large subsurface crack networks had been formed perpendicular to the surface (2). An increase in the impact energy increased the size of the cracks first observed at 17 J impact energy at 30° angle. At the highest impact energy of 37 J used in the current tests, the fracture network had propagated all the way to the top surface and almost through the whole sample thickness. The location of the crack network with respect to the pile-up region, however, was found to

depend on the impact energy, which probably is due to the different subsurface stress fields during the impacts of different energies. As regards the pile-up region, its importance was also demonstrated by with the presence of a surface crack network, which was first most likely initiated by the compressive stresses and then grown due to the tensile stresses behind the moving particle. The growth of these cracks can accelerate the wear because of the damage they produce already during the first impact on a virgin material. [133].

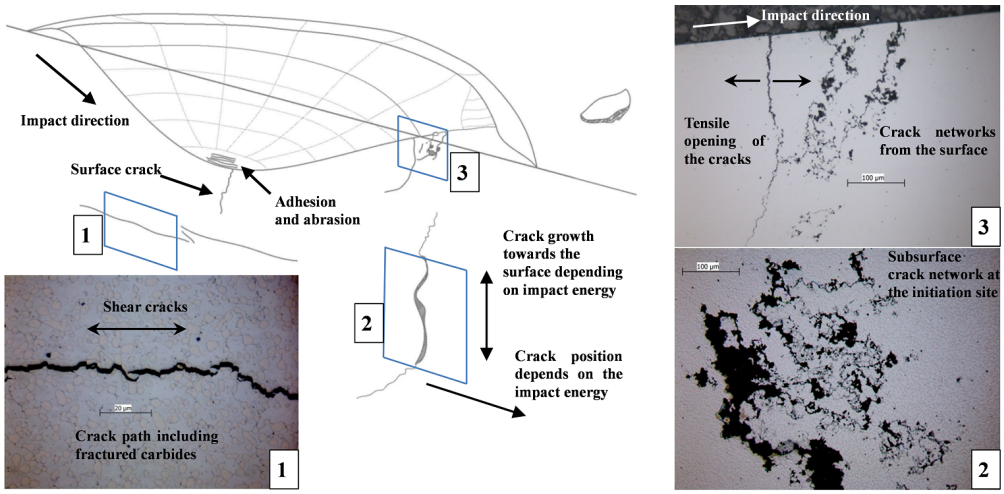

Figure 6.8: Damage characterization of a carbide reinforced steel sample after a 30° impact [133].

The microscopic study on the surface of the alloyed Hadfield steel revealed considerable amounts of fractures along the grain boundaries even quite far away (~1-2 times the crater length) from the crater, as seen in Figure 6.9. The ploughed end of the crater suffered from substantial deformation and removal of large wear particles, due to the large grain size of the material. Only slight adhesion marks were found at the bottoms of the craters indicating rather low-friction conditions between the contacting surfaces. The microhardness measurements performed in the vicinity of the crater edge showed highest values of around 700 HV, which are similar to the maximum hardness values measured at the failure point after tensile tests. Further away from the heavily deformed area, hardness decreases quite rapidly to a level existing in the sample before the impact test. [132].

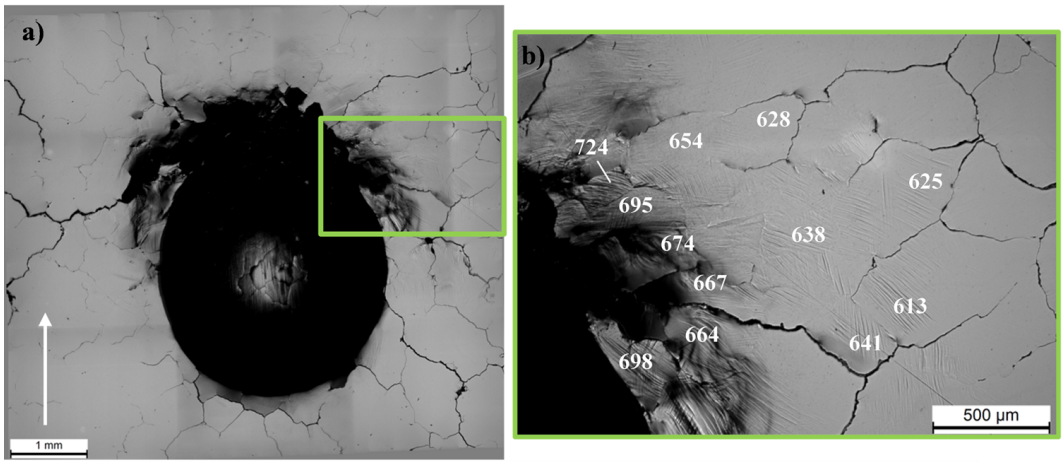

Figure 6.9: Impact crater on the surface of the in-service Hadfield sample after 17 J impact at 30° angle.

Figure 6.10 presents the cross-section of the impact crater, shown in Figure 6.9, on an in-service Hadfield steel sample after an impact at 17 J impact energy. The damage has developed even further away from the actual impact site and the network has propagated mainly along the grain boundaries almost to the depth of 5 mm. The location of the crack network is at the ploughed region of the crater, while at the surface the wear particles are visibly detached. It is expected that the pile-up region suffers from high stresses during and right after the incident. The crack paths seem to follow the grain boundaries. However, the partially detached grains at the surface, which are notable smaller than the general grain size, suggest that the fracture can take place also inside the grains, for example in shear bands or twin-matrix interfaces. [132].

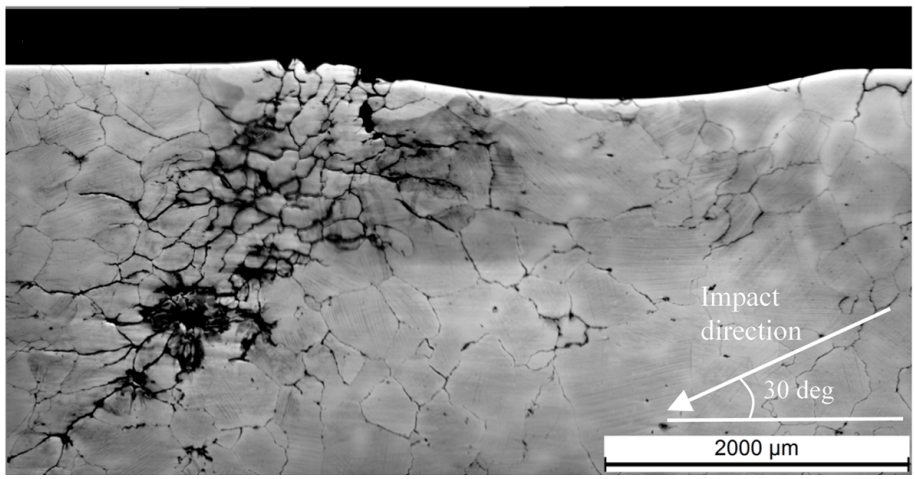

Figure 6.10: Cross-section of the impact crater on the Hadfield steel. The arrow indicates the impact direction [132].

Figure 6.11 shows the wear rates of the martensitic steels and the carbide reinforced steel, defined as volume loss per dissipated energy during the contact, as a function of impact

angle and impact energy. The wear maps divide the damage and wear behavior of the steels into four different regions; low wear region, moderate-to-high wear region, high wear region, and failure wear region.

For the martensitic alloys, the first three regions were identified. In the *low wear region*, the cutting mechanism prevails and the wear rates remain fairly low due to the high strength of the materials even at the highest impact energies of the tested range. In the *moderate-to-high* wear region, the steels generally exhibit shear banding and fracture initiation in the shear bands. This behavior was mainly observed in the 30° impact angle tests especially at high impact energies. The *high wear region* was mostly observed at high impact angles for all martensitic grades. Even with increasing plastic deformation in the crater, significant parts of the ploughed ridges had been cut off. Based on the observations, it is possible that the detected white layers in this region are remnants of adiabatic shear bands, i.e., the failure had propagated inside the shear band leaving a part/half of the shear band on the surface, which when etched appear as a white layer. In addition, clear signs of subsurface shear cracking were observed, which under continued impacting accelerate wear by fatigue. [133].

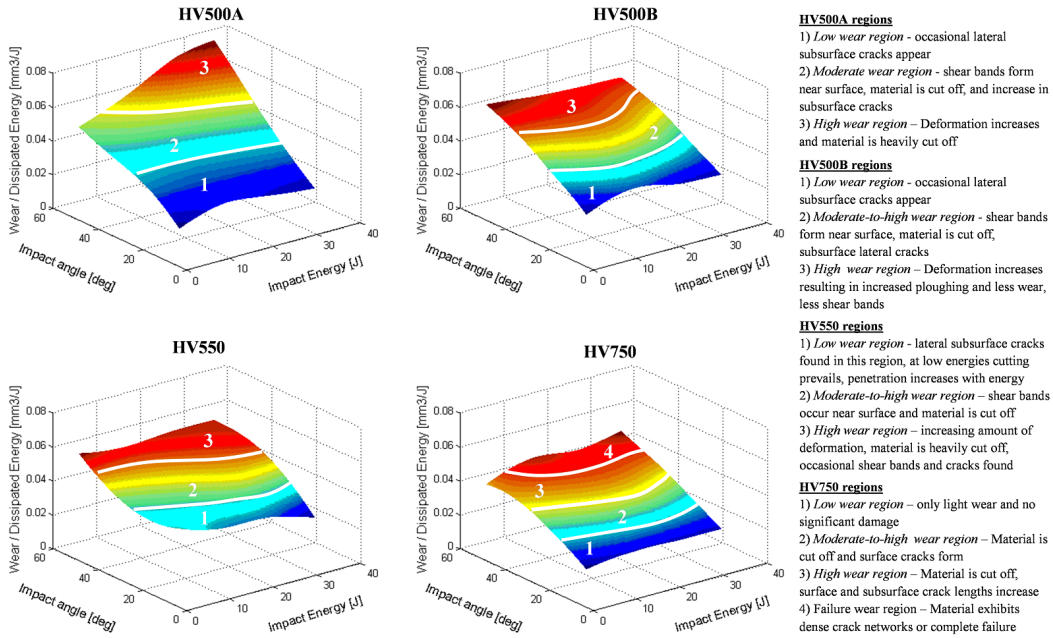

Figure 6.11: Summary of wear rates, wear mechanisms, and damage based on the characterization of single particle impact samples tested at angles between 15° and 60° [133].

The low wear region for the carbide reinforced steel was similar as for the martensitic steels, i.e., material is worn mainly by cutting, but the transition to the moderate wear region occurs likely due to two factors. Firstly, increasing impact energy at higher angles causes crack nucleation due to the exhaustion of the mechanical strength and energy absorption capability of the matrix and the carbides. Secondly, the increased strain rate was observed to activate dynamic failure mechanisms further promoting crack nucleation, which may be connected to the triggering effect of shear localization by the adiabatic shear bands in the matrix. In the high wear rate region subsurface and surface cracks

are more intensively observed and the cutting/removal of material increases. Finally, the transition to the failure region, at which the material is no longer usable, occurs at high impact angles and energies. In this region, the material fails catastrophically even as a consequence of a single impact.[133].

A similar wear mapping was not performed for the Hadfield steel. However, the volume loss results presented in Figure 6.3 revealed that despite the dissipated energy fraction does not depend notably on the plastic pre-strain, the connection between volume loss and energy dissipation is clear. When the dissipated energy is used as a normalizing factor, the volume loss values appear very similar at same pre-strains. This implies that wear increases steadily with increasing impact energy, at least in the current test range. Higher impact energies could trigger additional wear/failure mechanisms promoting volume loss, e.g., higher tendency for grain boundary fracture.

6.2 Effect of impact conditions - Results and discussion

This section presents and discusses the deformation, wear and failure characteristics of ultra high strength steel at the perpendicular angle, high strain rate, and multiple impact conditions.

6.2.1 Normal direction impacts

The effect of impact energy on the wear and deformation in a single impact was investigated with four increasing impact energies. Figure 6.12a shows that the volume loss depends in a quite linear manner on the impact energy. In the test range, also quite high cutting-to-ploughing (ϕ_{CP}) ratios were observed, varying mainly between 0.6 and 0.8 depending on the steel. The two HV500 grades showed increase in the ϕ_{CP} value as a function of impact energy, while for the two hardest steels (HV550 and HV750) ϕ_{CP} remained essentially at a constact value of 0.7. The wear results showed that initially higher quasi-static and dynamic strengths do not directly result in reduced wear in normal direction impacts, as seen for example in the comparison between the HV500A and HV500B grades, the latter having higher strength. On the other hand, the volume loss of the carbide reinforced steel HV750 was approximately 40-50 % smaller than that of the martensitic steel grades. [134].

The microscopic study on the craters, as exemplified by Figure 6.12b, revealed that material is both plastically displaced as well as removed by several mechanisms. However, as the fairly high ϕ_{CP} ratios also suggest, the edges of the craters did not show significant amounts of piled-up material. Still, the material is not only removed from the pile-up region, as in conventional cutting, but also from the crater bottom. Circumferential cracks were observed around the crater bottoms alongside with some visible adhesive damage. The small loose wear particles in the bottom and the light scratches suggest some scuffing type of wear. Some but not a significant amount of material was also adhered to the impacting ball surface. [134].

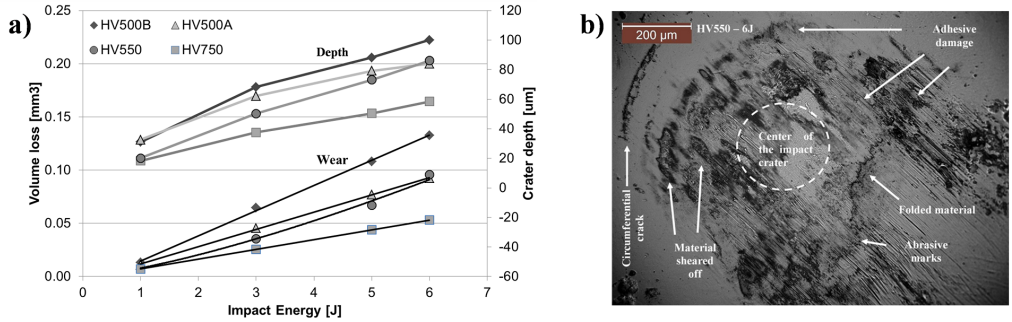

Figure 6.12: a) Effect of impact energy on the deformation and wear in normal direction single impacts, b) typical damage and material removal mechanisms observed in the impact crater in an HV550 specimen after a single 6 J impact [134].

The highest impact energy of 6 J used in the normal direction tests was chosen for the investigation of the effect of multiple impacts up to ten impacts. Figure 6.13a presents the effect of multiple impacts directed to the same area on the volume loss. The test rig provided good accuracy and the impacts hit the same location with good precision. Thus, the experiments simulate well the effect of surface hardening and possible accelerated wear in cyclic conditions. Figure 6.13b shows typical 2D profiles extracted from the 3D data, showing that despite the good accuracy of the test device, the profile is not perfectly symmetric. Therefore, the 3D volume loss provides more accurate values of the cutting-to-ploughing ratios, ranging between 0.7-0.8 after ten impacts for all studied steels. [134].

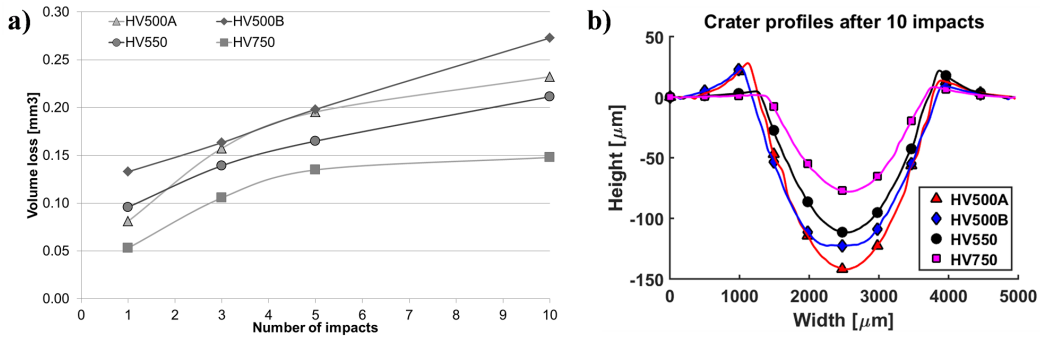

Figure 6.13: a) Volume loss of the tested steels after several impacts in the normal direction, b) 2D crater profiles after ten impacts [134].

The microscopy confirmed that the removal of material by a shear dominated mechanism, typical to oblique angle impacts, was not effective in the normal direction impacts. Instead, material was removed by adhesion and fracturing of the surface of the steel in the vicinity of the impact sites. The volume loss shows a decreasing trend for most of the steels because of surface hardening, and no evidence of surface fatigue accelerating wear was found in the current test range. The cross-sections did not either show any signs of crack networks developing in the subsurface, even in the HV750 steel. However, Ratia et al. [183] performed a 1000 impact test series for similar type of martensitic steels and observed a substantial amount of subsurface cracks and fibering of the microstructure.

Table 6.1: Material parameters and the target impact velocities used in the experiments [134].

Ball material	**Density** $[g/cm^3]$	**Projectile mass** $[g]$	**Hardness** [HV10]	**Impact velocity** $[m/s]$	
				6 J	**17 J**
Tungsten carbide $WC-Co$	14.95	5.69	1800	46	77
Zirconia ZrO_2	5.70	2.22	1240	72	122
Silicon nitride Si_3N_4	3.21	1.24	< 1600	98	165

Quite surprisingly, increasing initial hardness led to decreasing subsurface cracking, which could be a result of the fairly low impact energy used in the experiments. Nevertheless, the deformation analyses showed that the materials were not catastrophically failing even after such high number of impact cycles, indicating that this type of martensitic steels and carbide reinforced steels are capable of absorbing large amounts of impact energy in normal direction impacts.

6.2.2 Effect of impulse

The effect of strain rate (or impact impulse) at a constant impact energy was studied by increasing the impact velocity but using lighter projectile materials, as shown in Table 6.1. This approach allows to keep the volume and shape of the projectile constant, so that the impact incident can be easily analyzed with high speed photography. Two lighter ceramic materials were chosen for the study: zirconia (ZrO_2) and silicon nitride (Si_3N_4), both having high enough hardness/strength not to break during the impacts.

Figure 6.14 presents the measured volume loss of the steels under high velocity impacts at two different impact energies. The figure shows that when the impact energy is kept constant, the increase in the impact velocity causes an increase in the volume loss for all studied steels. However, at the higher impact energy of 17 J, the loss of material saturates to a more or less constant level when the impact velocity approaches 150 m/s. At 6 J such saturation is not observed, but on the other hand, the impact velocity did not exceed 100 m/s in these tests. With the martensitic grades, the material losses with zirconia and silicon nitride projectiles, requiring higher velocities to produce the pre-determined kinetic energies, were increased by 50-100 % when compared to the heavier tungsten carbide projectile launched at lower velocities.

The amount of dissipated energy during the contact depended both on the projectile material and the steel. In the experiments with the WC projectile, approximately 34-40 % of the initial kinetic energy was consumed, while the zirconia projectiles lost only 24-32 % and the silicon nitride projectiles 28-34 % of their initial kinetic energy. The differences in the energy dissipation could be linked to the slightly different frictional conditions between the material pairs and to the different mechanical properties of the projectiles, such as elastic constants.

The changes in the deformation mechanism can be expected to have an effect on the energy dissipation, as can be realized from the cutting-to-ploughing ratios listed in Table 6.2. Cutting in the martensitic grades increases, while HV750 with a different microstructure seems to be in this sense quite insensitive to the impact velocity, although some cracks appeared in its subsurface. The only minor increase in the volume loss of the HV750

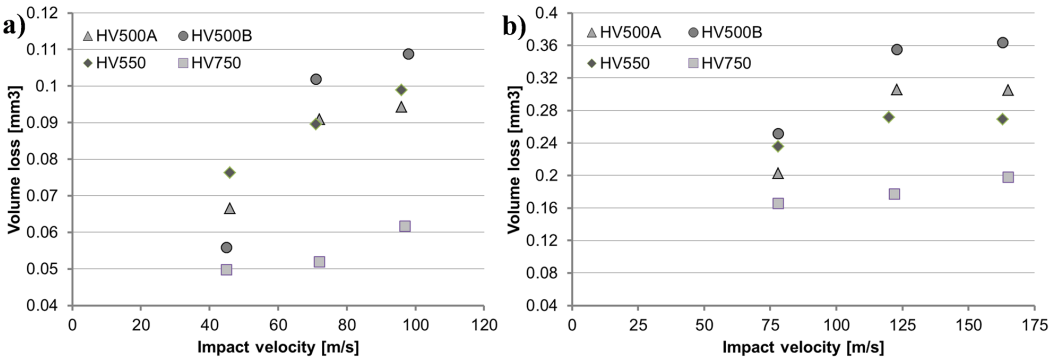

Figure 6.14: Effect of impact velocity at the constant energies of a) 6 J and b) 17 J on the volue loss [134].

Table 6.2: Cutting-to-ploughing ratios of the studied materials tested with three different projectile materials [134].

Impact energy	**6 J**			**17 J**		
Material	$WC-Co$	ZrO_2	Si_3N_4	$WC-Co$	ZrO_2	Si_3N_4
HV500A	0.55	0.60	0.66	0.50	0.62	0.60
HV500B	0.46	0.73	0.73	0.52	0.74	0.74
HV550	0.58	0.70	0.72	0.72	0.67	0.6
HV750	0.75	0.75	0.77	0.69	0.75	0.74
Target velocity $[m/s]$	46	72	98	77	122	165

steel suggests that the failure probability of the steel's microstructure by shear banding is not so drastically affected by the increased impact velocity or strain rate, while the martensitic steels showed increasing amount of shear bands.

6.2.3 Effect of multiple high velocity impacts

The capability of three selected steels to resist wear and absorb impact energy in the surface hardened conditions was investigated with repeated impacts subjected to the same site on the surface. An oblique angle of 30° was used because of its high tendency to cause wear in the present steels. Also in many applications, the impacts often occur at low angles. The impact energy used in the tests was 17 J. Figure 6.15 shows that the volume losses increased quite steadily throughout the tested number of impacts. At the same time, the cutting-to-ploughing ratios seemed to saturate after the first impacts, for martensitic steels between 0.5 and 0.6 and for the carbide reinforced steel between 0.6 and 0.7. [134].

The presentations of the two definitions of wear rates, as the removed volume per dissipated energy $[mm^3/J]$, and as the removed volume per a unit mass of erosive particles $[mm^3/kg]$ produced quite similar results, which means that the amount of dissipated energy during the consecutive impacts did not change significantly despite hardening of the target material. The consumed energy fractions remained in the typical 34-40 % range for the 30° impact angle. When comparing the results of the oblique angle HVPI tests with ten

impacts to the ones obtained in the normal direction impact tests, it can be noted that the wear is approximately 4-6 times more severe in the oblique angle tests. Interestingly enough, the cutting-to-ploughing ratios were about 0.2 higher in the normal direction impact tests, i.e., increasing from 0.5 to 0.7. On the other hand, the volumes displaced in the angular impacts were a magnitude higher increasing the probability to generate larger pile-up regions. [134].

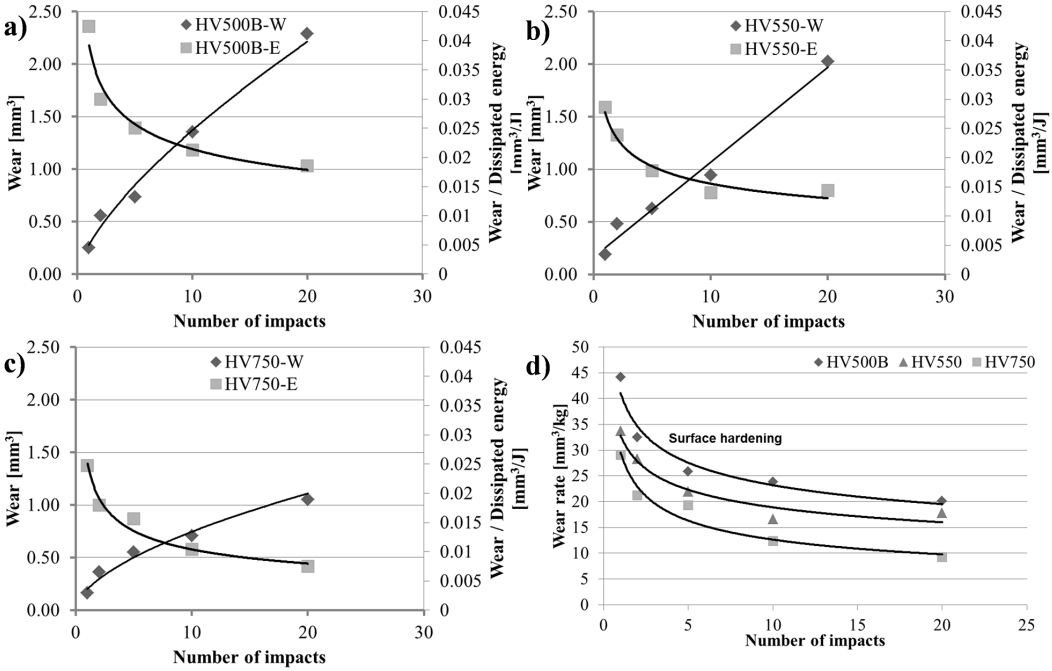

Figure 6.15: Effect of multiple impacts on the wear behavior of the martensitic and carbide reinforced steels during 30 degree impacts with a constant 17 J impact energy, a) HV500B, b) HV550, c) HV750 [134], d) wear behavior of the steels as volume loss per a kilogram of impacting particles.

Figure 6.16 shows the deformed crater areas after 20 impacts at 17 J. The HVPI test setup has a quite reasonable accuracy and it produces large enough craters to properly simulate impact wear. It is actually beneficial to aim impacts to partly overlap the previously ploughed ridges of the craters in order to gain information of the wear behavior of the priorly heavily deformed material at the ridges. The martensitic grades show notable plastic deformation and shear lips generated on the exit side of the crater in the impact direction. As a result of repeated impacts, the material develops also folded layers that can lead to subsurface shear localization. Such layers are prone to cutting off, as shown by the small detached particles in the impact region (Fig 6.16a and b). The shapes of the craters in HV750 suggest that it has experienced more cutting than pure plastic deformation, and that the material has been removed by shearing of wear particles from the surface. Moreover, the microscopic study revealed that the surface contained small cracks in the matrix that had propagated and released wear particles during continuous impacts. [134].

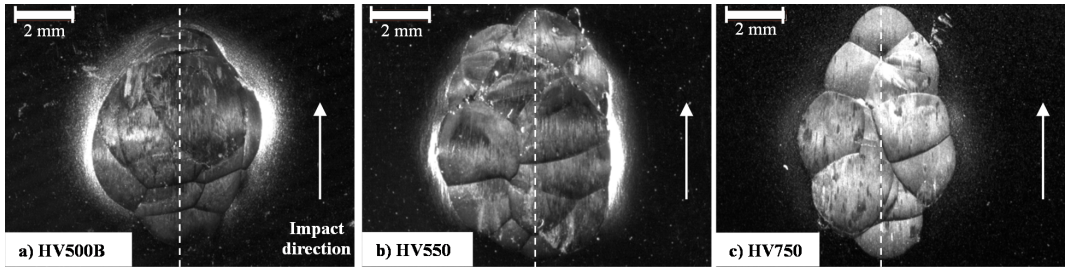

Figure 6.16: Surfaces of tested samples after 20 impacts at 17 J energy with a WC-Co projectile. The white dashed lines show to cutting lines for cross-sectional samples [134].

The cross-sectional study on the impact craters shows that the martensitic grades exhibit subsurface adiabatic shear banding in the heavily deformed regions, as seen in Figure 6.17. A concurrent failure mechanism not directly related to the adiabatic shear bands is the surface or subsurface formation of cracks. In addition, the subsequent impacts tend to generate a white layer on the surface with a thickness of ca. 10 μm. Hence, it is also possible that cracks initiate from this region and penetrate into the material. Both white layers and shear bands were observed after single impacts with either a high impact energy or high impact velocity, which suggests that prior deformation can also increase the probability for the shear band formation.

The multiple impact damage mechanism in the HV750 resembled the single impact cases as the fractures propagate mainly in the matrix, although some failed carbides were also found. However, extensive crack networks were also developed in the deformed volume below the surface, which was not yet observed in the single impacts at this impact energy, indicating that the steel might be susceptible to fatigue wear.

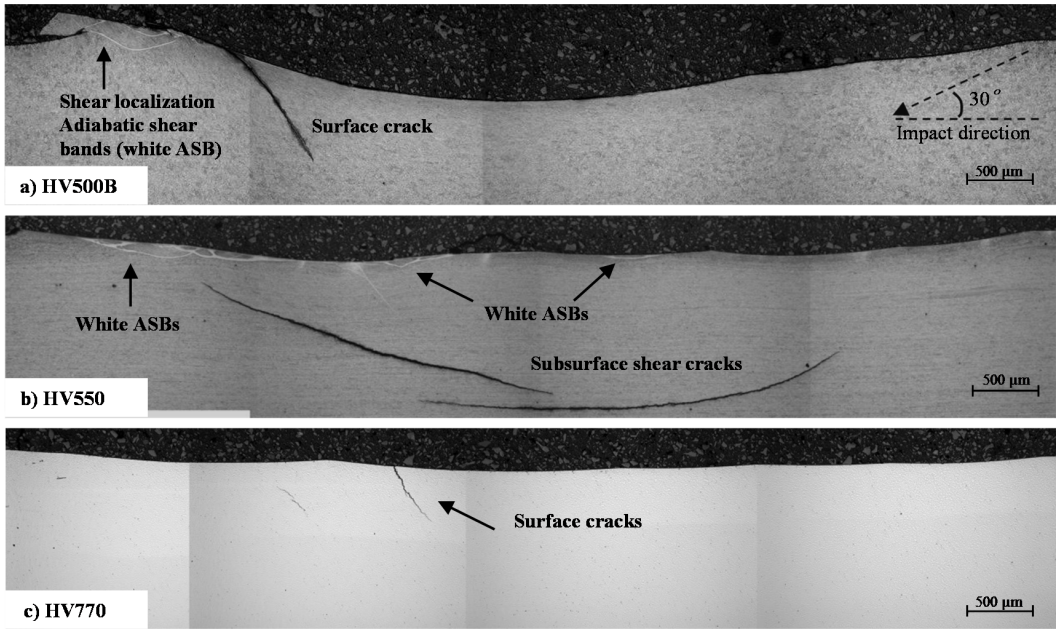

Figure 6.17: Cross-sectional views of impact craters shown in Figure 6.16 [134].

Figure 6.18 summarizes the observed wear behavior of the studied three ultra high strength steels. The interface damage dominates in normal direction impacts (a), shear localization near the pile-up regions is dominant in oblique angle impacts at high impact velocities (b), and multiple impacts promote the localization effects but hardening can saturate wear rate (c).

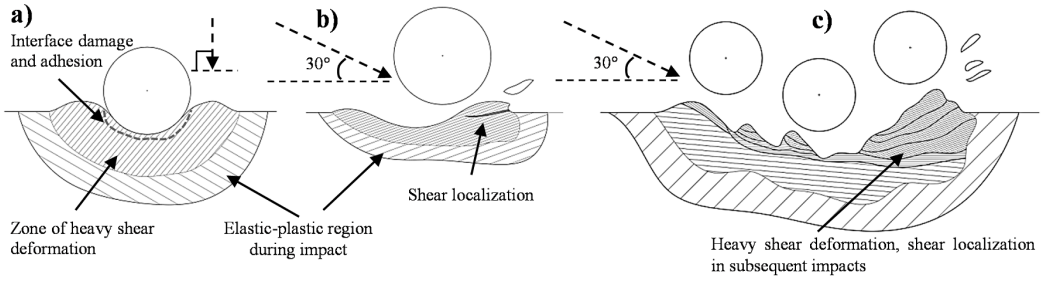

Figure 6.18: Impact deformation and wear characteristics of the ultra high strength steels in the studied conditions, a) normal direction impact, b) oblique angle impact at different velocities, c) multiple oblique impacts [134].

6.3 Summary and partial conclusions

An extensive test programme was performed to investigate the impact wear behavior of several ultra high strength steels and a Hadfield steel. Controlled test environments were provided by the high velocity particle impactor and drop test setups. The variables that were varied in the tests were the impact energy, impact angle, impact impulse, and number of impacts.

Based on the results and discussion presented above, the following summary and conclusions can be given.

Impact characteristics:

- The HVPI test is a good method to investigate the wear and damage characteristics of many material types. The method has very good repeatability.
- The energy dissipated during the impact depends on the material and impact angle, but it has fairly little dependence on the impact energy; for wear resistant steels generally around 20 %, 40 % and 80 % of the initial kinetic energy is consumed in the impact at 15, 30 and 60° impact angles, respectively.
- The different presentations of wear rate provide information about the material behavior from different points of view, e.g., about the material's capability to absorb impact energy relative to the lost material.

Ultra high strength grades and carbide reinforced steel:

- The cutting mechanism was found to prevail at low impact angles, but the contribution of plastic deformation (ploughing) increases in the transition from 15 to 30 degrees. In contrast to the general expectation that wear would be highest at around

30° angle [245], the Ultra High Strength Steels (UHSS) show higher volume losses due to combined heavy deformation and cutting at higher angles. This behavior is likely to arise from the high amount of energy transferred into the specimen at the 60° angle. However, adiabatic shear bands were not found responsible for the high wear rate as in the case of 30° angle.

- Deformed and transformed adiabatic shear bands are the prevailing cause for the damage and failure in the UHSS materials at high impact velocities and impact energies at low impact angles. The fracture develops inside the transformed adiabatic shear bands contributing heavily to the process of wear particle formation. Secondary failure mechanisms are also active leading to surface and subsurface cracking. The white surface layer can act either as a wear resisting tribolayer due to its high hardness, or it can promote cracking in certain impact conditions.

- Adiabatic shear bands can increase the wear rate by as much as 50 - 100 % in single impacts. Their appearance is dictated not only by the (high) impact energy, but the high strain rate alone has a promoting effect already at lower impact energies. Low angles generally promote the formation of ASBs because of the increased cutting effect. Multiple impacts can similarly produce adiabatic shear band networks already at moderate impact energies.

- The carbide reinforced steel showed lower volume losses than the martensitic steel grades due to its high strength and adeaquate strain hardening when the impact energy is not too high. At high impact angles and energies, excluding low energy normal direction impacts, the steel is susceptible to the development of subsurface crack networks that may limit its usability in certain conditions.

- The test materials generally showed good strain hardening capability under impacts without large changes in their behavior, except in the above mentioned conditions. Hardening of the subsurface depends on the existence of transformed and deformed shear bands, white layers, and deformed bulk material, the hardness of which decreases in this order due to their local differences in the microstructure.

Hadfield steel:

- In the Hadfield steel pre-straining reduces impact wear due to the strain hardening of the microstructure until 0.3 of macroscopic strain. Beyond this limit, the surface behaves in an increasingly brittle manner favoring the cutting mechanism. The highest wear rate under impacts occurs when the hardening limit is reached, for example in the service conditions, and the material begins to fracture mainly at the grain boundaries.

- Prior plastic deformation does not have a significant effect on the energy absorption capability of the Hadfield steel at the impact energy levels used in this study, as shown by the wear rate results normalized by the energy dissipated during the impact events.

7 High manganese austenitic steel - FCC crystal plasticity model

This section first briefly introduces the background of modeling approaches used in the modeling of twinning in single crystals, after which a short review of the large deformation framework used in this work is given with some aspects related to twinning. This is followed by the introduction of the phenomenological FCC crystal plasticity model including twinning. Its content is discussed in detailed; the flow and hardening rules are given and their meanings are discussed based on the physical aspects and experimental observations. The model is summarized and some of the key features of its implementation in the existing large deformation framework in Zébulon are presented.

The model parameters and their effects are presented with simple examples to elucidate the model's capabilities. The model parameter identification is performed for the conventional Hadfield steel based on the results available in the literature. The identification is done in two stages, where the first stage contains the initial identification for single crystals. In the second stage the parameters are fitted for polycrystalline representative volume elements. Some aspects of the physically observed behavior and model response are also discussed. The final result section exemplifies the model behavior in realistic type polycrystal aggregates in simple uniaxial deformation. A brief demonstration of a jaw crusher type surface loading is given to suggest a method for connecting two different scales to a multiscale approach, interconnecting the application level and the microstructural scale.

7.1 Modeling of slip and twinning in FCC metals

A considerable amount of single and polycrystal plasticity models are focused on moderate to high stacking fault energy FCC materials, such as Cu or stable austenitic steels, where the deformation predominately occurs by dislocation slip. Recent needs for higher strength high ductility steels have driven the development and utilization of TWIP steels. From the micromechanical point of view, the twinning phenomenon is a major contributor to the hardening behavior of these steels. Therefore, the models are required to include complex twin deformation and hardening mechanisms interacting with the conventional dislocations.

The modeling approaches including twinning can usually be distinguished by their contents into phenomenological models and dislocation dynamics driven physical models. The fairly recent papers [204, 217] review the most common approaches and developments of slip-twin crystal plasticity models in the past, and hence they are not repeated here. Nonetheless, although both phenomenological and DD-driven models simplify

the micromechanical behavior with various relations, the equations in the former take somewhat more simple form, as pointed out in Section 2.5. For example, the dislocation slip in both approaches usually takes a rate dependent form driven by the shear stress acting on the critical resistance of a slip system. The form, however, can be slightly more complicated in the DD-driven models including problem dependent variables such as temperature (and activation energies). The twinning, in turn, can be presented with similar type of equations, such as stress driven viscoplastic potential affected by numerous hardening mechanisms, or it can become very complex when the influence of the stacking fault energy, nucleation probabilities, and stress are considered, for example starting from the force action on two repulsive partial dislocations. In addition, the interactions between dislocations and twins, or twins and twins, further increase the complexity of the expressions and add the non-linearity of the problems. Furthermore, the critical stress of twinning may be linked to follow the Schmid type activation (phenomenological models) that includes all the physical aspects under one expression, or it can be constructed of the individual factors such as probabilities controlling twin activation (advanced DD-driven models). Ultimately, both approaches provide satisfactory results in terms of representing the micromechanical behavior of the modeled materials.

Another commonly accepted fact is that when the crystal plasticity is used in conjunction with finite elements, the twins are not explicitly presented in the microstructure, at least when larger polycrystal aggregates are considered. The continuously changing length and width of the twins in the nucleation and growth process would require high frequency remeshing, which is not very attractive. Thus, the twins acting in a material point are described as the volume fraction (or content) of the twins of the total volume, i.e., distinguishing which parts of that grain/volume are populated by twins and which parts are the matrix. The tracking of individual active twin systems by their individual contribution to the twin volume fraction is, however, possible when fixed twin systems are assigned. When twin volume fractions are used, the main question is whether to allow the shearing of existing twins by dislocations, or to suppress their movement inside the 'twinned' regions. The former causes little effect from twins to dislocations unless a strong hardening rule is used. The latter is more restrictive, and if a great amount of dislocation motion exists in the twinned regions, it is reasonable to account for the slip inside the twinned regions in the framework. Depending on the crystal structure, the slip inside twins can be included or excluded. However, when slip, twins, and slip-in-twins are operating in conjunction, their relative contributions to the plastic strain rate are given by their own equations of evolution including constraints and hardening rules.

The dislocation slip in FCC crystals occurs in 12 slip systems in the most densely packed atom planes. The {111} planes and <110> directions construct the slip systems according to cubic symmetry. To capture the deformation by twinning, the twin deformation modes are often constructed as pseudo-slip systems, i.e., $\dot{\gamma}_\beta^{tw} = \dot{f}^\beta \gamma_0^{tw}$, where shear deformation $\dot{\gamma}_\beta^{tw}$ is provided by the twinning rate $\dot{f}^\beta$ with the characteristic twin shear γ_0^{tw}. In other words, when these systems are active, they provide characteristic twin shear in the prescribed directions, which in the FCC case are expected to occur on the {111} planes in the $<11\bar{2}>$ directions, but only in the positive directions due to the polarized nature of twinning. A very extensive description of the crystallographic nature of twin shear and twin systems can be found in Christian and Mahajan [48, 203]. The twelve slip systems and twelve twin systems for the FCC structure are listed in Tables 7.1 and 7.2.

Table 7.1: The twelve {111} <110> slip systems with Schmid-Boas notation.

	(111)			$(1\bar{1}1)$			$(\bar{1}11)$			$(\bar{1}\bar{1}1)$	
$[\bar{1}01]$	$[0\bar{1}1]$	$[\bar{1}10]$	$[\bar{1}01]$	$[011]$	$[110]$	$[0\bar{1}1]$	$[110]$	$[101]$	$[\bar{1}10]$	$[101]$	$[011]$
B4	B2	B5	D4	D1	D6	A2	A6	A3	C5	C3	C1

Table 7.2: The twelve {111} <$11\bar{2}$> twin systems.

(111)			$(\bar{1}\bar{1}1)$			$(\bar{1}11)$			$(1\bar{1}1)$		
$[\bar{2}11]$	$[1\bar{2}1]$	$[11\bar{2}]$	$[2\bar{1}1]$	$[\bar{1}21]$	$[\bar{1}\bar{1}\bar{2}]$	$[211]$	$[\bar{1}\bar{2}1]$	$[\bar{1}1\bar{2}]$	$[\bar{2}\bar{1}1]$	$[121]$	$[1\bar{1}\bar{2}]$

Figure 7.1 presents a scale-by-scale approach for presenting crystal plasticity in FCC microstructures. The single crystal scale defines the micromechanical deformation behavior including the deformation mechanisms, i.e., dislocation slip and deformation twinning in this case. The choice of the prevailing deformation mechanisms and their interactions affects all of the following scales. The transition from single crystal behavior to the grain scale provides information about the grain level deformation, e.g., the competing effects of slip and twinning, and their contributions to hardening of the grain. The polycrystal scale finally describes the macroscopic behavior of the material as it summarizes the constraining effects of grain structure and texture. The performance of the material can be evaluated starting at the local scale or from the overall performance of the microstructure, depending which aspects are considered important. The failure initiates at a local scale and can then spread to the microstructure, but in contrast, strong hardening of a single grain does not guarantee that the whole microstructure exhibits strong strain hardening.

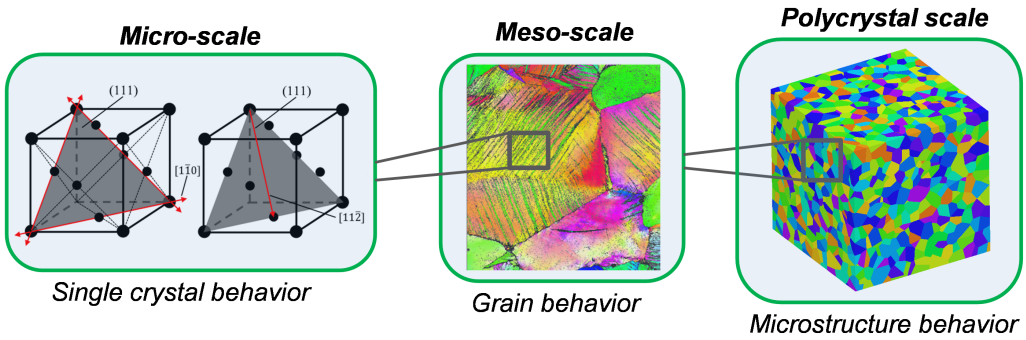

Figure 7.1: Scale-by-scale representation of the deformation in FCC microstructures, a) dislocation slip family {111} < 110 > and deformation twinning family {111} < $11\bar{2}$ > acting at the single crystal level, b) grain level deformation at the meso-scale, and c) polycrystal scale model with a representative grain structure.

This work aims to establish a presentation of the micromechanical behavior at all scales and to add to the current knowledge of the Hadfield steel behavior. A phenomenological crystal plasticity model is employed to describe the single crystal behavior to form a basis for the investigation. The model performance is first evaluated with single crystal simulations, which are compared to the experimental data. The polycrystal scale response

of the model is also compared with the experimental stress-strain behavior, and the simulated twin volume fractions of the aggregates are verified by microscopic studies. A novelty of the current approach is that some polycrystal aggregates are investigated with finite element discretized realistic-like microstructures instead of the common approach of using only self-consistent schemes to evaluate the material performance. Hence, the present approach may be used to investigate the local stress-strain behavior of the material in varying deformation conditions, which makes it a feasible tool to be used also in the application level studies in the future.

7.2 Finite strain formalism

The single crystal models proposed here are based on the finite strain formalism, which is implemented in the finite element code Zébulon/Zset. The small deformation theory based crystal plasticity models (e.g., [158]) have been successfully used for many industrial computations and polycrystalline aggregates [16, 36]. Due to the nature of wear problems, the deformation often reaches high strains, and thus large deformation theory needs to be considered. The current work is based on the numerical large deformation implementation in Zébulon, e.g., as used and developed further by Han [88] when studying the plastic behavior of irradiated stainless steels. Here, a basic FCC dislocation model is developed and expanded to include also twinning (this section). The same code is modified to study also BCC crystals, as explained later in Chapter 8. This part describes briefly the principles of the finite strain formalism based on the Mandel crystal plasticity [143].

The initial state of the material C_0 and its deformed counterpart at time t can be described by C_t, as shown in Fig. 7.2. Similarly, an initial position $\mathbf{X}$ in the initial configuration is transformed to the deformed actual configuration and denoted by $\mathbf{x}$. Then the deformation gradient, or the strain gradient, is written as $\underline{F} = \partial\mathbf{x}/\partial\mathbf{X}$.

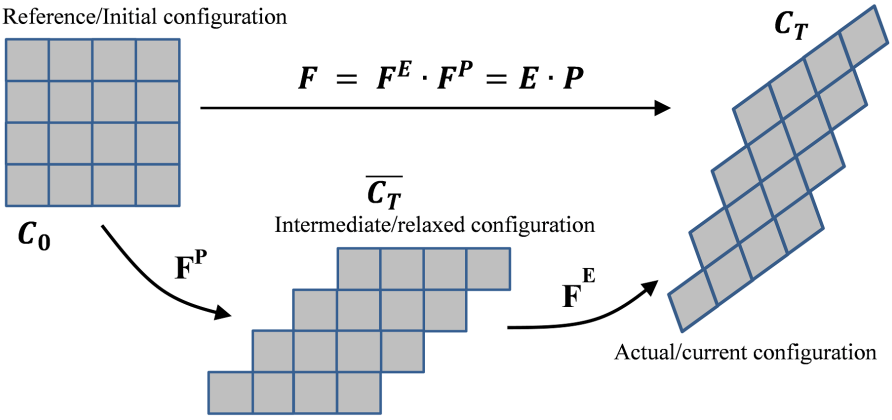

Figure 7.2: Multiplicative decomposition of the total deformation gradient F. The plastic part F^P relates to the reference and relaxed configurations, where the orientation tensors are calculated for dislocation slip. The elastic part F^E transforms the relaxed configuration to the current configuration by introducing elastic strains.

In the crystal plasticity approach, the multiplicative decomposition of the deformation gradient to elastic $\underline{E}$ and plastic parts $\underline{P}$; $\underline{F} = \underline{E} \cdot \underline{P}$ allows to treat the elastic and plastic parts separately. The plastic part accounts for the plastic deformation occurring

in different dislocation slip systems and possible twinning, while the elastic part consists of the elastic deformation and rigid body rotations of the crystal. Mandel proposed [143] an isoclinic intermediate configuration $\bar{C}_T$, which first realizes the plastic deformation part before the transformation to the actual configuration with elastic deformation. In this framework, the orientation of the crystal remains the same in the intermediate configuration as in the initial configuration prior to elastic transformation.

The velocity of the deformation of a point $\mathbf{x}$ in the actual configuration is $v = \dot{\mathbf{x}}$, and thus the velocity gradient is $\underline{L} = \partial\dot{\mathbf{x}}/\partial\mathbf{x}$. On the other hand, the derivative of the deformation gradient is $\dot{\underline{F}} = \dot{\underline{E}} \cdot \underline{P} + \underline{E} \cdot \dot{\underline{P}}$, and then the velocity gradient can be expressed as:

$$\underline{L} = \dot{\underline{F}} \cdot \underline{F}^{-1} = (\dot{\underline{E}} \cdot \underline{P} + \underline{E} \cdot \dot{\underline{P}}) \cdot \underline{P}^{-1} \cdot \underline{E}^{-1} \dot{\underline{E}} \cdot \underline{E}^{-1} + \underline{E} \cdot \dot{\underline{P}} \cdot \underline{P}^{-1} \cdot \underline{E}^{-1} = \underline{L}^e + \underline{E} \cdot \underline{L}^p \cdot \underline{E}^{-1} \quad (7.1)$$

where, $\underline{L}^e = \dot{\underline{E}} \cdot \underline{E}^{-1}$ and $\underline{L}^p = \dot{\underline{P}} \cdot \underline{P}^{-1}$

In the intermediate configuration the elastic dilations are here described with a right hand Cauchy-Green tensor, $\underline{C}^e = \underline{E}^T \cdot \underline{E}$, and the following elastic strains are defined by the Green-Lagrange strain:

$$\underline{E}_{gl} = \frac{1}{2}(\underline{C}^e - \underline{1}) = \frac{1}{2}(\underline{E}^T \cdot \underline{E} - \underline{1}) \quad (7.2)$$

The Cauchy stress $\underline{\sigma}$ is defined in the actual configuration. The second Piola-Kirchoff (PKII) $\underline{S}^e$ can be computed from the elasticity relations, in the intermediate configuration expressed as:

$$\underline{\sigma} = J_e^{-1} \underline{E} \cdot \underline{S}^e \cdot \underline{E}^T \rightarrow \underline{S}^e = J_e \underline{E}^{-1} \cdot \underline{\sigma} \cdot \underline{E}^{-T} \quad (7.3)$$

where $J_e = det(\underline{E}) = \rho_i/\rho = \rho_0/\rho$, and ρ_i, ρ_0, ρ are the densities in the intermediate, initial and actual configurations, respectively. In the plastic deformation of metals, the volume is considered constant and therefore the relationship $\rho_i = \rho_0$ is reasonable.

The power transformation can be written as [27]:

$$P = \frac{1}{\rho}\underline{\sigma} : \underline{D} = \frac{1}{\rho}\underline{\sigma} : \underline{L} = \frac{1}{\rho}\underline{\sigma} : (\underline{L}^e + \underline{E} \cdot \underline{L}^p + \underline{E}^{-1}) = \frac{1}{\rho}\underline{\sigma} : \underline{L}^e + \frac{1}{\rho}\underline{\sigma} : (\underline{E} \cdot \underline{L}^p \cdot \underline{E}^{-1}) \quad (7.4)$$

From this relationship it can be derived for the current framework [88] that the transformation takes the following form in the intermediate configuration:

$$P = \frac{1}{\rho_i}\underline{S}^e : \dot{\underline{E}}_{gl} + \frac{1}{\rho_i}\underline{M} : \underline{L}^p \quad (7.5)$$

Hence, the PKII stress can be used for the elastic model, while in conjunction with the velocity of the plastic deformation, the Mandel stress tensor $\underline{M} = J_e \underline{E}^T \cdot \underline{\sigma} \cdot \underline{E}^{-T}$ is used to describe the plastic flow behavior. Since the choice for elasticity is described as $\underline{S}^e = \underline{\underline{\Lambda}} : \underline{E}_{gl}$, where $\underline{\underline{\Lambda}}$ is the fourth order elasticity stiffness tensor, the Mandel stress can be expressed as:

$$\underline{M} = J_e \underline{E}^T \cdot \underline{\sigma} \cdot \underline{E}^{-T} = \underline{E}^T \cdot \underline{E} \cdot \underline{S}^e = \underline{C}^e \cdot \underline{S}^e \tag{7.6}$$

Finally, the elasticity of the single crystals follows the cubic elasticity definition with only three elasticity constants. The fourth order elasticity tensor is given in Equation 7.7. The elasticity constants are usually measured, for example recently with an indentation technique [177], or occasionally by fitting the simulation data [88], or using the values from the literature. The elastic values used in this work originate from the measured values for a variety of high manganese TWIP steels presented in ref. [177].

$$\underline{\underline{\Lambda}} = \begin{bmatrix} C_{11} & C_{12} & C_{12} & & & \\ C_{12} & C_{11} & C_{12} & & 0 & \\ C_{12} & C_{12} & C_{11} & & & \\ & & & C_{44} & & \\ & 0 & & & C_{44} & \\ & & & & & C_{44} \end{bmatrix} \tag{7.7}$$

In the crystal plasticity framework, the plastic deformation velocity gradient L^p is associated with the available slip/twin systems. In the case where only dislocation slip is considered, L^p can be expressed as:

$$\underline{L}^p = \sum_{s=1}^{n_{sys}} \dot{\gamma}^s \underline{N}^s \tag{7.8}$$

where $\underline{N}^s = \mathbf{m}^s \otimes \mathbf{n}^s$, which describes the slip geometry. The Schmid tensor $\underline{N}^s$ for a slip system s is defined as a tensor product of the slip direction $\mathbf{m}^s$ and the normal of the slip plane $\mathbf{n}^s$ in the intermediate configuration. Vector $\mathbf{l}$ denotes the direction of the stress σ. Figure 7.3 visualizes the Schmid representation for shear stress acting on each slip system, ϕ and θ denoting the angles between the direction of traction to the normal of the slip plane and the slip direction, respectively. The acting shear stress τ^s is computed making use of these angles with vectors $\mathbf{l}, \mathbf{m}^s, \mathbf{n}^s$. The traction σ is projected to a particular slip plane A as the resolved shear stress.

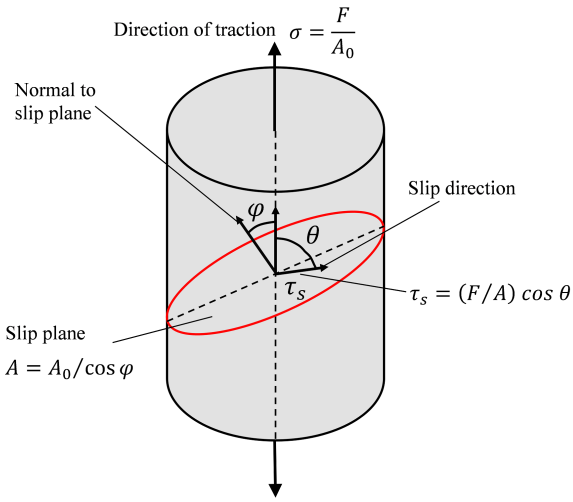

Figure 7.3: Single crystal representation of Schmid shear stress acting on a slip system

The resolved shear stress acting on a slip system can then be written as:

$$\tau_s = \underline{\sigma} : \underline{N}^s = \sigma(\mathbf{l} \otimes \mathbf{l})(\mathbf{m}^s \otimes \mathbf{n}^s) = \sigma(\mathbf{n}^s \cdot \mathbf{l})(\mathbf{m}^s \cdot \mathbf{l}) = \sigma(cos\phi\, cos\theta) \tag{7.9}$$

However, in the current approach with the Mandel stress based crystal plasticity one can write $\underline{M} : \underline{L}^p = \sum_{s=1}^{n_{sys}} \dot{\gamma}^s \tau^s$. In this case, the resolved shear stress in a system s is expressed as $\tau^s = \underline{M} : \underline{N}^s$. In general, the Schmid tensor is non-symmetric, but its decomposition to symmetric part can be written as:

$$\underline{N}^s_{sym} = (\mathbf{m}^s \otimes \mathbf{n}^s)_{sym} = \frac{1}{2}(\mathbf{m}^s \otimes \mathbf{n}^s + \mathbf{n}^s \otimes \mathbf{m}^s). \tag{7.10}$$

In metal plasticity with large deformations, the elastic deformation is small compared to the total deformation, ($\underline{C}^e \approx 1$ and $\underline{E}_{gl} \approx 0$), and the resolved shear stress can be reduced to:

$$\tau^s = \underline{M} : \underline{N}^s = (\underline{C}^e \cdot \underline{S}^e) : \underline{N}^s \approx \underline{S}^e : \underline{N}^s = \underline{S}^e : \underline{N}^s_{sym} \tag{7.11}$$

This approximation, however, was not used in the calculations of the present work. Instead, the finite strain formalism using Mandel stress and non-symmetric orientation tensor is used in the models of this work due to their mutual compatibility, which is denoted by $\tau^s = \underline{M} : \underline{N}^s$.

Special aspects of twinning in crystal plasticity schemes

Twin systems are usually incorporated in the crystal plasticity frameworks as pseudo-slip type twin systems. When the twins initiate and grow in the matrix, they reduce the volume fraction of the matrix and the lattice reorientations are governed gradually by dislocation slip and twinning with no direct relationship with twinned configuration. When the twin volume content increases to very large values, it becomes somewhat less accurate to approximate the stress state inside a grain or a volume by its original matrix

orientation. The approximation could be improved in two ways: by the slip-twin average stress scheme, or by the twin induced lattice reorientation scheme. Some studies prefer to use both [240], either one [203, 235], or sometimes neither [85] depending on their suitability for the framework and the level of simplifications made.

Average stress scheme

In order to improve the approximation for the average stress in the crystal, an extension including twin reorientation could be introduced. Van Houtte [98] suggested an additional reorientation scheme that accounts for the orientation difference between the matrix and a twin variant with a transformation tensor $\underline{Q}^{\beta}$, which assumes that the twinned region maintains a perfect twin orientation, i.e.,

$$\underline{Q}^{\beta} = 2\mathbf{n}^{\beta} \otimes \mathbf{n}^{\beta} - \underline{I} \tag{7.12}$$

where $\underline{Q}^{\beta}$ is the rotation tensor for the twin system β, $\mathbf{n}^{\beta}$ is the twin plane unit normal of the twin system β, and $\underline{I}$ is an identity tensor.

The volumetric stress and strain average can be assumed for simplicity, but also because of the necessary compatibility between the twin lamellae and the parent grain [54, 200]. For example, Kalidindi [110] suggested a transformation of the elastic stiffness tensor to calculate the stress of the twinned region using the following two equations:

$$\Lambda^{\beta}_{ijkl} = \Lambda^{m}_{pqrs} Q_{ip} Q_{jq} Q_{kr} Q_{ls} \tag{7.13}$$

$$\underline{\sigma}^{\beta} = \underline{\underline{\Lambda}}^{\beta} \underline{E} \tag{7.14}$$

where β denotes one twin variant and its corresponding transformed elastic stiffness and stress tensors, i.e., the stress tensor is different for each twin variant because $\underline{Q}^{\beta}$ can basically be unique for each system. The average stress is then computed as

$$\underline{\sigma}^{e} = \left(1 - \sum_{1}^{N_{\beta}} f^{\beta}\right) \underline{\sigma}^{e,m} + \sum_{1}^{N_{\beta}} f^{\beta} \underline{\sigma}^{e,\beta} \tag{7.15}$$

The simulations performed in this work do not use the extension of average stress for simplicity. If a framework also includes slip inside the twins, the stress values for each twin variant gain more relevance owing to the definition that stress inside the twinned region initiates slip. In that case it is important to use the stress of a twin variant and not the stress of the matrix orientation.

Twin induced reorientation scheme

The lattice reorientation scheme that results from intense twinning can be incorporated in the twinning models. If the twin volume content exceeds a limiting value, the lattice is reoriented. One issue related to this scheme is that if the lattice is reoriented using the transformation tensor $\underline{Q}^{\beta}$, according to which variant or the combination of variants of active twin systems the reorientation is to be performed. Staroselsky and Anand [203] suggested a scheme where the reorientation is performed according to the dominant twin system, i.e., the twin system that has the highest contribution to the twin volume

content, when the criterion triggering the reorientatation is met. The criterion initiating the reorientation process was adopted from Van Houtte [98], where the criterion has a statistical basis controlled by a random number, e.g., between 0.2 and 1.0 of twin fractions. In other words, this means that the reorientation may occur earlier in some grains than in the others, if separate values are used for different grains. Figure 7.4 presents the kinematics of the reorientation scheme used by Staroselsky and Anand [203].

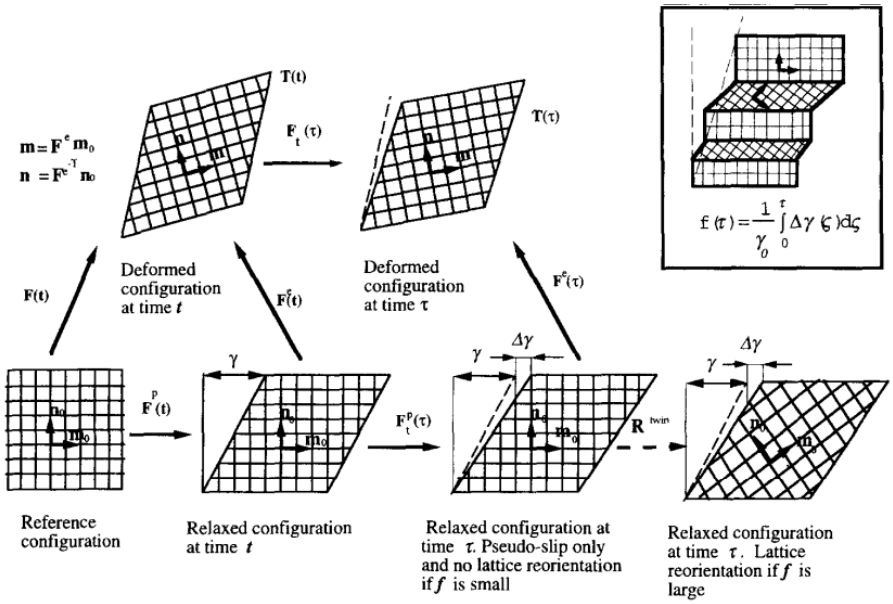

Figure 7.4: Twin reorientation scheme according to ref. [203]

Usually after the reorientation all twin volume fractions are set to zero. The hardening rules related to twinning are often connected to the twin volume content, and hence resetting the twin volume content can quickly lead to instabilities. To avoid this, Staroselsky and Anand [203] proposed that the hardening rules would be governed by the volume content of the dominant twin system prior to the reorientation. Also alternative reorientation schemes exist with similar features, for example Karaman et al. [113] suggested a scheme incorporated in the self-consistent viscoplastic framework. However, they abandoned the Van Houtte type statistical criterion for the activation of the reorientation process and used a different criterion instead, that is self-adjusted during the deformation.

The greatest restriction of these schemes is that if the reorientation is performed, it is dependent on the chosen criterion. If the value for reorientation is low, e.g., below 0.5, the reoriented lattice does not necessarily offer any better approximation because most of the grain would still be in the initial orientation and twinning in many cases is considered to be driven by the stress of matrix. If the value is high, e.g., around 0.7-0.8, the reorientation does not offer greatly improved approximation before this point. Furthermore, the concept of the transferring only the twin volume content of the dominant system to the new orientation and resetting other twin volume fractions to zero is questionable in terms of the hardening rules, especially if the hardening rules evolve with total twin volume content instead of the dominant twin volume content. The hardening can restrict twinning effectively in some cases, but if the total twin volume content of the grain is reset to zero, it most often increases the twinning rate. A similar observation was made by Karaman et

al. [113], i.e., that the twinning rate decreases at higher twin volume contents. In the present work, a simplification is made so that reorientation schemes are not incorporated in the framework, partly because of the incompatibilities of both of the above presented schemes with the current hardening models.

7.3 Phenomenological single crystal plasticity model including twinning

This section presents a single crystal model the a metallic material that deforms by dislocation slip and twinning. The current approach has a phenomenological basis, which dictates the type of the equations describing the microscopic behavior. Also, it is typical and appropriate for finite element approaches that microscopic features (i.e., existing or initiating micro shear bands or twins) are not explicitly described in the geometry because it would cause complicated meshes and the scale of the analysis would be restricted to extremely small. Additionally, it is quite difficult to verify between a simulation model and the physical behavior even with in-situ experiments. Therefore, the micromechanical deformation by dislocation slip and twinning is described as the deformation of a material volume (i.e., one gauss point in the finite element approach).

Depending on the state of the material, the material volume or a grain can have existing defects or microscopic deformation that composes of the micromechanical features. The existing defects include stored dislocations (defect dislocation population) that are formed during manufacturing, and in some cases twins (i.e., thermal twins). If prior deformation exists, which is the usual state of the material, certain amounts of twins and localized slip regions exist within the volume. Both initial defects and defects produced by previous deformation can be taken into account in the stored dislocation densities or twinned volume contents as average fields within the material volume. This simplification does not allow the explicit expression of twinned regions as part of the geometry (e.g., location or individual size, as seen in Fig. 7.5), but it is worth to note that the twin volume content and dislocation density of each included slip and twin system is tracked. For example, in Fig. 7.5b, the two deformed states can have equal amount of total twinned volumes $\sum f^{\beta}_{I/II}$, but it may be that the amount of twin volume contents in some twin systems are different, e.g., $f^{\beta 2}_{I}$ and $f^{\beta 2}_{II}$ in Figure 7.5. Hence, it is possible to capture the hardening effect of previous deformation and initial defects regardless of the phenomenological or geometrical simplifications. However, considering the present model, some challenges can arise from the definition of accumulated slip as the hardening parameter instead of directly using the dislocation densities, as in the current model the previous slip deformation is required to be presented with values of accumulated slip γ instead of dislocation densities.

Inspired by Kalidindi [110, 111], the plastic deformation velocity gradient $\underline{L}^p$, denoted by $\dot{\epsilon}^p$, is expressed as the sum of all effective micromechanical phenomena in Equation 7.16. The first term is the contribution of slip in untwinned crystals, the second part depicts the contribution of twinning, and the last part accounts for the slip inside the twinned regions.

$$\underline{\dot{\epsilon}}^p = \underbrace{(1-\sum_{\beta=1}^{N_\beta} f^\beta)\sum_{s=1}^{N_s}\dot{\gamma}^s \underline{m}^s}_{slip\ in\ matrix} + \underbrace{\sum_{\beta=1}^{N_\beta}\dot{f}^\beta\gamma^{tw}\underline{m}^t}_{twinning} + \underbrace{\sum_{\beta=1}^{N_\beta} f^\beta\left(\sum_{s_{tw}=1}^{N_{s_{tw}}}\dot{\gamma}^{s_{tw}}\underline{m}^{s_{tw}}\right)}_{slip\ in\ twins} \tag{7.16}$$

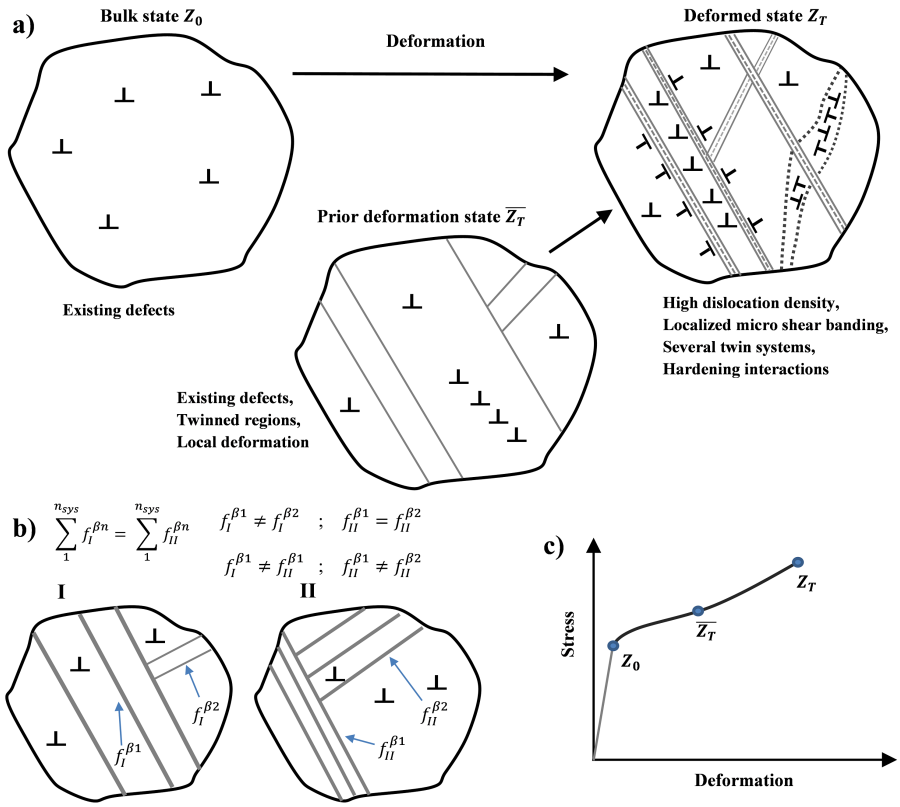

Figure 7.5: Presentation of the a) deformation from the bulk state including some defects and from the previously deformed state to the current deformed state of a grain, b) two definitions of the previous twin deformation in a grain with the same total twin volume fraction but different individual twin system volume fractions, and c) a macroscopic stress-strain curve showing the bulk and two deformed states of the material.

where $\dot{\gamma}^s$ denotes the shear rate of a slip system s, f^β the twin volume content of a twin system β, γ^{tw} is the constant shear strain associated with twinning (0.707 or $\sqrt{2}/2$ for FCC [48]), and $\underline{m}^s$,$\underline{m}^t$,$\underline{m}^{s_{tw}}$ are the Schmid tensors for slip in the matrix, twinning in an untwinned crystal, and slip inside the twins of each system. Similarly, the number of available systems of each contribution are N^s, N^β, and $N^{s_{tw}}$ for slip, twins and slip inside twins, respectively.

The slip is assumed to take place in the matrix region and twinning decreases the volume content of the matrix. In other words, by the definition of the model, the slip cannot shear the twinned regions. This is, obviously, a simplification in the present framework, and the contribution of slip inside the twins could be considered with an additional term. Alternatively, Jia et al. [105] did not pose the constraint of increasing twin volume content decreasing the matrix, and twins could always be sheared by the dislocations. It is difficult to assess the superiority of either model, as the current model may lead to the underestimation of the slip activity (especially if slip in twins is neglected), whereas the alternative model can easily over-estimate the slip activity and underestimate slip-twin hardening, if no restriction exists because of the twin boundaries.

On the other hand, considering that further slip could be allowed inside the twins, the activity of slip could still be quite restricted. This is because the twins in FCC metals often appear as bundles of thin twins with a layer of matrix in between [65]. High dislocation densities have been observed inside these regions, but in many cases the activity inside the twins is notably more limited than in the matrix, and dislocation pile-ups form at the twin boundaries. [48, 113]. It is worth noting that dissociation of perfect dislocations into Shockley partials can take place at the boundaries, and the products of this process may more easily penetrate into the twins. However, from a phenomenological modeling perspective, a simplification in the current work is made to neglect any further slip inside the twins, i.e., the last term in Equation 7.16 will be omitted.

7.3.1 Slip rate, slip hardening and interaction with twins

The flow rule or the slip rate of a slip system s used in this work is based on the viscoplastic model proposed by Méric and Cailletaud [34, 157]. As the model is rate-sensitive, it does not need specific algorithms to solve which slip systems are active, in contrast to some rate-independent formulations, presented for example in ref. [7]. The slip rate used in this work can be written according to Méric and Cailletaud as

$$\dot{\gamma^s} = \dot{\nu}^s \, sign(\tau^s - x^s) = \left\langle \frac{|\tau^s - x^s| - r^s - \tau_y}{K} \right\rangle^n sign(\tau^s - x^s) \tag{7.17}$$

where K and n are viscoplastic parameters in terms of Norton flow. The term r^s contains the combined hardening effects of dislocation-dislocation and twin-dislocation interactions. The τ^s is the resolved shear stress of the system, x^s is the parameter for kinematic hardening, and τ_y is the initial resolved shear stress. The Macaulay brackets ($<x>$) denote here that if $x > 0, x = x$, and otherwise zero. This means that if the absolute value of the effective resolved shear stress $\tau_{eff} = |\tau^s - x^s|$ overcomes the initial shear resistance and hardening effects, flow occurs, but if it remains lower, flow does not take place. The sign function dictates the direction of the flow, as the dislocation slip can occur in both <110> directions in the {111}<110> slip systems of FCC crystals.

The isotropic non-linear hardening rule is divided into two parts. The first term $r^{sl \to sl}$ on the right hand side of Equation 7.18 presents the contribution of dislocation-dislocation interactions, whereas the second term $r^{tw \to sl}$ describes the contribution of twin-dislocation interactions.

$$r^s = r^{sl \to sl} + r^{tw \to sl} \tag{7.18}$$

The isotropy in this context refers to a rule that both slip directions exhibit the same hardening response irrespective of the direction.

DISLOCATION-DISLOCATION INTERACTIONS AND HARDENING

The evolution of the hardening rule of a system s is inspired by the macroscopic models containing interactions between other slip systems. The amount of hardening is dependent on the accumulated values of slip in system r, and also on the number of active slip systems as the hardening sums over all slip systems. Thus, the model aims also to capture the effect of complex loading paths, or possible memory effects in uniaxial loading, by describing several interactions. This formulation describes the self and latent hardening

through an interaction matrix H_{rs}. In this work, the interaction matrix introduced by Franciosi [74] is adopted.

$$r^{sl\rightarrow sl} = bQ\sum_{r} H_{rs}\rho^{r} = Q\sum_{r} H_{rs}\{1 - exp(-bv^{r})\} \;;\; v^{r} = \int_{0}^{t} \dot{v}^{r} = \int_{0}^{t} |\dot{\gamma}^{r}| \qquad (7.19)$$

where ρ_r is the dislocation density of a system r, b is the coefficient for the saturation of hardening, and Q is the hardening coefficient.

The exponential form of the hardening rule permits the saturation of hardening in slip system s, which is suitable for large deformation use where saturation can occur. The key coefficient for the saturation is b, while Q is related to the maximum effect of slip hardening. The rate form of the dislocation density takes the following form:

$$\dot{\rho}^{s} = (1 - b\rho^{s})\dot{\nu}^{s} \qquad (7.20)$$

The hardening rule presented above is suited well for the short range interactions of dislocations, and is therefore related to dislocation densities (ρ^r) or alternatively to the accumulated values of slip in a slip system (v^r). The kinematic parameter, on the other hand, introduces the effect of long distance interactions and the evolution of the dislocation structure inside the grain. The term x^s in the flow rule Equation 7.17 is the internal back-stress. The model has a phenomenological basis on the kinematic hardening rule for metallic materials in macroscopic models, which translated to slip conditions affects the effective critical stress ($\tau^s - x^s$), which is the threshold for the flow rule [157].

$$x^{s} = c\alpha^{s} \quad \dot{\alpha}^{s} = (sign(\tau^{s} - x^{s}) - d\alpha^{s})\dot{\nu}^{s} \qquad (7.21)$$

where c and d are the parameters controlling the effectiveness of the model. In cyclic loading this model adapts a suitable back-stress that phenomenologically can describe the macroscopic Bauschinger effect, that could not be easily generated without this term in the absence of other mechanisms, such as twinning or martensitic transformation.

The hardening matrix consists of non-dimensional hardening coefficients. The self-hardening terms are the diagonal elements and the latent hardening coefficients the non-diagonal elements, both denoting the different dislocation interaction arrangements. In FCC crystals, the hardening matrix has 12x12 ($\sum$ 144) elements, as presented in Fig. 7.6.

The number of independent coefficients is reduced due to the occurrence of four <111> axes with ternary symmetry. This leads to six independent coefficients $h_0 - h_5$, which are related to each type of dislocation interaction listed in Table 7.3.

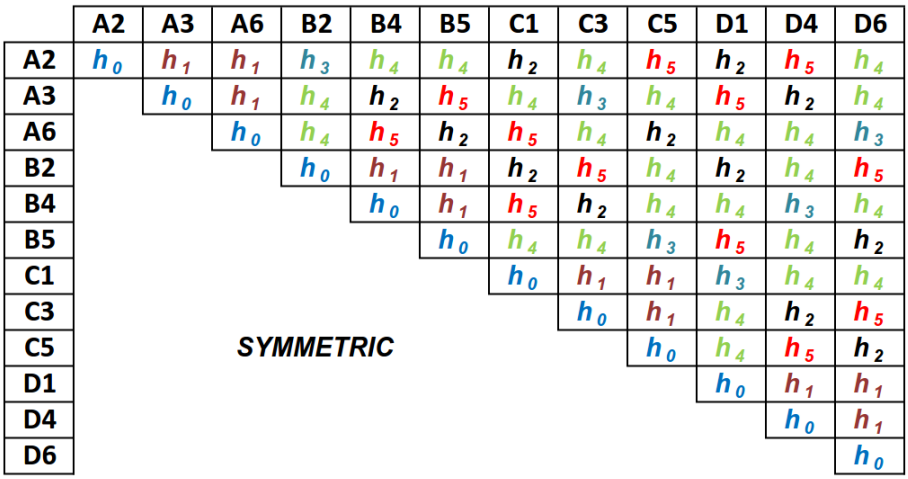

Figure 7.6: Interaction matrix for FCC crystals. Slip family is {111} <110> [74].

Table 7.3: Parameters of the interaction hardening matrix

	Interaction of dislocations of the same slip systems H_{rs} $r = s$, self-hardening
h_0	Interaction with self
	Interaction of dislocations in different slip systems H_{rs} $r \neq s$, latent hardening
h_1	Co-planar interaction (same slip plane)
h_2	Hirth junction, (orthogonal slip systems)
h_3	Collinear interaction (systems with same Burgers vector, cross-slip)
h_4	Glissile junctions
h_5	Sessile junctions, (Lomer-Cottrell lock)

The original shape of the matrix was defined by Franciosi et al. [75], and it has been implemented widely in either dislocation density based models (e.g., Equation 2.13) or in the models using local hardening (e.g., Equation 7.19). The identification and magnitude of each coefficient is still open to debate. Some studies rely on the identification procedure performed based on the macroscopic behavior of complex loading paths, which is a frequently used way, as summarized by Gérard et al. [81]. Alternatively, the identification may be performed based on the single crystal results [226]. A slightly more sophisticated way is to utilize dislocation dynamics simulations to classify the relative strength of each interaction, as was recently done for example by Devincre et al. [59], Madec et al. [58], and Alankar et al. [4]. These studies discuss in details the physical nature and strength of each interaction. However, the identification results are often quite different due to the fundamental difference in the formulation of the models. Often when the identification is not possible because of insufficient data, all of the latent terms are assumed equally strong and slightly stronger than the self-hardening term, using for example values of 1.0 for self-hardening and 1.4 for the latent terms.

TWIN-SLIP INTERACTION AND HARDENING DUE TO TWIN BOUNDARIES

The interaction of slip and twins is not straightforward. However, it is well-known [48] that twin boundaries cause reduction in the mean-free path of dislocations and thus promote dislocation storage. To account for this hardening effect caused by existing

non-coplanar twins and twin boundaries, the reduced matrix grain size may be modeled with a Hall-Petch (H-P) type relationship [111, 196, 197, 240]. It is, however, worth noting that the dislocations may shear the twins occasionally [48]. Therefore, the hardening rule rather characterizes general hardening caused by the barrier-like effect and does not separate individual cases. The hardening rule is idealized in Figure 7.7.

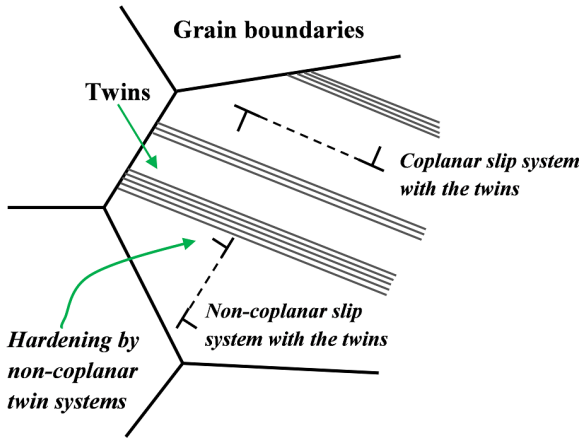

Figure 7.7: Effective twin barriers with dislocation pile-ups hardening the non-coplanar slip systems in a grain, modified from ref. [191]

In the present context, the H-P type hardening suggested by Kalidindi [111] is utilized. Ideally an array of parallel twins is assumed to have equal thickness and the twin volume fraction is considered inversely proportional to the average spacing of the twins, l_{tw} (i.e., $\sum f^{\beta} \propto l_{tw}^{-1}$). Given that the H-P relationship suggests that the flow stress has a dependence on the characteristic length as $\sigma \propto l_g^{-0.5}$, the hardening rule may be written as a function of twin volume fraction as:

$$r^{tw \to s} = H^{tw \to sl} \Big(\sum_{\beta = Non-coplanar}^{N_\beta} f^{\beta} \Big)^{0.5} \tag{7.22}$$

where $H^{tw \to sl}$ is the hardening coefficient characterizing the strength of the barriers. The rate form of Equation 7.22 can be written as

$$\dot{r}^{tw \to s} = 0.5 H^{tw \to s} \Big(\sum_{n=NC}^{N_\beta} f^{\beta} \Big)^{-0.5} \dot{f}^{\beta} \tag{7.23}$$

Thus, the hardening rule presents the collective effect of the twins in an average sense and no explicit expression of their placement within the volume is described by the rule, i.e., whether the twins are sparsely distributed or densely packed inside the volume.

7.3.2 Twinning rate and twin-twin and slip-twin interaction hardening

The twin nucleation and growth can be difficult to separate as mechanisms because of the complexity of the behavior. For example, Steinmetz et al. [204] suggested a combined

method for twin nucleation and growth based on the critical twin stress. This stress is computed utilizing the stacking fault energy and the theory of three-layered stacking faults, so that $\tau_c = \gamma_{sfe}/3b_c + 3Gb_c/L_0$, where γ_{sfe} is the stacking fault energy, b_c the magnitude of the Burgers vector, G the shear modulus, and L_0 the length related to the three layer stacking faults. Ideally, when the critical stress is overcome, the twin probability controls the twinning procedure with quite complex relations with dislocation densities that may initiate twinning. The beneficial side in this model is that the explicit definition of the stacking fault energy is possible, especially if a thermo-mechanical solver is used in the simulations. As the present model operates at the moment with a mechanical solver only, the twinning rate is written as a combination of nucleation and growth using a phenomenological description, still considering the fundamental ideas of twin stress.

$$Twinning\,rate:\ \dot{f}^{\beta} = \underbrace{(\dot{g}^{t_n} + \dot{g}^{t_g})}_{Combined\,twinning\,rate} \left(f_{max} - \sum_{\beta}^{N_\beta} f^{\beta} \right) \tag{7.24}$$

The phenomenological twinning rate model was proposed [85] to numerically describe the behavior of magnesium in cyclic loading with a mean field model. Equations 7.25 and 7.26 show the content of this model, which was intended to represent the evolution of compression twins. The twinning rate is driven by the equivalent plastic strain rate of slip in the matrix, $||\dot{\epsilon}^m||$. The twinning rate is constrained by the maximum value for the total twin volume fraction f_{max}. It requires the sum of all variants to saturate at this value and also constraints a twin variant to this maximum value. The twinning, in this model, is triggered by the stress in the matrix (untwinned part of the volume) with two additional constraints: if hydrostatic pressure is negative (dilation is negative, i.e., compression state) and the resolved shear stress is larger than the threshold stress τ_y^{tw} of a twin variant.

$$\text{twinning iff: } trace(\underline{\sigma}^m) < 0 \text{ and } ||\tau^{\beta}|| = \underline{\sigma}^m : \underline{m}^t > \tau_y^{tw} \tag{7.25}$$

$$\dot{f}_{CT}^{\beta} = k_c(f_{max} - \sum_{\beta} f^{\beta})(f_{max}^{\beta} - f^{\beta})||\dot{\epsilon}^m|| \tag{7.26}$$

where k_c is a coefficient controlling the intensity of twinning.

Inspired by this model, in this work the twinning rate is proposed to take the slip rate independent and dependent forms presented in Equations 7.27 and 7.28.

$$\dot{f}^{\beta} = k_c(f_{max} - \sum_{\beta} f^{\beta}) \left\langle \frac{|\tau^{\beta}| - r^{tw} - \tau_y^{tw}}{K_t} \right\rangle^{n_t} \tag{7.27}$$

$$\dot{f}^{\beta} = k_c(f_{max} - \sum_{\beta} f^{\beta}) \left\langle \frac{|\tau^{\beta}| - r^{tw} - \tau_y^{tw}}{K_t} \right\rangle^{n_t} (\sum_{s} \dot{\nu}^s) \tag{7.28}$$

where k_c is a coefficient controlling the intensity of twinning similarly as above, f_{max} is the constraining maximum amount of twinned volume content, K_t and n^t define the viscous behavior of the flow rule, r^{tw} is the isotropic hardening rule resisting twinning,

and τ_y^{tw} is the initial shear resistance. In this formulation, the initial shear resistance consists of the effects of stacking fault energy and the probability to generate a twin, but the total expression is much more simplified.

For the slip rate dependent model, $\sum_s \dot{\nu}^s$ is the sum of absolute slip rates, which acts as a constraint and also as a driving force for twinning. Both flow rules have a restriction that multiple slip must be activated before twinning can take place, i.e., plastic flow in at least two slip systems must have occurred to fulfill the demand for multiple slip activated twinning. The general flow rule for twinning without constraints uses the same description as for slip. By choosing the viscoplastic parameters, K and n, different from slip, it is possible to generate strain rate dependency for the twinning rate, e.g., increased twin propensity at high strain rates or vice versa. In addition, and quite crucially, this form of the flow rule allows the use of hardening as part of the flow model, i.e., if hardening is low, twinning with high rate is favored, and if hardening is high, the twinning rate is more limited. The dependent flow rule in Equation 7.28 can be used to apply more constraints on the twinning rate, if a direct relationship between active slip and twinning is required. The physical nature of slip activated twinning is captured by this model, but rather heavy constraints can exist to reduce the twinning rate, e.g., in the case of high strain rates. In contrast, if the independent model is used, it does not usually mean that twinning is highly dominant over slip because of the hardening effects used in the model. On the other hand, in some cases it may be beneficial and physically correct that twinning dominates without heavy constraints from the slip rate, as pointed out in [114] for the Hadfield steel. If the kinematic hardening rule is used for the slip model, it may be beneficial to choose the slip dependent twin flow rule, because if the back-stress restricts the magnitude of slip, twinning can easily overtake the deformation. In both cases, Schmid type behavior is assumed.

The fitting parameter k_c is included to adjust the intensity of either of the flow rules to accomplish the same twinning rate as observed in the experiments. The saturation value F_{max} controls only the maximum total amount of the twin population, which is required to remove the possibility for 100 % twin volume content. However, no direct constraint is placed for an individual twin system at present. This could, however, be included with the term $(f_{max} - \sum_\beta f^\beta)(f^\beta_{max} - f^\beta)$, but defining a maximum for a single system alongside the total maximum value can be a difficult task to extract from the experiments. Furthermore, the activation and suppression of the twin systems is aimed to be controlled by the hardening rules described below.

HARDENING DUE TO TWIN-TWIN INTERACTIONS

The hardening restricting the twin initiation and growth composes of two terms:

$$r^{tw} = r^{tw \to tw} + r^{sl \to tw} \tag{7.29}$$

By this expression, twin-twin interaction and the accumulated slip (or dislocation densities) have a suppressing effect on the twinning rate. The phenomena described in this form include, i) hardening related to the growth of co-planar twins, ii) hardening effect from the interaction with non-coplanar twins, e.g., twin intersections, and iii) the blocking effect of non-coplanar twins restricting the growth and penetration of the growing twins. The changes in the twin stress, therefore, are controlled by many variables. However, the self-hardening, i.e., the probability of a twin to grow after the initiation by overcoming the initial twin resistance, is also included in the co-planar term for simplicity: the resistance

against growth increases with the increasing volume fraction of the twins because the Hadfield steel usually forms thin twin bundles packed with individual twins instead of wide twins.

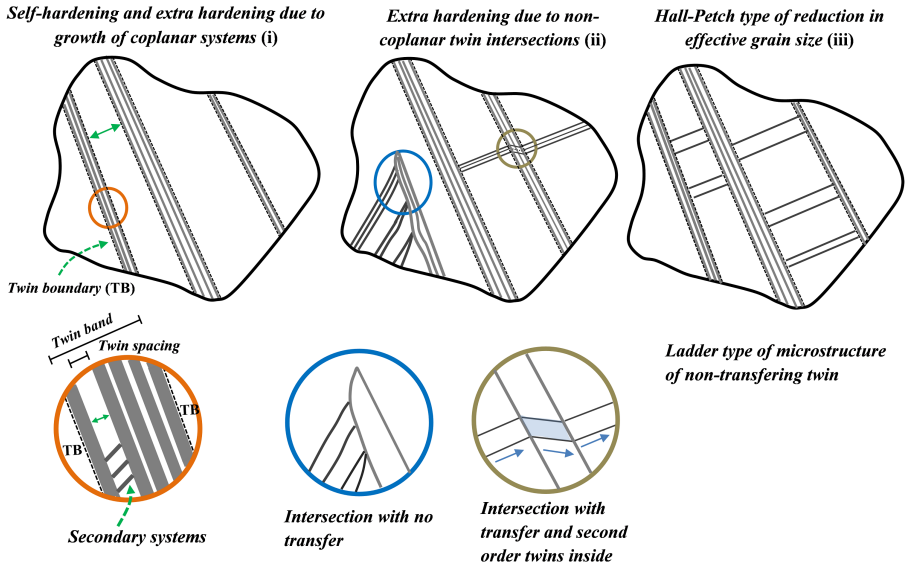

Figure 7.8: Schematic presentation of twin-twin interactions idealized from the experimental findings of this work and refs. [65, 159].

Based on the considerations above, the hardening rate due to the twin-twin interactions is divided into two parts following the expression proposed by Kalidindi [111]:

$$\dot{\tau}^{tw\to tw} = H_{nc}^{tw}\left(\sum f^{\beta}\right)^{b_t}\sum_{Non-coplanar}^{N_\beta}\gamma^{tw}\dot{f}^{\beta} + H_{cp}^{tw}\left(\sum f^{\beta}\right)^{g}\sum_{Co-planar}^{N_\beta}\gamma^{tw}\dot{f}^{\beta} \quad (7.30)$$

where H_{nc}^{tw} is the hardening coefficient characterizing the hardening due to the non-coplanar systems, H_{cp}^{tw} is the hardening coefficient of coplanar systems, and $\gamma^{tw}\dot{f}^{\beta}$ is the equivalent shear rate of a twin system. The first term on the right hand side then expresses hardening due to the creation of coplanar twins, and the second term represents hardening caused by the creation of coplanar twins. The distinction between the two terms is made to capture the evolution of the non-coplanar twins at the later stages of deformation. The exponent b_t can be chosen so that at the early stages of deformation the twinning takes place in co-planar systems, causing strong hardening to the non-planar twin systems. At higher strains it becomes more probable that the potential non-coplanar twin systems activate because the hardening effect is reduced. This ideology is schematically presented in Figure 7.9.

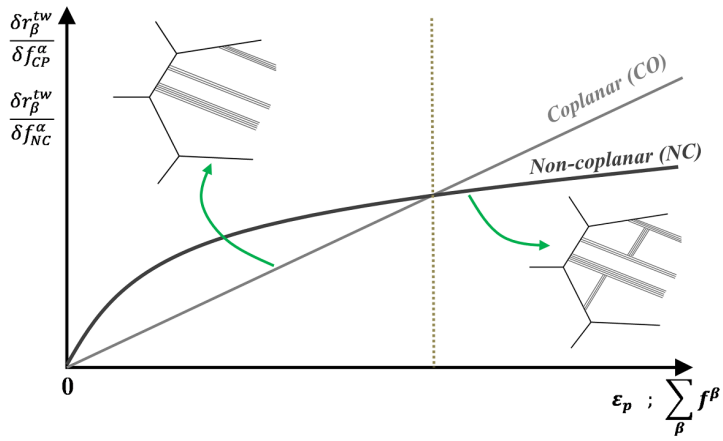

Figure 7.9: Hardening behavior due to twin-twin interactions as a function of increasing twin volume content (increasing with plastic strain) with a low exponent value for the non-coplanar hardening term and a linear behavior for the co-planar term, after ref. [191].

If the exponent b_t is chosen close to zero, it can be seen that the relative effect of the NC-term increases more slowly than its coplanar counterpart, when deformation or twin volume content increases. The form of the expressions is aimed to be rather simple, and more complex individual effects are not included separately, for example as seen in Fig. 7.8. An extension can be made by introducing exponent g to the coplanar hardening term. In the present work, the self-hardening and latent hardening with other coplanar twin systems is assumed to be the same, as noted above. It follows that it is quite likely that after the onset of twinning in a grain or in a material volume, the coplanar twins do not harden each other very strongly because of the low twin population. Hence, the hardening due to the coplanar term may be over-estimated with a linear expression only. Therefore a slight modification to the hardening rule is made by including the exponent g instead of the linear expression given by Kalidindi [111]. If the exponent g is chosen larger than 1, the hardening response is retarded towards higher twin volume contents, which may provide a better estimation of the hardening at low volume contents. Often, of course, the hardening caused by the coplanar twin-twin interactions is difficult to estimate from the experiments, and a simple form is adopted to describe the competition between co- and non-coplanar twins with appropriate fit of the hardening parameters.

HARDENING DUE TO SLIP-TWIN INTERACTIONS

The evolution of twin hardening due to their interaction with the slip systems is quite complex. The matrix itself hardens with the accumulation of slip, which was already treated in the slip-slip hardening rule. However, whether the accumulation of slip affects the twin initiation and growth remains an open question. Salem et al. [196] proposed a slip-twin interaction rule, where the accumulated plastic strain in the matrix leads to exponential hardening that inhibits twinning at large strains and provides saturation in a titanium alloy. It was observed in the experiments of this work that slip bands may have a pinning effect that restricts twin propagation. On the other hand, it was also observed that due to the reorientation of slip bands in the apparent grains, twinning may be initiated also inside these regions. To capture the former effect, the model uses the formulation of Salem et al. [196] for the rate of hardening, which is presented in

Equation 7.31. The latter effect is assumed to be included in the formulation through lattice reorientations, when significant amount of slip occurs in the crystal (i.e., slip softens the crystal by reorienting the slip plane and direction towards the tensile axis), and then possibly enables twinning in the reoriented regions.

$$\dot{r}^{sl\rightarrow tw} = H_{sl}^{tw}\left(\sum_s \nu^s\right)^d \sum_s \dot{\nu}^s \tag{7.31}$$

where H_{sl}^{tw} is the coefficient of hardening expressing the intensity of the term, and d is the exponent describing the form of the hardening with respect to the accumulated slip deformation $\sum_s \nu^s$ in the matrix . To avoid exaggeration of hardening, the rule can be chosen to increase hardening below certain values of $\sum_s \nu^s$, while beyond this limit the value remains constant.

7.3.3 Possible extensions to the model

The model could be extended to include more complex behavior if the experimental observations indicate that additional deformation mechanisms are required. For example, untwinning (or detwinning) could occur during deformation, but its origins cannot be identified from the presently available monotonic uniaxial data. Another important factor regarding untwinning is the polarized nature of twinning, i.e., the twins cannot be directly untwinned by the reversion of load. The second issue is what is the effect of accumulated slip in the matrix, i.e., immobile dislocations at the twin boundaries and their effect on the untwinning behavior. Similarly, complex twin structures including several interacting and possibly intercrossing twins are likely to have an effect on the probability of untwinning. Finally, considering that marked slip activity occurs inside the thick twinned regions, there is a question how strong resistance these slip concentrations would cause, e.g., already by crystal rotations. To summarize, too high uncertainty still exists related to this phenomenon, and hence untwinning is not included in the present modeling approach. One possibility for the untwinning scheme was presented by Wang et al. [217], but it seems that this concept is quite complex leading to reasoning that untwinning is disregarded in the majority of studies. Alternatively, it is possible to use reorientation schemes (see Figure 7.4), which reset the twin volume content to zero, promoting the possibility for further twinning in all of the twin systems, so that the untwinning scheme would not be required in the conventional sense.

Slip inside the twinned regions, on the other hand, is more straightforward to implement. Its downside, however, would be that a large number of slip systems is required to be tracked. The driving force for slip inside the twinned region is the stress computed in the twin orientation and not the one in the matrix, since the large deformation theory is used, i.e., $\tau^{twsl} = (\underline{\underline{C}}^e \cdot (\underline{\underline{\Lambda}}^\beta : \underline{\underline{E}}_{gl})) : \underline{\underline{N}}^{twsl}$. Here, the elastic stiffness, $\underline{\underline{\Lambda}}^\beta$, is rotated from the matrix by the rotation matrix related to the twin system β. It follows that there are 12 possible slip systems in each of the 12 twin systems possibly contributing to the deformation. It is highly plausible that some amount of slip activity or slip transfer crossing the twinned regions takes place, but for the current study it is assumed to be small compared to the slip in the matrix or to twinning. Therefore at the moment, slip inside twins was not included in the chosen modeling approach. Similarly, further twinning inside the twinned regions, i.e., second order twins, are not included in the model.

7.3.4 Summary of the FCC crystal plasticity model including twinning

Crystal plasticity framework for FCC including twinning

Plastic strain rate: $\underline{\dot{\epsilon}}^p = \underbrace{(1-\sum_{\beta=1}^{N_\beta} f^\beta)\sum_{s=1}^{N_s}\dot{\gamma}^s \underline{m}^s}_{slip\ in\ matrix} + \underbrace{\sum_{\beta=1}^{N_\beta}\gamma^{tw}\dot{f}^\beta \underline{m}^t}_{twinning}$

Dislocation slip terms:

Slip rate: $\dot{\gamma}^s = \left\langle \frac{|\tau^s| - r^s - \tau_y}{K} \right\rangle^n sign(\tau^s), \quad r^s = r^{sl\to sl} + r^{sl\to tw}$

Hardening of a slip system: $r^{sl\to sl} = Q\sum_r H_{rs}\{1-exp(-bv^r)\} = bQ\sum_r H_{rs}\rho^r$

Evolution of dislocation density : $\dot{\rho}^s = (1-b\rho^s)\Delta\nu^s$

Hardening by twins : $\dot{r}^{tw\to sl} = 0.5H^{tw\to s}(\sum_{\beta=Non-coplanar}^{N_\beta} f^\beta)^{-0.5}\dot{f}^\beta$

Twinning terms:

Twinning rate: $\dot{f}^\beta = k_c(f_{max} - \sum_\beta f^\beta)\left\langle \frac{|\tau^\beta| - r^{tw} - \tau_y^{tw}}{K_t} \right\rangle^{n_t} (\sum_s \dot{\nu^s}), \quad r_{tw} = r_{tw}^{tw} + r_{tw}^{sl}$

Hardening by other twins: $\dot{r}^{tw\to tw} = \gamma^{tw}\left(H_{nc}^{tw}\left(\sum f^\beta\right)^{b_t}\sum_{Non-coplanar}^{N_\beta}\dot{f}^\beta\right) + \gamma^{tw}\left(H_{cp}^{tw}\left(\sum f^\beta\right)^{g}\sum_{Coplanar}^{N_\beta}\dot{f}^\beta\right)$

Hardening to twinning by accumulated slip: $\dot{r}_{tw}^{sl} = H^{sltw}\left(\sum_s \nu^s\right)^d \sum_s \dot{\nu}^s$

7.4 Numerical implementation of the crystal plasticity models

The constitutive relations for the FCC-twinning model were presented in the preceeding parts of this section, and the Chapter 8 will discuss the contents of the BCC crystal plasticity models. Common for both models are the integration schemes introduced in the following. The integration methods have been implemented in the Zébulon/Zset code by Besson et al. [25, 26] and modified for large deformations, for example by Han [88]. The presentation here follows the ideas of the latter. Two integration methods, which are

implemented in Zébulon, will be used:

(I) Explicit integration: Runge-Kutta method of second order with adaptive time stepping

(II) Implicit integration: An implicit Newton-Raphson method with a local convergence loop

The integration is performed over all internal variables $\{v_{int}\}$ of the model. In the case of the FCC twin model, the equations of evolution were summarized in 7.3.4. Thus, the six internal variables introduced by this model are:

$$v_{int} = \{\underline{E}, (\nu^s, s = [1, N_s]), (\rho^s, s = [1, N_s]), (r^s_{sltw}, s = [1, N_s]), \\ (f^\beta, \beta = [1, N_\beta]), (r^\beta_{twtw}, \beta = [1, N_\beta])\} \quad (7.32)$$

The total number of components of the internal variables is dependent on the number of slip and twin systems, which is 12 in the present model for both mechanisms. Thus, taking this into account, the total number of variables becomes 81 (9 for $\underline{E}$, 12 for ν^s, 12 for ρ^s, 12 for r^s_{sltw}, 12 for f^β, 12 for r^β_{twtw}, and 12 for α^s).

The integration is performed so that at time t the internal variables v_{int} are integrated to provide the necessary values at $t + \Delta t$. In addition to the equations of evolution summarized in 7.3.4, the rate of elastic deformation $\underline{E}$ is needed, which can be derived from the multiplicative deformation gradient, i.e.,

$$\begin{aligned} &\underline{F} = \underline{E} \cdot \underline{P} \\ &\Rightarrow \dot{\underline{F}} = \dot{\underline{E}} \cdot \underline{P} + \underline{E} \cdot \dot{\underline{P}} \\ &\Rightarrow \dot{\underline{E}} = (\dot{F} - \underline{E} \cdot \dot{\underline{P}}) \cdot \underline{P}^{-1} \\ &\Rightarrow \dot{\underline{E}} = \dot{\underline{F}} \cdot \underline{F}^{-1} \cdot \underline{E} - \underline{E} \cdot \underline{L}^p \end{aligned} \quad (7.33)$$

where $\underline{L}^p$ is the plastic strain rate $\dot{\underline{\epsilon}}^p$as presented in the summary 7.3.4.

7.4.1 Explicit Runge-Kutta method for integration

The explicit integration provides an estimate of the next value $y_{t+\Delta t}$ by the sum of the current value y_t and the product of the step size Δt and the tangent (slope) of the function value. The generalized Runge-Kutta estimate may be written as

$$y_{t+\Delta t} = y_t + \Delta t \sum_{i=1}^{s} b_i k_i \quad (7.34)$$

where b_i and k_i depend on the order of the estimate.

In the current work the built-in Runge-Kutta routine in Zébulon was used, which is a second order estimate with automatic time stepping controlling the local accuracy and thus time-stepping. Then, the estimate for the next value $\{v^{t+\Delta t}_{int}\}$ is:

$$\{v\}_{int}(t+\Delta t) = \{v\}_{int}(t) + \{\dot{v}\}_{int}\Delta t + \{\ddot{v}\}_{int}(t)\frac{\Delta t^2}{2} + O(\Delta t^3) \tag{7.35}$$

With the use of Runge-Kutta, it is sufficient to provide only the rate of each variable. Therefore usually no complex partial derivatives with respect to the variables are needed, which makes the implementation more convenient. However, it is required to use a small time step to minimize the error of the solutions. Therefore a large number of time steps is needed when a certain period of time is investigated.

7.4.2 Implicit Newton method for integration

The implicit Newton integration is based on the θ-method, where θ is the integration weight, varying between $\{0, 1\}$. The most robust integration result is usually achieved with the value of 1 [237]. A local Newton-Raphson convergence loop is applied to evaluate the internal variables with respect to residuals. The present method is fully implicit, evaluating the variable values at the end of the increment $t+\Delta t$. A first order linearization of the system equations is performed, and the residuals are then written with respect to each variable:

The residuals of each internal variable (FCC twin model)

$$R_{\underline{E}} = \Delta\underline{E} - \Delta\underline{F}\cdot\underline{F}^{-1}\cdot\underline{E} + \underline{E}\cdot\left((1-\sum_{\beta=1}^{N_\beta} f^\beta)\sum\Delta\gamma^s\underline{m}^s + \sum\Delta f^\beta\gamma^{tw}\underline{m}^t\right)$$

$$R_{\nu^s} = \Delta\nu^s - \left(\frac{|\tau^s - x^s| - r^s - \tau_y}{K}\right)^n \Delta t$$

$$R_{\rho^s} = \Delta\rho^s - (1 - b\rho^s)\Delta\nu^s$$

$$R_{r^s_{twsl}} = \Delta r^{twsl} - 0.5H^{tw\to s}(\sum_{n=NC}^{N_{tw}} f^\beta)^{-0.5}\Delta f^\beta;\ iff\ f^\beta \in NC$$

$$R_{f^\beta} = \Delta f^\beta - K_c(f_{max} - \sum f^\beta)\left(\frac{|\tau^\beta| - r^{tw} - \tau_y^{tw}}{K_t}\right)^{n_t}\sum_s \Delta\nu^s$$

$$R_{r^\beta_{tw}} = \Delta r^{tw} - \gamma^{tw}\left[H^{tw}_{nc}\left(\sum f^\beta\right)^b \sum_{k=NC}\Delta f^k + H^{tw}_{co}\sum f^\beta\sum_{k=CO}\Delta f^k\right] + H^{sltw}\left(\sum_s \nu^s\right)^d\sum_s\Delta\nu^s$$

$$R_{\alpha^s} = \Delta\alpha^s - (sign(\tau^s - x^s) - d\alpha^s)\dot{\nu}^s$$

The linearized residual vector may be written for the n^{th} iteration of the Newton method as follows:

$$\{R\} = \{R\}(\{\Delta v_{int}\}) + \left[\frac{\partial R}{\partial\{\Delta v_{int}\}}\right]_n (\{v_{int}\}_{n+1} - \{v_{int}\}_n) = \{0\} \tag{7.36}$$

The updated variable values at time $t + \Delta t$ after convergence at the end of an increment are written as

$$\{v_{int}\}_{t+\Delta t} = \{v_{int}\}_t + \{\Delta v_{int}\}_{t+\Delta t} \tag{7.37}$$

The iteration procedure for the next time step $t + \Delta t$ and the update of the converged internal variables are presented for the FCC twin model below.

Newton-Raphson iteration loop to update the internal variables (FCC twinning model) for the next iteration

$$\begin{pmatrix} \Delta\underline{E}_{n+1} \\ \Delta\nu^s_{n+1} \\ \Delta\rho^s_{n+1} \\ \Delta r^{tw}_{n+1} \\ \Delta f^{\beta}_{n+1} \\ \Delta r^{tw}_{n+1} \\ \Delta\alpha^s_{n+1} \end{pmatrix} = \begin{pmatrix} \Delta\underline{E}_{n} \\ \Delta\nu^s_{n} \\ \Delta\rho^s_{n} \\ \Delta r^{twsl}_{n} \\ \Delta f^{\beta}_{n} \\ \Delta r^{tw}_{n} \\ \Delta\alpha^s_{n} \end{pmatrix} - \begin{bmatrix} \left[\frac{\partial R_{\underline{E}}}{\partial\Delta\underline{E}}\right] & \left[\frac{\partial R_{\underline{E}}}{\partial\Delta\nu^s}\right] & \left[\frac{\partial R_{\underline{E}}}{\partial\Delta\rho^s}\right] & \left[\frac{\partial R_{\underline{E}}}{\partial\Delta r^{twsl}}\right] & \left[\frac{\partial R_{\underline{E}}}{\partial\Delta f^{\beta}}\right] & \left[\frac{\partial R_{\underline{E}}}{\partial\Delta r^{tw}}\right] & \left[\frac{\partial R_{\underline{E}}}{\partial\Delta\alpha^s}\right] \\ \left[\frac{\partial R_{\nu^s}}{\partial\Delta\underline{E}}\right] & \left[\frac{\partial R_{\nu^s}}{\partial\Delta\nu^s}\right] & \left[\frac{\partial R_{\nu^s}}{\partial\Delta\rho^s}\right] & \left[\frac{\partial R_{\nu^s}}{\partial\Delta r^{twsl}}\right] & \left[\frac{\partial R_{\nu^s}}{\partial\Delta f^{\beta}}\right] & \left[\frac{\partial R_{\nu^s}}{\partial\Delta r^{tw}}\right] & \left[\frac{\partial R_{\nu^s}}{\partial\Delta\alpha^s}\right] \\ \left[\frac{\partial R_{\rho^s}}{\partial\Delta\underline{E}}\right] & \left[\frac{\partial R_{\rho^s}}{\partial\Delta\nu^s}\right] & \left[\frac{\partial R_{\rho^s}}{\partial\Delta\rho^s}\right] & \left[\frac{\partial R_{\rho^s}}{\partial\Delta r^{twsl}}\right] & \left[\frac{\partial R_{\rho^s}}{\partial\Delta f^{\beta}}\right] & \left[\frac{\partial R_{\rho^s}}{\partial\Delta r^{tw}}\right] & \left[\frac{\partial R_{\rho^s}}{\partial\Delta\alpha^s}\right] \\ \left[\frac{\partial R_{r^{twsl}}}{\partial\Delta\underline{E}}\right] & \left[\frac{\partial R_{r^{twsl}}}{\partial\Delta\nu^s}\right] & \left[\frac{\partial R_{r^{twsl}}}{\partial\Delta\rho^s}\right] & \left[\frac{\partial R_{r^{twsl}}}{\partial\Delta r^{twsl}}\right] & \left[\frac{\partial R_{r^{twsl}}}{\partial\Delta f^{\beta}}\right] & \left[\frac{\partial R_{r^{twsl}}}{\partial\Delta r^{tw}}\right] & \left[\frac{\partial R_{r^{twsl}}}{\partial\Delta\alpha^s}\right] \\ \left[\frac{\partial R_{f^{\beta}}}{\partial\Delta\underline{E}}\right] & \left[\frac{\partial R_{f^{\beta}}}{\partial\Delta\nu^s}\right] & \left[\frac{\partial R_{f^{\beta}}}{\partial\Delta\rho^s}\right] & \left[\frac{\partial R_{f^{\beta}}}{\partial\Delta r^{twsl}}\right] & \left[\frac{\partial R_{f^{\beta}}}{\partial\Delta f^{\beta}}\right] & \left[\frac{\partial R_{f^{\beta}}}{\partial\Delta r^{tw}}\right] & \left[\frac{\partial R_{f^{\beta}}}{\partial\Delta\alpha^s}\right] \\ \left[\frac{\partial R_{r^{tw}}}{\partial\Delta\underline{E}}\right] & \left[\frac{\partial R_{r^{tw}}}{\partial\Delta\nu^s}\right] & \left[\frac{\partial R_{r^{tw}}}{\partial\Delta\rho^s}\right] & \left[\frac{\partial R^{tw}_{r}}{\partial\Delta r^{twsl}}\right] & \left[\frac{\partial R_{r^{tw}}}{\partial\Delta f^{\beta}}\right] & \left[\frac{\partial R_{r^{tw}}}{\partial\Delta r^{tw}}\right] & \left[\frac{\partial R_{r^{tw}}}{\partial\Delta\alpha^s}\right] \\ \left[\frac{\partial R_{\alpha^s}}{\partial\Delta\underline{E}}\right] & \left[\frac{\partial R_{\alpha^s}}{\partial\Delta\nu^s}\right] & \left[\frac{\partial R_{\alpha^s}}{\partial\Delta\rho^s}\right] & \left[\frac{\partial R_{\alpha^s}}{\partial\Delta r^{twsl}}\right] & \left[\frac{\partial R_{\alpha^s}}{\partial\Delta f^{\beta}}\right] & \left[\frac{\partial R_{\alpha^s}}{\partial\Delta r^{tw}}\right] & \left[\frac{\partial R_{\alpha^s}}{\partial\Delta\alpha^s}\right] \end{bmatrix}^{-1} \begin{pmatrix} R_{\underline{E}} \\ R_{\nu^s} \\ R_{\rho^s} \\ R_{r^{twsl}} \\ R_{f^{\beta}} \\ R_{r^{tw}} \\ R_{\alpha^s} \end{pmatrix}$$

Updated internal varibles after n^{th} iteration with convergence

$$\begin{aligned} \underline{E}_{t+\Delta t} &= \underline{E}_t + \Delta\underline{E}_{t+\Delta t} \\ \nu^s_{t+\Delta t} &= \nu^s_t + \Delta\nu^s_{t+\Delta t} \\ \rho^s_{t+\Delta t} &= \rho^s_t + \Delta\rho^s_{t+\Delta t} \\ r^{twsl}_{t+\Delta t} &= r^{twsl}_t + \Delta r^{twsl}_{t+\Delta t} \\ f^{\beta}_{t+\Delta t} &= f^{\beta}_t + \Delta f^{\beta}_{t+\Delta t} \\ r^{tw}_{t+\Delta t} &= r^{tw}_t + \Delta r^{tw}_{t+\Delta t} \\ \alpha^s_{t+\Delta t} &= \alpha^s_t + \Delta\alpha^s_{t+\Delta t} \end{aligned}$$

The Jacobian matrix, where the partial derivatives with respect to each internal variable v_{int} are introduced at every time step, is a non-symmetric 81x81 matrix (6561 individual elements). The partial derivatives are derived in Appendix A for the FCC twin model. The integration algorithms and the development of the updated Lagrangian scheme for the large deformations in Zébulon are presented for example in ref. [88], which are utilized also in this work. If the implicit method does not converge, the integration is performed with the explicit method over that particular increment and then switched back to the original scheme.

7.5 Effect of model parameters

A large number of model parameters allows the description of complex material behavior in various conditions. However, the challenge in the use of a wide variety of more or less interconnected parameters is the validation of the correct response of the model when a parameter is altered. From the physical point of view this means that the effect of any of the parameters should be verifiable by experimentally observed behavior, as explained in the previous section. This requirement set boundary conditions to the parameters limits, which should lie within reasonable limits whenever such can be defined. In addition, since the model accounts for both slip and twinning, altering some of the parameters can lead to unexpected behavior. For example, suppressing slip rate may lead to increased twinning rate, or vice versa. This section demonstrates some of the effects of the most important model parameters to elucidate the model behavior with different sets of parameters. Simplified tension and compression tests (monotonic and cyclic) are performed on single crystals with a single element under loading, as presented in Figure 7.10.

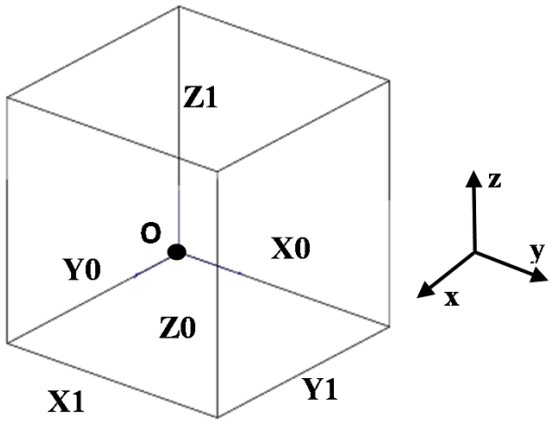

Figure 7.10: A single finite element used to study the effects of model parameters, showing the constraint planes for boundary conditions.

The initial model parameters, which act as a starting point in the following simulations, are listed in Table 7.4. The changes done in the the parameter values will be indicated in the figures, while the other parameters remain constant during the simulations. The interaction matrix for slip has been adapted from the results presented in Section 7.6. Other parameters are not connected to any particular material, but they only serve as example values for twinning or slip-only models. Their values were chosen to have only a moderate or small effect in the basic simulations to highlight the effect of the

Table 7.4: The parameters for an artificial model material

Anisotropic cubic elasticity	C_{11}		C_{12}		C_{44}		
	174 000		85 000		99 000		
Slip parameters	τ^{s0}	K	n	b	Q		
	92.0	80.0	8.0	2.35	140.0		
Interaction matrix coeff.	h_0	h_1	h_2	h_3	h_4	h_5	
	0.12	0.10	1.60	1.85	0.36	1.20	
Kinematic hardening	C	D					
	0.0	0.0					
Twin parameters	τ^{tw0}	Ks	ns	H_{sltw}	Htw_{NC}	Htw_{CO}	H_{twsl}
Kc = 0.08	95.0	95.0	10.0	130(50)	300(100)	800(160)	320
Hardening exponents				$p = 0.5$	$bt = 0.1$		$d = 0.7$
Units:	$\tau^s[MPa]$		$K[MPa.s^{1/n}]$		$Q[MPa]$		
	C [MPa]		D [MPa]		All H*[MPa]		

parameter under investigation. All simulations were performed with a constant strain rate of $10^{-4}s^{-1}$, except for the cases where strain rate is the variable. Two twin flow rules were demonstrated: the independent flow rule presented in Equation 7.27 and the dependent flow rule presented in Equation 7.28. The main difference between the rules is that the dependent model is always driven by the sum of slip rates, whereas the independent rule does not have this direct connection. The orientations of the single crystals were chosen for the simulation by their high tendency towards twinning to demonstrate the differences.

7.5.1 Effect of twinning

Figure 7.11 presents the stress-strain behavior for three orientations and the corresponding evolution of the twin volume fractions. In all cases, the stress response becomes softer after the initiation of twinning because of the additional deformation mechanism provided by the twin shear. The simulations showed that depending on the intensity of the slip hardening parameters b and Q, the softening effect can be more pronounced. On the other hand, if the hardening parameters related to twinning have high values, it leads to more complex behavior, i.e., twinning can easily provide strong hardening by the interaction with slip or other twin systems, and the twinning rate may be decreased.

The simulations shown in Figure 7.11 were run with the independent twin flow rule. The dependent flow rule did not provide a significantly different response, only changes in the twin volume contents were observed, leading to slightly different stress-strain curvature. However, another distinctive characteristic of the competition between slip and twinning is that when twinning saturates, the hardening increases notably. This occurs because the effective twin volume content already causes strong barriers according to the slip-twin hardening rule, and since the nominal shear contribution from slip is relatively low and no further twinning is allowed, the slip is required to govern the plastic strain causing an increase in the instantaneous strength. After further straining, saturation of slip activity can also take place, as is already visible in the $[\bar{1}11]$ orientation. In contrast, the [110] orientation shows marked hardening long after twin saturation. The twin effect on the slip activity becomes further more complex to investigate, as the twin activity affects the activity of slip systems by the hardening rule of non-coplanarity, i.e., if only slip is active, certain slip systems can dominate and contribute more to the deformation and hardening,

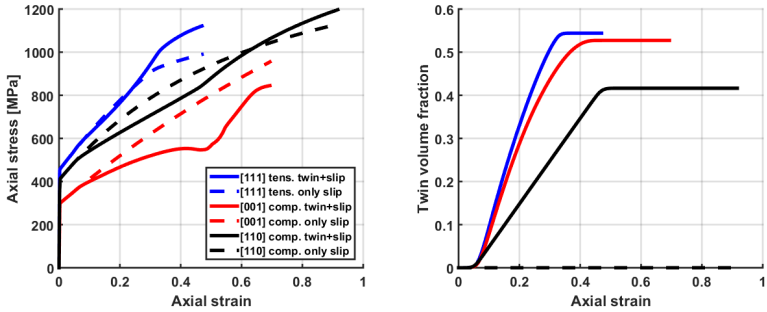

Figure 7.11: a) The effect of twinning as a concurrent deformation mechanism with dislocation slip to the stress-strain behavior of three orientations, and b) their corresponding evolutions of twin volume fractions.

while when twinning is active, the slip activity and its contribution can be drastically altered through hardening interactions. Hence, it appears that the curves with slip only and slip+twinning will likely never reach the same values as some slip systems remain suppressed and their slip activity history is different. For example, hardening of the cube orientation [001] increases the stress to a notable level, but it saturates before reaching the values observed in the slip-only simulations.

7.5.2 Effect of slip hardening parameters

Figure 7.12 shows the effect of the slip hardening parameter b characterizing the slip saturation for both twin flow rules in the $[\bar{1}11]$ orientation with twinning+slip or slip only. The increasing value of b causes a notable increase in the twinning rate because of the effective increase in the slip hardening. On the other hand, this is also clear if only slip is active. The hardening curve becomes steeper and steeper and the saturation is met at lower strains (or accumulated slip values). The difference between the two flow rules is notable in the current simulations. The dependent flow rule leads to lower twinning rates as the slip activity controls its magnitude to some extent. Also, significant twinning occurs at higher strains because of the suppressing effect of slip activity. Hence, in order to adjust the dependent flow rule results to a set of experimental data, it may be beneficial to adjust the twinning rate with the intensity coefficient K_c, which in the current simulations it was kept constant for both flow rules, partly also explaining the flow difference.

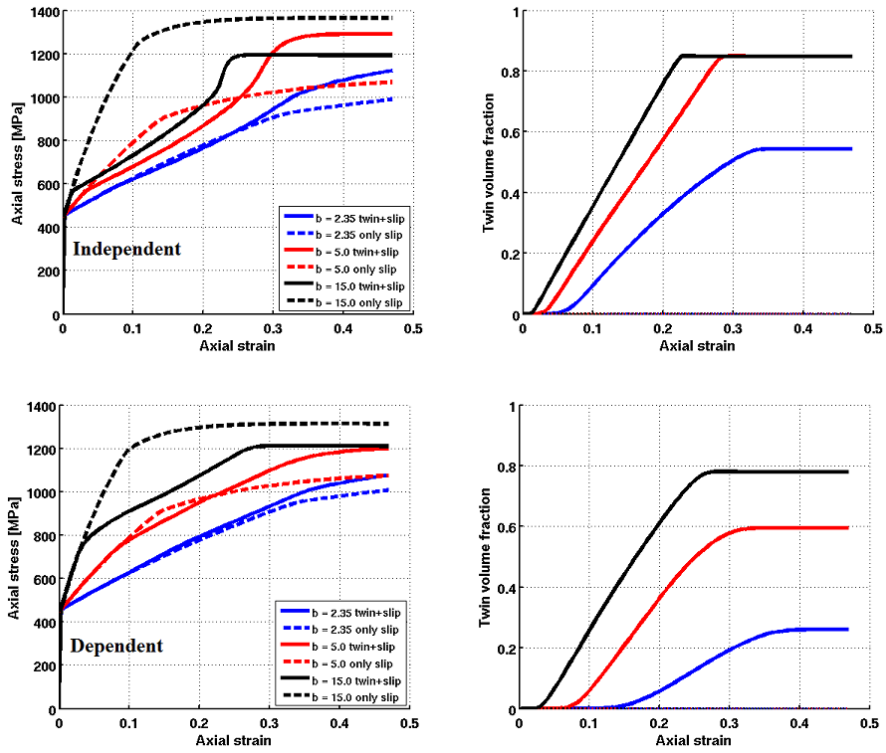

Figure 7.12: Effect of the slip saturation parameter b on the stress-strain and twinning behavior of $[\bar{1}11]$ orientation using both twin flow models.

The hardening coefficient Q describing the magnitude of slip hardening has a multifunctional effect:

- Coefficient Q characterizes the slope of the slip hardening, i.e., when b is small, Q increases the magnitude of hardening. After the twin saturation, the slip hardening has a marked effect on the stress-strain response.
- The value of Q affects the interaction of slip systems depending on the interaction matrix. Usually the slip systems are controlled by either suppressing or favoring their effect by the interaction matrix, e.g., collinear slip systems are made to cause highest hardening. However, in some cases it appeared in the simulations that if Q has a high value, it may suppress the collinear interactions (or others) and does not cause such high hardening that would be expected. Additionally, it could lead to early saturation because of the high contribution of some slip systems to the deformation and their effective saturation, while at the same time these systems cause strong hardening in the other systems prohibiting their activity.
- The effect of parameter Q on twinning is twofold. If Q has very high values, it leads to rather high twinning rates because slip is effectively reduced or partly suppressed by the hardening rule. In contrast, if Q is chosen small, the twinning rate can remain at very low values because the slip activity dominates with quite low glide resistance. The result was the same for both flow rules. However, when Q is high,

the dependent flow rule produced some direct effective hardening by reduced slip activity due to its relationship to slip rates.

As a conclusion, both of the parameters b and Q are sensitive to each other and both have a direct effect on twinning. Hence, to obtain good agreement with experimental results, balance between these parameters and their relationship to twinning and its saturation are essential to be defined.

7.5.3 Effects of twin-slip, twin-twin, and slip-twin interactions

Figure 7.13 shows the effect of the twin-slip hardening parameter H_{sltw} at three different values for both twin flow rules. In this particular case, the parameter describes the hardening caused by the twin barriers to slip through a Hall-Petch relationship. Hence a high value denotes a low probability for the slip to penetrate the twins, while a low value allows high dislocation mobility.

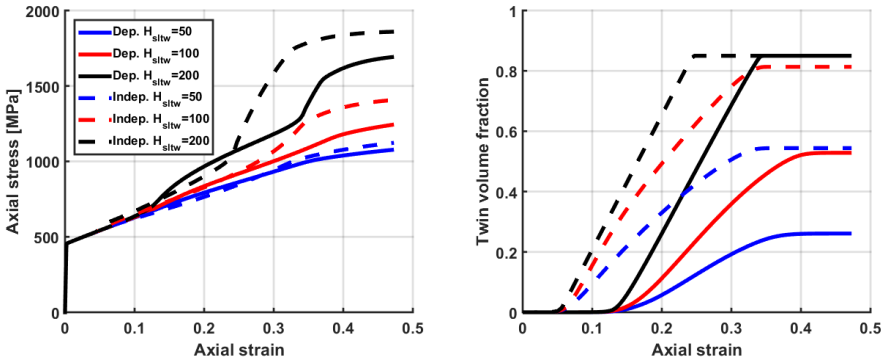

Figure 7.13: Effect of twin-slip interaction hardening on the stress-strain and twinning behavior of $[\bar{1}11]$ orientation using both twin flow models.

The results show very similar behavior as for the slip hardening parameter Q, but from the opposite point of view. If high hardening takes place due to a high value of the twin-slip hardening parameter, the slip activity is reduced and the twinning rate is high. In contrast, the low value of the parameter may cause favoring of slip activity leading to a decreased twinning rate. A moderate hardening value, 100 MPa in this case, shows the most stable response with a relatively low increase in the strength after twin saturation. A strong increase in the strain hardening is evident with the high value of the parameter, which could of course in reality take place as a prematurely developed twin texture. In such a situation, as the simulations show, high stress concentrations are generated because of the strong obstacle-like behavior of the twin-slip interfaces, which may initiate failure. The main difference between the flow rules is that twinning in the dependent model again shows low activity at low strains, which allows reasonable amount of slip activity. Therefore, the strain hardening increase after the twin saturation is more modest, at least with the present parameter set.

7.5.4 Effect of strain rate

The rate-dependence of the model is presented in 7.14 for three constant strain rates and the corresponding evolution of twin fractions. The choice of viscous parameters affects

the weight of the deformation mechanisms. In the current example, viscous parameters for twinning are chosen quite insensitive to strain rate, at least when compared to slip. As a consequence, when the strain rate increases, the viscous effect is stronger in slip and the twinning rate increases. Ideally this choice in the phenomenological framework could be understood to be related to the decreased success of dislocations to overcome obstacles in a shorter time, whereas twinning is less affected by time due to its short range movement of atoms. Another distinctive characteristic is that it decreases the macroscopic yield point because twinning becomes immediately active in the microyield-region after the multiple slip constraint is satisfied, providing an alternative deformation mechanism to slip. Since there are no rate dependent hardening rules involved, e.g., describing the time-dependent success rate for the dislocations to pass twin boundaries, it means that the twinning rate remains strong at high strain rates until saturation. After twin saturation strengthening is again observed, when the slip mechanism governs the deformation. Varying of the viscous parameters can have a very significant effect on twinning. For example, if the viscous exponent is small for twinning while keeping the viscous nominator equal to the critical resolved shear stress of a system, negative strain rate sensitivity may be observed for twinning.

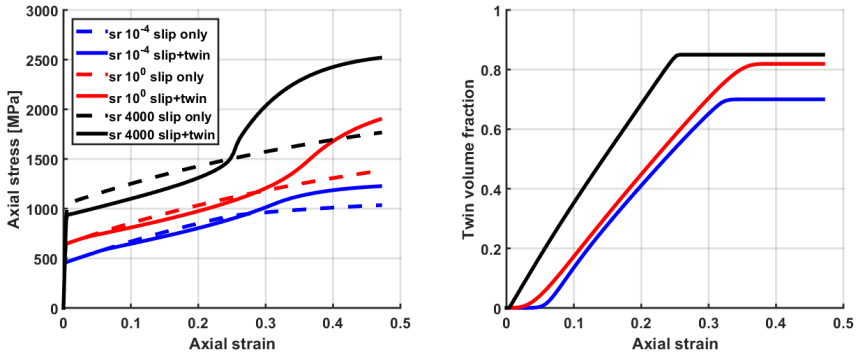

Figure 7.14: Effect of strain rate on the stress-strain and twinning behavior of $[\bar{1}11]$ orientation in the twin+slip and slip only cases.

The viscoplastic nature of twinning and slip with different material parameters leads to strain rate history dependent behavior. This phenomenon occurs because of the twin rate sensitivity, either positive or negative, with nominal strain rate. In the present model, many of the hardening parameters are dependent on the twin volume content, and hence a different path in the twin volume fraction evolution leads to different instantaneous hardening values. Figure 7.15 illustrates two strain rate jump tests, from a low strain rate to a high strain rate and vice versa, for the independent flow model (results were also very similar for the other model). The stress-strain response and the twin volume fraction evolution are presented for both loading histories alongside the stress-strain curves and twin fraction evolutions in the constant strain rate tests shown with the black curves.

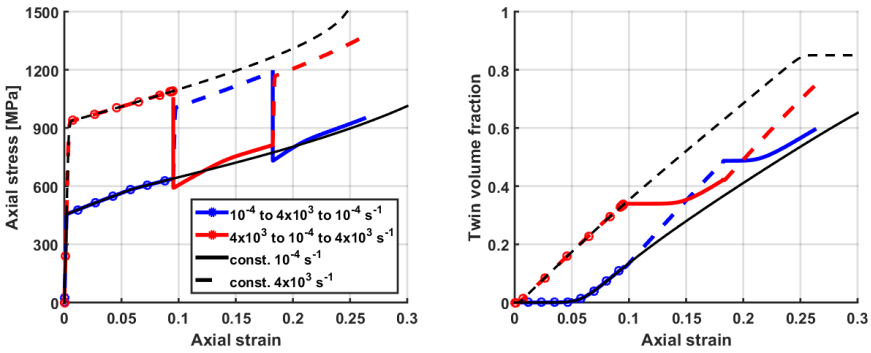

Figure 7.15: Effect of strain rate history on the stress-strain and twinning behavior of $[\bar{1}11]$ orientation. Black lines represent constant strain rate cases, while the colored lines represent the jump tests.

In many cases the stress response becomes more strain rate history independent if only slip is considered. However, the response is notably altered when twinning is included because of two major reasons, *suppressed twinning* and *history dependent twinning rate*. The suppressed twinning occurs when the strain rate is lowered back to the low rate in both simulated cases, i.e., the current critical stress for twinning is higher than the resolved stress value for twinning at the lower strain rate. As a consequence, a plateau in the twin volume content is observed. Slip dominates the deformation during this stage because of the high hardening that took place in the twin systems during the deformation at the high strain rate, when the flow stress was higher and favored twinning over slip. The strain hardening is now stronger, but is reduced when the twinning reactivates. The second aspect is that the twinning rate is not the same as in the constant strain rate cases, making the twinning rate history dependent especially at high strain rates. This is seen around especially at around 20 % of strain. In fact, the twinning rate always increased when the strain rate was increased with the current set of parameters. Generally, strain rate the jump from high to low and back shows a lower flow stress at the end of the simulation mainly because of the lower twin volume content. In contrast, the flow stress is higher at the end of the simulation in the other strain rate jump test, which can be attributed to the higher twin volume content.

7.5.5 Effect of kinematic hardening

Figure 7.16 presents the results of low strain cyclic loading for three different model parameter sets with the independent twin flow model. Two orientations were considered because of the slight difference in their behavior, but both orientations show tensile-compression asymmetry because of the biased twinning. If a notable Bauschinger effect exists, it cannot be captured easily with the models excluding kinematic hardening. Intuitively, the only possibility to expect such behavior would be that either the twinning rate increases drastically or crystal rotations cause a decrease in the flow stress when loading is reversed. Apart from these two special situations, the hardening rather increases with every cycle, which is more common for models without any back-stress. Hence, it could be more useful to include the kinematic hardening term in the model if sufficient experimental data is available. Figure 7.16 also demonstrates the effect of back-stress for slip-only and slip+twinning models.

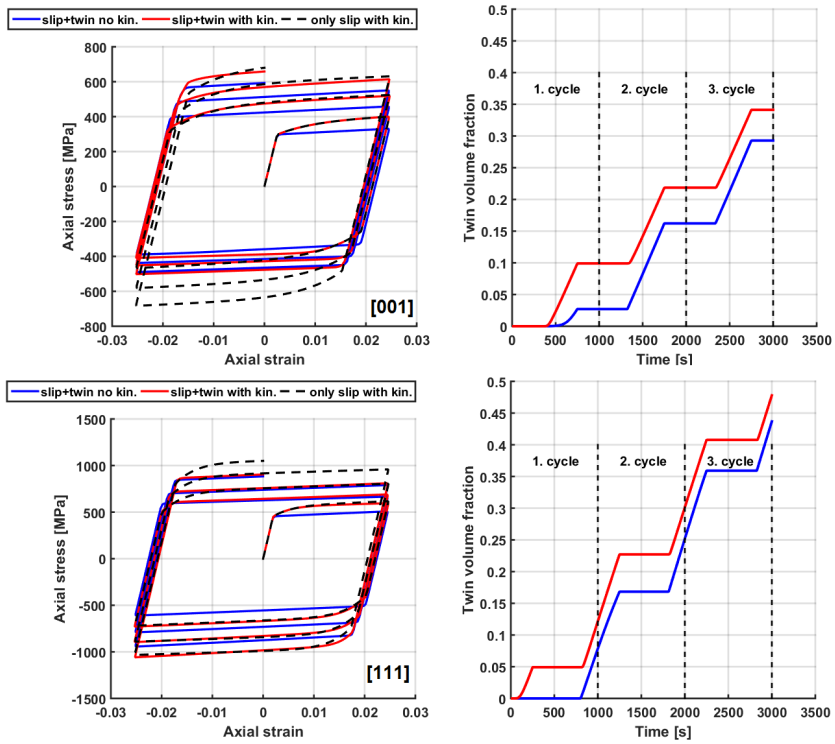

Figure 7.16: Effect of the kinematic hardening term on the cyclic stress-strain response and twinning behavior in two orientations using the independent model. The kinematic parameters for the slip flow rule were D =15000 MPa and C=500 MPa.

The Bauschinger effect is observed regardless of twinning being active or not, appearing as decreased flow stress when the loading is reversed from tension to compression. The current values for the kinematic parameters are quite strong because if the twin volume fraction is increased during the first loading sequence, it would generally cause hardening. However, it does not suppress the back-stress effect in the present simulations. In both orientations it appears that kinematic hardening causes accelerated twinning, which is expected by this model since it only affects slip flow directly. This effect is most clear in the $[\bar{1}11]$ orientation, where the twin volume fraction begins to increase already at quite small strains (or earlier in time) compared to the case where kinematic hardening is set to zero. The premature twinning, if it is undesired, can be reduced to some extent by using the dependent twin flow rule, but it did not completely disappear in the simulations performed with that model, either. Additionally, care should be exercised when identifying the kinematic parameters in materials that exhibit twinning because of the asymmetry of twinning, which can generate a non-symmetric stress response when reversing the loading. This is evidently seen in the [001] curves, where twinning is mainly active only in compression, or in the $[\bar{1}11]$ curves, where twinning occurs mainly in tension. Hence, it is possible that the initiating twinning can hinder the effect of the back-stress on slip.

7.6 Modeling of single crystal behavior

The model functionality is demonstrated and evaluated in this section based on the existing experimental single crystal results for a conventional Hadfield steel (12.34 Mn, 1.03 C). An experimental study on the uniaxial deformation of Hadfield steel single crystals was performed by Karaman et al. [114]. The study included detailed characterization revealing the prevailing deformation and hardening mechanisms. The use of the experimental single crystal results is a bit more controlled way to establish model parameters and to evaluate the model performance than the direct fitting of model parameters to polycrystal results. For example, the role of twinning is difficult to ascertain only from polycrystal computations, as the boundary conditions of complex microstructures may pose both hindering and promoting effects on the initiation and growth of twins, and their origin may remain unrevealed.

The simulations cover uniaxial tension and compression tests of [001], [$\bar{1}$11] and [$\bar{1}$23] oriented single crystals deformed to large strains and compared with the experimental results. The motivation to choose these orientations was to bias the deformation either towards dislocation slip or twinning [114]. Table 7.5 list the Schmid factors for slip and twinning, as well as the number of systems with equal Schmid factors for the chosen orientations. The Schmid factors of the leading and trailing Shockley partials are also given, as the intrinsic stacking faults play a definite role in twinning [114]. All simulations were performed at a constant strain rate of $10^{-4}s^{-1}$. An implicit form of the model (Theta-method integration scheme in Zébulon) was used in all cases, with a residual convergence criterion of 10^{-9}, maximum of 250 local iterations, and a θ value of 1.

Table 7.5: Maximum Schmid factors for slip and twinning and for the leading and trailing Shockley partials. The number of systems having equivalent Schmid factors are indicated with "sys". Table values are taken from ref. [114]

Axis	Tension Schmid factors				Compression Schmid factors			
	Slip	Twin	Partials		Slip	Twin	Partials	
[001]	0.41	0.23	trail	lead	0.41	0.47	trail	lead
	8 Sys.	8 Sys.	0.47	0.23	8 Sys.	4 Sys.	0.23	0.47
[$\bar{1}$11]	0.28	0.31	trail	lead	0.28	0.16	trail	lead
	6 Sys.	3 Sys.	0.16	0.31	6 Sys.	6 Sys.	0.31	0.16
[$\bar{1}$23]	0.46	0.47	trail	lead	0.46	0.34	trail	lead
	1 Sys.	1 Sys.	0.34	0.47	1 Sys.	1 Sys.	0.47	0.34

The simulations were performed with the same single element aggregate as in the previous section. The boundary conditions were also the same with MPC constraints, excluding the [$\bar{1}$23] single slip orientation, which was constrained from the origo with (U1=0, U2=0) and from a second corner with (U2=0) to avoid rigid body rotation. The loading was applied similarly on Z1 while Z0 was set constrained. All experiments and simulations were performed at room temperature. Both flow rules for twinning (Equations 7.28 and 7.27) were evaluated, but the result were almost identical for both cases with no notable difference. However, the parameters controlling the twinning magnitude were obviously different. The results presented below are based on the indirectly dependent flow rule of Equation 7.27. This choice was made for further use with polycrystals, as it was noted to give slightly faster convergence with the present integration schemes. However, it is required in the model that dislocation slip precedes twinning, i.e., twins may begin to grow only after multiple slip systems have activated. Figure 7.17 presents the initial and deformed states of the single crystal simulations. The boundary conditions generally are more restrictive for the multiple slip and twinning conditions, while in the single slip cases they allow more freedom in the deformed state.

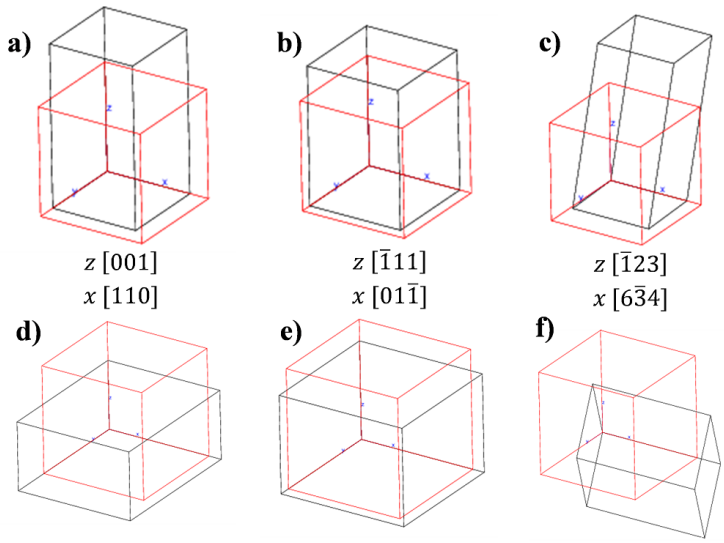

Figure 7.17: Deformed single crystal orientations after uniaxial loading in tension (a-c), and in compression (d-f).

7.6.1 General aspects and results of single crystal simulations

The number of active slip systems varied between one and eight, as expected for the FCC crystal structure. The actual number of the active systems is governed mainly by i) physical factors (e.g., defect population or prior hardening, orientation, etc.), ii) the choices in the constitutive model (e.g., interaction matrix), and iii) numerical factors (e.g., bifurcation). In a physical sense the activation of slip and twin systems is dependent on the local conditions, such as concentrations of solutes and existing stacking faults, which usually vary in the microstructure. For this reason, it is for example possible that the critical resolved shear stress required to activate the slip systems is not isotropic because of the existing dislocation density. For the modeling purposes it is, however, convenient to assume equal critical resolved shear stress for the activation in all systems, and hence

there may exist some differences between the experiments and simulations. Similarly, as the model uses simplified relations of the physical phenomena, it is obvious that the actual behavior may not be fully captured.

The current model assumes that also twinning is activated at the computed resolved shear stress of the twin system, which may cause some variations to the experimental observations. For example, if all twin systems have an equal triggering initial critical resolved shear stress value, many systems can activate simultaneously when the critical stress value is reached. Again, in reality it may be that some systems have a slightly lower critical resolved shear stress than the others because of existing defects or just because the probabilities may be favorable. This may trigger one system before the other systems with equal Schmid factors. At the same time, the model already accounts for the hardening from the active twin system to the other systems. Hence it may follow that the initially triggered system dominates the deformation, partly or completely suppressing the other systems in contrast to the theoretical case, or vice versa, that no single system is dominant because of the more or less isotropic hardening. Finally, when a large number of slip or twin systems are active, numerical instabilities can arise from the bifurcation phenomenon. For example, Han [88] identified two main reasons causing bifurcation behavior when using the same numerical basis as utilized in the current work: i) the anisotropy in the interaction matrix, and ii) the viscoplastic parameters of the model. Increasing viscosity or reducing anisotropy in the interaction matrix can reduce the bifurcation phenomenon. Similarly, the fairly complex twinning hardening parameters and the viscoplastic flow rule of twinning may also lead to the same bifurcation phenomenon. It was noted also by Han[88] that explicit schemes are more prone to this behavior than the implicit ones. A more detailed discussion of this phenomenon related to slip, kink and shear band formation in single crystals is provided by Forest [71], also pointing out that the classical crystal plasticity lacks some of the features of generalized crystal plasticity features.

Figures 7.18a and b present both experimental and simulation results of the stress-strain response of the studied orientations in tension and compression. The stress-strain behavior of the Hadfield steel is evidently dependent on the orientation of the single crystal, i.e., the loading direction. For example, the $[\bar{1}11]$ orientation shows first quite limited strain hardening, but this orientation exhibits a notable increase already around 0.2 of plastic strain in both tension and compression, but essentially for different reasons. In tension, the deformation is dominated by twinning and regulated by its self and latent hardening, while the interaction with slip is more limited. The deformation in compression is dominated only by the multiple slip systems, and twinning is completely suppressed. The upward strain hardening curvature in compression is somewhat unexpected, when twinning is not observed. This points to the activation of a localized deformation process at the beginning of the curve, softening the response. In contrast, the nominally linear hardening response of [001] in tension is produced by slip-slip interactions only, while its counterpart in compression again is dominated by twinning, causing a notably softer response. The experimental results on the $[\bar{1}23]$ orientation in both loading directions show fairly low strain hardening at the initial stage, which is expected from a single active slip system. The hardening at the later stages of deformation indicates also activation of the secondary systems.

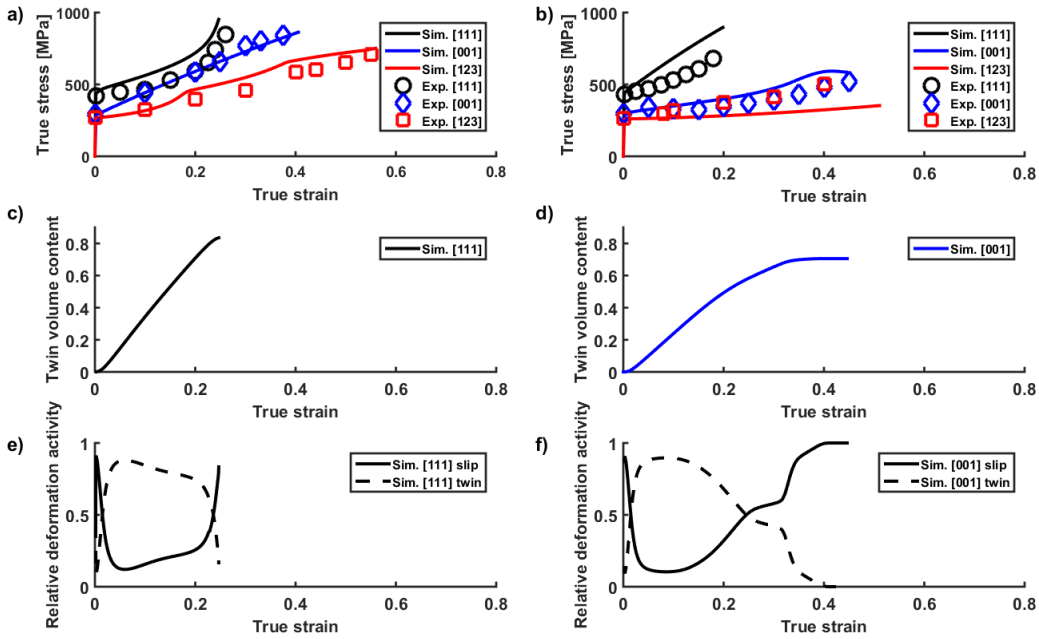

Figure 7.18: Simulated and experimental stress-strain curves of Hadfield single crystals a) in tension, b) and compression, c) twin volume content of $[\bar{1}11]$ orientation in tension, d) and [001] orientation in compression, e) relative shear contributions of $[\bar{1}11]$ in tension, f) and [001] in compression. The experimental values were taken from ref. [114], and the strain rate was a constant $10^{-4}s^{-1}$.

Figure 7.18 shows the twin volume fraction evolutions (c,d) and the instantaneous[1] relative contribution of slip and twinning to the shear deformation (e,f) for both loading directions. As pointed out above, the twin volume fraction remains essentially zero (below 0.1 %) in other cases than $[\bar{1}11]$ and [001]. The relative shear contribution, however, differs in these two twinning dominated orientations a little. The $[\bar{1}11]$ orientation in tension shows first almost fully twin dominated deformation, but its contribution reduces already below 0.1 of plastic strain. At the twin saturation, slip becomes almost a sole deformation mechanism, which is consistent with the experimental observations. In contrast, the twin dominance in the [001] orientation extends to larger strains, and its decrease is more gradual, indicating deactivation of some of the twin systems during the deformation.

7.6.2 Aspects of parameter identification

The parameter identification was performed manually without any homogenization algorithms. This is also the main reason for using only one element in the identification process, i.e., to achieve a reasonable computational time despite the large number of iterations needed. The values identified from the single crystal results are used as initial

[1]Instantaneous contribution to shear is defined by the contribution of incremental rates as: $\Delta\epsilon^p_{sl}/\Delta\epsilon^p$ and $\Delta\epsilon^p_{tw}/\Delta\epsilon^p$, where $\Delta\epsilon^p$ is the incremental total plastic strain rate. This expression is more sensitive to changes in shear mechanism rather than the accumulated values of shear contributions that are sometimes used, i.e., $\int_0^t \dot{\epsilon}^p_{sl} / \int_0^t \dot{\epsilon}^p$. For example, accumulated values can easily hinder the activation or deactivation of twin systems as there are no drastic changes in the contribution.

values for the finalization of the parameter identification with the polycrystal aggregates, which are presented in the next section in Table 7.6. The main objective of the use of single crystal results is to adjust the interaction matrix of slip and other parameters so that the deformation behavior would resemble that observed in the experiments, i.e., not only by the apparent shape of the stress-strain curve but also considering the physical features of slip and twinning controlled deformation.

The initial critical resolved shear stress threshold was identified using only slip as an active deformation mechanism, since it is assumed that twinning is activated slightly delayed. In all cases the fits were very reasonable. The initial critical twinning stress was selected only slightly higher, since the twins were observed to activate early in some orientations, but its value falls quite close to the twin stress values suggested by Karaman et al. [114]. The exact fit for the critical twinning stress is more difficult to obtain than for slip because there is no information available on the evolution of the twin volume content, which could be utilized to verify the initiation of twinning and also the correct twinning rate evolution, including saturation. The identification of the viscous parameters (K,n) is not straightforward for strain rate sensitive metals. The experimental results on the strain rate dependence reported in the literature are somewhat uncertain for the conventional Hadfield grades, partly due to the slightly varying compositions. Depending on the strain rate range, both *negative* (NSRS) and *positive* strain rate sensitivity (PSRS) observations exist, as discussed in Section 4.1.1. For many Hadfield grades, the dynamic strain aging phenomenon tends to cause negative strain rate sensitivity at very low strain rates, while above the strain rate of $1s^{-1}$, positive strain rate dependence is normally observed. The present flow models are aimed to reproduce only positive strain rate sensitivity that was observed in the experiments of this work. This is justified also because many TWIP steels experience positive strain rate sensitivity, widening the possible use of the current model also to other steel grades. The magnitude of the increase of flow stress with increasing strain rate was considered to depend on the strain rate range, being small at low strain rates but notable towards the $10^3 s^{-1}$ range. This is a compromise on one hand to respect the very limited positive effect observed by Canadinc et al. [40] for the strain rate of $1s^{-1}$, and on the other hand to reproduce the stronger increase at dynamic strain rates reported by Lee and Chen [122], which still was smaller than the behavior observed for the alloyed Hadfield steel in this work.

The viscous parameters related to twinning are even more complex to identify from a limited amount of available experimental results. No information is usually provided of the twinning rate at different strain rates, i.e., the values of accumulated twin volume fraction at different amounts of strain especially at high strain rates. It was found in the present characterization of the alloyed Hadfield steel that a great amount of twin or slip band boundaries exist after deformation at a high strain rate, at least based on a visual inspection. What is also less known is that at high strain rates the slip-slip, slip-twin, and twin-twin interactions may become more complex and more time dependent. Hence it is possible that the twinning rate is either increased or decreased at the dynamic strain rates, depending on the alloy. Secondly, the saturation of twinning may be altered, for example because of the hardening effect of slip bands on the growth of twins. Physically these effects are plausible, as on one hand the dislocations are intermittently stopped in front of the obstacles and at high strain rates they also face various drag effects, while twinning can be less affected due to its short distance kinetics, which may *increase* the twinning rate. On the other hand, if high strain rates favor the generation of wide slip bands, it can affect the twin growth by *decreasing* the twinning rate. For example, if the size of the wide slip bands diminishes, the probability to inhabit twins inside the band is

likely to reduce, which would have a negative effect on the twinning rate. Although this point is not explicitly presented in the model, it could be taken into account in a simple way as the sensitivity of the slip-to-twin hardening parameter, if so desired. Hence, for the time being these quite relevant questions remain open and the effect of strain rate on twinning can be either positive or negative. In this work, the viscosity parameter K is chosen to the classical value with a low viscous effect equal to the initial critical resolved shear stress [85], while n has a slightly higher value than for slip. For the current model this means that the twinning rate at high strain rates is mainly the same or marginally higher than at low strain rates. However, it was found that the volume content may reach higher values before saturation because of this choice, mainly at the dynamic strain rate range.

The limiting value for the maximum twin volume content, F_{max} , at a gauss point was set to a quite high value of 0.85. This value is considered to be a suitable approximation, because regardless that the average total twin volume fraction even in a highly twinned grain may not reach such a value easily, a smaller partial volume of that grain can do that, e.g., when a grain is discretized by the finite elements. The concept of a gauss point presenting a part of the grain is not analogous to the whole grain, since the present work mainly aims to utilize the model for FE discretized microstructures, and hence the volume related to a gauss point could virtually be even fully twinned. However, if one considers this possibility, in the FCC structure the apparent twinned region is not necessarily fully occupied by twins but rather forms a band that contains condensed thin twins spaced with small regions of untwinned matrix in between, as was observed in the TEM investigations of Christian and Mahajan [48]. Also, as already pointed out, recently Efstathiou and Sehitoglu [65] characterized twin bands in a deformed Hadfield steel and suggested that only approximately 80 % of the apparent twin band is made of twins. They also noted that thin secondary twins exist between the primary twins. Hence, a slightly higher total value of 0.85 is assumed in this work.

7.6.3 The [001] orientation in tension

The formation of twins was not observed in either the experiments or simulations for the [001] orientation in tension, and multiple slip is the cause for the almost linear hardening throughout the deformation range. Hardening caused by slip suppresses twinning even at higher strains, which is also in line with the experimental observations. This points out that the reproduced shape of the multiple slip hardening is in line with the experiments, and the slip-to-twin hardening rule is justified to avoid premature initiation of twinning. All of the dislocation interaction types are present in this case due to the high number active slip systems (eight in total), which makes the simulation dependent on all of the identified interaction coefficients. In the identification process it appeared that the most critical ones of these coefficients are the collinear interaction (H3) and Hirth junction (H2), followed by the glissile junction (H4) and with some importance the Lomer-Cottrell locks (H5) as well. Self and coplanar slip interactions appeared to have quite little importance, probably due to the small value of their coefficients. If the values for the interaction types were chosen too high or too low, e.g., very high values for collinear interaction, the simulated curve saturated too quickly and hardening was drastically reduced.

7.6.4 The [001] orientation in compression

In the compression test of the [001] oriented single crystal, the low strain hardening extending up to large strains is mainly caused by twin dominated deformation without

interaction with other mechanisms. Karaman et al. [114] observed a strong dominance of a single twin system and early activation of secondary system(s). They also noted that in the tests where the deformation was seized at low strains for microscopic analysis and then continued to higher strains, the same predominant twin system continued governing the deformation. Simultaneously, the secondary system continued to grow, but no marked hardening was observed from the twin-twin interaction until high strains, likely because of the lower twin volume contribution of the secondary system(s). Very similar behavior was observed in the present simulations, where one twin system was dominant and accompanied by other twin systems. The hardening is contributed mainly by the non-coplanar interactions, but also partially from the slip-to-twin interactions. However, the major difference with the experimental observations is that because the model assumes isotropic critical values for the resolved shear stress, the number of twinning systems corresponds to four active mechanisms as predicted in Table 7.5, whereas the characterization of Karaman et al. [114] revealed only two main twin systems with two extra minor contributing systems. The number of active slip systems in the simulations was eight, i.e., the same as predicted by the Schmid factors.

This mismatch in twinning does not necessarily render the model invalid, but rather indicates that the model follows the theoretical behavior as expected. One explanation for this behavior is that, in reality, the activation of a system is likely more or less anisotropic, as noted by Karaman et al. [114] depending on the loading direction, defect populations, solute atoms, etc. Furthermore, material flaws can cause early activation of some systems, whereas the twin-twin hardening due to this system may further suppress other twin systems, or simply easy growth of a twin system prevails after the initiation, and hence just one or two systems could remain dominant. For example, it is possible to reduce the effect of secondary twin systems in the model by increasing the relevant twin-twin hardening parameters to a high value, but then their importance can be easily overestimated, as the early activation could already suppress activity in other systems. Even so, the present experimental data is insufficient to adjust the individual critical resolved shear stresses of the twin systems in one particular case. Their values may also easily vary between individual experimental samples with slightly different material flaws, or due to the deviations from the ideal crystal orientations. The latter aspect is especially noteworthy, since small deviations in the orientation can favor some twin system over the other due to the strict competition between the twin-twin and slip-twin mechanisms. For these reasons, the isotropic definition of the activation stresses for twinning is retained, and the final twin hardening parameters are further adjusted with polycrystal simulations, where the values identified based on the single crystal results act as initial guesses.

7.6.5 The $[\bar{1}11]$ orientation in tension

Twinning is the main deformation mechanism in the $[\bar{1}11]$ orientation before the saturation of twinning. Karaman et al. [114] investigated the early stages (<1% of strain) of the deformation with transmission electron microscopy and observed slip activity and abundant stacking faults preceding twin activation, i.e., generating the required conditions for twinning. The low strain hardening is caused by twin dominant deformation until high strains where twinning saturates and the deformation is progressed almost solely by slip. If the deformation was seized at around 25 % of plastic strain, a high volume content of twins was observed in the experiments. Further loading of the sample by 1 % showed mainly growth of the twins, and the low dislocation density between the twins prevailed before and after this strain increment, which further confirms the low activity of slip.

However, after the saturation of twinning already at around 27-28 %, the slip activity increased rapidly in the experiments, which is also clearly visible in the simulation result in Figure 7.18e. According to the experimental observations with optical microscopy and TEM, the twin shear is accomplished by two high activity twin systems. Their interaction facilitates the stronger strain hardening at the later stages of deformation, i.e., a notable upward curvature takes place in the hardening, which is also finally accompanied by hardening due to slip-twin interaction before microscopic shear bands cause a tensile failure.

This hardening behavior is generally supported by the simulations, too. However, simulations predict a slightly overestimated curve with the present twin hardening parameters. This occurs simply because in the simulations the number of active twin systems is three instead of two dominant mechanisms causing stronger hardening. The number of twin systems therefore is equal to the number suggested in Table 7.5 with equal Schmid factors, while the number of active slip systems is the same as expected, i.e., six. The contribution of these active twin systems to shear is equal (their volume contents and rates are almost equal) in the simulations, and since the hardening of these three systems is non-coplanar in nature, each system over-hardens the other two, increasing the overall hardening. The discrepancy here could be explained by the points brought up in the previous section, but the experiments and simulations both agree on the deformation mechanisms and their overall contribution in this orientation, which are the matters of importance. Finally, the actual rate of twinning is difficult to verify because no information about the evolution of the volume content is available, but the result seems quite reasonable considering the experimental observations. In another context, Karaman et al. [113] proposed also quite high twin volume content of 0.7 for this orientation in their self-consistent modeling approach, but no certainty was presented over this number in that occasion, either. In the simulations, they could reproduce the stress-strain behavior of the $[\bar{1}11]$ orientation in tension, which was also solely used for the parameter identification of their model. However, it remained uncertain how the model would perform in all of the orientations investigated here.

7.6.6 The $[\bar{1}11]$ orientation in compression

The simulations predict a strong strain hardening behavior for the orientation $[\bar{1}11]$ in compression, which could be expected from FCC crystals with multiple slip activity. The number of active slip systems in the simulations was six, which agrees with the theoretical number. The experimental data first shows low strain hardening, which is followed by an abrupt increase. According to the experimental characterization [114], the low strain hardening is featured by the development of macroscopic shear bands in the sample, explained by a Lüders type of propagation. At a later stage, the interaction with the bands increases the hardening rapidly. A shear band was characterized with EBSD and the misorientation was found to be only about 9°, which further confirms that it is a slip related band rather than a twin band. In fact, similar bands were observed also in the polycrystal samples of this work, as explained in Section 4.1.2. The current model does not allow any additional shear banding that would arise from specialized slip interactions causing easy-glide, and therefore overestimation of the hardening is observed. It could be possible to include a similar framework as proposed in Section 8.3.1, but that is now omitted for the sake of simplicity. For example Jia et al. [105–108] incorporated microscopic non-crystallographic shear banding alongside slip and twinning in FCC crystals and found a reasonable agreement with experiments. Nevertheless, it is

possible that the experimental curve could coincide with the currently simulated curve at higher strains, but no experimental data extending to higher strains is available to confirm this.

7.6.7 The $[\bar{1}23]$ orientation under both tension and compression

The simulations and experiments support that the $[\bar{1}23]$ orientation undergoes deformation mainly by dislocation slip. Karaman et al. [114] observed a noticeable amount of easy glide dislocations with an edge character in one system at the early stages of deformation. The primary slip system continues to govern the deformation that is affected by secondary system(s), leading to dislocation bundles. As a result, the strain hardening is low at the early stage of the deformation. In tension, the simulations confirm the experimental observations of high activity of a single slip system that is followed by a secondary system at moderate strains and a third system at higher strains. The activation of other slip systems is seen in the stress-strain curve as an easy glide region after an upward-type hardening of the previous system(s), i.e., at strains around 18 % and 38 %. Although a single twin system has a relatively high Schmid factor, no twins were observed in the experiments. The simulations show that this twin system, in fact, would activate around the strain of 38 %. However, the slip-to-twin hardening was calibrated in order to prevent this so that the simulation of this orientation matches the experimental observations, i.e., by choosing a sufficient hardening coefficient with an exponent value having more significance at higher strains.

In compression, the simulations predict lower hardening response than observed in the experiments. This is explained simply by two factors. First, regardless that the secondary slip system activates similarly as in tension, only little activity exist in this secondary slip system. A third system is also activated, but its contribution is even more minimal. It follows that the observed hardening in the simulated stress-strain curve, which in fact is still notable by an increase of roughly 35 % from the yield stress, results mainly from the self-hardening of the primary slip system. It is possible to calibrate this curve to match the experimental observations by choosing artificially high self-hardening and a very low Hirth junction hardening, which promotes activity in the secondary system. However, this would lead to non-ideal behavior in the other orientations and also physically to an unlikely situation where self-hardening interaction would exceed the more severe interaction types, e.g., glissile junctions. If such fitting is made, activation of the secondary system is increased, but it still does not yield a significantly better estimation but even worse in some cases. Hence, the self-hardening model, or in other words, the evolution of dislocation density may be too simplified to present this particular situation correctly, and the Hirth type of interaction value may be slightly overestimated because of the compromise made in the overall fitting.

7.6.8 Remarks on the model parameter effect based on the single crystal simulations

The simulations can reproduce quite satisfactorily the experimental tension and compression test results on FCC single crystals. It appears that the hardening rules of the model are generally suitable to present the slip-slip interactions, slip-twin interactions and twin-twin interactions taking place in Hadfield steels. The identified slip-slip interaction follows the common understanding of their relevance discussed in section 7.3.1. The collinear interactions followed by the junction-forming interactions (Hirth junction, glissile

junction, and Lomer-Cottrell locks) are of the highest importance, while the self- and co-planar interactions have the least effect. The coefficient b that characterizes the rate of saturation of the slip hardening rule was set to a reasonably low value for various reasons. The experimental observations show that slip activity occurs in the vicinity of twins bundles and in the rest of the matrix and does not saturate easily, i.e., both low and high dislocation density zones are observed until high strains. Also, in the slip governed deformation the saturation of strain hardening does not take place until high strains, which is a strong indication of slow saturation. Finally, if a high value for the saturation coefficient is chosen, it tends to change the behavior drastically towards overshooting of the strain hardening, e.g., see Figure 7.12 demonstrating this. This means that the curve would resemble the typical convex behavior of strong hardening (the opposite of the concave curvature) at first, and then a rather low strain hardening rate follows at higher strains, which was not observed with this material. The isotropic hardening parameter Q, which describes the magnitude of slip hardening, was chosen to match the observed strain hardening behavior. A too low value would result in too soft response, while a too high value would result in early saturation of the hardening curve with the present dislocation model.

The parameters related to twinning were chosen to match the experimental observations. In the absence of data on the evolution of the twin volume fraction, which would be one of the most critical pieces of information, the exact values related to twinning are difficult to obtain with a high certainty. Furthermore, as the simulations showed in some cases higher number of active twin systems or their relative contributions were higher, it affects the magnitude of the hardening coefficients in twin-slip and twin-twin interactions. For example, if a twin system has a high contribution to shear (its volume content is higher than in the experiments), it directly results that this particular system may have a non-coplanar interaction with some slip systems causing stronger hardening than in the experiments. In turn, if this twin system was suppressed by other twin systems, it leads to lower hardening subjected to the slip systems because of a lower twin volume fraction. At the same time, if other twin systems are more active, they may also subject hardening to other slip systems. As a simplified example, if twin systems are active on planes (111) and $(\bar{1}\bar{1}1)$, one on each with an equal volume content, and slip activity is assumed in both planes, hardening is generated in these slip systems from both of the active twin systems by an equal amount. Now, if it is assumed that the twin system on (111) is highly dominant, it hardens the slip systems on $(\bar{1}\bar{1}1)$, but as the volume content of the other twin system is low, it does not generate much hardening in the slip systems on (111), which can change the hardening behavior even quite much. This points out that in order to capture the deformation behavior of the material correctly, the twinning behavior is in a quite important role. Hence, it is possible that the hardening coefficient, H_{sltw} could be underestimated by the single crystal fitting process. Similarly, because the discrepancy in the activity of the twin systems exists, it is equally possible that the non-coplanar and coplanar hardening coefficients are underestimated to provide a more similar curvature to the experiments. For these reasons, the twin parameters are used as initial guesses for the polycrystal aggregates, and the parameters are then adjusted to generate more realistic behavior at the macroscopic scale. At least in an average sense, this presumably provides a better estimation of the twinning behavior.

7.7 Parameter identification of Hadfield steel with polycrystal aggregates

This section describes the process utilized to identify the parameters of the conventional Hadfield steel with the aid of polycrystal aggregates (representative volume elements). The main objective of this study is to provide a more accurate macroscopic description of the behavior in an average sense. The parameters that are found in the single crystal simulations do not necessarily directly generate the expected behavior in polycrystals because of the localized effects facilitated, for example, by intra- and intergranular behavior of the grains. Ultimately, the strain gradients developing inside a polycrystalline material should be captured with the actual morphology of grains and with a sufficient amount of discretization inside the grains to ensure a link between the simulations with a representative microstructure and realistic microstructures. For example, considering the present modeling approach, it is no surprise that twinning could initiate more easily from any stress concentrations generated by high misorientations between grains near grain boundaries, where the deformation incompatibilities between the grains are required to be habilitated. Furthermore, if any material flaws (voids, carbides, etc.) exist, the stress concentrations around these regions could provide favorable zones for localization processes, however, their effects are not included in this study. Before the calculations with more realistic type of microstructure aggregates are performed to shed light on the observed material behavior of the Hadfield steels, it is necessary to conduct additional simulations to identify the material parameters with more computationally efficient simplified polycrytalline aggregates, i.e., with simplified representative volume elements.

7.7.1 Aspects of polycrystal simulation with RVEs

The choice of using simplified representative volume elements means that the idealized microstructure consists of regular meshes with no actual link to the grain morphology, i.e., of primitive geometric forms such as blocks or cubes, which represent the discretized grains but lack the complexity of the grain structure in general. For example, one block element equals one grain, or a group of block elements constructs one grain. Regardless of the simplification, it is not unusual that in many cases these microstructures lay the foundation for the identification process. Some of the most important aspects related to the use of these aggregates in the identification process are listed and discussed in the following.

- **Grain morphology:** The realistic type of grain morphology can yield more accurate description of the local stress and strain concentrations. However, the main reason for using simplified aggregates in the identification process is simply the computational efficiency that stems from the quite low number of elements needed. If the grain morphology is complex, it is required to be discretized by a high number of elements in order to respect the various curvatures, which directly increases the number of DOFs. Li et al. [129] used a realistic type of aggregate in their identification process, but performed the identification only in one texture direction, probably partly due to the high cost of computational iterations. In contrast, Staroselsky and Anand [203], among others, found the use of simplified aggregates to suit the parameter fitting process including slip and twinning, concluding that the macroscopic stress-strain response as well as the evolution of texture can be predicted with a reasonable accuracy. It is noteworthy that if a homogenization loop is available as the first step for the model parameter identification, the realistic

microstructure can be used as the final step with only a low number of iterations to verify the model behavior as well [168].

- **Grain and element density and intragranular aspects:** Diard et al. [60] performed a study on the effect of aggregate features on the identification process in the small deformation framework. If only macroscopic stress-strain curve is a matter of interest, they concluded that the number of elements is less important than the number of intergration points inside a grain, pointing out that coarse meshes are sufficient as long as 27 integration points are introduced per grain. Also, depending on the material, already only 100 orientations (or grains) can describe the macroscopic behavior with satisfactory accuracy. Osipov [168] and Han [88] investigated the effect of mesh density on the stress-strain response at moderate and large deformations. Their results confirm the same conclusions, that already a low number of grains/orientations can reproduce the macroscopic stress-strain curve, but the local gradients can be captured better with dense meshes. The latter aspect was investigated in detail by Diard et al. [60], who noted that in order to capture the intragranular heterogeneities it would be advisable to have around 400 gauss points per orientation, which essentially leads to the use of a greater number of elements per grain, and/or higher order elements (increasing the number of gauss points). The same observation was made by Han [88] when studying the stress-strain variations arising from the mesh density effect. It was found that the convergence was achieved with around 27 elements per grain, while at the same time the difference between reduced and full integration may become important depending on the ultimate aim of the simulations. For example, the intragranular heterogeneities become more important when damage or fracture are included in the model [37].
- **Boundary conditions:** The boundary conditions can have multiple effects on the behavior of the representative volume element, e.g., a cube in this work. In large strain computations, if the constraints are too 'soft', it may quickly lead to a state where the grains deform freely outwards from the initial cube-type geometry and reduce stresses. Barbe et al. [16, 17] studied several aggregates and boundary conditions constraining the aggregate and confirmed the more or less pronounced effect of the softening behavior caused by the free edges. This behavior is not necessarily desired when uniaxial deformation is aimed, and it may appear as a too soft response in the stress-strain curve. Mathieu [146] also noted that sufficient constraining of the volume element resulted in a quite similar behavior as generated by the homogenization schemes. For this reason, quite recently in a number of studies [84, 88, 146, 192] constraints were used to restrict the deformation of the free faces to bind the deformation in a well-behaving manner with respect to the original geometry. This could, at least in principle, provide better deformation conditions in uniaxial loading. However, the nature of these boundary conditions, and some others as well, can lead to stress concentrations at the sharp edges of a cube. As a consequence, sometimes the outermost layer of elements in every direction is excluded from the computation of the average stress-strain curve, which can reduce the effect of artificial stress spikes [2]. On the other hand, if a small number of elements is used in the first place, it may lead to a situation where a too small number of grains/orientations are included, which is controversial to the above mentioned points of acceptable descriptive meshes. Depending on the stress measure used to fit the model parameters, some smoothing schemes could provide a more successful description of the stress state inside an aggregate, which

may be altered by the high compressive states [146]. However, it was pointed out that care should be exercised when using any smoothing to remove artificial stress concentrations but not to over-damp the stress gradients. Finally, it should be noted that Barbe et al. [17] found, based on a review of other classical results, that despite the surface effects of the boundary conditions, the neighborhood of a grain has more relevance to its mechanical response than the boundary conditions.

- **Computational efficiency:** The level of simplifications and compromises dictate the efficiency of the computations. According to the above mentioned aspects, if a large number of grains and/or elements is used, the number of DOFs is increased, usually leading to a higher computational time. At element level two factors affect the computational time: first, the number of gauss points either can decrease (reduced integration scheme) or increase the computational time (full integration scheme). Second, if low order elements are used, the number of gauss points is reduced as a consequence, leading to faster computations but may be at the expense of the local accuracy.

To conclude, for most of the cases that use representative volume elements as a part of the identification process, it can be sufficient to use a reasonable number of grains (> 100), 27 integration points per element, and one element per grain/orientation to capture the stress-strain behavior of the material. Accordingly, in the present study these requirements were fulfilled as a compromise between the accuracy and computational efficiency. The model parameters are identified using the polycrystal aggregates with 8x8x8 elements (512 elements), with one element per grain (512 orientations), and fully integrated quadratic brick elements (27 GP in each). The size of the aggregate was chosen as 1 mm x 1 mm x 1 mm. The orientation distribution was chosen to be random in all simulations. In the light of good computational efficiency and agreement with the experimental results of the earlier studies [84, 88, 146, 192] using the small and large deformation frameworks, the fixed boundary conditions making use of the multi-point constraints were adopted. Figure 7.19 shows the boundary conditions for the aggregates.

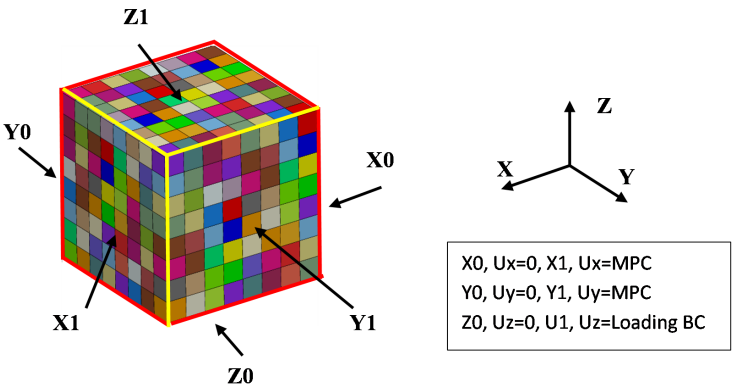

Figure 7.19: A polycrystal representative volume element with 512 grains and the boundary conditions for the simulations.

In the following, a brief study is first performed with higher number of grains to show the mesh dependency from this point of view. Then, uniaxial tension and compression simulation results are shown and compared with the experimental stress-strain results

to verify the acceptability of the parameter fits for the conventional Hadfield steel. The experimental polycrystal stress-strain curves were also extracted from ref. [114]. This is followed by the identification process for the alloyed Hadfield steel based on the experimental results of this work.

7.7.2 Mesh density effect in polycrystal parameter identification

Figure 7.25 illustrates the different polycrystal representative volume elements with varying number of grains. One element presents one grain in all of the example aggregates. Hence, each color basically represents an orientation in the computations. However, the coloring scheme used here is not directly IPF related but used only for illustration purposes. A uniaxial tensile displacement loading was subjected to the aggregates resulting in a total strain of roughly 26 %. Figure 7.21 presents the simulation results. The model parameters are presented in Table 7.6 in Section 7.7.3.

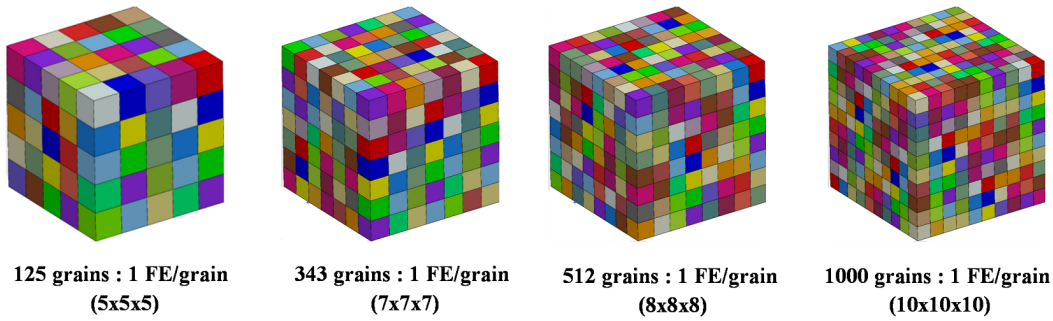

Figure 7.20: Polycrystal aggregates for the parameter identification process with 125, 343, 512, and 1000 grains.

The Mises stress and the twin volume content (fraction) presented in Figure 7.21a for the aggregate are averages over all grains in tension. The difference between the aggregates is almost negligible, as the maximum stress variation is only around 2 %. Surprisingly, a dense mesh does not always result in a reduced average stress value, which could be expected when the grains located at the vicinity of the boundary conditions have less weight. In the current simulations it appeared that the 125 and 343 grain aggregates have first an almost identical stress response, but at higher strains the stress in the 125 grain aggregate of these two tends to drop closer to the 512 and 1000 grain result. In general, it seems that the stress response converges already with the 512 grain aggregate, at least in the present case. The maximum difference in the twin volume fractions at high strains was quite insignificant as well, the total twin volume fractions being approx. 36.1 % for the 125/343 grains and 34.6 % for the 512/1000 grains.

One explanation for the marginally higher stress response of the 343 grain aggregate compared to the 125 grain aggregate could be found from the grain level stress-strain behavior shown in Figure 7.21b. Here, the Mises stress is presented as the element average of 27 integration points belonging to the same orientation. Some of the individual stress-strain curves in the 343 aggregate tend to show higher amount of high stress response grains. The exact source for this is difficult to find. It could, for example, be that the effect of boundary conditions simply is more pronounced if a suitable orientation is assigned to the edge elements with a tendency to generate stress a concentration at the boundary by chance. Otherwise it appears that typical scatter between the grains

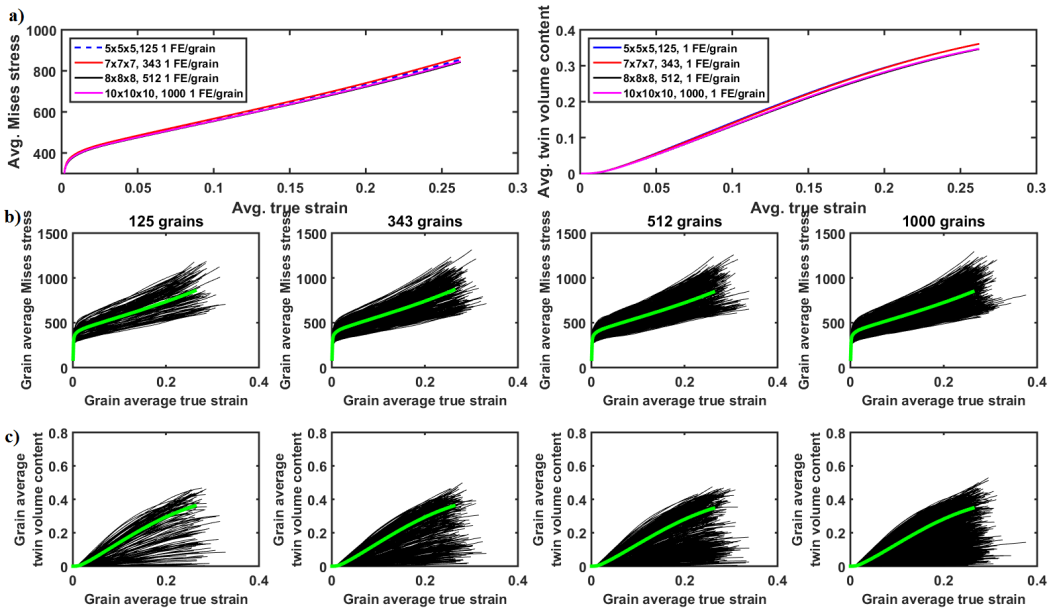

Figure 7.21: a) Average stress-strain behavior and twin volume evolution, b) local grain scale stress-strain behavior, and c) local grain scale evolution of the twin volume content for four aggregates.

occurs where low, close to the average, and high stress response orientations are observed. Figure 7.21c shows the grain level evolution of the twin volume fractions. An essential observation is that the maximum twin volume fraction does not reach the maximum saturation value of 0.85 in any of the grains, even though the average evolution of the twin volume fraction in the aggregate shows weak signs of saturation in its rate. In other words, this means that the twin volume fractions at the gauss points can reach the maximum value, but the values at other points tend to balance the average of the grain to a lower value. At the grain level this, in fact, coincides with the experimental observations presented in Section 4.1.2, showing that in some parts of the grains the twin volume fraction can be very high while the other regions show significantly less twins. Also, the variations between the grains confirm the expected result that some grains exhibit high amounts twins while the other grains contain only a small amount or no twins at all.

The comparison between full integration with 27 gauss point and reduced integration with 8 gauss points is presented in Figure 7.22. The results show a quite marked difference in the twin volume fractions. As a consequence, the stress-strain curve of the reduced integration cube shows lower values than the full integration cube. This could be explained partly by the notable variations in the twin volume content within one grain (or element in this case), and hence the reduced form is more sensitive to average the values so that lower values are obtained. Therefore, the full integration is selected in the present simulations because it provides more individual material points per grain and hence possibly gives a better overall estimation when the representative volume elements are used for parameter identification.

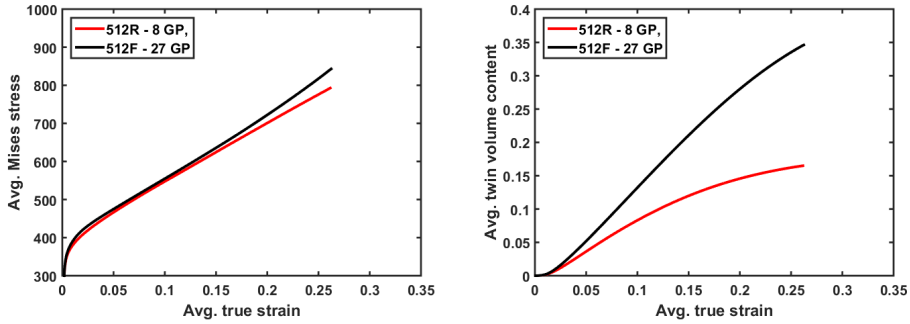

Figure 7.22: a) Stress-strain behavior in tension and b) evolution of twin volume content for a 512 grain aggregate with reduced and full integration schemes.

As a conclusion, based on the current results it appears that the mesh density has a reasonably small effect on both the stress-strain response of an aggregate and the average evolution of the twin volume fraction in it. Even with 125 grains the difference to the 1000 grain aggregate is small. Thus, to achieve the maximum computational efficiency in the parameter identification process with polycrystal aggregates, the 125 grain aggregate could also be used with a satisfactory accuracy. Despite this, in the present work the 512 grain aggregate was chosen. It may also be that an increasing number of orientations could better predict the evolution of the texture. This was not investigated in this work, but for example Staroselsky and Anand noted that already with a 7x7x7 (343 grain) aggregate the texture was in good agreement in the experiments and simulations [203].

7.7.3 Behavior of conventional Hadfield steel under tension and compression - parameter identification

Figure 7.23 presents the results from the simulations and experiments at a constant strain rate of $10^{-4}s^{-1}$. The error limit of +-5 % reported in [114] is presented by a dashed red line, whereas the average stress of the aggregate is presented by a black solid line. The simulated average stress-strain response of the aggregate is in reasonable agreement with the experimental curve when considering the given error limit, as is evident in Figure 7.23a. Also, the simulated curvature can capture the upward tendency of the experimental stress-strain behavior. To capture the asymmetric stress-strain behavior of the Hadfield steel, the fit was performed as a compromise between tension and compression.

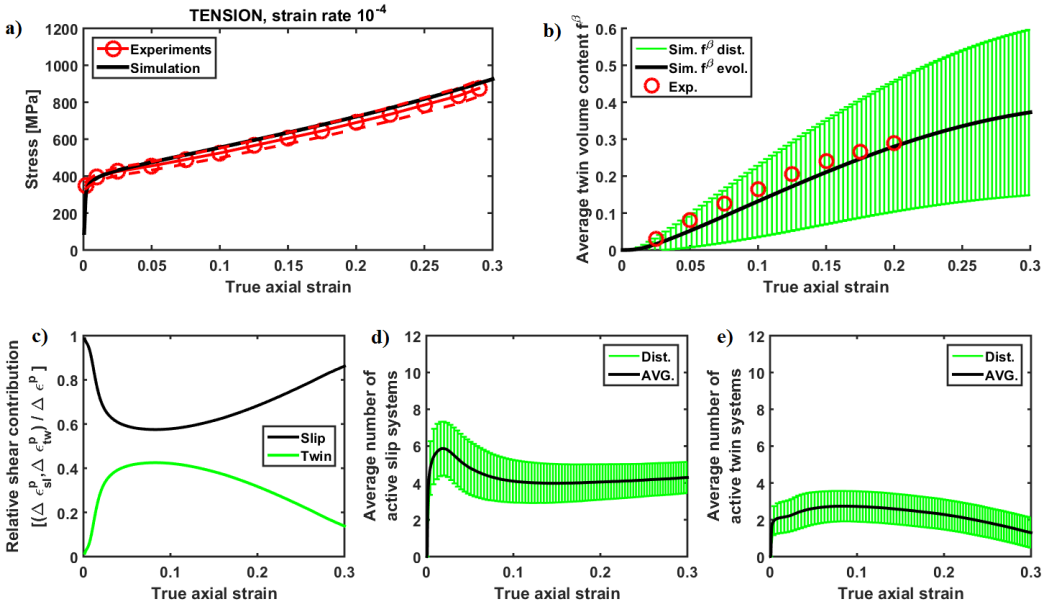

Figure 7.23: Fitting response of a polycrystal aggregate with 512 grains, including the evolution of twin volume content in tension. The relative shear contributions and average number of active deformation systems are also presented for the whole aggregate.

The evolution of the experimental twin volume fraction was obtained from ref. [113], where a conventional Hadfield steel with the same composition and very similar grain size (around $120\mu m$) as in ref. [114] was tested. The simulation fits the experimental values reasonably well, considering that the available data of the twin volume content is limited to around 20 % of strain only, excluding any information about the saturation behavior because of the relatively low strain level. Hence, the saturation of twinning seen in the simulations could not be fully verified, but it may begin already slightly earlier than observed in the simulations. First indications of saturation are also visible in the stress-strain curve. When the twin volume content is relatively high and the twinning saturates, slip becomes a more dominant mechanism. At the same time, the twin boundaries act as strong obstacles and cause strong strain hardening through the dynamic Hall-Petch phenomenon in the simulation model. This, of course, presumes that the twin volume content actually is high at a local scale, otherwise the low dislocation density (or the accumulated slip causing hardening) in the matrix and the low amount of twin boundaries retard hardening. To investigate this, the scatter bars indicate the standard deviation from the mean value of the twin volume content. This value, however, is not intended to describe the error in the conventional sense, but it rather confirms the expected result that the twin volume content in some grains (or gauss points) reaches high values at higher strains, whereas in some grains it remains very low eventually leading to higher scatter.

The instantaneous contribution of slip and twins to the shear deformations in Figure 7.23c shows that the twin activity becomes quite significant after initiation and the initial 'incubation' period. The twin activity decreases towards saturation when slip becomes even more dominant. Indirectly this means that if the twin volume content is high towards the saturation and the deformation is continued mainly by slip, the hardening from the

slip-twin interaction can become significant causing a stronger upward curvature. The average numbers of slip and twin systems (not integers because they are average values over the whole aggregate) in Figure 7.23d,e represent the evolution of simultaneously active systems. It appears that at the initial stage of deformation, a high number of active slip systems contribute to the deformation, decreasing towards higher strains due to the deactivation caused by hardening. However, as soon as the twinning rate shows signs of reduction, the number of active slip systems is increased slightly to accommodate the deformation. The number of active twin systems does not show any drastic changes either, and after initial activation, the number generally remains between 2-3. Also here the error bars indicate simply the deviation from the mean value. It should be noted that the average values of the slip or twin systems do not directly indicate whether the same systems remain active or if hardening of one system leads to the activation of other systems instead. For example, if three twin systems are active, it remains unknown whether the systems have a coplanar or non-coplanar relation based only on this average value. This information could, of course, be extracted locally whenever needed for any particular grains or zones of interest. The simulations showed that the stability of the model is quite good at least in the global level, because the average shear contributions did not show any sudden decreases or increases as a result of instabilities (e.g., a sudden activation of many twin systems).

Figure 7.24 presents the corresponding results for the compression case. The fitting result shows good agreement with the experimental results also in this loading direction. The twinning rate and its evolution are slightly lower in compression than in tension. However, no information is available to fully ascertain the simulation results about the twin evolution due to lack of twin volume fractions at certain plastic strains. The twin contribution to shear is also lower in compression than in tension as a consequence of the lower twinning rate. The number of slip systems does not drastically differ from tension either, but a slightly higher scatter is observed at the initial stages of twinning followed by a similar behavior as in tension. As a comparison of the strain hardening capability of the material, a difference between tension and compression is observed. For example, the macroscopic flow stress at around 20 % of strain is roughly 700MPa in tension and 800MPa in compression, which shows that the model is capable of describing the tension-compression asymmetry in the stress-strain behavior.

Table 7.6 lists the parameter values obtained from the identification process. The values in parenthesis are the original values identified with single crystals and later modified to conform with the polycrystal simulations.

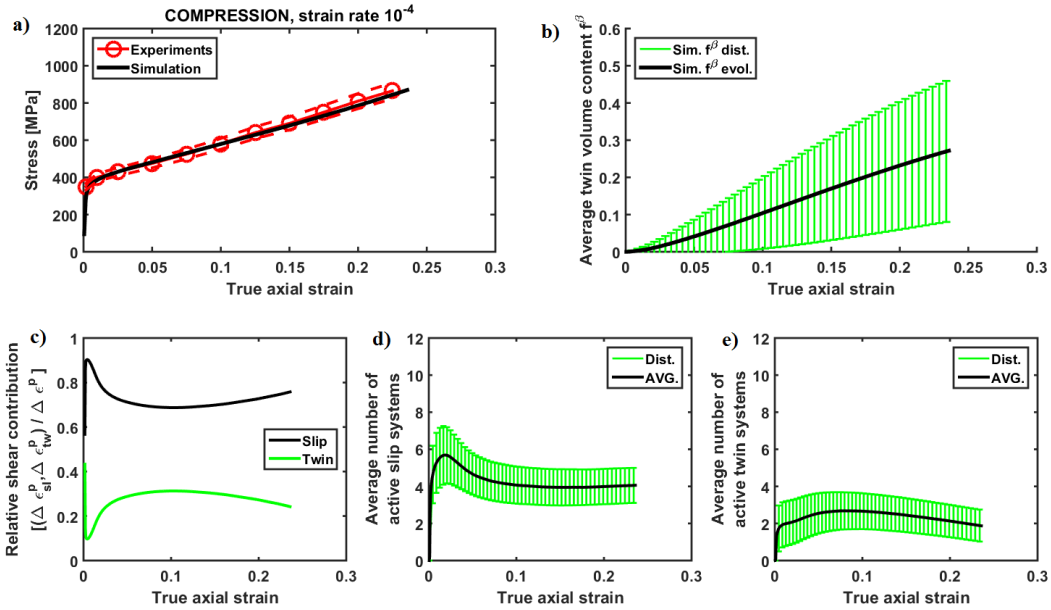

Figure 7.24: Fitting response of a polycrystal aggregate with 512 grains, including the evolution of twin volume content in compression.

Figure 7.25 shows contours of the nodal interpolated Mises stress values of the deformed representative volume elements and their accumulated twin volume fractions at the gauss points. The stress contours indicate that with the current aggregate it is possible to examine the stress heterogeneities even inside the simplified structure, which was also observed by Diard et al. [60]. The twin volume fractions in both loading cases show similar features, i.e., some grains are already saturated with twins while some grains contain almost no twins at all. Furthermore, the intergranular twin volume fractions are not equal (variations between the gauss points between elements/grains), which again

Table 7.6: Model parameters identified with uniaxial deformation of single crystals and polycrystal aggregates

Anisotropic cubic elasticity	C_{11}		C_{12}		C_{44}		
	174 000		85 000		99 000		
Slip parameters	τ^{s0}	K	n	b	Q		
	87.0	87.0	10.0	2.35	140.0		
Interaction matrix coeff.	h_0	h_1	h_2	h_3	h_4	h_5	
	0.12	0.10	1.60	1.85	0.36	0.80	
Kinematic hardening	C	D					
	0.0	0.0					
Twin parameters	τ^{tw0}	Ks	ns	H_{sltw}	Htw_{NC}	Htw_{CO}	H_{twsl}
Kc = 0.03	90.0	90.0	12.0	130(50)	500(120)	600(200)	340
Hardening exponents				$p = 0.5$	$b = 0.2$	g=1.0	$d = 0.7$
Units:	$\tau^s[MPa]$		$K[MPa.s^{1/n}]$		$Q[MPa]$		
	C [MPa]		D [MPa]		All H*[MPa]		

is consistent with the experimental observations. Detailed inspection of the aggregates reveals a four additional observations: i) in the grains, where the twin volume content has reached high value in many gauss points, stress concentrations are generated as a result of the slip activity followed by heavy twinning and its hardening interaction with slip, ii) the grains with low overall twin volume content do not show very high stress values because slip alone is capable of causing moderate hardening only, iii) if moderate twinning is observed in the majority of the gauss points inside an element, the stress response remains at a moderate level as twinning softens the response, and iv) the neighboring effect can be best seen when the interpolated values are used for stress. If neighboring grains have a high twin volume content in one grain on average and a low volume content in the other, stress concentrations are generated at the shared nodes. If the stress values are investigated at gauss point level, the stress behavior follows the first three points and no evident information can be extracted from the neighboring effect.

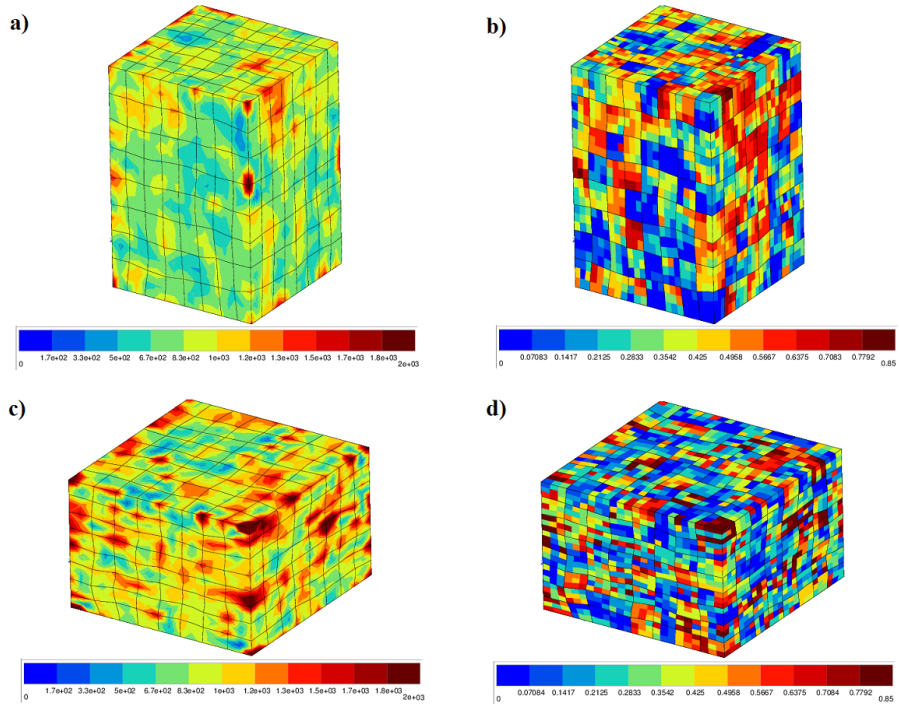

Figure 7.25: Nodal Mises stresses for a) tension and c) compression, and twin volume fractions at gauss points in b) tension and d) compression for the 512 grain aggregates.

7.7.4 Parameter identification of the alloyed Hadfield steel

Parameter identification was also performed on the available compression data of the alloyed Hadfield grade studied in the experimental part of this work. In addition, to investigate the asymmetric stress-strain behavior of this grade as well, a tension test was simulated and compared with the experimental data. The alloyed Hadfield grade exhibits positive strain rate dependence suitable for the current modeling approach, and hence the effect of strain rate was studied in the fitting process. The numerical simulations were performed using two representative volume elements with 125 and 512 grains in random

orientations and with 27 gauss points. The boundary conditions were selected to be the same as in the previous section.

Figure 7.26a shows the macroscopic stress-strain curves obtained from the FE simulations and from the experiments at three strain rates in compression. The numerical predictions agree reasonably well with the experiments considering that the large grain size showed some variations in the experiments. Hence, a 5% fitting limit was accepted for convergence (black lines show these limits). No significant difference in the stress-strain curve was observed between the 125 and 512 orientation representations. The stress-strain curve takes an upturn when the strain increases in all simulated cases. As with the conventional grade, this is a direct result of twinning since the simulations performed without twinning showed more classical curvature, which fails to represent the strong hardening. For example at 0.25 of plastic strain, the flow stress was around 20 % lower (not shown in the figures).

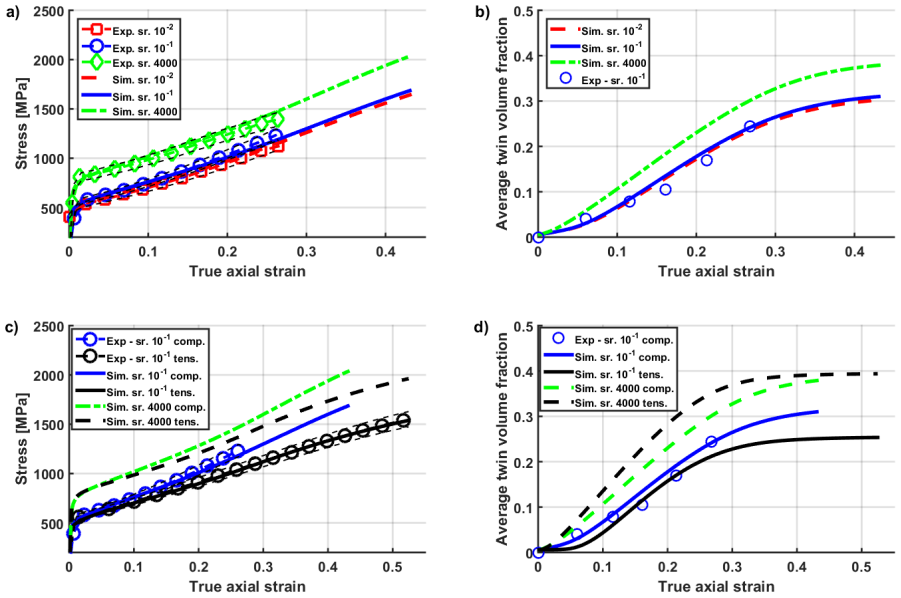

Figure 7.26: Experimental and simulated stress-strain curves at three strain rates of the alloyed Hadfield steel a) in compression, b) the corresponding evolutions of twin volume fractions of the aggregates, c) experimental results and simulations of the asymmetric stress-strain behavior of the Hadfield steel in tension and compression at the strain rates of 10^{-1} s^{-1} and 4000 s^{-1}, and d) the corresponding evolution of twin volume fractions.

The macroscopic twinning volume fractions, on the other hand, showed a slight difference between the two RVEs. This mismatch may arise from the fact that the higher number of orientations tends to increase the possibility for favorable orientations for twinning but also leads to saturation, as pointed out in Section 7.7.2. The numerical results correlate quite well with the twin volume fractions measured at various strains in the tests at the constant strain rate of $10^{-1}s^{-1}$. The viscous parameters for slip and twinning were chosen to represent the increase in flow stress with increasing strain rate, so that the dislocation slip is more strain rate dependent than twinning. The results clearly indicate that because of this choice also the twin volume fraction exhibits positive strain rate dependence with increasing strain rate. This is basically because the slip is inhibited by

'viscosity', while twinning becomes more dominant as a deformation mechanism due to its lower sensitivity to strain rate. Hence, the physical aspect of twinning being more favored at high strain rates can be represented by the model. At the moment, however, the present experimental data was inconclusive in terms of twin volume fraction after high strain rate compression, and as a consequence the actual level of twinning cannot be verified for comparison with the numerical simulations. Therefore, a slight but still notable increase in the twin volume content at high strain rates was accepted with the present parameter set, while retaining almost insensitive behavior at quasi-static strain rates.

The asymmetric stress-strain behavior in tension and compression seen in Figure 7.26 can be represented well by the model at the constant strain rate of 10^{-1} s^{-1}. The simulated and experimental curves agree very well until the tensile failure occurring at slightly over 0.5 of strain in the experiments. The evolution of the twin volume fraction appears lower in the tensile deformation based on the simulations. Quite notable saturation takes place above the strain of 0.3, after which the strain hardening rate differs from the compression loading. The tensile curve shows slightly decreasing strain hardening rate after the saturation begins to affect the behavior, instead of the upward curvature observed in the compression cases. At high strain rates in tension, the stress-strain response still remains lower than in compression. However, based on the current simulations, the evolutions of twin volume fractions shows that tension is slightly more sensitive to strain rate because the twinning rate is higher in tension than in compression. In both loading directions, twinning rate saturates at around 0.4 of plastic strain.

The effect of slip-twin interaction was considered to increase the resistance to twinning at higher strains because of the higher probability to generate slip bands in the matrix, which leads to the later occurrence of hardening. However, the strains limited to around 25 % in the compression tests do not allow characterization of the actual saturation of twinning or the full stress-strain curves. On the other hand, the well-fitting tensile stress-strain curve shows that the material behavior corresponds to the experiments even at higher strains. The EBSD mapping performed on the experimental sample with ca. 40 % of compressive plastic strain showed large amounts of slip bands and twins, which are likely to cause strong resistance to both dislocation motion and the growth of twins. Therefore, it is quite plausible that the simulation curves are showing a correct type of behavior also in compression, at least in principle. It is still worth noting that the lack of a failure model, of course, allows to continue hardening without any fracture taking place. Hence, the stress-strain behavior of the steel and the evolution of twins remains partially open at high strains.

Table 7.7 lists the parameters used in the simulations. The elastic parameters were taken as the same as with the conventional grade. Also, the interaction matrix was left unchanged because no single crystal data was available to study the effects of any changes, e.g., due to the different composition containing more manganese and chromium.

Table 7.7: Model parameters identified for the alloyed Hadfield steel

Anisotropic cubic elasticity	C_{11}		C_{12}		C_{44}		
	174 000		85 000		99 000		
Slip parameters	τ^{s0}	K	n	b	Q		
	91.0	91.0	14.0	2.35	180.0		
Interaction matrix coeff.	h_0	h_1	h_2	h_3	h_4	h_5	
	0.12	0.10	1.60	1.85	0.36	0.80	
Kinematic hardening	C	D					
	0.0	0.0					
Twin parameters	τ^{tw0}	Ks	ns	H_{sltw}	Htw_{NC}	Htw_{CO}	H_{twsl}
Kc = $1.0e^{-5}$	98.0	98.0	30.0	170	650	1550	550
Hardening exponents				$p = 0.5$	$b = 0.3$	g=0.9	$d = 1.3$
Units:	$\tau^s[MPa]$		$K[MPa.s^{1/n}]$		$Q[MPa]$		
	C [MPa]		D [MPa]		All H*[MPa]		

7.8 Application I - Deformation and twin evolution in polycrystal aggregates

This section presents the results of computations of polycrystal aggregates in uniaxial compression loading and compares the response of two aggregates with a different grain size and grain morphology. The focus is placed on the evaluation of the model performance in computations of synthetic microstructures. The simulated material behavior is compared to the experimental observations and the strain hardening behavior of Hadfield type steels.

7.8.1 Modeling conditions

The conventional Hadfield steel was chosen as the test material for the simulations. The strain rate was in all cases set to a constant value of $10^{-4}s^{-1}$. The boundary conditions were also the same as for the representative volume elements (for parameter identification) in the previous section, (see Figure 7.19, where the aggregate side faces are fixed or constrained with the MPCs). In both cases, the mesh density or the number of gauss points were chosen fairly coarse/limited to minimize the computational time in the simulations. The integrations in both cases were performed with Runge-Kutta because of its slightly faster convergence with the present heavily viscoplastic model. The internal Zebulon parameters were $1e^{-4}$ and $1e^{-4}$, which are the convergence criterion and the minimum value for normalization, respectively [236].

Table 7.8 lists the aggregate parameters and the polycrystal meshes used in the computations (colors represent different grains). Type I is a coarse mesh with quadratic elements, and the grain size is fairly uniform around $200\mu m$. The second mesh, Type II, is more refined using linear elements to reduce the computational time. The grain structure of Type II is more complex and it is aimed to imitate the grain morphology of the Hadfield steels (see the micrographs in Section 7.7.2). The microstructure has a grain size from approximately 200 to 600 μm, providing a more realistic link to the cast structure of Hadfield steel with widely varying grain size. The orientations assigned to the grains are in both cases random, Type I having 250 and Type II 183 orientations/grains. Hence, each grain is always in the same initial orientation neglecting any internal variations at the beginning of the simulations, which is consistent with the characterization of the bulk

microstructures. Both finite element meshes aim to respect the grain boundaries without any staircase-like boundaries, and to avoid cases where some elements are shared by two grains with gauss points between the grains. For this reason the tetrahedron elements discretize the shape better than the block elements. The macroscopic dimensions of the aggregates were 1 mm x 1 mm x 1mm.

The macroscopic stress-strain and twin volume fraction curves were the produced by first averaging the values at the grain level from all of the gauss points. Then the average grain values were averaged over the whole aggregate to generate the macroscopic response. Alternatively, a volume based averaging scheme was also performed after extracting the results at the grain level and weighting the grain results by their volume with respect to the total volume of the aggregate. The volume averaged results are denoted as $< \sigma >$. The macroscopic strain hardening rate is here defined as $\Delta\sigma^{Mises}/\Delta\epsilon$, which describes the instantaneous slope of the hardening curve. The strain of the aggregate was computed from the volume average of the grains reproducing the axial total strain, or by using a single node at the surface, where the displacement boundary conditions were applied. No marked difference existed between the two methods in the present simulations.

7.8.2 Macroscopic behavior of microstructure aggregates

Figures 7.27a and b present a comparison of the macroscopic stress-strain curves and the strain hardening rates of the aggregates in compression. Type II aggregate with varying grain size shows clearly higher hardening behavior after almost identical yield behavior of the two. The use of volume averaged stress does not make any noticeable difference in the curves (dashed vs. solid lines), and for example the curves of the Type I aggregate are almost perfectly overlapping. With the Type II aggregate, the difference arises only because of selecting the grain average based strain instead of using the strain from a single point representing the total aggregate. However, besides the minor differences

Table 7.8: Mesh details for the polycrystal aggregates

Polycrystal mesh	TYPE I	TYPE II
Number of grains	250	183
Average grain size [μm]	150-200	200-600
Mesh type	quadratic tetrahedron	linear tetrahedron
Number of elements	25798	154330
Number of GP	128990	154330
Number of global DOF	113478	96081
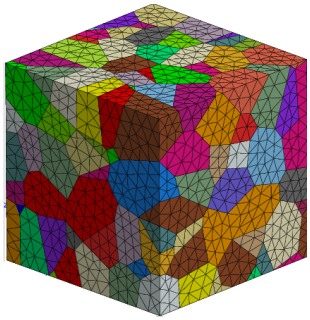		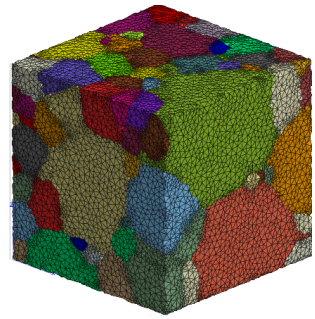
TYPE I		TYPE II

in the averaging schemes, the main difference in the behavior of the two aggregates is also distinguishable in the strain hardening rates. Type II shows a clear increase in the hardening rate slope between 0.1 and 0.25 of strain. Type I, on the other hand, does not show such a marked increase in the strain hardening rate, although a slight increase may be observed also in this case.

The strong evolution of the twin volume fraction in the Type II aggregate in Figure 7.27c shows that the increased strain hardening rate is significantly affected by twinning. Both aggregates exhibit twinning at the early stage, due to relatively low threshold for twinning, but the twinning rate in Type I is clearly lower. The twin saturation begins at around 0.15-0.2 of strain as a combined effect of twin-twin and slip-twin hardening. A connection to the reduced twinning rate can be seen in the strain hardening rate of the Type II aggregate as an pronounced increase in the hardening taking place between 0.15 and 0.25 of strain. After this range of strain, the hardening rate is reduced. The reduction in twinning leads also to a lower number of active twinning systems (see Figure 7.29c later), which reduces the degree of freedom of alternative deformation mechanisms. Hence, dislocation slip will contribute more to the deformation, but the upward curvature of the hardening curve is caused by the existing twins interfering with the dislocation motion. The Type I aggregate did not show the same strong hardening behavior, owing much to its lower average overall twin volume fraction. Because of the fairly smooth saturation behavior, the dislocation slip contributes continuously to the deformation.

Figure 7.27d shows the probability density distribution of the average twin volume content in a grain of the two aggregates at strains 0.1 and 0.4. It can be seen that both aggregates have a number of non-twinned or low-twin grains at the low macroscopic strain level of 0.1. However, twins will develop essentially in all grains at least to some extent in both aggregates. The illustrations of the Mises stresses and twin volume fractions in Figure 7.28 demonstrate non-uniform distributions of stress and twin volume fractions in the polycrystalline aggregates at four different strains.

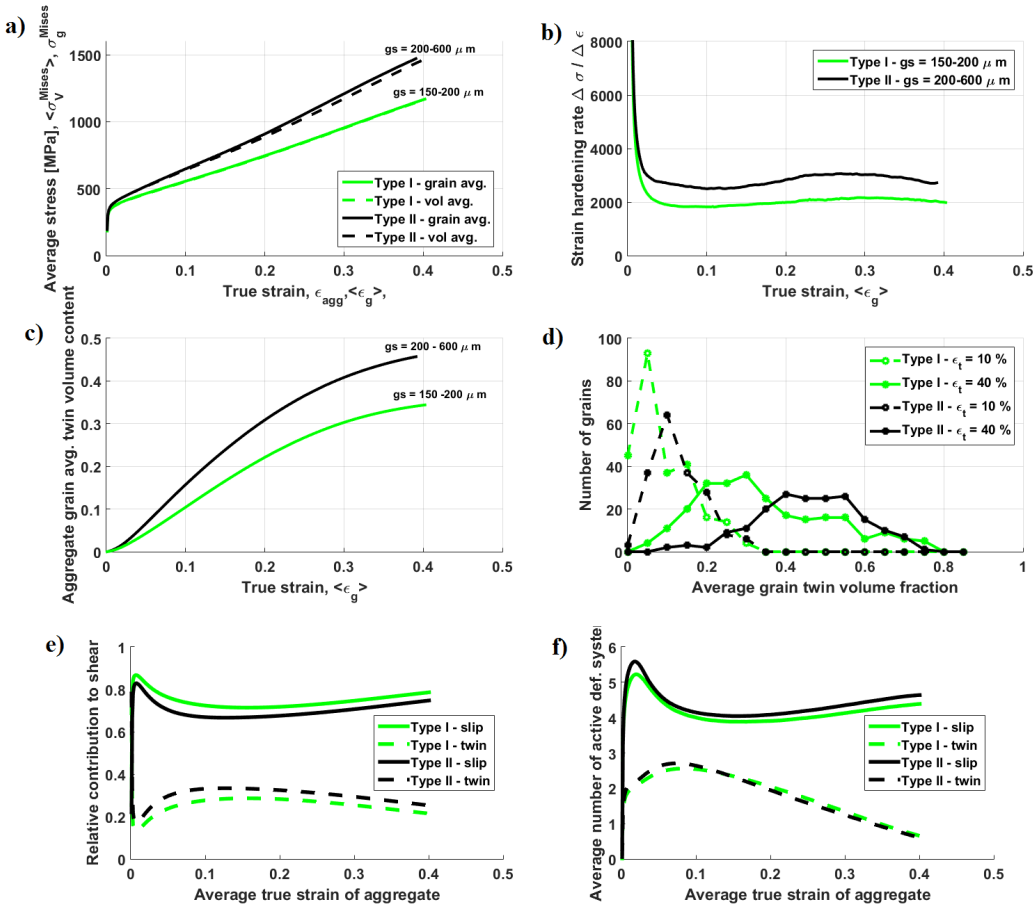

Figure 7.27: Simulated results for two polycrystalline aggregates: a) stress-strain behavior, b) strain hardening rate, c) evolution of twin volume fraction, d) average twin volume fraction distribution in grains at constant strains, e) relative contributions of deformation mechanisms to shear, and f) average number of active deformation mechanism systems in the whole aggregate.

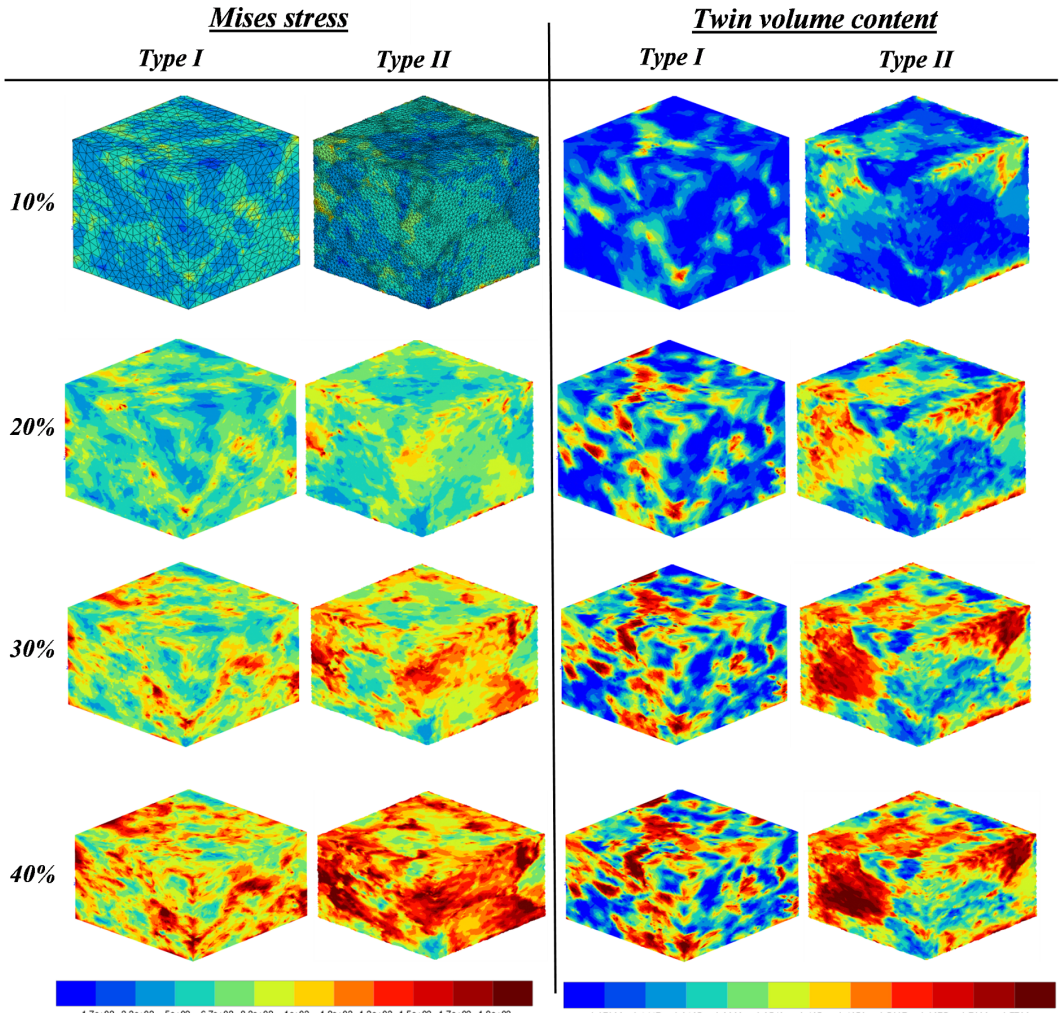

Figure 7.28: Mises stress and twin volume fraction evolution contours at four constant strains for two polycrystalline aggregates in compression.

It is apparent for both aggregates that the grains do not have a uniform stress field, i.e., the stress is higher in some parts of the grains than in the others. Twins tend to develop first in those grains which more easily exceed the critical stress required for twinning. This is consistent with the experimental observations that some grains are highly twinned even at quite low macroscopic strains. Increasing macroscopic strain initiates twinning throughout the microstructure, but the twin volume fraction still continues to increase in many of the already active grains. Finally this leads to stress concentrations in particular in the grains with reasonable amounts of twins. However, the contours show that the whole grain does not necessarily share the high stress state. In addition, it can be observed that stress concentrations may arise at the grain boundaries between two grains, where one of the grains has a low twin volume fraction and the other grain has a moderate to high volume fraction of twins.

7.8.3 Grain level stress-strain behavior

To investigate the local deformation behavior and twin evolution, six random grains were chosen from each aggregate compressed to the strain of 0.4. Figure 7.29c,d. visualizes these grains. The evolution of the twin volume fractions shows that among the chosen grains there are lowly, moderately, and highly twinned grains. Marked twinning at the local scale leads to an upward curvature in the grain's stress-strain curve, whereas more slip controlled deformation results in the typical hardening shape for both simulated aggregates. The local scale deformation resembles the macroscopic stress-strain behavior of the aggregate by increasing the strain hardening rate of the grain when the strongly twinning controlled deformation changes to slip controlled. The initial yielding of the individual grains depends mainly on their orientation, and twinning is activated only after slip first occurs in the grain, as is explicitly constrained by the model.

The average number of active slip and twin systems varies between 4 and 6 and between 1 and 3, respectively. It is, however, seen that a high number of slip and twin systems can be active at the same time regardless that generally it appears that high twinning reduces the slip activity. For example, the grain number 93 in the Type II aggregate showed high deformation activity with both mechanisms. It is evident that the added number of active deformation mechanisms leads to a lower stress-strain response in this case. On the other hand, when slip dominates the deformation, the stress-strain response of a grain remains generally at a higher level than of the grains exhibiting more twinning, at least before the twinning rate saturates and is followed by a strong local hardening. This is visible for example in grains 42 and 203, as compared to the grains 80 and 196 in Type I aggregate.

By comparing the grains 129 and 164 in the Type II aggregate, it can be seen that the neighbouring grains can affect the twinning propensity of a grain. The highly twinned grain 129 has a very high twin volume fraction close to all its boundaries, while the grain 164 shows intense twinning only near the boundary shared with the grain 129. For the grain 164 this suggests that a reasonable amount of its moderate total twin volume fraction originates from the part of the grain close to the boundary shared with the grain number 129.

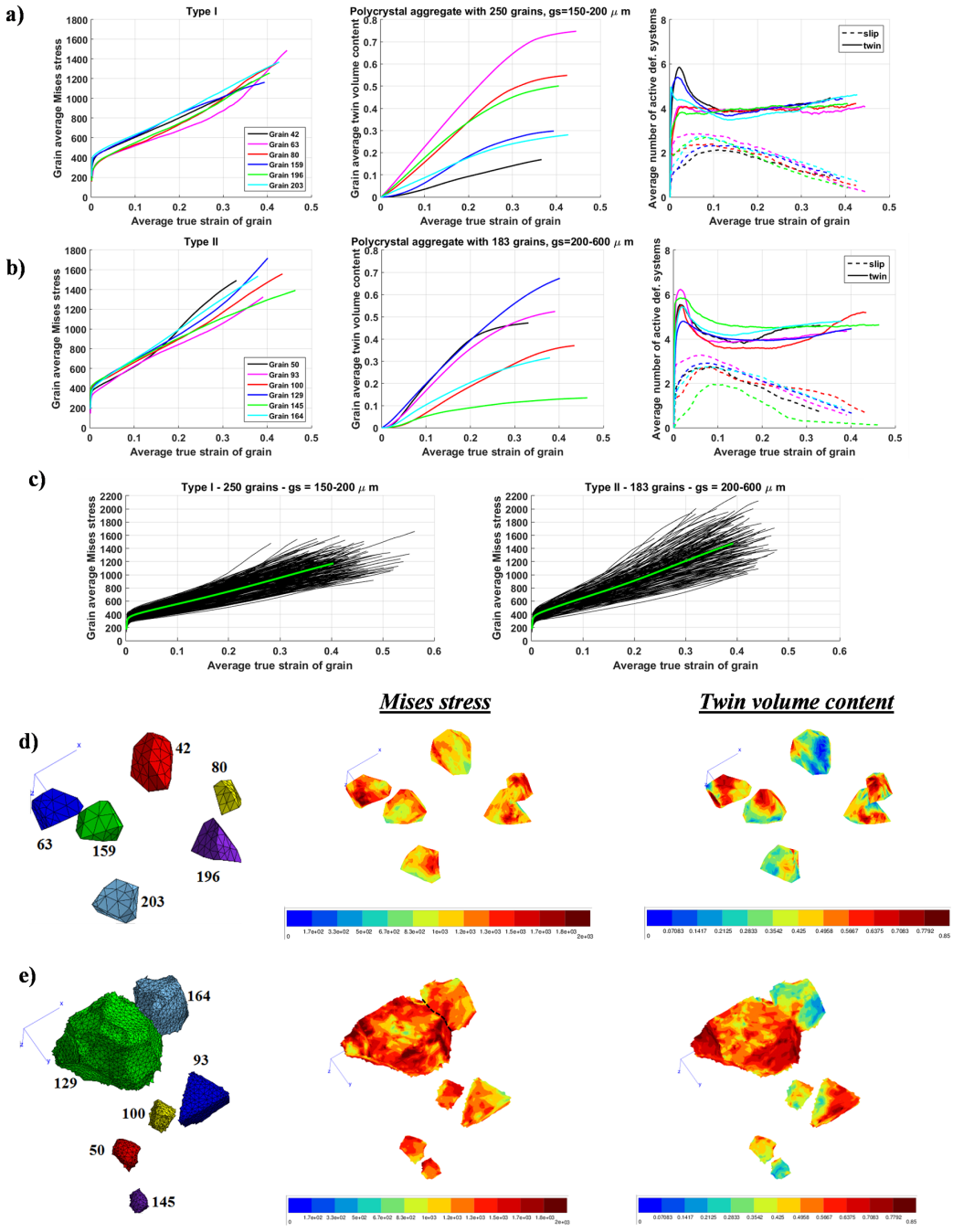

Figure 7.29: Individual grain simulations of the stress-strain behavior, evolution of twin volume fraction, and average number of active slip/twin systems in Type I (a) and Type II (b) aggregates. c) The stress-strain behavior of all individual grains in the aggregates and their average for Type I and Type II microstructures. Selected six grains from the two aggregates (d) and (e), the Mises stresses and twin volume fractions at the strain of ca. 40 %.

7.8.4 Discussion and remarks on Application I

The present simulations of the polycrystalline behavior of two types of aggregates describing different microstructures of the conventional Hadfield steel show that twinning has a significant role in the strain hardening behavior arising from the grain scale. The simulation results suggest that greater variation in the grain structure, including small and large grains, tends to promote twinning and hence causes stronger strain hardening than a grain structure with more uniform small grains. The strain hardening itself depends on the competition between slip and twinning. High slip activity without marked twinning at local level leads to a typical curve shape in the strain hardening of an individual grain. This curve shape transfers to the macroscopic level if there exists a large number of grains exhibiting low twinning, which could be somewhat observed in the case of Type I aggregate. The upward stress-strain curvature, on the other hand, is mainly based on the evolution of the twin volume fraction and the saturation of twinning in the Type II aggregate. This result suggests that the used model is able to capture some of the most crucial strain hardening phenomena of the Hadfield steel, such as twin-slip interaction.

At the local grain level, the strain hardening depends markedly on the twinning rate and its saturation. Upward curvature is most effectively generated in a grain, where the twin volume fraction increases at a reasonable rate before saturating at higher strains, causing hardening for the dislocation slip. Due to the nature of the hardening rule planarity, i.e., whether the twin system is coplanar or non-coplanar with the slip system, the hardening of the slip systems is directly linked to the number of active twin systems contributing to the deformation. For example, if a large number of twin systems are active, as was observed at the beginning of the deformation in both aggregates, there is a higher probability that the slip systems are affected by the non-coplanar twin systems reducing the mean slip distance, especially if the active twin systems are acting on different planes. It is quite plausible that most of the slip systems experience hardening from the twins, as there were usually 1-3 twin systems active over the strain history, but the magnitude of the hardening depends on the sum of the volume fractions of non-coplanar twins relative to these slip systems. As the deformation continues to higher strains, the effect of twin-slip hardening becomes slightly less effective because new twin barriers are no longer effectively generated and slip-slip hardening becomes more important instead. The present EBSD results do not allow to estimate the twin volume fraction at high strains (e.g., around 40 %) to characterize the effectiveness of the two deformation mechanisms. However, the low identification quality, especially in the vicinity of the twins, suggests that dislocation pile-ups are likely present at the matrix-twin boundaries confirming the simulation result of their strong interaction.

The study on the individual grains revealed that orientation has the most significant role in the twin nucleation and growth at low macroscopic strains, as can be expected in a polycrystal microstructure. However, towards higher strains the nucleation of twins in the less favorable grains becames more probable in the simulations because of the hardening of the slip systems and the crystal reorientation in the highly deformed regions. The highly reoriented regions can develop suitable conditions for twinning, as was observed for example in the experiments by the occurrence of twins inside slip bands. The neighboring grains can have some effect on the twinning of the other grains. The results showed that stress concentrations can easily be generated at the grain boundary of lowly and highly twinned grains, as was also found in tensile experiments performed on TWIP steels [87].

As a remark, it should still be noted that the results are not fully conclusive concerning the effect of grain size, since only two cases were investigated and the meshes were

slightly different. Thus it may be that the results obtained with a relatively small number of gauss points could be slightly different when a higher number of gauss points are introduced, as observed already in Section 7.7.2. In addition, the morphology of the grains was different being of the typical Voronoi type for Type I and of a more arbitrary geometry for Type II, which ideally resembles more the cast grain structure of the Hadfield steels. It is also plausible that the grain geometry has an effect on the twin propensity. These aspects should be investigated in the future to shed more light on the behavior of Hadfield steels and the effects of grain size and morphology. The failure modeling of the austenitic microstructure could also provide interesting aspects for finding the optimal microstructure for different wear applications. In such cases, for example, damageable grain boundaries could be explicitly introduced as one source of failure.

7.9 Application II - Deformation of polycrystal aggregate in jaw crusher application

This section demonstrates the use of microstructural models in conjunction with an actual application. The common use of Hadfield steels in mineral crushers makes it a natural choice for the demonstration. Embedded microstructural aggregates in the computations at an application level are usually not a very attractive choice when considering the computational costs. Hence, instead, a deformation history imitating the surface deformation of a jaw crusher is in this example assigned to the microstructural aggregate. The measurement of the deformation history in the application may not be easily conducted, which makes a simulation model more suitable to extract this information. However, at present there is no measured or simulated deformation history available describing the conditions at the surface of a jaw crusher, and therefore a virtual loading history was generated for the simulation.

7.9.1 Modeling conditions

The virtual loading history comprises compression and tension load cycles. For simplicity, only uniaxial deformation of the aggregate surface is assumed. In reality, different contact pressure distributions load the surface of the material. With the finite element discretization of the jaw crusher surface, even the simplified alternative would resemble the deformation behavior of one surface node. The main objective of this approach is to evaluate the material performance at the surface of the jaw crusher based on the stress-strain response of the microstructure aggregates. Given that the microstructural aggregate can describe the macroscopic behavior of the material, it is assumed that the local scale deformation is also described with sufficient accuracy. Hence, by changing some variable in the microstructure, such as the grain size, it is possible to evaluate the effect of these variables on the deformation response, for example to quantify the distributions of stress concentrations in the microstructure that could cause failure. As an alternative to importing the deformation history, which is the product of the macroscopic stress-strain behavior, it is also possible to use the detailed force history. However, in the case of a force history, it is important to ensure correct scale transitions between the macroscopic and microscopic meshes (e.g., contact area) to maintain realistic pressure distributions, etc. Figure 7.30 shows the simplified virtual deformation history used in the current simulations, and its idealized origin from the crushing event.

The loading history contains 50 cycles with durations ranging from 10 ms up to 1000 ms, with an average of around 500 ms for each individual load increment. The strain rate

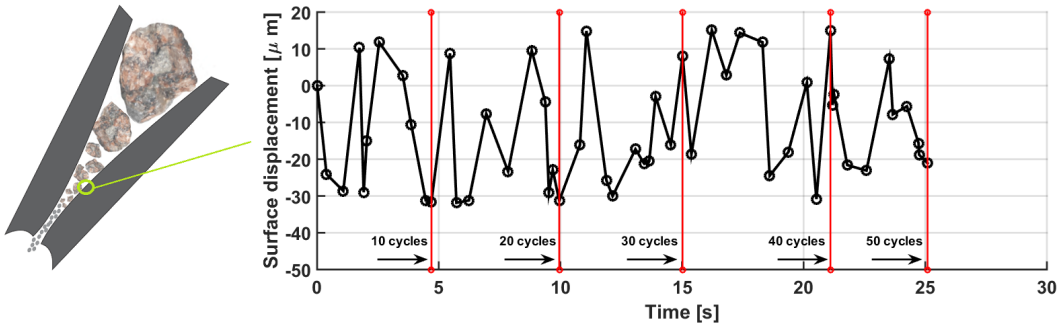

Figure 7.30: Virtual displacement history of a surface material point in a jaw crusher application with 50 loading cycles.

then varies between 0.01 and 1.0 s^{-1}. The amplitude was chosen relative low to decrease the computational time, i.e., quite small macroscopic deformations are applied to the aggregate. The Type II aggregate presented in Table 7.8 was chosen for the simulations due to its more realistic grain morphology. The rate of equivalent plastic strain (eqv. Mises strain) shown in the result contours is defined as:

$$\begin{aligned} &\dot{\epsilon}_p^{eqv} = \sqrt{\frac{2}{3}\underline{\dot{\epsilon}}_p : \underline{\dot{\epsilon}}_p}, \\ &with\ \underline{\dot{\epsilon}}_p = (1 - \sum_\beta f^\beta)\underline{\dot{\epsilon}}_p^{sl} + \underline{\dot{\epsilon}}_p^{tw}, \\ &where\ \underline{\dot{\epsilon}}_p^{sl} = \sum_s \dot{\gamma}^s \underline{m}^{sl},\ and\ \underline{\dot{\epsilon}}_p^{tw} = \sum_\beta \gamma^{tw} \dot{f}^\beta \underline{m}^t \end{aligned} \tag{7.38}$$

The total equivalent plastic strain is achieved by integration over the total computation time.

7.9.2 Results and discussion

Figures 7.31a and b present the evolution of the stress state in the aggregate and grain levels. The average aggregate stress level increases as a function of cycles until ca. 20 cycles or 10 seconds of loading. This is also evident in the grain scale stresses, where only minor changes in the local stress states are observed at higher numbers of loading cycles. Similarly, the average twin volume fraction of the 183 grain aggregate saturates to a more or less constant level of 0.3 after ca. 15 seconds of loading. The grain level twin volume fraction averages remain also quite constant, as the amplitudes of the virtual loading cycles are not sufficient to initiate twinning to a large extent. Because of the increased flow stress of the material, many parts of the grains start to behave elastically and the plastic deformation is accommodated mainly by slip and and to a small extent by twinning.

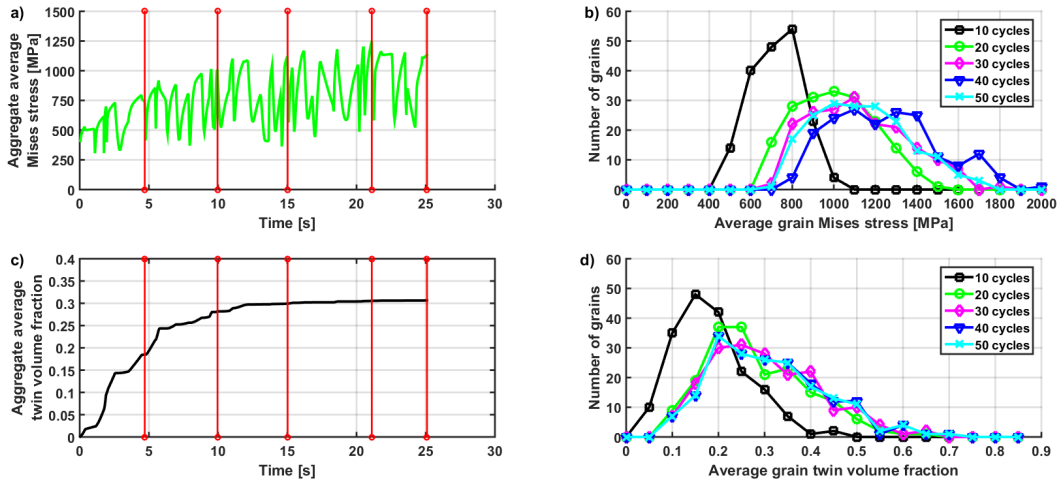

Figure 7.31: Evolution of a) the average Mises stress in the whole aggregate, b) average Mises stress in the grains after different numbers of cycles , c) twin volume fraction average in the whole aggregate, and d) average twin volume fractions in the grains after different numbers of cycles.

The contours in Figure 7.32 illustrate the instantaneous stress state, accumulated twin volume content, and the equivalent plastic strain state after different numbers of loading cycles. The overall stress state of the aggregate depends on the magnitude of the applied displacement at the boundary given by the deformation history. However, some stress concentrations are developed because of the evolution of slip and twinning inside the grains, generating partially heavily twinned grain regions.

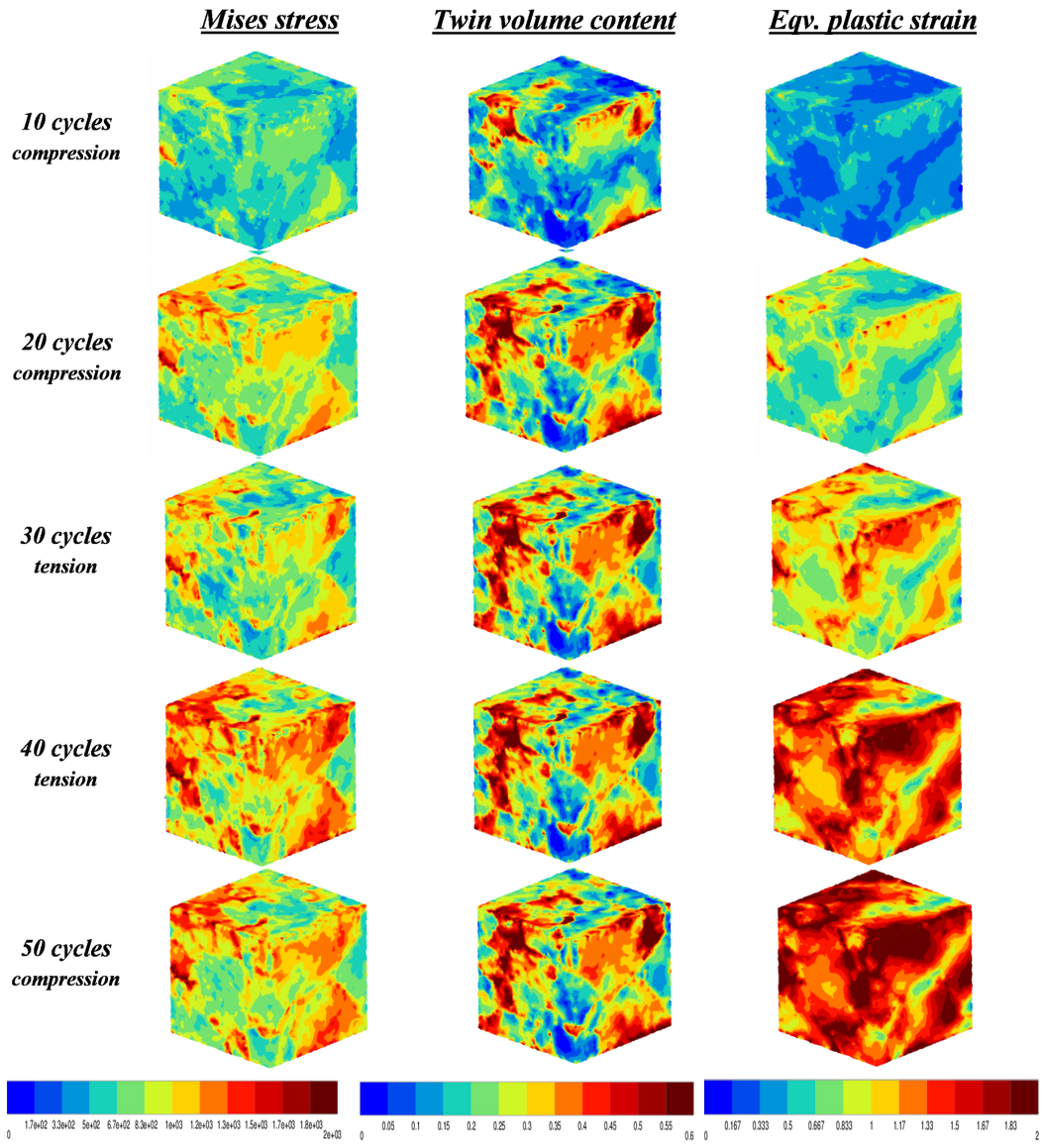

Figure 7.32: Mises stress, twin volume content and equivalent plastic strain after different numbers of loading cycles. Compression/tension expresses the current state of deformation at a particular number of cycles.

The local grain level stress-strain behavior can vary significantly, as presented in Figure 7.33a for two grains, which have ca. 50 % difference in the average stress states. The difference in the average twin volume fractions, in turn, is not necessarily that high (Figure 7.33b), which indicates that twinning is not solely responsible for the hardening. Some of the chosen grains can reach up to 0.7 in the twin volume fraction, while their stress state corresponds roughly to the one seen for grain 88 in Figure 7.33a. The intragranular stresses, on the other hand, can be elevated when a dense twin population exist in some part of the grain. Also, the cyclic loading builds up stress concentrations near the grain

boundaries, which is one of the main sources of failure in the current material, as was observed in the impact experiments. The strain is distributed heterogeneously in the microstructure depending on the activity of the different deformation mechanisms.

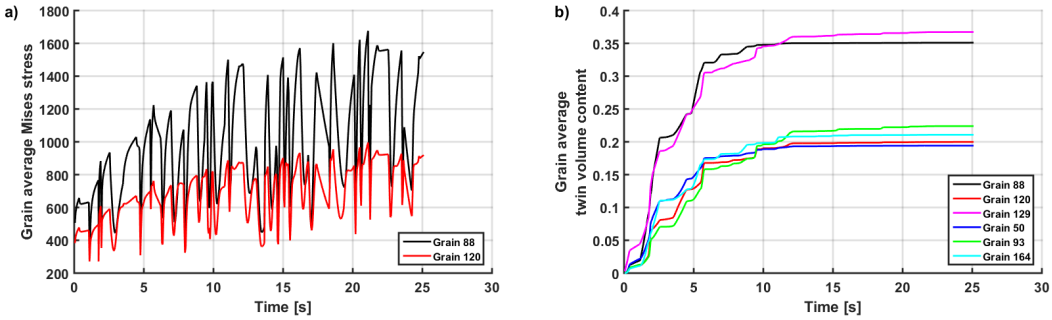

Figure 7.33: a) Average stress-strain evolution in two grains, and b) average evolution of the twin volume fraction in several grains.

7.10 Summary and partial conclusions

A phenomenological crystal plasticity model was developed for FCC crystal structures including dislocation slip and twinning as concurrent deformation mechanisms. The model was implemented within the large deformation framework to investigate the strain localization and large macroscopic strains observed in steels in wear conditions. Numerical implementation was done using explicit and implicit integration methods in Zébulon commercial software. The model comprised different hardening descriptions related to slip and twinning, including slip-slip, twin-slip, twin-twin, and slip-twin interactions, which were included in the model based on the experimental observations on the deformed Hadfield steel microstructure and literature describing the deformation behavior of TWIP and Hadfield steels.

The model characteristics were demonstrated for a wide range of conditions to describe the effects of the most important model parameters. The model verification was first performed on Hadfield steel single crystals. The identification was then continued with the polycrystal representative volume elements representing the macroscopic behavior of Hadfield steels. The following observations and conclusions were made:

- Care should be exercised when dealing with the complex nature of the model parameters and their interactions, e.g., when presenting uniaxial deformation, kinematic conditions, or strain and strain rate history.
- The present crystal plasticity model describes the stress-strain behavior of some selected orientations of the Hadfield steel single crystals in tension and compression with a reasonable accuracy. The orientation dependent biasing of slip or twinning as the main deformation mechanism can be captured by the model.
- Some discrepancies existed in the compression behavior of two orientations mainly because of the localized deformation observed in the experiments and because of the partly suppressed activation of secondary systems in the single slip case. Both cases represent special deformation cases, which do not necessarily often take place

in polycrystalline structures, as was found in the experimental characterization of the polycrystalline Hadfield steel.

- The computations performed with the polycrystalline structure verified that the model is capable of describing the macroscopic stress-strain behavior and the twin evolution of a Hadfield steel. The tension-compression asymmetry was presented well by the model.

- Simulations performed in compression and tension for another Hadfield steel alloy verify that the macroscopic stress-strain behavior and twin evolution can be well reproduced for different alloys.

- The simulations pointed out that the current modeling approach is capable of describing the macroscopic stress-strain response at various strain rates from quasi-static to dynamic with an acceptable accuracy, when positive strain rate dependency exists in the material. The strain rate dependency of dislocation slip and twinning were captured by the model based on the physical aspects. However, further characterization including the volume fractions of twins at high strain rates is required to fully verify the model performance.

To demonstrate the model performance with actual grain morphologies, fairly large uniaxial plastic deformation was subjected to two different types of randomly oriented polycrystal aggregates with different grain size and grain morphology. The stress/strain localization and the twin volume fraction evolution were studied at the macroscopic and grain levels. The following observations and conclusions were made:

- The stress-strain responses of the two types of aggregates were different mainly because of the dissimilar twin evolution, which had a significant effect on the strain hardening behavior of the aggregates. Based on the present simulations, twinning is more preferential in the microstructure containing a variety of small and large grains in comparison to the microstructure containing only small grains with a more or less uniform size.

- The macroscopic strain hardening showed an upward curvature, which is caused by the quickly increasing twin volume fraction followed by its saturation, creating strong obstacles to dislocation slip. A more typical stress-strain curve shape was observed when twinning had a less significant role in the deformation, which was the case for the aggregate with small uniformly sized grains.

- At the grain level, the local stress-strain curvature depended in a similar manner directly on the twin volume fraction evolution, high twin volume fraction resulting in an upward curvature of the flow stress curve. The number of active slip or twin systems depends mainly of the initial orientation of the grain and the hardening related to the deformation mechanism. Generally, twins are developed first in one or two systems, which is followed by additional systems before hardening suppresses the average number back to one in the grain level. This behavior is in good agreement with the experimental observations of the Hadfield steel. The average number of active dislocation slip systems in a grain generally varies between four and six, occasionally reaching up to eight. The number of slip systems usually saturates to four systems.

- The selection of grains that are susceptible to twinning is controlled by their orientation relative to the loading direction. At small macroscopic strains only these grains develop twins, but higher macroscopic strains increase the number of twinned grains. The boundary condition effect from the neighboring grains can have some effect on the development of twinning and stress concentrations.
- The model simulated the intra-grain homogeneities fairly well. This was verified by the experimental observations, showing that there are highly twinned and highly slip controlled regions in a grain, especially in the larger grains.

In addition, a virtual deformation history was used to simulate the behavior of a polycrystal aggregate in the conditions existing on the surface of a mineral crusher jaw. The following observations and conclusions can be presented based on these simulations.

- The local hardening of the grains develops a reasonable resistance against deformation in a small amplitude cyclic deformation. The twinning and slip activities saturate at the aggregate level, when the hardening increases the plastic flow stress to a certain threshold level, i.e., the material's surface hardness is increased. The probability of stress concentrations, however, was increased with increasing number of loading cycles, which can have a deteriorating effect on the wear resistance if damage nucleates and propagates in these regions.
- The loading history concept of a surface node showed a feasible way to incorporate the application level deformation to the local level in the jaw crusher application. The method allows to study the localization of stresses and strains in the microstructure as a consequence of different loading conditions during the deformation, instead of only characterizing the post-mortem state of the deformed material.

8 Martensitic steels - BCC crystal plasticity models

The following section introduces a crystal plasticity model for BCC metals, which is implemented in the same large deformation framework in Zébulon as the FCC model discussed in Section 6. The basic crystal plasticity model is extended with a simple phenomenological description of shear banding, which in the current work is aimed to provide additional functionality over the conventional crystal plasticity description of BCC microstructures at high strain rates. Both models are discussed and demonstrated with some examples, and an initial parameter search is performed. The ultimate aim of the models is to study the deformation behavior of martensitic wear steel, which will be briefly exemplified in the final part of the section.

8.1 Modeling of deformation in martensitic microstructure

In the literature, the martensitic steels have received fairly little attention in the field of crystal plasticity modeling despite the continuous use of these types of steels. One reason for the use hard martensitic steels is that for example mining industry needs materials that can withstand extremely harsh deformation conditions and wear. From the modeling point of view, besides the great uncertainty over the boundary conditions that the steels face in such mining applications, the modeling of large deformations in fine microstructures is also computationally heavy. For example, fine lath martensite microstructure including a large number of details quickly increases the number of discretizing elements required to represent the complex structure. At the same time, large deformations tend to cause mesh distortions further increasing the risk for numerical divergence, especially in the case of shear localization phenomena, such as shear banding. Another challenging feature is the actual representation of the microstructure in generic forms. The algorithms, essential in generating representative volume aggregates, are still largely under development. The ones that exist are often designed to simplify the microstructure to some extent, for example as discussed by Osipov [168]. Alternatively, the EBSD technique can provide meshable 'correct' microstructures for 2D use. However, the two dimensional structure lacks the in-depth behavior of the material, which has a quite substantial effect on the material behavior, as pointed out by Musienko et al. [160]. It is possible to extrude the 2D microstructure to 3D, but the extruded geometric models are still quite far from reality. A more correct type of 3D microstructure can be achieved, for example, by using the slice-by-slice method with focused ion beam milling (or simply polishing off the material) and measuring the microstructure with EBSD at the x-y location. This technique is rather time consuming and thus expensive, but it can provide more realistic microstructures for simulations. One possibility to obtain a realistic type of a microstructure is to

use 3D tomography techniques, such as Xray radiography/tomography. In summary, in order to compute martensitic microstructures (or alikes) effectively, the synthetic microstructures require some amount of simplifications, but they can perform better yielding more information about the grain structure. More detailed information can be achieved from the realistic type of microstructure, i.e., by representing the actual microstructure in correct scale with only minor discretization errors.

The challenges in the modeling of the microstructure geometry of the martensitic steels do not rule out the common developments of the BCC crystal plasticity framework. In fact, a number of these models exists, however, mostly addressing other grain structures and assemblies, as for example in refs. [164, 171, 173, 202, 227]. The modelling approaches include both phenomenological and DD-driven models similar to the FCC (and HCP) crystal structure models, depending on the purpose of the models. The complexity of the models can become significant and computationally heavy, when detailed dislocation dynamics inspired descriptions of dislocation interactions are accounted for. The studies focusing especially on martensitic steels aim to understand the deformation behavior of the steels from different perspectives, approaching the subject piece by piece. For example, Maresca et al. [144] aimed to reveal the importance of the lath microstructure and to investigate the effect of retained austenite. They found that at the microscale the retained austenite has a quite significant effect on the flow behavior, which was also observed by Wu et al. [225]. Li et al. [124] incorporated the length-scale in their crystal plasticity model by introducing geometrically necessary dislocations. Their approach was restricted to 2D microstructures with 12 slip systems, but the addition of the length-scale performed quite well when non-explicitly presented lath sizes and precipitates were involved, i.e., these features are not required to be presented in the computational mesh as a courtesy of the model. The study of Shanthraj and Zikry [201] on the failure propensity of different simplified computational martensitic microstructures showed the importance of the grain structure to the failure behavior.

The number of slip systems providing deformation in the BCC crystal structure can vary from 12 through 24 to 48, comprising of twelve {110} <111>, twelve {112} <111>, and 24 {123} <111> systems, as described in the studies mentioned above. Often a simplification is made to reduce the number of slip systems to 12 to reduce the degrees of freedom in the deformation by concentrating either on the type {110} <111> or {112} <111> slip system family, while the 24 {123} <111> systems are considered to become activated only at higher temperatures. Also, a common way is to include both of the {110} <111> and {112} <111> families, totalling in 24 slip systems, as listed in Tables 8.1 and 8.2. This work adopts the choice of 24 slip systems, since the model is aimed to operate at room temperature only. Some studies (but surprisingly not many), e.g., [55, 144, 171, 232], address the non-Schmid effects in the BCC slip related to the cross-slip, that inevitably causes some deviation from the Schmid law. However, the present approach assumes the Schmid type rule to hold for simplicity, and the further implementations of this effect are left for future developments of the model.

Table 8.1: The twelve independent BCC {110} <111> slip systems

(110) $(\bar{1}10)$ $(1\bar{1}0)$ $(11\bar{1})$	(101) $(\bar{1}01)$ $(10\bar{1})$ $(1\bar{1}1)$	(011) $(0\bar{1}1)$ $(01\bar{1})$ $(\bar{1}11)$
$[\bar{1}11]$ $[1\bar{1}1]$ $[111]$ $[11\bar{1}]$	$[11\bar{1}]$ $[\bar{1}11]$ $[111]$ $[1\bar{1}1]$	$[11\bar{1}]$ $[1\bar{1}1]$ $[111]$ $[\bar{1}11]$

Table 8.2: The twelve independent BCC 112 <111> slip systems

(112) (1̄12) (11̄2)	(121) (1̄21) (12̄1)	(211) (2̄11) (21̄1)
[11̄1̄] [11̄1] [1̄11] [111]	[11̄1] [11̄1̄] [111] [1̄11]	[1̄11] [111] [11̄1̄] [11̄1]

Figure 8.1 illustrates the transition from the single crystal behavior to the polycrystal aggregate scale. The single crystal model describes the behavior of the crystal structure with a certain orientation or a group of orientations at the grain scale. The information of the prior austenite grain size, block and packet sizes observed at the grain scale, is important in determining the deformation behavior at the local scale. The difference to an actual austenitic microstructure is that one prior austenite grain already includes a number of subgrain structures underlining the significance of these structures. The overall performance of a microstructure can be obtained when larger polycrystal microstructures are investigated, as the compound effect of the grain structure is more easily revealed. Thus, in order to properly understand the behavior of these type of microstructures, it is advisable to divide the process into steps beginning from the model development that includes the most essential micromechanical phenomena, ultimately ending in the transition from the small scale to macro-scale behavior.

The present work concentrates on the development of the single crystal models in order to provide tools for future use. First the implementation of a phenomenological model to the large deformation code is performed, and the preliminary identification of the parameters is done for one martensitic steel grade studied in this work. The lack of shear banding models in the above mentioned approaches on the martensitic steels is addressed by developing a way to include shear banding as a phenomenological deformation mechanism. Its significance is demonstrated with single crystal simulations at various strain rates. The actual computations with large scale polycrystal aggregates are left beyond this work, already due to the large computational time required for their completion. However, the model implementations allow to use the current approaches even in loading conditions that cause heavy deformation in the aggregate, which is also one of the main objectives of this work.

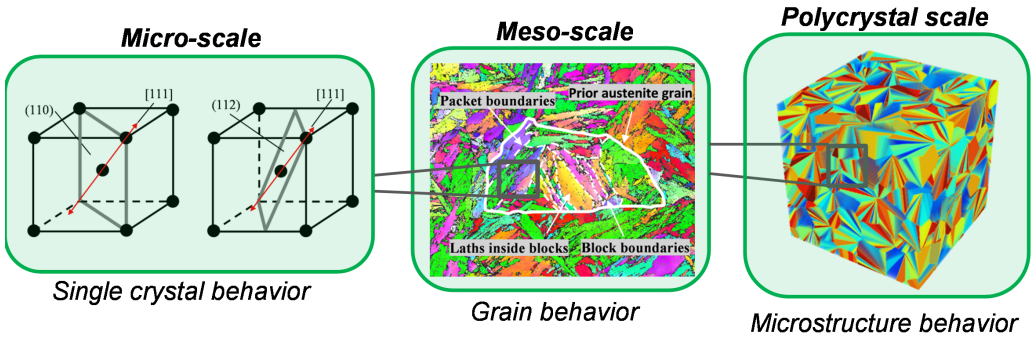

Figure 8.1: Multi-scale representation of micromechanical deformation in martensitic microstructures.

8.2 Single crystal plasticity BCC model

The BCC crystal plasticity model follows the same framework as presented in the previous chapter for FCC crystals. In the current model, the plastic strain is accommodated in the BCC crystal only by dislocation slip, i.e.,

$$\underline{\dot{\epsilon}}^p = \sum_{s=1}^{N_s=24} \dot{\gamma}^s \underline{m}^s \tag{8.1}$$

Here, the model is referred to as the 'BCC basic model' to make a difference for the shear band extended model, which will be presented later in this chapter.

8.2.1 Slip rate

The same phenomenological flow model as before is adopted here as well with a possibility to introduce kinematic hardening parameters by x^s. However, in the absence of cyclic experimental data, the kinematic terms are set to zero in all calculations. The same constraints describing the activation of slip systems apply to this flow model as was presented with the FCC flow rule, i.e., slip is only activated when the critical resolved shear stress of a system is exceeded.

$$\dot{\gamma^s} = \dot{\nu}\, sign(\tau^s) = \left\langle \frac{|\tau^s - x^s| - r^s - \tau_y}{K} \right\rangle^n sign(\tau^s - x^s) \tag{8.2}$$

$$x^s = c\alpha_s \;;\; \dot{\alpha}_s = (sign(\tau^s - x^s) - d\alpha^s)\dot{\nu}^s \tag{8.3}$$

Both of the included slip families $\{110\} < 111 >$ and $\{112\} < 111 >$ share the same flow rule. However, the viscous parameters K and n can be different in addition to dissimilar critical resolved shear stresses for the activation, if necessary, and the parameters can be identified from the experimental data and characterizations. All of the slip systems in a slip family are assumed to have the same critical value for activation.

8.2.2 Hardening through slip-slip interaction

Isotropic hardening is assumed for all systems with the following equation of evolution including self and latent hardening. The present expression considers the interactions between the two slip families in contrast to an alternative model utilized by Osipov [168] for bainitic steels, where a slip family only interacts with itself.

$$r^s = bQ \sum_{s}^{n_s} h_{n_s} \rho^s = Q \sum_{r} H_{rs}\{1 - exp(-bv^r)\} \quad \dot{\rho}^s = (1 - b\rho^s)\dot{\nu}^s \tag{8.4}$$

The interaction matrix is adopted from the work of Hoc and Forest [91] on an IF-Ti alloy. They noted that a simplified expression including only the self-hardening coefficient (a^{ss}) and the latent hardening coefficient (a^{su}) suffice to describe monotonic loadings, but fail to represent complex strain paths. For this reason, they suggested a modification that introduces a 24x24 interaction matrix composing of six different coefficients. A

Table 8.3: The coefficients for the interaction matrix in BCC crystals [91]

Plane	$\{110\} \cap \{110\}$	$\{110\} \cap \{112\}$	$\{112\} \cap \{112\}$
Same	a_0 (h_8)		$k_{s0}a_0$ (h_1)
Collinear	k_1a_0 (h_2)	$k_{p1}a_0$ (h_3)	$k_{s0}k_1a_0$ (h_6)
No collinearity	$k_2k_1a_0$ (h_4)	$k_{p2}k_{p1}a_0$ (h_5)	$k_{s0}k_2k_1a_0$ (h_7)

classification of the slip systems belonging to the same slip family, to a collinear system or to a non-collinear system was made, as presented in Table 8.3.

Hoc and Forest [91] assumed the interaction between planes {110} to be smaller than between planes {112}. A similar assumption with some additional simplifications was made by Mathieu [146] in the case of ferrite. The results showed good agreement with the experiments in both cases, and hence the model with a 24x24 interaction matrix was seen sufficient also for the present work. The amount of interaction coefficients H_i is increased to eight, when each interaction type is considered separately.

8.2.3 Summary of the BCC basic model

The residuals of the basic BCC model are presented in the following box. The hardening of a slip system is not considered as an internal variable, but it is rather embedded in the residual of the flow rule.

The residuals for each internal variable (BCC basic model)

$$R_{\underline{E}} = \Delta\underline{E} - \Delta\underline{F} \cdot \underline{F}^{-1} \cdot \underline{E} + \underline{E} \cdot \left(\sum \Delta\nu^s \underline{m}^s sign(\tau^s - x^s) \right)$$

$$R_{\nu^s} = \Delta\nu^s - \left(\frac{|\tau^s - x^s| - r^s - \tau_y}{K} \right)^n \Delta t$$

$$R_{\rho^s} = \Delta\rho^s - (1 - b\rho^s)\Delta\nu^s$$

$$R_{\alpha^s} = \Delta\alpha^s - (sign(\tau^s - x^s) - d\alpha^s)\Delta\nu^s \text{ if kinematic hardening is used}$$

The updating of the variables is performed in the same way as presented in the previous chapter.

8.3 Extension of micro shear banding in BCC crystal plasticity

In this section a phenomenological description of shear bands is incorporated in the BCC basic model. This extension is suggested to the current modeling framework for future studies concentrating on the shear banding of martensitic wear resistant steels, occurring for example in the impact conditions as a consequence of stress concentrations and high strain rates. As it stands, the basic model is not capable of reproducing softening at high strain rates, since the model assumes continuous strengthening of the material, i.e., higher strain rates only shift the curve to higher flow stresses.

To capture the effect of shear banding and strain localization, which are two obvious reasons for the softening and failure at high strain rates, a phenomenological description of

the shear band phenomenon is introduced to complement the basic approach of dislocation slip controlled plastic flow presented in the previous section. The shear banding is assumed to be triggered only by dislocation slip when the activation criterion, i.e., the critical threshold stress for shear banding is met. The formulation is considered analogous to the flow behavior of dislocations to provide a physically similar behavior and to combine it with rate dependency. Thus, the following extension does not aim to replace the typical combinations of slip planes and directions, but rather to offer an alternative deformation mechanism that the basic model is not necessarily capable of providing.

It is worth noting that as the present framework is not currently coupled with temperature, the flow model is driven by stress and controlled by the activity of conventional slip systems (and their rate) to couple the model to the common conditions required for shear banding. Also, as a consequence, the phenomenological description does not make a difference between adiabatic shear bands and highly deformed shear bands. The former, for example, could in some cases form quite early at high strain rates, whereas the latter is assumed to occur only when high stress concentrations build up in the microstructure due to extensive shear deformation regardless of the strain rate. In fact, the model extension aims to capture both of these shear band mechanisms by utilizing the effect of positive strain rate dependence and its coupling to stress. High strain rates increase the flow stress making the conditions also more favorable for shear band activation. In addition, the high plastic strains accompanied by strain hardening have the same effect of increasing the flow stress that can trigger shear banding, if it is considered that the conventional dislocation slip does not greatly increase the resistance to the shear band mechanism.

Another aspect of the extension is that the model is formulated with respect to the principal directions of the stress tensor, which both evolve during the computations. It follows that due to this choice, the shear band systems do not necessarily respect the common crystallographic planes and directions, and hence the term 'non-crystallographic' is often adopted. Instead, the material is considered as a continuum that can deform in these virtual 'slip systems', as was originally suggested by Anand and Su [8]. The reason for using such a way is to reduce the complexity of the shear banding phenomenon at the crystallographic level, and simply to describe shear banding in a more close relation to the material damage-like behavior, which is often controlled for example by the principal stresses.

In the modeling approach of Anand and Su [8] they considered the deformation of amorphous glasses by virtual shear band slip systems. The constitutive model in their work was intended to describe decohesion of the material. Following the same principal ideas, Wei et al. [221] performed studies on the grain boundary decohesion of nanocrystalline metallic materials alongside a more classical approach of crystal plasticity in the grain interiors. Recently, Jia and coworkers [105 – 108] used a similar approach, extending the functionality of slip and twin controlled deformation in the FCC structures to include also shear banding. In addition, they utilized the same model for the BCC shear banding of pure metals. Their approach differs from the two former studies by considering shear banding as an additional deformation mechanism contributing to the total shear of the material instead being only a direct cause of failure. However, the studies utilizing a similar shear band approach mainly focus on either non-metallic materials or pure metals, and they do not account for any relationship to high strain rate or high strain triggered shear banding, which makes the use of these models somewhat insufficient for modeling of the high and ultra high strength steels. Hence, the present model aims to include shear banding at room temperature, but mainly at high strain rates or high strains to elucidate

the localized deformation behavior in the microstructures of martensitic steels.

8.3.1 Incorporation of potential shear band systems

The shear band mechanism adopted in the present model is suggested by Anand and Su [8], as already pointed out. In this approach, the potential shear band systems are constructed relative to the three principal directions of the second Piola-Kirschoff stress tensor. It is assumed that shear banding favors the directions of the principal stresses in the material causing the highest probability for localized phenomena. In the present framework it would be consistent to extract the principal stress directions from the Mandel stress tensor $\underline{M}$. However, to avoid imaginary roots of a non-symmetric tensor, which is possible for a Mandel stress tensor, the systems are extracted also from the symmetric second PK stress tensor. To include the potential shear band systems into the present framework, the plastic velocity gradient is modified to add the contribution of micro shear banding as

$$\underline{\dot{\epsilon}}^p = \underbrace{\sum_{s=1}^{N_s} \dot{\gamma}^s \underline{m}^s}_{Slip} + \underbrace{\sum_{\chi}^{N_\chi} \dot{\gamma}^\chi \underline{m}^\chi}_{Shear\ banding} \tag{8.5}$$

where $\dot{\gamma}^\chi$ is the shear rate of a micro shear band system χ^s and $\underline{m}^\chi$ is the orientation tensor consisting of the slip plane normal and the slip direction. The decomposition of the PKII stress in Equation 8.6 provides the principal directions of the tensor from which the potential systems are constructed. It is worth noting that the shear bands in the current framework contribute only to the plastic strain rate and share the same orientation with the matrix (grain).

$$\underline{S} = \sum_{i=1}^{3} \sigma_i \hat{e}_i \otimes \hat{e}_i \tag{8.6}$$

where σ_i are the principal stresses and $\hat{e}_i$ the orthogonal principal directions. The principal stresses are strictly ordered as $\sigma_1 \geq \sigma_2 \geq \sigma_3$. Each ($\hat{e}_i$ - $\hat{e}_j$) has two potential shear band systems in the defined direction $\mathbf{m}^*$ on the plane $\mathbf{n}^*$.

$$\begin{aligned} m^{(1)} &= cos(\pi/4)e_i + sin(\pi/4)e_j \\ n^{(1)} &= sin(\pi/4)e_i - cos(\pi/4)e_j \\ m^{(2)} &= cos(\pi/4)e_i - sin(\pi/4)e_j \\ n^{(2)} &= sin(\pi/4)e_i + cos(\pi/4)e_j \end{aligned} \tag{8.7}$$

where indices i and j range from 1 to 3 and $i \neq j$ (in 3D cases). The final number of the shear band systems is six.

The micro shear band slip directions and plane normals

$$
\begin{aligned}
m^{(1)} &= cos(\pi/4)e_1 + sin(\pi/4)e_3 \;;\; n^{(1)} = sin(\pi/4)e_1 - cos(\pi/4)e_3 \\
m^{(2)} &= cos(\pi/4)e_1 - sin(\pi/4)e_3 \;;\; n^{(2)} = sin(\pi/4)e_1 + cos(\pi/4)e_3 \\
m^{(3)} &= cos(\pi/4)e_1 + sin(\pi/4)e_2 \;;\; n^{(3)} = sin(\pi/4)e_1 - cos(\pi/4)e_2 \\
m^{(4)} &= cos(\pi/4)e_1 - sin(\pi/4)e_2 \;;\; n^{(4)} = sin(\pi/4)e_1 + cos(\pi/4)e_2 \\
m^{(5)} &= cos(\pi/4)e_2 + sin(\pi/4)e_3 \;;\; n^{(5)} = sin(\pi/4)e_2 - cos(\pi/4)e_3 \\
m^{(6)} &= cos(\pi/4)e_2 - sin(\pi/4)e_3 \;;\; n^{(6)} = sin(\pi/4)e_2 + cos(\pi/4)e_3
\end{aligned}
$$

There are some cases, e.g., $\sigma_1 > \sigma_2 = \sigma_3$, where there is an infinite number of orthonormal vectors $\hat{e}_2$ and $\hat{e}_3$ to $\hat{e}_1$ [8]. Therefore, an arbitrary pair of orthonormal vectors $\hat{e}_2$ and $\hat{e}_3$ perpendicular to $\hat{e}_1$ is chosen, which causes the slip system selection to be ambiguous.

8.3.2 Flow rule of the micro shear bands

The kinematic description of the equation is formulated analogous to the slip flow rules used in this work. However, the flow rule is constrained by the activity of conventional slip systems so that shear banding may only take place when dislocations are mobile ($\sum_{i=1}^{24} |\dot{\gamma}| > 0$), i.e., these dislocations are the fundamental driving force establishing micro shear bands and controlling their growth. The viscoplastic formulation acts as a secondary constraint controlling the magnitude of the contribution to the overall plastic strain rate. For example, the parameters can be chosen so that shear bands are triggered only at high strain rates where the flow stress is higher, or after an extensive shear strain has taken place, as pointed out above. The following equation presents the formulation:

$$\dot{\gamma^{\chi}} = \dot{\chi^{r}}\, sign(\tau^{\chi r}) = K_b \left\langle \frac{|\tau^{\chi r}| - r^{\chi}}{K_{\chi}} \right\rangle^{n_{\chi}} sign(\tau^{\chi r}) \sum_{1}^{s} \Delta\nu^{s} \tag{8.8}$$

where K_b is a fitting coefficient to control the intensity of shear banding and K_{χ} and n_{χ} are the viscous parameters.

The shear band activity is restricted by the critical resolved shear stress of a shear band system, according to which a shear band system activates only when $|\tau^{\chi r}| > r^{\chi}$, where r^{χ} is the total resistance against shear banding, including both the initial resistance and the isotropic hardening part. It is worth noting that the present model uses the same flow rule for the initiation and growth, which is a common simplification over some more complicated modelling approaches using different constitutive models for the nucleation and growth, as discussed in Section 2.3.

8.3.3 Hardening of the potential shear band systems

In a previous study performed by Jia et al. [106] with a similar non-crystallographic shear band model for FCC structures, they proposed that the main reason for the discrepancy between the experimental results and simulations was due to the lack of hardening of the shear band systems in their model. To suggest an improvement to this problem and to make the model more stable, simple hardening schemes are implemented to account for the different phenomena potentially causing hardening against the nucleation and growth

of the shear band systems. Also, Jia and coworkers disregarded any possible softening arising from the emerging shear band due to the incompatibilities in their framework. In contrast, Anand and Su [8] used a softening model preceding decohesion, while Wei et al. [221] used a more conventional damage model as a basis. Slightly differently to the previous studies, in the present model the hardening/softening of the shear band systems is based on the following assumptions and simplifications:

I Slip activity of the shear band systems causes self-hardening when the shear strain contributed from the shear band increases. Complex dislocation density models including evolution of the dislocation structure inside the shear band core, e.g., refs. [67, 68, 188], are not accounted for in the present model for simplicity. Instead, a phenomenological exponential law is used. Alternatively, to investigate the stability of the model, the hardening coefficient can be taken as negative to cause self-softening. This reduces the need of a damage model since only higher shear band activity is permitted as a result of softening. This idea is partly justifiable since although after the initiation the shear bands may grow spontaneously, when DRX occurs and self-organization of the shear band core microstructure has taken place, it could be expected that hardening again overcomes softening [97, 152].

II The crossing micro shear band systems are assumed to cause hardening in each other. When shear strain, or cumulated shear band activity, increases in the shear band cores, it is assumed that the penetration becomes more difficult. In addition, the hardening parameters can be chosen so that already nano-shear bands can cause significant hardening in the other shear band systems, as it is experimentally observed that the shear strains can already be quite high even in thin bands [97].

III Slip activity in the matrix is considered to increase the resistance against shear banding. Hong et al. [97] characterized shear band-matrix interfaces and noted a transition layer between the matrix and the shear band core. They observed that the shear band core began to spread at the expense of the high dislocation density transition layer only after high local strains developed inside the nano-sized core of the shear band. Inversely this suggests that high dislocation density can have a barrier like effect on the shear band growth, at least to some extent.

IV The question of the shear bands causing hardening to dislocations by barrier-like effect remains open. The hardening could be justified following the reasoning in point II and considering the shear bands causing Hall-Petch type hardening via grain size reduction. However, at present no direct hardening effect caused by shear band systems to slip is described, mainly because no volume fraction of shear bands is used or no explicit definition in the mesh exists for the shear bands, which rules out the use of a similar hardening scheme as for the twin-slip interaction taking the grain size reduction into account.

The self-hardening term follows the same rule as the slip hardening, as described in point I. The ‘dislocation density’ evolves and saturates in a similar manner according to a exponential evolution law as for slip. In the present case, the hardening/softening is a function of accumulated shear of the shear band systems instead of the dislocation density assigned to the shear bands because of the complex dislocation structures forming inside the shear bands. Choosing of a negative value for coefficient Q will cause softening of a shear band system when it evolves. To incorporate softening at the early stages of

deformation followed by hardening at the later stages due to the recrystallization process, a two-term hardening law could be used. However, in the present simulations only a single term hardening or softening law is adopted, mainly because no simple evolution law for hardening after the DRX process has been proposed in the literature so far.

$$r_r^{\chi} = b_{\chi} Q_{\chi} H_{\chi} \rho^{\chi r} = Q_{\chi} H_{\chi} \{1 - exp(-b_{\chi} \chi^{\chi r})\} \tag{8.9}$$

The activity of other shear band systems s causes latent-like hardening in a system r, which restricts the evolution of system r according to point II. A power law form is used, in which the exponent characterizes the effectiveness of the hardening with respect to the sum of all accumulated shear produced by other shear band systems. A low exponent value causes effective hardening already at low strains, whereas a high value of the exponent retards the hardening effect. The rate of this hardening rule is:

$$\dot{r}_{\chi}^{\chi} = H_{sbnd} \left(\sum_{r \neq s} \chi^s \right)^f \sum_{r \neq s} \Delta \chi^s \tag{8.10}$$

Following the ideas of accumulated slip activity in the matrix provided in the previous section, the evolution of hardening caused by the sum of accumulated slip described in point III is formulated as:

$$\dot{r}_{\nu}^{\chi} = H_{slsb} \left(\sum_{s} \nu^s \right)^d \sum_{s} \Delta \nu^s \tag{8.11}$$

The total hardening of a shear band system χ^r may be given as the sum of external hardening factors (latent terms) and by its self-hardening, i.e.,

$$r_t^{\chi} = r_r^{\chi} + \underbrace{\int_0^t \dot{r}_{\chi}^{\chi} + \int_0^t \dot{r}_{\nu}^{\chi}}_{r_{ext}^{\chi}} \tag{8.12}$$

Finally, the resistance against shear banding, which must be exceeded by the resolved shear stress, can be expressed as:

$$r^{\chi} = \tau_0^{\chi} + r_t^{\chi} \tag{8.13}$$

where τ_0^{χ} is the initial threshold for shear banding.

8.3.4 Summary of the micro shear band BCC model

The ingredients of the present BCC crystal plasticity framework including shear banding are gathered in the following summary. The dislocation density terms are not necessary directly in the context of the computations of this work since the slip-slip hardening and shear band self-hardening are functions of the accumulated shear values v^s and χ^r. However, these terms can be modified to include the dislocation based hardening/softening

evolutions in the future developments of the model, e.g., by adding temperature effects in the model.

Crystal plasticity framework for BCC micro shear band

Plastic strain rate:

$$\underline{\dot{\epsilon}}^p = \underbrace{\sum_{s=1}^{N_s} \dot{\gamma}^s \underline{m}^s}_{Slip} + \underbrace{\sum_{\chi=1}^{N_\chi} \dot{\gamma}^\chi \underline{m}^\chi}_{Shear\ banding}$$

Dislocation slip terms:

Slip rate: $\dot{\gamma^s} = \left\langle \frac{|\tau^s| - r^s - \tau_0^s}{K} \right\rangle^n sign(\tau^s)$

Hardening of a slip system: $r^s = bQ \sum_{s=1}^{n_s} h_{n_s} \rho^s = Q \sum_r H_{rs}\{1 - exp(-bv^r)\}$

Dislocation density evolution: $\dot{\rho}^s = (1 - b\rho^s)\dot{\nu}^s$

Shear band terms:

Shear band rate: $\dot{\gamma^\chi} = K_b \left\langle \frac{|\tau^{\chi r}| - r^\chi}{K_\chi} \right\rangle^{n_\chi} sign(\tau^{\chi r}) \sum_{s=1}^{n_s} \Delta\nu^s \ ; \ r^\chi = \tau_0^\chi + r_s^{\chi s} + r_{\chi_r}^{\chi s} + r_\nu^\chi$

Shear band self-hardening $r_r^\chi = b_\chi Q_\chi H_\chi \rho^{\chi r} = Q_\chi H_\chi\{1 - exp(-b_\chi \chi^{\chi r})\}$

Shear band hardening due to other shear bands: $\dot{r}_\chi^\chi = H_{sbnd} \left(\sum_{r \neq s} \chi^s \right)^f \sum_{r \neq s} \Delta\chi^s$

Shear band hardening due to accumulated

plastic strain in the matrix: $\dot{r}_\nu^\chi = H_{slsb} \left(\sum_s \nu^s \right)^d \sum_s \Delta\nu^s$

Similarly, the residuals are written in the common form for the Newton integration. The internal variables v_{int} are again updated at every time step. The Jacobian matrix becomes a non-symmetric 45x45 (9+24+6+6) without dislocation terms, and 75x75 (9+24+24+6+6+6) with the dislocation terms. The necessary partial derivatives required in the iterations are given in Appendix B for the shear band model.

The residuals for internal variables (BCC micro shear band)

$$R_{\underline{E}} = \Delta\underline{E} - \Delta\underline{F}\cdot\underline{F}^{-1}\cdot\underline{E} + \underline{E}\cdot\left(\sum_s \Delta\gamma^s\underline{m}^s + \sum_\chi \Delta\gamma^\chi\underline{m}^\chi\right)$$

$$R_{\nu^s} = \Delta\nu^s - \left(\frac{|\tau^s| - r^s - \tau_0^s}{K}\right)^n \Delta t$$

$$R_{\rho^s} = \Delta\rho^s - (1 - b\rho^s)\Delta\nu^s$$

$$R_{\chi^r} = \Delta\chi^r - K_B\left(\frac{|\tau^{\chi r}| - (r_t^{\chi r} + \tau_0^{\chi r})}{K_\chi}\right)^{n_\chi}\sum_s \Delta\nu^s$$

$$R_{r_{ext}^{\chi r}} = \Delta r_{ext}^{\chi r} - \left[H_{slsb}(\sum_s \nu^s)^d \sum_s \Delta\nu^s + H_{sbnd}(\sum_{r\neq s}\chi^s)^f \sum_{r\neq s}\Delta\chi^r\right]$$

$$R_{\rho_\chi^s} = \Delta\rho_\chi^s - (1 - b_\chi\rho_\chi^s)\Delta\chi^s$$

The shear band self-hardening was selected to evolve with the shear band rate term in the same way as in the slip. Therefore, only the external hardening $r_{ext}^{\chi r}$ terms together were considered as an individual internal variable.

8.4 Model parameter identification for the BCC basic model

The parameter identification for the BCC basic model was performed for the HV500A steel using experimental data from uniaxial compression tests at three strain rates. The tests included two quasi-static and one dynamic test. Two identification routines were used, which are embedded in the Zébulon finite element suite. The Berveiller-Zaoui (BZ) routine was utilized as the primary method for identification, but in addition the parameter search was also performed with the Beta-method for comparison. Figure 8.2 shows the results of the identification process for both methods.

At present, the commonly available BZ and Beta routines in Zébulon are mainly limited to the small deformation framework and therefore not be used with the present large deformation framework. Despite this, it was for simplicity decided to use these routines, although the error can become somewhat higher at larger strains. Taking into consideration that the experimental stress-strain behavior of the material does not show significant changes even at higher strains in the quasi-static range, the present identification result was accepted. Additionally, the search routines are much faster than the use of actual finite element structures with a large amount of orientations and elements, such as was used in the previous section.

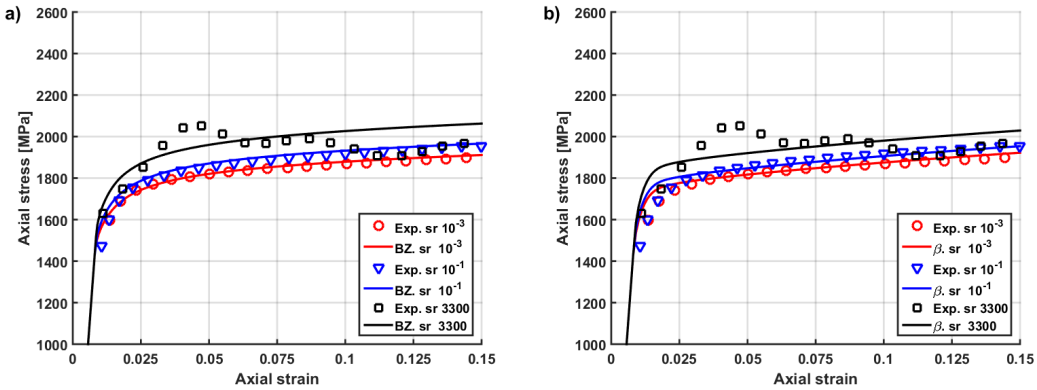

Figure 8.2: Experimental stress-strain data with simulated curves fitted with a) BZ-routine, b) Beta-routine.

The value for the shear modulus μ in the BZ routine was taken as 70.7 GPa, and the Poisson's ratio as 0.3 (simplified routine in Zébulon). For the Beta-method, the Young's modulus of 210 GPa with the Poisson's ratio of 0.3 were used. The Beta-method values were identified as 230 for D and 0.02 for δ. Total of 500 random orientations were used for both methods with equal weights in the computations, since no particular distributions of phase fractions or texture were experimentally identified

The identified material parameters were τ_0^{110}, τ_0^{112}, K, n, b and Q. Without any better knowledge of the initial slip activation (experiments or characterization), the initial resolved shear stress values were taken equal for both slip families. The elastic constant data for the material was taken from ref. [168]. The coefficients of the interaction matrix rely on the values proposed by Hoc and Forest [91], which were identified for complex loading paths. The kinematic hardening terms were set to zero in the absence of suitable cyclic experimental data for fitting of the parameters. All of the used values for the parameters are presented in Table 8.4.

Table 8.4: Model parameters used in the simulations and the coefficients identified in the process for the BCC basic model

Parameter	C_{11}	C_{12}	C_{44}	τ_0^{110}	τ_0^{112}	K	n	b	Q
	219540	78125	70700	367.0	367.0	367.0	120	3.0	32.0
Interaction matrix	h_1	h_2	h_3	h_4	h_5	h_6	h_7	h_8	
coefficients	1.3	1.0	1.05	1.15	1.1025	1.3	1.495	1.0	

All units in MPa
Interaction coefficients with: $a_0 = 1$, k_1=1, $k_2 = 1.15$, $k_{p1} = 1.05$, $k_{p2} = 1.05$, $k_{s0} = 1.3$

The results of the fitting process, presented in Figure 8.2, show good agreement with the experimental data using both methods at the quasi-static strain rate range. A discrepancy exists at the higher strain rate range because the model does not include any additions to the constitutive behavior that would cause reduced hardening or softening. Hence, both simulations over-estimate the experimental result by ca. 5 % at around 0.15 of total strain at the strain rate of 3300 s^{-1}. The reason for the fairly low overall error between the results is that the material is not highly strain rate sensitive or it does not show very substantial strain hardening. The yield points were predicted quite well, acknowledging that the yield point in the high strain rate curve is not often very accurately measured with the Hopkinson apparatus, especially with the protective inserts used in the experimental setup causing some interference in the pulses.

8.5 Numerical examples of BCC single crystal deformation

8.5.1 Modeling conditions and simulation parameters

The numerical applications of the modeling approach are demonstrated in this section for single crystals. Some common rolling texture orientations [120] were chosen for the simulations to study the propensity of shear banding in these orientations. One of the most important texture components in BCC metals is of type $\{001\} < 110 >$, which appears for example in hot rolling. Additionally, the effect of strain rate was studied at both quasi-static and dynamic ranges. The effect of model parameters related to shear banding was demonstrated with two examples, showing the sensitivity of the model response to viscosity and self-hardening/softening of the shear band. The former dictates the probability of the activation of the shear band depending on the strain rate, while the latter demonstrates the suitability of the softening criterion for the modeling framework.

The basic model parameters were taken from the identification process presented in the previous section. Table 8.5 lists typical BCC polycrystal texture orientations. However, the simulations were performed with single crystals by adopting the listed orientations. The additional model parameters for shear banding are included in Table 8.6, which are used as base values for the computations. All variations from these values are provided in the figures depending on the studied conditions. The simulations were performed mainly in tension in the ND direction using a single element with the large deformation framework and the implicit/explicit integration schemes. The boundary conditions were the same as described in Section 7.5.

Table 8.5: Common rolling textures in BCC polycrystals

Texture	Indices ND RD	Zébulon rotation
BCC1	(001) [110]	x3 0. 0. 1. x1 1. 1. 0.
BCC2	(211) [01$\bar{1}$]	x3 2. 1. 1. x1 0. 1. -1.
BCC3	(110) [001]	x3 1. 1. 0. x1 0. 0. 1.
BCC4	(111) [0$\bar{1}$1]	x3 1. 1. 1. x1 0. -1. 1.

Table 8.6: Model parameters used in the single crystal simulations with the shear band model, alternative parameter values marked in the figures.

Parameter	C_{1111}	C_{1122}	C_{1212}	τ_0^{110}	τ_0^{112}	K	n	b	Q
BCC-basic	219540	78125	70700	367.0	367.0	367.0	120	3.0	32.0
Parameter	τ_0^{χ}	K^{χ}	n^{χ}	C^{χ}	H_{slsb}	d_{sb}	H_{sbsb}	f_{sb}	
Shear banding	1100.0	1200.0	5.0	20.0	100.0	1.5	200.0	0.5	
	Q_{sb}	b_{sb}	H_{sb}						
	-150.0	3.0	1.0						
Interction matrix	h_1	h_2	h_3	h_4	h_5	h_6	h_7	h_8	
coefficients	1.3	1.0	1.05	1.15	1.1025	1.3	1.495	1.0	

All units in MPa
Interaction coefficients with: $a_0 = 1$, k_1=1, $k_2 = 1.15$, $k_{p1} = 1.05$, $k_{p2} = 1.05$, $k_{s0} = 1.3$

The threshold for shear banding was chosen quite high for the demonstrations, roughly three times the initial resolved shear stress of conventional slip. The viscous parameters were also shifted according to the threshold, choosing the exponent n quite low, which renders the flow behavior strain rate sensitive. The external hardening rule parameters related to shear banding the effect of slip to shear bands H_{slsb}, and the interaction between shear bands H_{sbsb}, were taken similarly quite low to limit their effect. The value for the exponent controlling slip-shear band interaction was chosen quite high to cause more hardening at higher strains. In contrast to partially restrict shear band propagation, the interaction between shear bands was presumed to be strong already at low strains, and therefore a smaller value for the exponent was chosen than for the slip-shear band interaction. The magnitude of the self-hardening/softening coefficient was selected to be relatively high, or alternatively softening was generated by choosing a negative value.

8.5.2 Single crystal simulation results including shear banding

Figure 8.3 shows the tensile stress-strain curves and the contributions of different deformation mechanisms for four single crystal orientations at constant 3300 s^{-1} (a,b) and 10^{-3} s^{-1} (c,d) strain rates for the shear band model. The single crystal orientations [111] and [211] show higher flow stress than the softer orientations [001] and [110]. The onset of shear banding can be observed already at low strains at the quasi-static strain rate for the [111] and [211] orientations. The significance of shear band systems increases for both orientations at the high strain rate as expected. The stress-strain response of the BCC-basic model (dashed line in Figures 8.3a and c) for the [111] orientation differed from the shear band model showing higher flow stress values in the cases where shear banding is observed. It can be seen that the shear band mechanism provides some softening in the curves, as is expected from the activation of an additional deformation mechanism with a relatively low hardening capability. In the present simulations, the orientations [001] and [110] did not activate shear band systems even at high strains, indicating that they are not very susceptible to shear banding at least with the present threshold for the activation. The shear banding response of the studied orientations does not change significantly when compression is applied instead of tension.

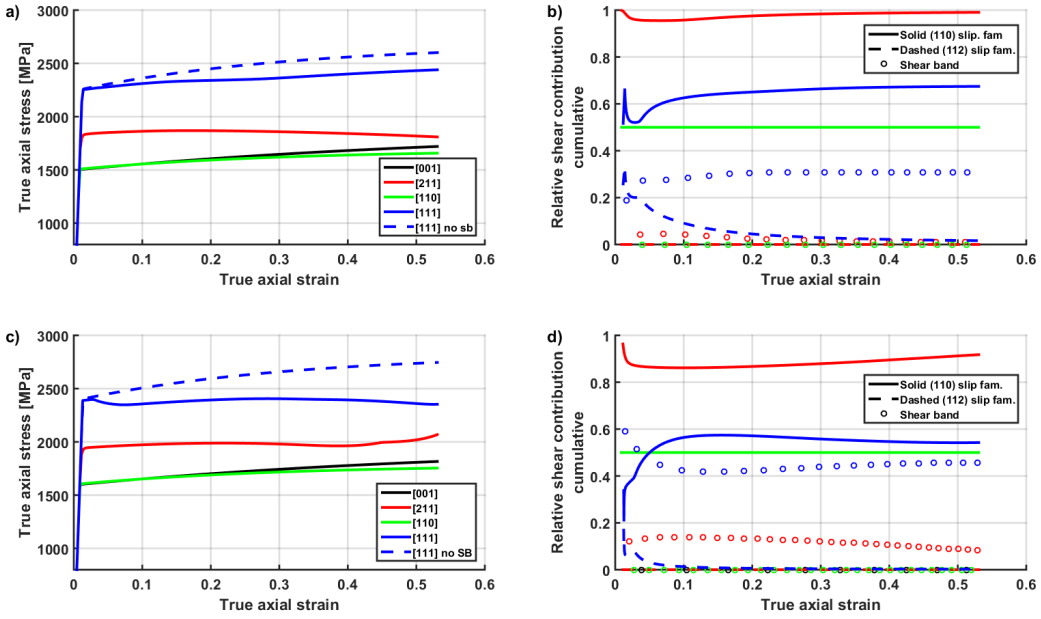

Figure 8.3: Stress-strain response of four single crystal orientations in tension at strain rates 10^{-3} s^{-1} (a) and 3300 s^{-1} (c) of the shear band model, and the corresponding relative contributions of each deformation mechanism to total shear b) and d).

The shear banding shows varying magnitude in the different orientations. The shear band systems in [211] orientation are more active at the beginning of the deformation with a decreasing trend when the total strain increases at both strain rates. In contrast, the [111] orientation shows more or less constant shear band activity at the quasi-static strain rate, but the activity shows variations at high strain rates, initially reaching up to 60 % of shear contribution. In both cases, shear banding usually decreases the slip activity on the {112}<111> than {110}<111> slip family. Jia et al. [105] observed stronger reorientation of the FCC crystals when shear banding is active compared to the slip+twin controlled deformation. Hence, one explanation could be that the reorientation of the crystal takes place favoring {110}<111> slip systems and further shear banding, when shear band systems contribute to the deformation in a notable manner.

To study the characteristics of the shear band model and the propensity of the shear banding at various conditions, based on the current results [111] was selected as the main orientation due to its high tendency to develop shear bands. Figure 8.4 demonstrates the effect of strain rate on shear banding in the [111] initial orientation, showing that increasing strain rate increases the probability of shear banding due to choice of the viscoplastic parameters that increase shear banding when the strain rate increases.

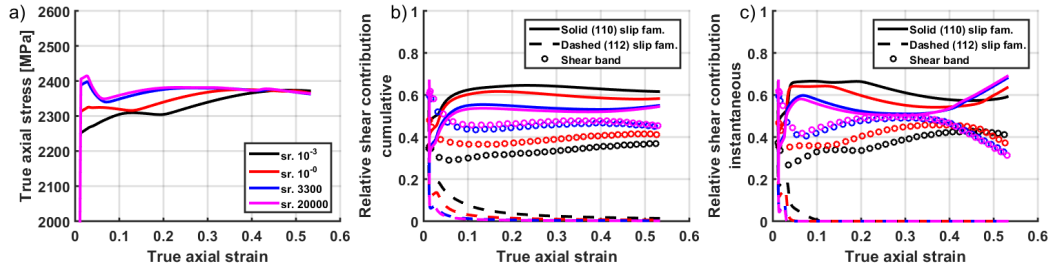

Figure 8.4: Effect of strain rate to the shear banding of a single crystal orientation [111], a) stress-strain behavior, b) cumulative shear contribution of the deformation mechanisms, and c) instantaneous shear contributions.

At low strains, there is a marked drop in the flow stress at the two highest strain rates due the decrease in the instantaneous contribution of the shear bands to the total shear (Figure 8.4c). When the shear band contribution again starts to increase also the flow stress increases by some amount. This could be partly explained by the external hardening caused by multiple shear band systems to each other, as well as the by the accumulated slip in the matrix increasing the shear band resistance. From another point of view, the decreased shear banding at low-to-medium strains allows more slip deformation, which does not immediately cause strain hardening, probably due to the high number of available slip systems having low slip resistance. This assumption was confirmed by investigating the individual contributions of the slip systems to the total shear, according to which the additional slip systems activated when the shear banding decreased. The activation of the additional slip systems may also be affected by the crystal rotations, as in the model the shear banding also contributes to the total lattice rotations.

The effects of viscous parameters are shown in Figure 8.5a for the self-softening and self-hardening schemes. A decrease in the viscosity parameter K promotes shear band activity, while a suppressing effect is observed with higher K values. The downside of using low value for K is that the explicit integration may be prone to the bifurcation phenomenon, which is reduced when the K value is higher. The choice of the hardening/softening parameter Q affects the stress-strain behavior by either increasing or decreasing the flow stress after the initial stage of shear banding. Figure 8.5b shows the cumulative relative shear contributions for different viscous parameters with the self-softening scheme. A quite remarkable increase in the contribution of the shear band systems is observed when lower K values are used. However, the instantaneous shear contribution in Figure 8.5c illustrates that if the shear band activity is initially high, the instantaneous shear contribution of the shear bands is decreased when strain increases. On the other hand, if the viscous parameter is high, the shear bands contribute more at higher strains. Hence, the main effect of the viscosity value on the physical behavior of the material, is that a high value leads to an incubation time before shear banding commences.

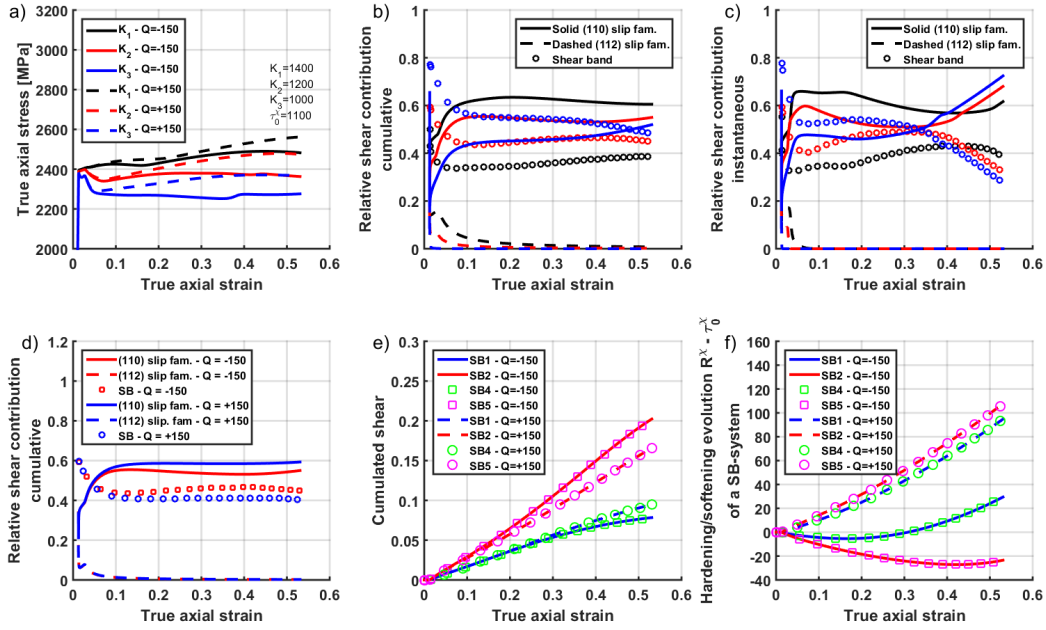

Figure 8.5: Effect of viscosity on the shear banding with self-hardening and self-softening schemes, (a-c). Difference between the hardening and softening schemes in shear contribution (d), evolution of shear strain in active shear band systems (e), and the evolutions of individual shear band system hardening for both cases with a K value of 1200 (f). The single crystal orientation is [111].

Figure 8.5d shows the difference between the softening and hardening schemes with $K = 1200$ in the relative contributions of shear bands to the total shear deformation of a the [111] orientated single crystal. Softening concentrates more deformation to the shear band systems after the softening has become more significant, i.e., the shear band has grown to the critical size. At higher strains, a slight decrease in the shear band activity is seen due to external hardening. Figure 8.5e,f illustrates the cumulative shear contributions of the individual active shear band systems and the evolution of the shear resistance. The difference is not very significant in the cumulative shear contributions of the systems. However, the increasing individual shear contributions of shear band systems SB2 and SB5 (Fig. 8.5e) are caused by the quite significant softening (Figure 8.5f) that allows more activity. In the same way, the two other active shear band systems, SB1 and SB4, show increased activity in spite of the transition from softening to hardening at higher strains. It is also worth noting that even though the hardening of the both sets of shear band systems (SB2,SB5 and SB1,SB4) show quite similar hardening when coefficient Q is positive, their shear contributions are not the same. This is an expected result since the resolved shear stresses acting in these different sets of systems are not the same. Also, one explanation for the high shear band activity in the [111] orientated crystal is that activity takes place in all of the three shear band planes, of which the plane containing the maximum and minimum principal stress directions ($\hat{e}_1$ and $\hat{e}_3$) exhibits the highest combined activity in (systems SB1 and SB2). There is no difference between two equally active systems, e.g., SB1 and SB2, in the present case due to the isotropic hardening rule and because the crystal is only uniaxially deformed.

Figure 8.6 demonstrates the BCC basic and BCC shear band models in uniaxial cyclic loading of the [111] orientation at the strain rate of 3300 s^{-1}. A total of ten loading cycles were simulated. The shear band softening parameter, Q, was chosen as -150 MPa. The BCC-basic model excluding kinematic hardening shows the typical behavior, where the flow stress continues to increase as no back-stress is introduced in the model. When the kinematic term is included in the model, the response changes notably. The evolution of the kinematic hardening parameter causes a noticeable concave curvature to the stress-strain behavior. When the loading is reversed from tension to compression, a slight Bauschinger effect is observed. However, its magnitude is rather low due to the choice of relatively mild parameters for this particular example. A very different behavior can be seen in the response of the shear band model. The shear bands become active already in the first tension cycle continuing their activity also in compression, but no marked signs of asymmetric stress-strain behavior is observed. When the number of loading cycles increases, the shear contribution from the shear bands exceeds the contribution of the dominant slip family {110}<111>. Also, at higher number of cycles, the stress-strain curve shows increasing hardening. Although the model shows fairly good stability, still some stress jumps are observed during the last three cycles because of the intermittent activation and deactivation of shear band and slip systems.

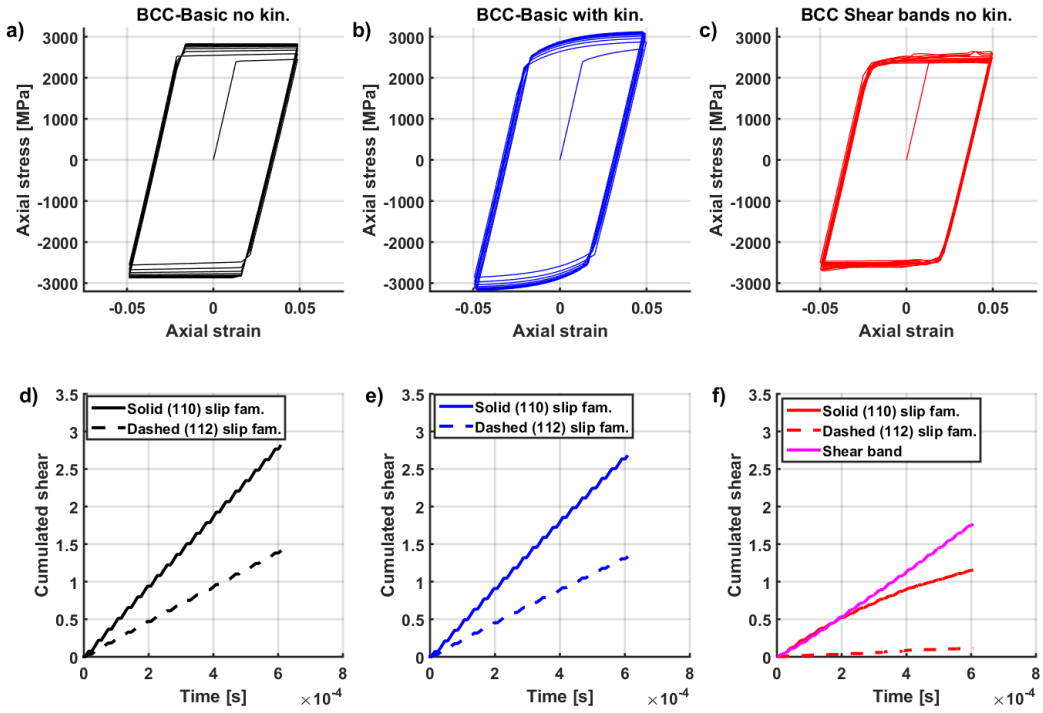

Figure 8.6: Response of three models to cyclic loading, a) BCC-basic model without kinematic hardening, b) BCC-basic model with kinematic hardening, c) BCC shear band model without kinematic hardening, and the corresponding shear strain contributions of the deformation mechanisms at high strain rate loading at 3300 s^{-1} (d-f).

Finally, as the shear band systems tend to activate already during the first tension half cycle, the model does not take into account the resistance developed in the existing shear bands during the load reversion. For example, the model does not include a definition

for the possibly recristallized shear band zones that may cause a higher resistance to further growth of the shear band. On the other hand, the model framework is purely phenomenological and no direct relationship of the shape or size factors exists, therefore the continuous growth of the shear bands at this strain rate could be understood as a growth of the shear bands in the most potential regions. For example, the stress concentrations in the transition zones of the shear bands could act as further initiation sites due to the forming dislocation pile-ups [97].

8.6 Summary and conclusions

In summary, an implementation of a phenomenological single crystal plasticity model with 24 slip systems suitable for the BCC crystal structure was carried out for the large deformation framework, ultimately aiming for further use with realistic types of microstructural aggregates. The initial parameter search for the BCC basic model was based on the uniaxial deformation of an ultra high strength steel at three strain rates using the existing Berveiller-Zaoui and Beta-fitting routines in Zébulon. The following conclusions can be made:

- In general, both BZ and Beta routines were suitable to describe the mechanical behavior of polycrystalline ultra high strength steels in uniaxial conditions, but some error is caused by the assumption of small deformations in these routines.
- The model was found to be capable of describing the steel's behavior well at the quasi-static strain rate range under uniaxial loading. However, some discrepancy was observed at the dynamic strain rate range due to the softening occurring in the experimental curve, but its magnitude remained relatively low due to rather limited hardening capability of the material.

The BCC crystal plasticity model was extended to include a phenomenological definition of shear banding to expand the model capability to describe also strain localization caused by high strain rates and high localized stress concentrations. The formulation is based on the 'non-crystallographic' definition of micro shear bands, and their formation is controlled by the time-dependent flow rule consistent with the conventional dislocation slip. The flow of the shear bands is restricted by the rate of the conventional dislocation slip. The non-crystallographic shear band systems were chosen to evolve in the directions of the principal stresses in the crystal to maximize the to shear banding probability. The model characterizes the material's resistance to shear banding according to the Schmid law and external and internal hardening/softening rules. Simulations were performed for single crystals under uniaxial deformation to study the effects of orientation, strain rate and viscosity, and hardening/softening schemes on the shear banding occurrence in the material. The following observations and conclusions were made:

- Orientation of a single crystal has a significant role in the activation of shear banding. Of the studied four typical polycrystal orientations [001],[211] [110] and [111], orientations [111] and [211] showed the highest probability for shear banding in the simulations with the present parameter set.
- The model can phenomenologically describe the increasing probability of shear banding at high strain rates, or alternatively the increased probability of shear

band activity at high strains when the local stresses increase as a consequence of hardening. The model parameters can control the kinetics of the shear banding making it more dynamic or delaying the shear band growth and magnitude.

As a final remark, the use of shear band models with polycrystalline materials is at the moment restricted by the insufficient identification of the model parameters, the stress-strain curves do not necessarily reveal correctly the localized evolution of the shear bands. One method to obtain more accurate information for the validation of the model performance could be the use of in-situ characterization methods at the conditions, where the shear bands develop. For example, the use of digital image correlation techniques in to high strain rate experiments on samples with a known initial crystalline structure (e.g., EBSD maps) could provide important new data to validate and support the further development of the numerical models.

9 Summarizing conclusions

This section presents the general conclusions of this work, based on the results and discussions and the more detailed partial summaries presented at the end of Chapters 4 - 8.

9.1 Brief overall summary

The characterization part of this work started with the experimental determination of the mechanical behavior of the test materials at quasi-static and dynamic strain rates, ranging from 10^{-3} to 4000 s^{-1}, in uniaxial loading conditions at room temperature. After mechanical testing, the deformation and failure behavior of the materials was examined for using various characterization techniques to form a solid basis for the crystal plasticity modeling. This was followed by the characterization of in-service samples from a jaw crusher (austenitic manganese steel, an alloyed Hadfield steel), and from the cutting edge of a bucket loader (a martensitic wear resistant steel, HV500A).

The experimental work included abrasion experiments with preliminary multiple contact tests, and single contact scratch tests with natural rocks and diamond indenters. The wear behavior and surface hardening of the steels were experimentally characterized in heavy abrasion conditions. The impact experiments focused on the investigation of high velocity single impact events at various conditions, covering a wide range of impact angles and energies, impulses, and multiple impacts. The strain hardening, plastic deformation, and wear and failure behaviors of the test materials were characterized to expose the dynamic failure properties of the steels. The experimental methods were also further developed to suit better for the studies of wear resistant steels.

Two crystal plasticity approaches were developed to study the micromechanical behavior of austenitic manganese steels and martensitic wear resistant steels. The phenomenological crystal plasticity model for the FCC structures including twinning aimed to capture the most essential micromechanical phenomena related to the deformation and unusual strain hardening behavior of the austenitic manganese steels. The modeling approach included the development of the framework, single crystal studies, model parameter fitting, and demonstrations of the polycrystal behavior. Also, the first demonstration of the multi-scale approach of modeling to the micromechanical behavior of materials used in jaw crusher conditions was presented. The phenomenological crystal plasticity modeling of martentisic steels focused on two aspects: identification of the model parameters for ultra high strength martensitic steels without shear banding, and development of a micromechanically driven phenomenological description of shear banding. The propensity and significance of shear banding was investigated using single crystal studies to demonstrate the model behavior.

9.2 General conclusions

9.2.1 Experimental and simulation methods

The experimental part of the work focused on *research question 1*, i.e., the choice of wear testing methods and their correlation with realistic conditions. The multiple contact wear tests were found effective when studying the overall performance of a steel in some specific conditions. However, the large number of contacts easily masks the individual characteristics of the contacts between abrasive or impacting particles and the steel surface. Single scratches with a natural rock indenter can provide useful and detailed information about the contact, but the controllability of the experiments is limited because of the arbitrary tip geometries and failure-prone rock chacteristics easily changing the contact conditions. The more rigid and well-defined geometry of a diamond indenter suits better for investigating the surface hardening and wear behavior of wear resistant steels. Single scratches, however, do not offer sufficient information when the steels have a significant capability to strain harden. It was established that 5-10 cycles in the same wear track can cause saturation of the surface hardening of the studied steel grades, giving a good basis for future tests with this type of materials instead of the commonly used single scratch method.

The developed high velocity particle impactor test setup provides an excellent method to study the effects of impact angles and energies, impulses, and effects of prior deformation on the material behavior in a strictly controlled environment. The choice of simple geometries allows easy comparison of the experiments, combined with the good accuracy of the method resulting in excellent repeatability of the tests. Instead of the common approach of using small impacting particles in the experiments, the relatively large size of the projectiles also makes it possible to in-situ observe the impact incident with high speed imaging and to determine some of the important impact variables, such as the amount of consumed kinetic energy of the projectile during the incident. Furthermore, the large size of the impact craters is beneficial in the characterization of the local deformation mechanisms, such as shear banding. Relatively high impact energies can be produced with the setup without using extremely high impact velocities, which is beneficial in terms of characterizing the correct range of strain rates. The test method is easily modifiable, for example, experiments at sub-zero or even elevated temperatures may be performed when suitable modifications to the test setup are made.

The accuracy and limiting factors of the FCC crystal plasticity model were evaluated to answer *research question 2*. The developed crystal plasticity model representing the deformation behavior of an austenitic manganese steel is capable of describing the single crystal behavior of the material rather well. The polycrystal behavior was also captured in terms of stress-strain behavior, at least in the range of the available experimental data. The comparison of results of the simulations performed on the polycrystal aggregates representing realistic-like austenitic microstructure with the experimental observations indicated that the model can imitate the local behavior of the grains with a reasonable accuracy. The model was designed to produce positive strain rate dependence, which it was found to accomplish for the studied alloyed Hadfield grade in compression. At present, however, the dynamic strain aging, which is known to affect the strain rate dependency of Hadfield type steels at low strain rates, was omitted in the model. The simplified demonstration of the jaw crusher-like conditions showed that the modeling and multi-scale approach can be used to increase the understanding of the material behavior in real applications by examining the local deformations of the microstructure. However,

detailed information can only be extracted when also the loading boundary conditions are properly known.

The performance of the BCC crystal plasticity model in describing the deformation behavior of martensitic wear steels was examined according to *research question 3*. The phenomenlogical model for the martensitic steels showed that their macroscopic stress-strain behavior can be reproduced in compression with satisfactory accuracy by the self-consistent schemes. The strain softening occurring at the high strain rates cannot be directly presented by the basic model that does not include any softening behavior. To compensate for this, a local phenomenological description of shear banding was implemented in the model, which could induce softening in the local stress-strain behavior of the single crystals. It was also found that the shear banding phenomenon is orientation dependent based on the present simulations on single crystals.

9.2.2 Material deformation and wear behavior

The deformation, strain hardening, and failure characteristics of the studied materials was constituted *research question 4*. The main findings and aspects answering this question are summarized in the following three subsections.

High maganese austenitic steel

The manganese austenitic steel with a manganese content higher than the conventional Hadfield steel exhibits positive strain rate dependence at all strain rates studied in this work. Hence, no significant effect of dynamic strain aging that could cause negative strain rate dependence was observed to take place in the present steel grade. The strong strain hardening behavior of the studied steel with an upward curvature is a result of the competing effects of twinning and dislocation slip and their interactions. In addition to the conventional dislocation slip-slip interactions, hardening is produced also by the slip-twin interactions at the twin-matrix boundaries, twin-twin interfaces with a boundary effect, twin-twin transmitting intersections, and by wide slip bands either promoting or inhibiting twinning depending on their general orientation.

Twinning promotes the local hardening, increasing the hardness of the grains with high twin volume fractions. At a macroscopic scale, the increasing twin volume fraction also increases strain hardening, twinning first occurring in the favorably oriented grains. Further macroscopic straining promotes twinning in an increasing number of grains for two reasons: the critical twin stress is exceeded due to strain hardening, and stress concentrations caused by the neighboring grains either initiate new twins near the grain boundaries or cause a transmission-like effect of twins from the already twinned grains. In general, similar observations of the deformation mechanisms were made from the samples of the laboratory experiments and from the in-service samples.

The crystal plasticity simulations confirm that the evolution of the twin volume fraction has a significant effect on the strain hardening behavior. At the single crystal level, dominating twinning has a softening effect until saturation of the twinning, after which strong hardening takes place because of the barrier effect of twin boundaries to dislocation slip. This translates to the polycrystal scale as an upward curvature in the macroscopic stress-strain curve. In turn, multiple active slip systems harden the material rather linearly. At the grain level, twinning occurs mostly in one to three dominating twin systems, the activation of which can depend on the local strains and strain hardening. Observations on the deformed microstructures confirmed similar behavior. The preliminary results on two different grain structures suggest that stronger strain hardening and twinning take

place in polycrystals containing a combination of small and large grains compared to constant sized grains. Conclusive results, however, still require simulations with a large set of different grain structures.

Strong strain hardening capability and reasonable ductility of the steel provide a good combination of properties for both abrasive and impact conditions. The performance of the hardened surface of the Hadfield steel against rigid sliding particles in the scratch tests was at the same level as that of the martensitic steels at high loads. In contrast, the higher wear rate of the Hadfield steel at lower loads suggests that the material requires continuously a reasonable amount of deformation to sufficiently maintain its hard and wear resistant surface against indenting particles. The increasing macroscopic strain rate, on the other hand, first has a positive effect in terms of the Hadfield steel's impact resistance, but the resulting loss of ductility may promote wear by causing opening of the grain boundaries.

Ultra high strength martensitic steels

The investigated martensitic wear steels show moderate strain hardening until high strain rates, i.e., 2200-3600 s^{-1}, where only gradually decreasing flow stresses are observed after yielding. This behavior may be attributed to localization effects such as development of adiabatic shear bands along which the material eventually fails. The failure appears to happen inside the shear bands instead of the interface between the bulk and the shear bands. This may be explained by the suggested failure mechanism occurring as a part of the dynamic recrystallization process. The DRX is one of the most plausible explanations for the observed high hardness fine grain structure inside the shear bands, forming due to the combined effect of local heating, high shear strains, and high strain rates. The alternative explanation of diffusion controlled austenization does not seem to have sufficient time to take place, but martensitic reversion is also plausible followed by the DRX process refining the microstructure. The microstructures of the steels are capable of strain hardening at dynamic conditions before failure by shear banding, increasing the material hardness by 19 - 34 % from the initial hardness. However, the propensity of shear bands depends on the initial microstructure, high initial hardness combined with low ductility promoting the adiabatic shear banding.

The existence of tribolayers can a have significant effect on the wear behavior of the martensitic steel grades. Tribolayers with oriented microstructures easily develop during heavy abrasion, increasing the surface hardness of the steels even 50 % above the bulk hardness. Cracks appearing in the tribolayer region can cause detachment of wear particles, but all of the studied steel grades showed good resistance against crack propagation by stopping the cracks at the interface between the bulk and the tribolayers at the latest. From this point of view, the high hardness tribolayers are beneficial by protecting the surface against hard contacting particles, while the interior remains ductile. Also another type of a tribolayer can form on the surface of the UHS steels, resembling the microstructure of adiabatic shear bands with highly refined grain size and high hardness. The formation of these tribolayers may be explained by the frictional heating of the material surface at high contact pressures and high sliding velocities. Characterization of the in-service samples and the cross-sections of high velocity impact craters revealed that they both have this kind of layers at the surface. The impact tests subjecting multiple impacts on the same crater showed that these layers do not significantly promote wear, but instead the surface hardening decreases and saturates the wear rate. However, the long-term effects remain uncertain at present, for example the possible acceleration of the wear rate due to surface fatigue.

The impact conditions have a notable effect on the wear and deformation behavior of the studied steels. Low impact angles favor cutting type of wear, while the higher impact angles cause larger indents as well as increase the wear rate because of the limited ductility of the steels and the higher fraction of the initial impact energy being consumed in the impacts. The change in the wear mechanism as a result of increased impact energy, promoting for example adiabatic shear banding, also increases the wear rate by the detachment of wear particles due to fracturing along the shear bands. Shorter impulse/higher strain rate favors the formation of shear bands, which also increases the wear rates at constant impact energies.

Carbide reinforced steel

The flow stress of the carbide reinforced steel is significantly higher than that of the austenitic manganese steel or the martensitic steels, reaching over 3000 MPa at dynamic conditions. However, the ductility of the carbide reinforced steel is restricted by its cracking-prone microstructure, including high hardness chromium carbides and martensitic matrix. The cracks develop mainly at the interfaces between the carbides and the matrix, but to some extent also in the matrix and inside the carbides. Fragmentation of the material is accelerated at the dynamic strain rates, where several main cracks develop simultaneously in the microstructure. The hardening capability of the steel is limited due to its already high initial strenght and indentation hardness.

On the other hand, for the same reason it has the best resistance of the tested steels against abrasion. The surface is not easily deteriorated, it for example does not show any signs of accelerated development of crack networks in abrasive conditions, since the carbides protect the softer matrix while the matrix provides sufficient support for the carbides. Impact conditions, however, are more challenging for this steel grade. It performs well when the impact angle is low or when the impact energy remains at low or moderate levels, but higher impact angles and higher energies may make the material unsuitable for applications with such conditions due to the increasing possibility of nucleation and propagation of large subsurface crack networks, increasing the probability of a sudden failure.

Bibliography

[1] M. Abbasi, S. Kheirandish, Y. Kharrazi, and J. Hejazi. On the comparison of the abrasive and wear behavior of aluminum alloyed and standard hadfield steels. *Wear*, 268:728 – 734, 2010.

[2] H. Abdolvand, M.R. Daymond, and C. Mareau. Incorporation of twinning into a crystal plasticity finite element model: Evolution of lattice strains and texture in zircaloy-2. *International Journal of Plasticity*, 27:1721 – 1738, 2011.

[3] K. Adachi and I.M. Hutchings. Wear-mode mapping for the micro.scake abrasion test. *Wear*, 255:23 – 29, 2003.

[4] A. Alankar, I. N. Mastorakos, and H.M. Zbib. Determination of dislocation interaction strengths using discrete dislocation dynamics of curved dislocations. *Journal of Engineering Materials and Technology*, 134:1 – 4, 2012.

[5] S. Allain, J-P. Chateau, O. Bouaziz, S. Migot, and N. Guelton. Correlations between the calculated stacking fault energy and the plasticity mechanisms in fe – mn – c alloys. *Materials Science and Engineering A*, 387-389:158 – 162, 2004.

[6] R. Ambati and H. Yuan. Fem mesh-dependence in cutting process simulations. *The International Journal of Advanced Manufacturing Technology*, 53(1):313 – 323, 2011.

[7] L. Anand and M. Kothari. A computational procedure for rate-independent crystal plasticity. *Journal of the Mechanics and Physics of Solids*, 44(4):525 – 558, 1996.

[8] L. Anand and C. Su. A theory for amorphous viscoplastic materials undergoing finite deformations, with applications to metallic glasses. *Journal of the Mechanics and Physics of Solids*, 53:1362 – 1396, 2005.

[9] U. Andrade, M.A. Meyers, K.S. Vecchio, and A.H. Chokshi. Dynamic recrystallization in high-strain, high-strain-rate plastic deformation of copper. *Acta Metallurgica et Materialia*, 42(9):3183 – 3195, 1994.

[10] M. Apostol, T. Vuoristo, and V-T. Kuokkala. High temperature high strain rate testing with a compressive shpb. *Journal de Physique IV*, 110:459 – 464, 2003.

[11] M. Apostol, V-T. Kuokkala, A. Laukkanen, K. Holmberg, R. Waudby, and M. Lindroos. High velocity particle impactor - modeling and experimental verification of impact wear test. In *Proceedings of the 5th World tribology congress WTC*, Turin, Italy, sept 2013.

[12] P. Areais and T. Belytschko. Two-scale shear band evolution by local partition of unity. *International Journal for Numerical Methods in Engineering*, 66:878 – 910, 2006.

[13] A. Arsenlis and D.M. Parks. Modeling the evolution of crystallographic dislocation density in crystal plasticity. *Journal of the Mechanics and Physics of Solids*, 50: 1979 – 2009, 2002.

[14] R.J. Asaro and A. Needleman. Texture develpoment and strain hardening in rata dependent polycrystals. *Acta Metallurgica*, 33(6):923 – 953, 1985.

[15] G. Bao and Z. Lin. High strain rate deformation in particle reinforced metal matrix composites. *Acta Materialia*, 44:1011 – 1019, 1996.

[16] F. Barbe, L. Decker, D. Jeulin, and G. Cailletaud. Intergranular and intragranular behavior of polycrystalline aggregates. part i: Fe model. *International Journal of Plasticity*, 17(4):513 – 536, 2001.

[17] F. Barbe, S. Forest, and G. Cailletaud. Intergranular and intragranular behavior of polycrystalline aggregates. part ii: results. *International Journal of Plasticity*, 17 (4):537 – 563, 2001.

[18] J.L. Bassani and T.Y. Wu. Latent hardening in single crystals ii: Analytical characterization and predictions. *Proceedings of the Royal Society A*, 435:21 – 41, 1991.

[19] M.N. Bassim and A.G. Odeshi. Shear strain localization and fracture in high strength structural materials. *Archives of Materials Science and Engineering*, 31 (2):69 – 74, 2008.

[20] R.C. Batra and L. Chen. Effect of viscoplastic relations on the instability strain, shear band initiation strain, the strain corresponding to the minimum shear band spacing, and the band width in a thermoviscoplastic material. *International Journal of Plasticity*, 17:1465 – 1489, 2001.

[21] R.C. Batra and C.H. Kim. Effect of thermal conductivity on the initiation, growth and bandwidth of adiabatic shear bands. *International Journal of Engineering Science*, 29(8):949 – 960, 1991.

[22] R.C. Batra and Z. Peng. Development of shear bands during the perforation of a steel plaste. *Computational Mechanics*, 47:326 – 334, 1996.

[23] E. Bayraktar, C. Leivaillant, and S. Altintas. Strain rate and temperature effect on the deformation behavior of the original hadfield steel. *Journal de Physique III*, 3: 61 – 66, 1993.

[24] M. Berveiller and A. Zaoui. An extension of the self-consistent scheme to plastically-flowing polycrystals. *Journal of the Mechanics and Physics of Solids*, 26:325 – 344, 1979.

[25] J. Besson and R. Foerch. Object-oriented programming applied to the finite element method part i. general concepts. *Revue Européenne des Éléments Finis*, 7(5): 535 – 566, 1998.

[26] J. Besson, R. Leriche, R. Foerch, and G. Cailletaud. Object-oriented programming applied to the finite element method part ii. application to material behaviors. *Revue Européenne des Éléments Finis*, 7(5):567 – 588, 1998.

[27] J. Besson, G. Cailletaud, J-L. Chaboche, and S. Forest. *Non-linear Mechanics of Materials*. Springer Netherlands, 2010.

[28] I.J. Beyerlein, L. Capolungo, P.E. Marshall, R.J. McCabe, and C.N. Tomé. Statistical analyses of deformation twinning in magnesium. *Philosophical Magazine A*, 90 (16):2161 – 2190, 2010.

[29] I.J. Beyerlein, R.J. McCabe, and C.N. Tomé. The effect of grain size and grain orientation on deformation twinning in a fe – 22 wt. *Journal of the Mechanics and Physics of Solids*, 59:988 – 1003, 2011.

[30] L. Bracke, L. Kestens, and J. Penning. Direct observation of the twinning mechanism in an austenitic fe-mn-c steel. *Scripta Materilia*, 61:220 – 222, 2009.

[31] D.W. Brown, S.R. Agnew, M.A.M. Bourke, T.M. Holden, S.C. Vogel, and C.N. Tomé. Internal strain and texture evolution during deformation twinning in magnesium. *Materials Science and Engineering A*, 399:1 – 12, 2005.

[32] J. Cai, Y. Chen, V.F. Nesterenko, and M.A. Meyers. Influence of particle volume fraction, shape and aspect ratio on the behavior of particle-reinforced metal-matrix composites at high rates of strain. *Acta Materialia*, 46(16):5633 – 5646, 1998.

[33] J. Cai, Y. Chen, V.F. Nesterenko, and M.A. Meyers. High strain rate properties of a unidirectionally reinforced c/al metal matrix composite. *Materials Science and Engineering A*, 485:681 – 689, 2008.

[34] G. Cailletaud. A micromechanical approach to inelastic behaviour of metals. *International Journal of Plasticity*, 8:55 – 73, 1992.

[35] G. Cailletaud and P. Pilvin. Utilisation de modèles polycristallins pour le calcul par éléments finis. *Revue Européenne des Éléments*, 3(4):515 – 541, 1994.

[36] G. Cailletaud, J-L. Chaboche, S. Forest, and L. Rémy. On the design of single crystal turbine blades. *Revue de Métallurgie*, 2:165 – 271, 2001.

[37] G. Cailletaud, O. Diard, F. Feyel, and S. Forest. Computational crystal plasticity : From single crystal to homogenized polycrystals. *Technische Mechanik*, 23(2-4): 130 – 145, 2003.

[38] D. Canadinc, I. Karaman, H. Sehitoglu, Y.I. Chumlyakov, and H.J. Maier. The role of nitrogen on the deformation response of hadfield steel single crystals. *Metallurgical and Materials Transactions A*, 34:1821 – 1831, 2003.

[39] D. Canadinc, H. Sehitoglu, H.J. Maier, and Y.I. Chumlyakov. Strain hardening behavior of aluminum alloyed hadfield steel single crystals. *Acta Materialia*, 53: 1831 – 1842, 2005.

[40] D. Canadinc, C. Efstathiou, and H. Sehitoglu. On the negative strain rate sensitivity of hadfield. *Scripta Materialia*, 59:1103 – 1106, 2008.

[41] A.A. Cenna, N.W. Page, E. Kisi, and M.G. Jones. Single particle impact tests using gas gun and analysis of high strain-rate impact events in ductile materials. *Wear*, 271:1497 – 1503, 2011.

[42] A.A. Cenna, K.C. Williams, and M.G. Jones. Analysis of impact energy factors in ductile materials using single particle impact tests on gas gun. *Tribology International*, 4:1920 – 1925, 2011.

[43] D. Cereceda, M. Diehl, F. Roters, D. Raabe, J.M. Perlado, and J. Marian. Unraveling the temperature dependence of the yield strength in single-crystal tungsten using atomistically-informed crystal plasticity calculations. *International Journal of Plasticity*, 78:242 – 265, 2015.

[44] L. Chen and R.C. Batra. Effect of material parameters on shear band spacing in work-hardening gradient dependent thermoviscoplastic materials. *International Journal of Plasticity*, 15:551 – 574, 1999.

[45] L. Chen and R.C. Batra. Microstructural effects on shear instability and shear band spacing. *Theoretical and Applied Fracture Mechanics*, 34:155 – 166, 2000.

[46] L. Chen, Y. Zhao, and X. Qin. Some aspects of high manganese twinning-induced plasticity (twip) steel, a review. *Acta Metallurgica Sinica*, 26(1):1 – 15, 2013.

[47] W. Chen, Z. Xu, and C. Wu. Analyses of adiabatic shear in some metals from calculations of the temperature distribution and the cooling rate. *Chinese Journal of Metal Science and Technology*, 5:8 – 13, 1989.

[48] J.W. Christian and S. Mahajan. Deformation twinning. *Progress in Material Science*, 39:1 – 157, 1995.

[49] A.H. Cottrell and A. Bilby. A mechanism for the growth of deformation twins in crystals. *Philosophical Magazine*, 42(329):573 – 581, 1951.

[50] S. Curtze and V-T. Kuokkala. Dependence of tensile deformation behavior of twip steels on stacking fault energy, temperature and strain rate. *Acta Materialia*, 58: 5129 – 5141, 2010.

[51] Sven Curtze. *Characterization of the dynamic behavior and microstructure evolution of high strength sheet steels*. PhD thesis, Tampere University of Technology, 2009.

[52] L.H. Dai, L.F. Liu, and Y.L. Bai. Effect of particle size on the formation of adiabatic shear band in particle reinforced metal matrix composites. *Materials Letters*, 58: 1773 – 1776, 2004.

[53] L.H. Dai, L.F. Liu, and Y.L. Bai. Formation of adiabatic shear band in metal matrix composites. *International Journal of Solids And Structures*, 41:5979 – 5993, 2004.

[54] S. Dancette, L. Delannay, K. Renard, M.A. Melchior, and P.J. Jacques. Crystal plasticity modeling of texture develpoment and hardening in twip steels. *Acta Materialia*, 60:2135 – 2145, 2012.

[55] M. Dao and R.J. Asaro. Localized deformation modes and non-schmid effects in crystalline solids. part i. critical conditions of localization. *Mechanics of Materials*, 23:71 – 102, 1996.

[56] Y.N. Dastur and W.C. Leslie. Mechanism of work hardening in hadfield manganese steel. *Metallurgical and Materials Transactions A*, 12(5):749 – 759, 1981.

[57] J. Dean, C.S. Dunleavy, P.M. Brown, and T.W. Clyne. Energy absorption during projectile perforation of thin steel plates and the kinetic energy of ejected fragments. *International Journal of Impact Engineering*, 36:1250 – 1258, 2009.

[58] B. Devincre, L. Kubin, and T. Hoc. The role of collinear interaction in dislocation-induced hardening. *Science*, 301:1879 – 1882, 2003.

[59] B. Devincre, L. Kubin, and T. Hoc. Physical analyses of crystal plasticity by dd simulations. *Scripta Materialia*, 54:741 – 746, 2006.

[60] O. Diard, S. Leclercq, G. Rousselier, and G. Cailletaud. Evaluation of finite element based analysis of 3d multicrystalline aggregates plasticity application to crystal plasticity model identification and the study of stress and strain fields near grain boundaries. *International Journal of Plasticity*, 21:691 – 722, 2005.

[61] B. Dodd and Y. Bai. *Adiabatic shear localization (second edition)*. Elsevier, 2012.

[62] M. Dolinski, D. Rittel, and A. Dorogoy. Modeling adiabatic shear failure from energy considerations. *Journal of the Mechanics and Physics of Solids*, 55(11): 1759 – 1775, 2010.

[63] D. Dorner and S. Zaefferer. Microstructure and texture of shear bands in cold rolled silicon steel single crystals of goss orientation. *Solid State Phenomena*, 105:239 – 244, 2015.

[64] C.Z. Duan, L.C. Zhang, H.Y. Yu, and M.J. Wang. An investigation into the microstructure of adiabatic shear banding in aisi 1045 hardened steel due to high speed machining. *Advanced Materials Research*, 154-155:321 – 324, 2011.

[65] C. Efstathiou and H. Sehitoglu. Strain hardening and heterogeneous deformation during twinning in hadfield steel. *Acta Materialia*, 58:1479 – 1488, 2010.

[66] E. El-Danaf, S.R. Kalidindi, and R.D. Doherty. Influence of grain size and stacking-fault energy on deformation twinning in fcc metals. *Materials Science and Engineering A*, 30(5):1223 – 1233, 1999.

[67] Y. Estrin, L.S. Tóth, A. Molinari, and Y. Bréchet. A dislocation-based model for all hardening stages in large strain deformation. *Acta Materialia*, 46:5509 – 5522, 1998.

[68] Y. Estrin, L.S. Tóth, Y. Bréchet, and H.S. Kim. Modelling of the evolution of dislocation cell misorientation under severe plastic deformation. *Materials Science Forum*, 304-305:675 – 680, 2006.

[69] B. Fekete and A. Szekeres. Investigation on partition of plastic work converted to heat during plastic deformation for reactor steels based on inverse experimental-computational method. *European Journal of Mechanics A/Solids*, 53:175 – 186, 2015.

[70] P.S. Follansbe and U.F. Kocks. A constitutive description of the deformation of copper based on the use of the mechanical threshold stress as an internal state variable. *Acta Metallurgica*, 36(1):81 – 93, 1988.

[71] S. Forest. Modeling slip, kink, and shear banding in classical and generalized single crystal plasticity. *Acta Materialia*, 46(9):3265 – 3281, 1998.

[72] S. Forest. Strain localization phenomena in generalized single crystal plasticity. *Journal of the Mechanical Behavior of Materials*, 11(1-3):45 – 50, 2000.

[73] S. Forest and G. Cailletaud. Strain localization in single crystals: bifurcation analysis, effects of boundaries and interfaces. *European Journal of Mechanics, - A/Solids*, 14:747 – 771, 1995.

[74] P. Franciosi. The concepts of latent hardening and strain hardening in metallic single crystals. *Acta Metallurgica*, 33:1601 – 1612, 1985.

[75] P. Franciosi, M. Berveiller, and A. Zaoui. Latent hardening in copper and aluminum single-crystals. *Acta Metallurgica*, 28:273 – 283, 1980.

[76] G. Frommeyer, U. Brüx, and P. Neumann. Supra-ductile and high strength manganese trip/twip steels for high energy absorpation purposes. *ISIJ International*, 43:438 – 446, 2003.

[77] W.M. Garrison. Abasive wear resistance: the effect of ploughing and the removal of ploughed material. *Wear*, 114:239 – 247, 1986.

[78] J.D. Gates, G.J. Gore, M.J-P. Hermand, M.J-P. Guerineau, P.B. Martin, and J. Saad. The meaning of high stress abrasion and its application in white cast irons. *Wear*, 263:6 – 35, 2007.

[79] M.A. Gharghouri, G.C. Weatherly, J.D. Embury, and J. Root. Study of the mechanical properties of mg-7.7at.% al by in-situ neutron diffraction. *Philosophical Magazine A*, 79(7):1671 – 1695, 1999.

[80] J. Gittus, J. Zarka, and V. Nemat-Nasser. *Large deformations of solids: Physical basis and mathematical modelling.* Elseview science publishing Co. Inc., 1986.

[81] C. Gérard, G. Cailletaud, and B. Bacroix. Modeling of latent hardening produced by complex loading paths in fcc alloys. *International Journal of Plasticity*, 42: 194 – 212, 2013.

[82] O. Grässel, L. Krüger, G. Frommeyer, and L.W. Meyer. High strength fe – mn – (al, si) trip/twip steels development — properties — application. *International Journal of Plasticity*, 16:1391 – 1409, 2000.

[83] P.R. Guduru, A.J. Rosakis, and G. Ravichandran. Dynamic shear bands: an investigation using high speed optical and infrared diagnostics. *Mechanics of Materials*, 33:371 – 410, 2001.

[84] Yoann Guilhem. *Numerical investigation of the local mechanical fields in 316L steel polycrystalline aggregates under fatigue loading.* PhD thesis, MINES ParisTech, 2011.

[85] C. Guillemer, M. Clavel, and G. Cailletaud. Cyclic behavior of extruded magnesium: Experimental, microstructural and numerical approach. *International Journal of Plasticity*, 27:2068 – 2084, 2011.

[86] I. Gutierrez-Urrutia and D. Raabe. Study of deformation twinning and planar slip in a twip steel by electron channelling contrast imaging in a sem. *Materials Science Forum*, 702-703:523 – 529, 2012.

[87] I. Gutierrez-Urrutia, S. Zaefferer, and D. Raabe. The effect of grain size and grain orientation on deformation twinning in a fe – 22 wt. *Materials Science and Engineering A*, 527(15):3552 – 3560, 2010.

[88] Xu Han. *Modeling of cavity swelling-induced embrittlement in irradiated austenitic stainless steels*. PhD thesis, MINES ParisTech, 2012.

[89] J.A. Hines and K.S Vecchio. Recrystallization kinetics within adiabatic shear bands. *Acta Materialia*, 45(2):635 – 649, 1997.

[90] J.A. Hines, K.S Vecchio, and S. Ahzi. A model for microstructure evolution in adiabatic shear band. *Metallurgical and Materials Transactions A*, 29:191 – 203, 1998.

[91] T. Hoc and S. Forest. Polycrystal modelling of if-ti steel under complex loading path. *International Journal of Plasticity*, 17:65 – 85, 2001.

[92] T. Hoc, C. Rey, and J.L. Raphanel. Experimental and numerical analysis of localization during sequential test for an if – ti steel. *Acta Materialia*, 49(10): 1835 – 1846, 2001.

[93] J. Hodowany, G. Ravichandran, A.J. Rosakis, and P. Rosakis. Partition of plastic work into heat and stored energy in metals. *Experimental Mechanics*, 40(2):113 – 123, 2000.

[94] Mikko Hokka. *Effects of strain rate and temperature on the mechanical behavior of advanced high strength steels*. PhD thesis, Tampere University of Technology, 2008.

[95] K. Hokkirigawa and K. Kato. An experimental and theoretical investigation of ploughing, cutting and wedge formation during abrasive wear. *Tribology International*, 21:51 – 57, 1988.

[96] K. Holmberg, A. Laukkanen, H. Ronkainen, K. Wallin, S. Varjus, and J. Koskinen. Tribological contact analysis of a rigid ball sliding on a hard coated surface. part i: Modelling stresses and strains. *Surface and Coatings Technology*, 200:3793 – 3809, 2006.

[97] C.S. Hong, N.R. Tao, X. Huang, and K. Lu. Nucleation and thickening of shear bands in nano-scale twin/matrix lamellae of a cu – al alloy processed by dynamic plastic deformation. *Acta Materialia*, 58:3103 – 3116, 2010.

[98] P. Van Houtte. Simulation of the rolling and shear texture of brass by the taylor theory adapted for mechanical twinning. *Acta Metallurgica*, 26(4):591 – 604, 1978.

[99] IM. Hutchings and RE. Winter. The erosion of ductile metals by spherical particles. *Journal of Physics D: Applied Physics*, 8:8 – 14, 1975.

[100] IM. Hutchings and RE. Winter. A simple small-bore laboratory gas-gun. *Journal of Physics E: Instruments*, 8(2):84 – 86, 1975.

[101] IM. Hutchings, NH. Macmillan, and DG. Rickerby. Further studies of the oblique impact of a hard sphere against a ductile solid. *International Journal of Materials Science*, 23(11):639 – 646, 1981.

[102] J.W. Hutchinson. Bounds and self-consistent estimates for creep of polycrystalline materials. *Proceedings of the Royal Society A*, 348:101 – 127, 1976.

[103] H. Idrissi, K. Renard, L. Ryelandt, D. Schryvers, and P.J. Jacques. On the mechanisms of twin formation in fe-mn-c twip steels. *Acta Materialia*, 58:2464 – 2476, 2010.

[104] Matti Isakov. *Strain rate history effects in a metastable austenitic strainless steel*. PhD thesis, Tampere University of Technology, 2012.

[105] N. Jia, P. Eisenlohr, F. Roters, D. Raabe, and X. Zhao. Orientation dependence of shear banding in face-centered-cubic single crystals. *Acta Materialia*, 90:3415 – 3434, 2012.

[106] N. Jia, F. Roters, P. Eisenlohr, C. Kords, and D. Raabe. Non-crystallographic shear banding in crystal plasticity fem simulations: Example of texture evolution in α-brass. *Acta Materialia*, 60:1099 – 1115, 2012.

[107] N. Jia, F. Roters, P. Eisenlohr, D. Raabe, and X. Zhao. Simulation of shear banding in heterophase co-deformation: Example of plane strain compressed cu – ag and cu – nb metal matrix composites. *Acta Materialia*, 61:4591 – 4606, 2013.

[108] N. Jia, D. Raabe, and X. Zhao. Texture and microstructure evolution during non-crystallographic shear banding in a plane strain compressed cu – ag metal matrix composite. *Acta Materialia*, 76:238 – 251, 2014.

[109] G.R. Johnson and W.H. Cook. A constitutive model and data for metals subjected to large strains, high strain rates and high temperatures. *Proceedings of the 7th International Symposium on Ballistics*, 54:1, 1983.

[110] S.R. Kalidindi. Incorporation of deformation twinning in crystal plasticity models. *Journal of the Mechanics and Physics of Solids*, 46(2):267 – 290, 1998.

[111] S.R. Kalidindi. Modeling anisotropic strain hardening and deformation textures in low stacking fault energy fcc metals. *International Journal of Plasticity*, 17: 837 – 860, 2001.

[112] R. Kapoor and S. Nemat-Nasser. Determination of temperature rise during high strain rate deformation. *Mechcanis of Materials*, 27:1 – 12, 1998.

[113] I. Karaman, H. Sehitoglu, A.J. Beaudoin, Y.I. Chumlyakov, H.J. Maier, and C.N. Tomé. Modelling the deformation behavior of hadfield steel single and polycrystals due to twinning and slip. *Acta Materialia*, 48:2031 – 2047, 2000.

[114] I. Karaman, H. Sehitoglu, K. Gall, Y.I. Chumlyakov, and H.J. Maier. Deformation of single crystal hadfield steel by twinning and slip. *Acta Materialia*, 48:1345 – 1359, 2000.

[115] K. Kato and K. Adachi. *Wear mechanisms - Modern tribology handbook*. CRC Press, 2001.

[116] K. Keltamäki and M. Ylitolva. *Kaivoskoneen kauhan huulilevyn kulumistutkimus (in Finnish)*. Lapin ammattikorkeakoulun julkaisuja, Raportit ja selvitykset 17-2014, 2014.

[117] S. Kibey, J.B. Liu, D.D. Johnson, and H. Sehitoglu. Predicting twinning stress in fcc metals: Linking twin-energy pathways to twin nucleation. *Acta Materialia*, 55: 6843 – 6851, 2007.

[118] E. Kinnunen, I. Miettunen, M. Somani, D. Porter, P. Karjalainen, I. Alamattila, and A. Kemppainen. Development of a new direct quenched abrasion resistant steel. *International Journal of Metallurgical And Materials Engineering*, 1:27 – 34, 2013.

[119] U.F. Kocks and H. Mecking. Physics and phenomenology of strain hardening: the fcc case. *Progress in Materials Science*, 48:171 – 273, 2003.

[120] U.F. Kocks, C.N. Tomé, and H-R. Wenk. *Texture and Anisotropy - Preffered orientations in Polycrystals and their effect on materials propertiesl*. Cambridge university press, Cambridge, United Kingdom, 1998.

[121] S. Lee, K-M. Cho, C.S. Lee, and W.Y. Choo. Microstructural study of adiabatic shear band. *Metallurgical and Materials Transactions*, 24(1):2217 – 2224, 1993.

[122] W-S. Lee and T-H. Chen. Plastic deformation and fracture characteristics of hadfield steel subjected to high-velocity impact loading. *Proceedings of the Institution of Mechanical Engineers, Part C: Journal of Mechanical Engineering Science*, 216(10): 971 – 982, 2002.

[123] Y-K. Lee, H-C. Shin, D-S. Leem, J-Y. Choi, W. Jin, and C-S. Choi. Reverse transformation mechanism of martensite to austenite and amount of retained austenite after reverse transformation in fe – 3si – 1 3cr – 7ni (wt-%) martensitic stainless steel. *Materials Science and Technology*, 19:393 – 398, 2003.

[124] D-F. Li, B.J. Golden, and N.P. O'Dowd. Multiscale modelling of mechanical response in a martensitic steel: A micromechanical and length-scale-dependent framework for precipitate hardening. *Acta Materialia*, 80:445 – 456, 2014.

[125] S. Li and W.K. Liu. *Meshfree particle methods*. Springer, Dordrecht, Berling, Heidelberg, New York, 2002.

[126] S. Li, W. Hao, and W.K. Liu. Mesh-free simulations of shear banding in large deformation. *International Journal of Solids and Structures*, 37:7185 – 7206, 2000.

[127] S. Li, W.K. Liu, D. Qian, P.R. Guduru, and A.J. Rosakis. Dynamically shear band propagation and micro-structure of adiabatic shear band. *Computer Methods in Applied Mechanics and Engineering*, 191:73 – 92, 2001.

[128] S. Li, W.K. Liu, A.J. Rosakis, T. Belytschko, and W. Hao. Mesh-free galerkin simulations of dynamic shear band propagation and failure mode transition. *International Journal of Solids and Structures*, 39:1213 – 1240, 2002.

[129] Y. Li, L. Zhu, Y. Liu, Y. Wei, Y. Wu, D. Tang, and Z. Mi. On the strain hardening and texture evolution in high manganese steels: Experiments and numerical investigation. *Journal of the Mechanics and Physics of Solids*, 61:2588 – 2604, 2013.

[130] S.C. Lim. Recent developments in wear-mechanism maps. *Tribology International*, 31(1-3):87–97, 1998.

[131] M. Lindroos, V-T. Kuokkala, A. Lehtovaara, and P. Kivikyto-Reponen. Effects of strain and strain rate on the abrasive wear behavior of high manganese austenitic steel. *Key Engineering Materials*, 527:211–216, 2013.

[132] M. Lindroos, M. Apostol, V. Heino, K. Valtonen, A. Laukkanen, K. Holmberg, and V-T. Kuokkala. The deformation, strain hardening, and wear behavior of chromium-alloyed hadfield steel in abrasive and impact conditions. *Tribology Letters*, 57(3): 1–11, 2015.

[133] M. Lindroos, M. Apostol, V-T. Kuokkala, A. Laukkanen, K. Valtonen, K. Holmberg, and O. Oja. Experimental study on the behavior of wear resistant steels under high velocity single particle impacts. *International Journal of Impact Engineering*, 78: 114–127, 2015.

[134] M. Lindroos, V. Ratia, M. Apostol, K. Valtonen, A. Laukkanen, W. Molnar, K. Holmberg, and V-T. Kuokkala. Experimental study on the behavior of wear resistant steels under high velocity single particle impacts. *International Journal of Impact Engineering*, 328-329:197–205, 2015.

[135] M. Lindroos, K. Valtonen, A. Kemppainen, A. Laukkanen, K. Holmberg, and V-T. Kuokkala. Wear behavior and work hardening of high strenght steels in high stress abrasion. *Wear*, 322-323:32–40, 2015.

[136] J.F.C Lins, H.R.Z. Sandim, H-J. Kestenbach, D. Raabe, and K.S. Vecchio. A microstructural investigation of adiabatic shear bands in an interstitial free steel. *Materials Science and Engineering A*, 457:205–218, 2007.

[137] F.C. Liu, Z.N. Yang, C.L. Zheng, and F.C. Zheng. Simultaneously improving the strength and ductility of coarse-grained hadfield steel with increasing strain rate. *Scripta Materialia*, 66(7):431–434, 2012.

[138] G.R. Liu and Y.T. Gu. *An Introduction to Meshfree Methods and Their Programming.* Springer, Dordrecht, Berling, Heidelberg, New York, 2005.

[139] S. Forest M. Fivel. *Plasticité cristalline et transition d'échelle : cas du monocrista - Techniques de l'Ingénieur - Doc. M4016.* 2004.

[140] A. Ma, F. Roters, and D. Raabe. Studying the effect of grain boundaries in dislocation density based crystal-plasticity finite element simulations. *International Journal of Solids and Structures*, 43:7287–7303, 2006.

[141] A. Ma, F. Roters, and D. Raabe. A dislocation density based constitutive model for crystal plasticity fem including geometrically necessary dislocations. *Acta Materialia*, 8:2169–2179, 2006.

[142] S. Mahajan and G.Y. Chin. Formation of deformation twins in f.c.c. crystals. *Acta Metallurgica*, 21(10):1353–1363, 1973.

[143] J. Mandel. Equations constitutives et directeurs dans les milieux plastiques et viscoplastiques. *International Journal of Solids and Structures*, 9:725–740, 1973.

[144] F. Maresca, V.G. Kouznetsova, and M.G.D. Geers. Subgrain lath martensite mechanics: A numerical-expermental analysis. *Journal of the Mechanics and Physics of Solids*, 73:69 – 83, 2014.

[145] J-P. Massoud, S. Bugat, D. Lidbury, B. Marini, and S. Van Dyck. *Perfect consortium, Final activity report.* European commission, Euratom research and training programme on nuclear energy within sixth framework programme, 2002-2006.

[146] Jean-Philippe Mathieu. *Analyse et modélisation micromécanique du comportement et de la rupture fragile de l'acier 16MND5: prise en compte des hétérogénéités microstructurales.* PhD thesis, Arts et Métiers ParisTech, 2006.

[147] H. Mecking and U.F. Kocks. The concepts of latent hardening and strain hardening in metallic single crystals. *Acta Metallurgica*, 29:1865 – 1875, 1981.

[148] S. N. Medyanik, W. K. Liu, and S. Li. On criteria for dynamic adiabatic shear band propagation. *Journal of Mechanics and Physics of Solids*, 55:1493 – 1461, 2007.

[149] Metso. *Nordberg C-series jaw crusher, products [www].* Metso Minerals, www.metso.com, 2015.

[150] M.A. Meyers and H-R. Pak. Observation of an adiabatic shear band in titanium by high-voltage transmission electron microscopy. *Acta Metallurgica*, 34(12):2493 – 2499, 1986.

[151] M.A. Meyers, J.C. LaSalvia, V.F. Nestorenko, Y.J. Chen, and B.K. Kad. Dynamic recrystallization in high strain rate deformation. In *Proceedings of ReX 96, The third international Conference on Recrystallization and related phenomena*, pages 279 – 286, Monterey,California USA, October 1996.

[152] M.A. Meyers, V.F. Nesterenko, J.C. LaSalvia, and Q. Xue. Shear localization in dynamic deformation of materials: microstructural evolution and self-organization. *Materials Science and Engineering A*, 317:204 – 225, 2001.

[153] M.A. Meyers, Y.B. Xu, Q. Xue, M.T. Pérez-Prado, and T.R. McNelley. Microstructural evolution in adiabatic shear localization in stainless steel. *Acta Materialia*, 51: 1307 – 1325, 2003.

[154] S. Miura, JI. Takamura, and N. Narita. Orientation dependence of flow stress for twinning in silver crystals. *Transactions of the Japan Institute of Metals*, S9:555, 1968.

[155] W. Molnar, S. Nugent, M. Lindroos, M. Apostol, and M. Varga. Ballistic and numerical simulation of impacting goods on conveyor belt rubber. *Polymer Testing*, 42:1 – 7, 2015.

[156] E. De Moor, S. Lacroix, A.J. Clarke, J. Penning, and J.G. Speer. Effect of retained austenite stabilized via quench and partitioning on the strain hardening of martensitic steels. *Metallurgical And Materials Transactions A*, 39:2586 – 2596, 2008.

[157] L. Méric and G. Cailletaud. Single crystal modeling for structural calculations. part 2: F.e. implementation. *Journal of Engineering and Materials Technology*, 113: 171 – 182, 1991.

[158] L. Méric, P. Poubanne, and G. Cailletaud. Single crystal modeling for structural calculations. part 1: Model presentation. *Journal of Engineering and Materials Technology*, 113:162 – 170, 1991.

[159] P. Mullner, C. Solenthaler, and M. Speidel. Second order twinning in austenitic steel. *Acta Metallurgica et Materialia*, 42(5):1727 – 32, 1994.

[160] A. Musienko, A. Tatschl, K. Schmidegg, O. Kolednik, R. Pippan, and G. Cailletaud. Three-dimensional finite element simulation of a polycrystalline copper specimen. *Acta Materialia*, 55(12):4121 – 4136, 2007.

[161] N. Nakada, T. Tsuchiyama, S. Takaki, and S. Hashizume. Variant selection of reversed austenite in lath martensite. *ISIJ International*, 47(10):1527 – 1532, 2007.

[162] N. Nakada, R. Fukagawa, T. Tsuchiyama, S. Takaki, D. Ponge, and D. Raabe. Inheritance of dislocations and crystallographic texture during martensitic reversion into austenite. *ISIJ International*, 53(7):1286 – 1288, 2013.

[163] JH. Neilson and A. Gilchrist. Erosion by a stream of solid particles. *Wear*, 11 (111-122), 1968.

[164] S. Nemat-Nasser, T. Okinaka, and L. Ni. A physically-based constitutive model for bcc crystals with application to polycrystalline tantalum. *Journal of the Mechanics and Physics of Solids*, 46(6):1009 – 1038, 1998.

[165] V.F. Nesterenko, M.A. Meyers, J.C. LaSalvia, M.P. Bondar, Y.J. Chen, and Y.L. Lukyanov. Shear localization and recrystallization in high-strain, high-strain-rate deformation of tantalum. *Materials Science and Engineering A*, 229:23 – 41, 1997.

[166] AG. Odeshi, MN. Bassim, S. Al-Ameeri, and Q. Li. Dynamic shear band propagation and failure in aisi 4340 steel. *Journal of Materials Processing Technology*, 169(2): 150 – 155, 2005.

[167] N. Ojala, K. Valtonen, P. Kivikyto-Reponen, P. Vuorinen, P. Siitonen, and V-T. Kuokkala. Effect of test parameters on large particle high speed slurry erosion testing. *Tribology - Materials, Surface and Interfaces*, 8(2):98 – 104, 2014.

[168] Nikolay Osipov. *Génération et calcul de microstructures bainitiques, approche locale intragranulaire de la ruptur*. PhD thesis, MINES ParisTech, 2007.

[169] W.S. Owen and M. Grujicic. Strain aging of austenitic hadfield manganese steel. *Acta Materialia*, 47(1):111 – 126, 1999.

[170] S.H. Park, S-G. Hong, and C.S. Lee. Activation mode dependent {10-12} twinning characteristics in a polycrystalline magnesium alloy. *Scripta Materialia*, 62:202 – 205, 2010.

[171] A. Patra, T. Zhu, and D. L. McDowell. Constitutive equations for modeling non-schmid effect in single crystal bcc-fe at low and ambient temperatures. *International Journal of Plasticity*, 59:1 – 14, 2014.

[172] P.D.Wu, K.W. Neale, and E. Van der Giessen. Simulation of the behavior of fcc polycrystals during reversed torsion. *International Journal of Plasticity*, 12: 1199 – 1219, 1996.

[173] B. Peeters, S.R. Kalidindi, P. Van Houtte, and E. Aernoudt. A crystal plasticity based work-hardening/softening model for b.c.c. metals under changing strain paths. *Acta Materilia*, 48:2123 – 2133, 2000.

[174] D. Peirce, R.J. Asaro, and A. Needleman. Material rate dependence and localized deformation in crystalline solids. *Acta Metallurgica*, 31(12):1951 – 1976, 1983.

[175] J. Peirs, W. Tirry, B. Amin-Ahmadi, F. Coghe, P. Verleysen, L. Rabet, D. Schryvers, and J. Degrieck. Microstructure of adiabatic shear bands in ti6al4v. *Materials Characterization*, 75:79 – 92, 2013.

[176] Y. Petrov, V. Gavriljuk, H. Berns, and F. Schmalt. Surface structure of stainless and hadfield steels after impact wear. *Wear*, 260:687 – 691, 2006.

[177] D.T. Pierce, K. Nowag, A. Montagne, J.A. Jiménez, J.E. Wittig, and R. Ghisleni. Single crystal elastic constants of high-manganese transformation- and twinning-induced plasticity steels determined by a new method utilizing nanoindentation. *Materials Science and Engineering A*, 578:134 – 139, 2013.

[178] D.T. Pierce, J.A. Jiminez, J. Bentley, D. Raabe, and J.E. Wittig. The influence of stacking fault energy on the microstructural and strain-hardening behavior of fe-mn-al-si steels during tensile deformation. *Acta Materialia*, 100:178 – 190, 2015.

[179] B. Podgornik, S. Hogmark, O. Sandberg, and V. Leskovsek. Wear resistance and anti-sticking properties of duplex treated forming tool steel. *Tribology International*, 254:1113 – 1121, 2003.

[180] C.C. Poteet and I.W. Hall. High strain rate properties of a unidirectionally reinforced c/al metal matrix composite. *Materials Science and Engineering A*, 222:35 – 44, 1997.

[181] V. Ratia, I. Miettunen, and V-T. Kuokkala. Surface deformation of steels in impact abrasion: the effect of sample angle and test duration. *Wear*, 301:94 – 101, 2013.

[182] V. Ratia, V. Heino, K. Valtonen, M. Vippola, A. Kemppainen, P. Siitonen, and V-T. Kuokkala. The effect of abrasive properties on the high-stress three-body abrasion of steels and hard metals. *TRIBOLOGIA - Finnish Journal of Tribology 1*, 32:3 – 18, 2014.

[183] V. Ratia, H. Rojacz, J. Terva, K. Valtonen, E. Badisch, and V-T. Kuokkala. Effect of multiple impacts on the deformation of wear-resistant steels. *Tribology Letters*, 57(15):1 – 16, 2015.

[184] D. Rittel. On the conversion of plastic work to heat during high strain rate deformation of glassy polymers. *Mechanics of Materials*, 31:131 – 139, 1999.

[185] D. Rittel and S. Osovski. Dynamic failure by adiabatic shear banding. *International Journal of Fracture*, 162(1):177 – 185, 2010.

[186] D. Rittel, G. Ravichandran, and A. Venkert. The mechanical response of pure iron at high strain rates under dominant shear. *Materials Science and Engineering A*, 432:191 – 201, 2006.

[187] D. Rittel, Z.G. Wang, and M. Merzer. Adiabatic shear failure and dynamic stored energy of cold work. *Physical Review Letter*, 96(075502):1 – 4, 2006.

[188] D. Rittel, P. Landau, and A. Venkert. Dynamic recrystallization as a potential cause for adiabatic shear failure. *Physical Review Letter*, 101(165501):1 – 4, 2008.

[189] F. Roters, D. Raabe, and G. Gottstein. Work hardening in heterogenous alloys - a microstructural approach based on three internal state variables. *Acta Materilia*, 48:4181 – 4189, 2000.

[190] F. Roters, P. Eisenlohr, T.R. Bieler, and D. Raabe. *Crystal Plasticity Finite Element Methods*. Wiley-VCH, 2010.

[191] F. Roters, P. Eisenlohr, L. Hantcherli, D.D. Tjahjanto, T.R. Bieler, and D. Raabe. Overview of constitutive laws, kinematics, homogenization and multiscale methods in crystal plasticity finite-element modeling: Theory, experiments, applications. *Acta Materialia*, 58:1152 – 1211, 2010.

[192] Franz Roters. *Advanced material models for the crystal plasticity finite element method - Habilation thesis*. PhD thesis, Technischen Hochschule Aachen genehmigte, 2011.

[193] A. Sabih and J.A. Nemesh. Experimental and finite element simulation study of the adiabatic shear band phenomenon in cold heading process. *Journal of Materials Processing Technology*, 212:1089 – 1105, 2012.

[194] T. Sakai, A. Belyakov, R. Kaibyshev, H. Miura, and J.J. Jonas. Dynamic and post-dynamic recrystallization under hot, cold and severe plastic deformation conditions. *Progress in Materials Science*, 60:130 – 207, 2014.

[195] N.A. Sakharova, J.V. Fernandes, J.M. Antunes, and M.C. Oliveira. Comparison between berkovich, vickers and conical indentation tests: A three-dimensional numerical simulation study. *International Journal of Solids and Structures*, 46(5): 1095 – 1104, 2009.

[196] A.A. Salem, S.R. Kalidindi, and S.L. Semiatin. Strain hardening due to deformation twinning in α-titanium: Constitutive relations and crystal-plasticity modeling. *Acta Materialia*, 53:3495 – 3502, 2005.

[197] A.A. Salem, S.R. Kalidindi, R.D Doherty, and S.L. Semiatin. Strain hardening due to deformation twinning in α-titanium: Mechanisms. *Metallurgical and Materials Transactions A*, 37A:259 – 268, 2006.

[198] E. Sarlin, M. Apostol, M. Lindroos, V-T. Kuokkala, J. Vuorinen, T. Lepisto, and M. Vippola. Impact properties of novel corrosion resistant hybrid structures. *Composite Structures*, 108:886 – 893, 2014.

[199] E. Sarlin, M. Lindroos, M. Apostol, V-T. Kuokkala, J. Vuorinen, T. Lepisto, and M. Vippola. The effect of test parameters on the impact resistance of a stainless steel/rubber/composite hybrid structure. *Composite Structures*, 113:469 – 475, 2014.

[200] J. G. Sevillano. An alternative model for the strain hardening of fcc alloys that twin, validated for twinning-induced plasticity steel. *Scripta Materialia*, 60(5):336 – 339, 2009.

[201] P. Shanthraj and M.A. Zikry. Optimal microstructures for martensitic steels. *Journal of Materials Research*, 27(12):1598 – 1611, 2012.

[202] L. Stainier, A.M. Cuitino, and M. Ortiz. Multiscale modelling of hardening in bcc crystal plasticity. *Journal de Physique IV*, 105:157–164, 2003.

[203] A. Staroselsky and L. Anand. Inelastic deformation of polycrystalline face centered cubic materials by slip and twinning. *Journal of the Mechanics and Physics of Solids*, 46(4):671–696, 1998.

[204] D.R. Steinmetz, T. Jäpel, B. Wietbock, P. Eisenlohr, I. Gutierrez-Urrutia, A. Saeed-Akbari, T. Hickel, F. Roters, and D. Raabe. Revealing the strain-hardening behavior of twinning-induced plasticity steels: Theory, simulations, experiments. *Acta Materialia*, 61:494–510, 2013.

[205] P. Suikkanen and J. Kömi. Microstructure, properties and design of direct quenched structural steels. *Materials Science Forum*, 783-786:246–251, 2014.

[206] G. Sundararajan. The energy absorbed during the oblique impact of a hard ball against ductile target materials. *International Journal of Impact Engineering*, 9(3): 343–358.

[207] G. Sundararajan and R.G. Shewmon. The oblique impact of a hard ball against ductile, semi-infinite target materials - experiment and analysis. *International Journal of Impact Engineering*, 6(1):3–22, 1987.

[208] C.K. Syn, D.R. Lesuer, and O.D. Sherby. Microstructure in adiabatic shear bands in a pearlitic ultrahigh carbon steel. *Materials Science and Technology*, 21(3):317–324, 2005.

[209] L. Tabourot, M. Fivel, and E. Rauch. Generalised constitutive laws for f.c.c. single crystals. *Materials Science and Engineering A*, 234-236:639–642, 1997.

[210] C. Teodosiu. A physical theory of the finite elastic-viscoplastic behaviour of single crystals. *Engineering Transactions*, 23:157–183, 1975.

[211] J. Terva, T. Teeri, V-T. Kuokkala, P. Siitonen, and J. Liimatainen. Abrasive wear of steel against gravel with different rock–steel combinations. *Wear*, 267:1821–1831, 2009.

[212] J. Terva, V-T. Kuokkala, and P. Kivikyto-Reponen. Multiple pass scratch testing with natural rock indenter. In *14th Nordic Symposium on Tribology*, pages 1–8, Storforsen, Sweden, 2010.

[213] S.M. Toker, D. Canadinc, A. Taube, G. Gerstein, and H.J. Maier. On the role of slip–twin interactions on the impact behavior of high-manganese austenitic steels. *Materials Science and Engineering A*, 593:120–126, 2014.

[214] J.A. Venables. The nucleation and propagation of deformation twins. *Philosophical Magazine*, 6(33):379–396, 1961.

[215] J.A. Venables. The nucleation and propagation of deformation twins. *Journal of Physics and Chemistry of Solids*, 25(7):693–700, 1964.

[216] B. Venkataraman and G. Sundararajan. Correlation between the characteristics of mechanically mixed layer and wear behavior of aluminium, al-7075 alloy and al-mmcs. *Wear*, 245(1-2):22–38, 2000.

[217] H. Wang, P.D. Wu, J. Wang, and C.N. Tomé. A crystal plasticity model for hexagonal close packed (hcp) crystals including twinning and de-twinning mechanisms. *International Journal of Plasticity*, 49:36 – 52, 2013.

[218] X. Wang and J. Shi. Validation of johnson-cook plasticity and damage model using impact experiment. *International Journal of Impact Engineering*, 60:67 – 75, 2013.

[219] R. Waudby, T. Varis, T. Suhonen, K. Holmberg, M. Apostol, and M. Lindroos. High velocity impact testing on thermal spray hard carbide coatings on steel substrate. In *Proceedings of the 5th World tribology congress WTC*, Turin, Italy, 2013.

[220] Q. Wei, L. Kecskes, T. Jiao, K.T. Hartwig, K.T. Ramesh, and E. Ma. Adiabatic shear banding in ultrafine-grained fe processed by severe plastic deformation. *Acta Materialia*, 52:1859 – 1869, 2004.

[221] Y. Wei, C. Su, and L. Anand. A computational study of the mechanical behavior of nanocrystalline fcc metals. *Acta Materialia*, 54:3177 – 3190, 2006.

[222] Y.H. Wen, H.B. Peng, H.T. Si, R.L. Xiong, and D. Raabe. A novel high manganese austenitic steel with higher work hardening capacity and much lower impact deformation than hadfield manganese steel. *Materials et Design*, 55:798 – 804, 2014.

[223] RE. Winter and IM. Hutchings. Solid particle erosion studies using single angular particles. *Wear*, 29:181 – 194, 1974.

[224] T.W. Wright. *The physics and mathematics of adiabatic shear bands*. Cambridge university press, The Edinburgh Building, Cambridge CB2 2RU, United Kingdom, 2002.

[225] Q. Wu, P. Shanthraj, and M.A. Zikry. Modelling the heterogenous effects of retained austenite on the behavior of martensitic high strenght steels. *International Journal of Fracture*, 184(1):241 – 252, 2013.

[226] T.Y. Wu, J.L. Bassani, and C.Laird. Latent hardening in single crystals i: Theory and experiments. *Proceedings of the Royal Society A*, 435(1893):1 – 19, 1991.

[227] C.L. Xie, S. Ghosh, and M. Groeber. Modeling cyclic deformation of hsla steels using crystal plasticity. *Journal of Engineering Materials and Technology*, 126: 339 – 352, 2004.

[228] X. Xu, S. van der Zwaag, and W. Xu. A novel multi-pass dual-indenter scratch test to unravel abrasion damage formation in construction steels. *Wear*, 322-323:51 – 60, 2015.

[229] X.L. Xu and Y.T. Zhu. Inverse grain-size effect on twinning in nanocrystalline ni. *Physical Review Letters B*, 101(2):025501 – 025504, 2008.

[230] Y.B. Xu, W.L. Zhong, Y.J. Chen, L.T. Shen, Q. Liu, Y.L. Bai, and M.A. Meyers. Shear localization and recrystallization in dynamic deformation of 8090 al – li alloy. *Materials Science and Engineering A*, 299:287 – 295, 2001.

[231] Y.B. Xu, J. Zhang, Y. Bai, and M.A. Meyers. Shear localization in dynamic deformation: Microstructural evolution. *Metallurgical and Materials Transactions A*, 39:811 – 843, 2008.

[232] T. Yalcinkaya, W.A.M. Brekelmans, and M.G.D. Geers. Bcc single crystal plasticity modeling and its experimental identification. *Mechanics of Materials*, 16(8):1 – 16, 2008.

[233] W. Yan, L. Fang, K. Sun, and Y. Xu. Effect of surface work hardening on wear behavior of hadfield steel. *Materials Science and Engineering A*, 460-461:542 – 549, 2007.

[234] H. Yang, J.H. Zhang, Y. Xu, and M.A. Meyers. Microstructural characterization of the shear bands in fe-cr-ni single crystal by ebsd. *Journal of Materials Science and Technology*, 24(6):819 – 828, 2008.

[235] C. Yu, G.Kang, and Q. Kan. Crystal plasticity based constitutive model for uniaxial ratchetting of polycrystalline magnesium alloy. *Computational Materials Science*, 84:63 – 73, 2014.

[236] Z-set. *Zset user's manual - Materials manual*. 2015.

[237] Z-set. *Zset user's manual - User's manual*. 2015.

[238] C. Zener and J.H. Hollomon. Effect of strain rate upon plastic flow of steel. *Journal of Applied Physics*, 15(1):22 – 32, 1944.

[239] F.J. Zerilli and R.W. Armstrong. The effect of dislocation drag on the stress-strain behavior of f.c.c. metals. *Acta Metallurgica et Materialia*, 40(8):1803 – 1808, 1992.

[240] J. Zhang and S.P. Joshi. Phenomenological crystal plasticity modeling and detailed micromechanical investigations of pure magnesium. *Journal of the Mechanics and Physics of Solids*, 60(5):945 – 972, 2012.

[241] Z. Zhang and R.J. Clifton. Shear band propagation from a crack tip subjected to mode ii shear wave loading. *International Journal of Solids and Structures*, 44: 1900 – 1926, 2007.

[242] M. Zhou, G. Ravichandran, and A.J. Rosakis. Dynamically propagating shear bands in impact-loaded plates - ii. numerical simulations. *Journal of the Mechanics and Physics of Solids*, 44(6):1007 – 1032, 1996.

[243] Y.T. Zhu, X.Z. Liao, X.L. Wu, and J. Narayan. Grain size effect on deformation twinning and detwinning. *Journal of Materials Science*, 48(13):4467 – 4475, 2013.

[244] B.K. Zuidema, D.K. Subramanyam, and W.C. Leslie. The effect of aluminum on the work hardening and wear resistance of hadfield manganese steel. *Metallurgical and Materials Transactions A*, 18(9):1629 – 1639, 1987.

[245] K-H. Zum-Gahr. Wear by hard particles. *Tribology International*, 31(10):587 – 596, 1998.

[246] K-Z. Zum-Gahr. *Microstructure and wear of materials*. Tribology Series vol 10 - Elsevier, 1987.

A First Appendix

A.1 Notation

The mathematical notation follows the notation derived and utilized in ref. [88]

Tensors and tensorial operations:

- Rank 2 identity tensor : $\underline{1} = I_{ij} = \delta_{ij}$
- Rank 4 identity tensor : $\underline{\underline{1}} = I_{ijkl} = \frac{1}{2}(\delta_{ik}\delta_{jl} + \delta_{il}\delta_{jk})$
- $\underline{C} = \underline{A} \cdot \underline{B} \qquad C_{ij} = A_{im}B_{mj}$
- $C = \underline{A} : \underline{B} \qquad C = A_{ij}B_{ij}$
- $\underline{C} = \underline{\underline{\Lambda}} : \underline{B} \qquad C_{ij} = \Lambda_{ijkl}B_{kl}$
- $\underline{\underline{C}} = \underline{A} \underline{\otimes} \underline{B} \qquad C_{ijkl} = A_{ik}B_{jl}$
- $\underline{\underline{C}} = \underline{A} \otimes \underline{B} \qquad C_{ijkl} = A_{ij}B_{kl}$
- $\underline{\underline{C}} = \underline{A} \overline{\otimes} \underline{B} \qquad C_{ijkl} = A_{il}B_{jk}$
- $\underline{\underline{C}} \cdot \underline{B} = A_{ijkn}B_{nl} = A_{ijmn}\delta_{mk}B_{nl} = A_{ijmn} : (\delta_{mk}B_{nl})_{mnkl} = \underline{\underline{A}} : (\underline{1} \underline{\otimes} \underline{B})$
- $\underline{A} \cdot \underline{\underline{B}} = A_{in}B_{njkl} = A_{in}\delta_{mk}B_{njkl} = (A_{in}\delta_{mj})_{imnj} : B_{njkl} = (\underline{A} \underline{\otimes} \underline{1}) : \underline{\underline{B}}$
- $(\underline{A} \underline{\otimes} \underline{B}) : (\underline{1} \overline{\otimes} \underline{1}) = A_{im}B_{jn}\delta_{ml}\delta_{nk} = A_{il}B_{jk} = \underline{A} \overline{\otimes} \underline{B}$

Partial derivatives:

$$\frac{\partial \underline{A} \cdot \underline{B}}{\partial \underline{B}} = \frac{\partial A_{im}B_{mj}}{\partial B_{kl}} = A_{im}\frac{\partial B_{mj}}{\partial B_{kl}} = A_{im}\frac{\partial B_{mj}}{\partial B_{kl}} = A_{im}\delta_{mk}\delta_{jl} = A_{ik}\delta_{jl} = \underline{A} \underline{\otimes} \underline{1}$$

$$\frac{\underline{A} \cdot \underline{B}}{\partial \underline{A}} = \frac{\partial A_{im}B_{mj}}{\partial A_{kl}} = \frac{\partial A_{im}}{\partial A_{kl}}B_{mj} = \delta_{ik}\delta_{ml}B_{mj} = \delta_{ik}B_{lj} = \delta_{ik}B^T_{jl} = \underline{1} \underline{\otimes} \underline{B}^T$$

$$\frac{\partial \underline{A} \cdot \underline{B} \cdot \underline{C}}{\partial \underline{B}} = \frac{\partial A_{im}B_{mn}C_{nj}}{\partial B_{kl}} = A_{im}\frac{\partial B_{mn}}{\partial B_{kl}}C_{nj} = A_{im}\delta_{mk}\delta_{nl}C_{nj} = A_{ik}C_{lj} = A_{ik}C^T_{jl} = \underline{A} \underline{\otimes} \underline{C}^T$$

A.2 PARTIAL DERIVATIVES FCC MODEL

A.2.1 Partial derivatives

$$R_E = \Delta\underline{E} - \Delta\underline{F}\cdot\underline{F}^{-1}\cdot\underline{E} + \underline{E}\cdot\left((1-\sum_{\beta=1}^{N_\beta} f^\beta)\sum \Delta\gamma^s\underline{m}^s + \sum \Delta f^\beta\gamma^{tw}\underline{m}^t\right)$$

with $\Delta\gamma^s = \Delta\nu^s sign(\tau^s)$, where ν^s is the accumulated slip, which is the internal variable in the model. All partial derivatives are considered with respect to ν^s.

A.2.1.1 R_E Terms

- Partial derivative: $\Delta\underline{E}$

$$\frac{\partial R_E}{\partial\Delta\underline{E}} = \underline{\underline{1}} - \frac{\partial\underline{A}\cdot\underline{E}}{\partial\underline{E}} : \frac{\partial\underline{E}}{\partial\Delta\underline{E}} + \frac{\partial\underline{E}\cdot\underline{B}}{\partial\underline{E}} : \frac{\partial\underline{E}}{\partial\Delta\underline{E}}$$

where $\underline{E} = \underline{E}_t + \Delta\underline{E}$, $\underline{A} = \Delta\underline{F}\cdot\underline{F}^T$, $\underline{B} = ((1-\sum_\beta f^\beta)\sum_s \Delta\gamma^s\underline{m}^s + \sum_\beta \Delta f^\beta\gamma^{tw}\underline{m}^t)$

$$\frac{(\partial\underline{E}_t + \Delta\underline{E})}{\partial\underline{E}} = \underline{\underline{1}}$$

$$\frac{\partial\underline{A}\cdot\underline{E}}{\partial\underline{E}} = A_{im}\frac{\partial E_{mj}}{\partial E_{kl}} = A_{im}\delta_{mk}\delta_{jl} = A_{ik}\delta_{jl} = \underline{A}\underline{\otimes}\underline{1}$$

$$\frac{\partial\underline{E}\cdot\underline{B}}{\partial\underline{E}} = \frac{\partial E_{im}}{\partial E_{kl}}B_{mj} = \delta_{ik}\delta_{ml}B_{mj} = \delta_{ik}B^T_{jl} = \underline{1}\underline{\otimes}\underline{B}^T$$

$$\frac{\partial R_E}{\partial\Delta\underline{E}} = \underline{\underline{1}} - (\Delta\underline{F}\cdot\underline{F}^T)\underline{\otimes}\underline{1} + \underline{1}\underline{\otimes}\left((1-\sum_\beta f^\beta)\sum_s \Delta\gamma^s\underline{m}^s + \sum_\beta \Delta f^\beta\gamma^{tw}\underline{m}^t\right)$$

- Partial derivative: $\Delta\nu^r$

$$\frac{\partial R_E}{\partial\Delta\nu^r} = \underline{E}\cdot\left((1-\sum_\beta f^\beta)\underline{m}^s_r sign(\tau^s) + \sum_\beta \gamma^{tw}(K_c(F_{max} - \sum f^\beta)\phi_t)\underline{m}^t\right)$$

- Partial derivative: Δf^β

$$\frac{\partial R_E}{\partial\Delta f^\beta} = \underline{E}\cdot(\sum_s -\Delta\nu^s\underline{m}^s sign(\tau^s) + \gamma^{tw}\underline{m}^t_\beta)$$

- Partial derivatives: $\Delta\rho^r$; Δr^{twsl}; Δr^{tw}

$$\frac{\partial R_E}{\partial\Delta\rho^r} = 0 \;;\; \frac{\partial R_E}{\partial\Delta r^{tw}} = 0 \;;\; \frac{\partial R_E}{\partial\Delta r^{tw}} = 0$$

A.2.1.2 R_{ν_s} Terms

$$R_{\nu^s} = \Delta\nu^s - \left(\frac{|\tau^s| - r^s - \tau_y}{K}\right)^n \Delta t$$

- Partial derivative: $\Delta\underline{E}$ (Mandel stress)

$$\frac{\partial R_{\nu^s}}{\partial \Delta\underline{E}} = \frac{\partial R_{\nu^s}}{\partial \underline{M}} : \frac{\partial \underline{M}}{\partial \underline{C}^e} : \frac{\partial \underline{C}^e}{\partial \underline{E}} : \frac{\partial \underline{E}}{\partial \Delta\underline{E}}$$

$$\frac{\partial R_{\nu^s}}{\partial \underline{M}} = -\Delta t \frac{\partial \phi}{\partial x}\frac{\partial x}{\partial \tau^s}\frac{\partial \tau^s}{\partial \underline{M}} = -\Delta t \phi' sign(\tau^s)\underline{m^s} = -\Delta t \phi' \underline{m^s} sign(\tau^s)$$

where $\phi(x) = \left\langle \frac{x}{K} \right\rangle^n$, $\phi(x)' = \frac{n}{K}\left\langle \frac{x}{K} \right\rangle^{n-1}$, and $x = |\tau^s| - r^s - \tau_y$

$$\frac{\partial \underline{M}}{\partial \underline{C}^e} = \frac{\partial \left[\underline{C}^e \cdot \left(\underline{\underline{\Lambda}} : \frac{1}{2}(\underline{C}^e - \underline{1})\right)\right]}{\partial \underline{C}^e} = (\underline{1} \underline{\otimes} \underline{S}^e) + \frac{1}{2}(\underline{C}^e \underline{\otimes} \underline{1}) : \underline{\underline{\Lambda}}$$

$$\frac{\partial \underline{C}^e}{\partial \underline{E}} = \frac{\partial \underline{E}^T \underline{E}}{\partial \underline{E}} = \frac{\partial E_{ni}}{\partial E_{kl}} E_{nj} + E_{ni}\frac{\partial E_{nj}}{\partial E_{kl}} =$$
$$\delta_{nk}\delta_{il}E_{nj} + E_{ni}\delta_{nk}\delta_{jl} = \delta_{il}E^T_{jk} + E^T_{ik}\delta_{jl} = (\underline{1} \overline{\otimes} \underline{E}^T + \underline{E}^T \underline{\otimes} \underline{1})$$

$$\frac{\partial R_{\nu^s}}{\partial \Delta\underline{E}} = (-\Delta t \phi' \underline{m^s} sign(\tau^s)) : \left((\underline{1} \underline{\otimes} \underline{S}^e) + \frac{1}{2}(\underline{C}^e \underline{\otimes} \underline{1}) : \underline{\underline{\Lambda}}\right) : \left((\underline{1} \overline{\otimes} \underline{E}^T + \underline{E}^T \underline{\otimes} \underline{1})\right)$$

- Partial derivative: $\Delta\nu^r$

$$\frac{\partial R_{\nu_s}}{\partial \Delta\nu^r} = \frac{\partial \phi}{\partial x}\frac{\partial x}{\partial r^s}\frac{\partial r^s}{\partial \nu}$$

$$\frac{\partial \phi}{\partial x}\frac{\partial x}{\partial r^s} = -\phi(x)'\Delta t(-1)$$

$$\frac{\partial r^s}{\partial \nu} = (bQH_{rs}exp(-b\nu^r))$$

$$\frac{\partial R_{\nu_s}}{\partial \Delta\nu^r} = \delta_{rs} + \phi'(x)\Delta t(QH_{rs}exp(-b\nu^r))$$

- Partial derivative: $\Delta\rho^r$

$$\frac{\partial R_{\nu_s}}{\partial \Delta\rho^r} = \frac{\partial \phi}{\partial x}\frac{\partial x}{\partial r^s}\frac{\partial r^s}{\partial \Delta\rho^r} = \Delta t \phi'(x)(bQH_{rs})$$

- Partial derivative: Δr^{sltw}

$$\frac{\partial R_{\nu_s}}{\partial \Delta r^{sltw}} = \frac{\partial \phi}{\partial x}\frac{\partial x}{\partial r^s}\frac{\partial r^s}{\partial \Delta r^{sltw}} = -\Delta t \phi'(x)(-1) = \Delta t \phi'(x)$$

- Partial derivative: Δf^{β}

$$\frac{\partial R_{\nu_s}}{\partial \Delta f^{\beta}} = \frac{\partial \phi}{\partial x}\frac{\partial x}{\partial r^s}\frac{\partial r^s}{\partial \Delta f^{\beta}}$$

$$\frac{\partial r^s}{\partial \Delta f^{\beta}} = 0.5 H^s_{tw}(\sum_{NC} f^{\beta})^{-0.5}$$

$$\frac{\partial R_{\nu_s}}{\partial \Delta f^{\beta}} = -\Delta t \phi'(x)(-1)(0.5 H^s_{tw}(\sum_{NC} f^{\beta})^{-0.5}) = \Delta t \phi'(x)(0.5 H^s_{tw}(\sum_{NC} f^{\beta})^{-0.5})$$

- Partial derivative: Δr^{tw}

$$\frac{\partial R_{\nu_s}}{\partial \Delta r^{tw}} = 0$$

A.2.1.3 R_{ρ_s} Terms

$$R_{\rho^s} = \Delta \rho^s - (1 - b\rho^s)\Delta \nu^s$$

- Partial derivative: $\Delta \nu^r$

$$\frac{\partial R_{\rho^s}}{\partial \Delta \nu^r} = -(1 - b^s \rho^s)\delta_{rs}$$

- Partial derivative: $\Delta \rho^r$

$$\frac{\partial R_{\rho^s}}{\partial \Delta \rho^r} = \delta_{rs} - b\Delta \nu_s \delta_{rs}$$

- Partial derivatives: Δr^{sltw} ; Δf^{β} ; Δr^{tw} ; $\Delta \underline{E}$

$$\frac{\partial R_{\rho^s}}{\partial \Delta r^{sltw}} = 0 \ ; \ \frac{\partial R_{\rho^s}}{\partial \Delta f^{\beta}} = 0 \ ; \ \frac{\partial R_{\rho^s}}{\partial \Delta r^{tw}} = 0 \ ; \ \frac{\partial R_{\rho^s}}{\partial \Delta \underline{E}} = 0$$

A.2.1.4 $R_{r^{sltw}}$ Terms

$$R_{r^{sltw}} = \Delta r^{sltw} - 0.5 H^{tw \to s} (\sum_{n=NC}^{N_{tw}} f^{\beta n})^{-0.5} \sum_{n=NC}^{N_{tw}} \Delta f^{\beta n}$$

- Partial derivative: Δr^{sltw}

$$\frac{\partial R_{r_s^{sltw}}}{\partial \Delta r_r^{sltw}} = \delta_{rs}$$

- Partial derivative: Δf^{β}

$$\frac{\partial R_{r^{sltw}}}{\partial \Delta f^{\beta}} = \frac{H_{tw}^{s} \Delta f^{\beta}}{4(\sum_{NC} f^{\beta})^{\frac{3}{2}}} - \frac{H_{tw}^{s}}{2(\sum_{NC} f^{\beta})^{0.5}}$$

- Partial derivatives: $\Delta \underline{E}$; $\Delta \nu^{r}$; $\Delta \rho^{r}$; Δr^{tw}

$$\frac{\partial R_{r^{sltw}}}{\partial \Delta \underline{E}} = 0 \ ; \ \frac{\partial R_{r^{sltw}}}{\partial \Delta \nu^{s}} = 0 \ ; \ \frac{\partial R_{r^{sltw}}}{\partial \Delta \rho^{s}} = 0 \ ; \ \frac{\partial R_{r^{sltw}}}{\partial \Delta r^{tw}} = 0$$

A.2.1.5 $R_{f^{\beta}}$ Terms

$$R_{f^{\beta}} = \Delta f^{\beta} - \underbrace{K_c (f_{max} - \sum f^{\beta})}_{\psi} \underbrace{\left\langle \frac{|\tau^{\beta}| - r^{tw} - \tau_y^{rw}}{K} \right\rangle^{m}}_{\phi_t} \sum_{s} \Delta \nu^{s}$$

- Partial derivative: $\Delta \underline{E}$

$$\frac{\partial R_{f^{\beta}}}{\partial \Delta \underline{E}} = \frac{\partial R_{f^{\beta}}}{\partial \underline{M}} : \frac{\partial \underline{M}}{\partial \underline{C}^{e}} : \frac{\partial \underline{C}^{e}}{\partial \underline{E}} : \frac{\partial \underline{E}}{\partial \Delta \underline{E}}$$

$$\frac{\partial R_{f^{\beta}}}{\partial \underline{M}} = -D \phi_t'(x) sign(\tau^{t}) \underline{m}^{t} (\sum_{s} \Delta \nu^{s})$$

where $\phi_t(x) = \left\langle \frac{x}{K} \right\rangle^{n}$, $\phi_t'(x) = \frac{n}{K} \left\langle \frac{x}{K} \right\rangle^{n-1}$, and $x = |\tau^{\beta}| - r^{tw} - \tau_y^{tw}$; Coefficients n and K are different than in slip deformation. $D = K_c (f_{max} - \sum f^{\beta})$

$$\frac{\partial \underline{M}}{\partial \underline{C}^{e}} = (\underline{1} \overline{\otimes} \underline{S}^{e}) + \frac{1}{2} (\underline{C}^{e} \underline{\otimes} \underline{1}) : \underline{\underline{\Lambda}}$$

$$\frac{\partial \underline{C}^{e}}{\partial \underline{E}} = \frac{\partial \underline{E}^{T} \underline{E}}{\partial \underline{E}} = (\underline{1} \overline{\otimes} \underline{E}^{T} + \underline{E}^{T} \underline{\otimes} \underline{1})$$

$$\frac{\partial R_{f^\beta}}{\partial \Delta \underline{E}} = \left(-D\phi_t'(x) sign(\tau^t) \underline{m}^t (\sum \Delta \nu^s)\right) : \left((\underline{1} \underline{\otimes} \underline{S}^e) + \frac{1}{2}(\underline{C}^e \underline{\otimes} \underline{1}) : \underline{\underline{\Lambda}}\right) : \left((\underline{1} \overline{\otimes} \underline{E}^T + \underline{E}^T \underline{\otimes} \underline{1})\right)$$

- Partial derivative: $\Delta \nu^r$

$$\frac{\partial R_{f^\beta}}{\partial \Delta \nu^s} = -D\phi_t(x))$$

- Partial derivative: Δf^β

$$\frac{\partial R_{f^\beta}}{\partial \Delta f^\alpha} = \delta_{\alpha\beta} - \left(\frac{\partial \psi}{\partial \Delta f^\alpha} \phi_t \sum_s \Delta \nu^s + \psi \frac{\partial \phi_t}{\partial \Delta f^\alpha} (\sum_s \Delta \nu^s) + \psi \phi_t \frac{\partial (\sum_s \Delta \nu^s)}{\partial \Delta f^\alpha}\right)$$

$$\frac{\partial \psi}{\partial \Delta f^\alpha} \phi_t(x) (\sum_s \Delta \nu^s) = (-K_c) \phi_t(x) (\sum_s \Delta \nu^s)$$

$$\psi \frac{\partial \phi_t}{\partial \Delta f^\alpha} (\sum_s \Delta \nu^s) = \psi [\frac{\partial \phi_t}{\partial x} \frac{\partial x}{\partial r_\beta^{tw}} \frac{\partial r_\beta^{tw}}{\partial \Delta f^\alpha}] (\sum_s \Delta \nu^s) = \psi \phi_t'(x) (\sum_s \Delta \nu^s) \frac{\partial r^{tw}}{\partial \Delta f^\alpha} = 0$$

$$\psi \phi_t \frac{\partial \sum_s \Delta \nu^s}{\partial \Delta f^\alpha} = 0$$

$$\frac{\partial R_{f^\beta}}{\partial \Delta f^\alpha} = \delta_{\alpha\beta} - \left(-K_c \phi_t \sum_s \Delta \nu^s\right)$$

- Partial derivatives: $\Delta \rho^r$; Δr^{tw} ; $\Delta \tau^{tw}$

$$\frac{\partial R_{f^\beta}}{\partial \Delta \rho^s} = 0 \ ; \ \frac{\partial R_{f^\beta}}{\partial \Delta r^{sltw}} = 0 \ ; \ \frac{\partial R_{f^\beta}}{\partial \Delta r^{tw}} = 0$$

A.2.1.6 $R_{r^{tw}}$ Terms

$$R_{r^{tw}} = \Delta r_{tw} - \gamma^{tw} \left[H_{tt}^{NC} \left(\sum f^\beta\right)^b \sum_{k=NC} \Delta f^\beta + H_{tt}^{CO} (\sum f^\beta)^g \sum_{k=CO} \Delta f^\beta\right]$$
$$- H^{sltw} \left(\sum_s \nu^s\right)^d \sum_s \Delta \nu^s$$

- Partial derivative: $\Delta \nu^r$

$$\frac{\partial R_{r^{tw}}}{\partial \Delta \nu^s} = -H^{sltw} \left(d \left(\sum_s \nu^s \right)^{d-1} \sum_s \Delta \nu^s + \left(\sum_s \nu^s \right)^d \right)$$

- Partial derivative: Δf^β

$$\frac{\partial R_{r^{tw}}}{\partial \Delta f^\beta} = -H_{tt}^{NC} \gamma^{tw} \left[b(\sum_\beta f^\beta)^{b-1} (\sum_{NC} \Delta f^\beta) + (\sum_\beta f^\beta)^b \delta_{NC} \right] - H_{tt}^{CO} \gamma^{tw} \left[g(\sum_\beta f^\beta)^{g-1} (\sum_{CO} \Delta f^\beta) + (\sum_\beta f^\beta)^g \delta_{CO} \right]$$

- Partial derivative: Δr^{tw}

$$\frac{\partial R_{r_\beta^{tw}}}{\partial \Delta r_r^{tw}} = \delta_{r\beta}$$

- Partial derivatives: $\Delta \underline{E}$; $\Delta \rho^r$; Δr^{tw}

$$\frac{\partial R_{r^{tw}}}{\partial \Delta \underline{E}} = 0 \ ; \ \frac{\partial R_{r^{tw}}}{\partial \Delta \rho^s} = 0 \ ; \ \frac{\partial R_{r^{tw}}}{\partial \Delta r^{tw}} = 0$$

B Second appendix

B.1 PARTIAL DERIVATIVES FOR BCC MODELS

B.1.1 BCC MODEL WITH KINEMATIC HARDENING

B.1.1.1 R_E Terms

- Partial derivative: $\Delta\underline{E}$

$$\frac{\partial R_E}{\partial \Delta \underline{E}} = \underline{\underline{1}} - (\Delta \underline{F} \cdot \underline{F}^T) \underline{\otimes} \underline{1} + \underline{1} \underline{\otimes} \left(\sum_s \Delta \nu^s \underline{m}^s sign(\tau^s - x^s) \right)$$

- Partial derivative: $\Delta\nu^s$

$$\frac{\partial R_E}{\partial \Delta \nu^r} = \underline{E} \cdot (\underline{m}^s sign(\tau^s - x^s))$$

- Partial derivative: $\Delta\rho^r$

$$\frac{\partial R_E}{\partial \Delta \rho^r} = 0$$

If kinematic hardening is active,

- Partial derivative: $\Delta\alpha^r$

$$\frac{\partial R_E}{\partial \Delta \alpha^r} = 0$$

B.1.1.2 R_{ν_s} Terms

$$\frac{\partial R_{\nu^s}}{\partial \Delta \underline{E}} = (-\Delta t \phi' \underline{m^s} sign(\tau^s - x^s)) : \left((\underline{1} \underline{\otimes} \underline{S^e}) + \frac{1}{2} (\underline{C^e} \underline{\otimes} \underline{1}) : \underline{\underline{\Lambda}} \right) : \left((\underline{1} \overline{\otimes} \underline{E}^T + \underline{E}^T \underline{\otimes} \underline{1}) \right)$$

- Partial derivative: $\Delta \nu^r$

$$\frac{\partial R_{\nu_s}}{\partial \Delta \nu^r} = \delta_{rs} + \phi'(x) \Delta t (Q H_{rs} exp(-b\nu^r))$$

- Partial derivative: $\Delta \rho^r$

$$\frac{\partial R_{\nu_s}}{\partial \Delta \rho^r} = \Delta t \phi'(x) (bQ H_{rs})$$

If kinematic hardening is active,

- Partial derivative: $\Delta \alpha^r$

$$\frac{\partial R_{\nu_s}}{\partial \Delta \alpha^r} = \delta_{rs} \phi'(x) sign(\tau^s - x^s)$$

B.1.1.3 R_{ρ_s} Terms

$$R_{\rho^s} = \Delta \rho^s - (1 - b\rho^s) \Delta \nu^s$$

- Partial derivative: $\Delta \underline{E}$

$$\frac{\partial R_{\rho^s}}{\partial \Delta \underline{E}} = 0$$

- Partial derivative: $\Delta \nu^r$

$$\frac{\partial R_{\rho^s}}{\partial \Delta \nu^r} = -(1 - b^s \rho^s) \delta_{rs}$$

- Partial derivative: $\Delta \rho^r$

$$\frac{\partial R_{\rho^s}}{\partial \Delta \rho^r} = \delta_{rs} - b \Delta \nu_s \delta_{rs}$$

- Partial derivative: $\Delta \rho^r$

$$\frac{\partial R_{\rho^s}}{\partial \Delta \alpha^r} = 0$$

B.1.1.4 R_{α_s} Terms

If kinematic hardening is used, the non-zero partial derivatives are:

$$R_{\alpha^s} = \Delta\alpha^s - (sign(\tau^s - x^s) - d\alpha^s)\Delta\nu^s$$

- Partial derivative: $\Delta\nu^s$

$$\frac{\partial R_{\alpha^s}}{\partial \Delta\nu^s} = -\left(sign(\tau^s - x^s) - D\alpha^s\right)\delta_r s$$

- Partial derivative: $\Delta\alpha^r$

$$\frac{\partial R_{\alpha^s}}{\partial \Delta\alpha^r} = \delta_{rs}(1 + D\Delta\nu^s)$$

B.2 PARTIAL DERIVATIVES BCC MODEL INCLUDING SHEAR BANDING

Remark: The shear band systems constructed from the 2nd PK stress tensor are generated only at the end of the increment, i.e., the next increment uses the systems constructed from the old tensor. This simplification leads to the requirement of using sufficiently small time steps to minimize error. Also as a consequence of the simplification, the complex partial derivatives with respect to $\underline{m}^\chi$ become zero, for example:

$$\frac{\partial \underline{m}^\chi}{\partial \Delta \underline{E}} = 0 \ ; \ \frac{\partial \underline{m}^\chi}{\partial \underline{S}^e} = 0$$

B.2.0.1 R_E Terms

- Partial derivative: $\Delta\underline{E}$

$$\frac{\partial R_E}{\partial \Delta \underline{E}} = \underline{\underline{1}} - \frac{\partial \underline{A}\cdot\underline{E}}{\partial \underline{E}} : \frac{\partial \underline{E}}{\partial \Delta \underline{E}} + \frac{\partial \underline{E}\cdot\underline{B}}{\partial \underline{E}} : \frac{\partial \underline{E}}{\partial \Delta \underline{E}}$$

where $\underline{E} = \underline{E}_t + \Delta\underline{E}$, $\underline{A} = \Delta\underline{F}\cdot\underline{F}^T$, $\underline{B} = (\sum_s \Delta\gamma^s \underline{m}^s + \sum_\chi \Delta\gamma^\chi \underline{m}^\chi)$

$$\frac{(\partial \underline{E}_t + \Delta\underline{E})}{\partial \underline{E}} = \underline{\underline{1}}$$

$$\frac{\partial \underline{A}\cdot\underline{E}}{\partial \underline{E}} = A_{im}\frac{\partial E_{mj}}{\partial E_{kl}} = A_{im}\delta_{mk}\delta_{jl} = A_{ik}\delta_{jl} = \underline{A}\underline{\otimes}\underline{1}$$

$$\frac{\partial \underline{E}\cdot\underline{B}}{\partial \underline{E}} = \frac{\partial E_{im}}{\partial E_{kl}}B_{mj} = \delta_{ik}\delta_{ml}B_{mj} = \delta_{ik}B^T_{jl} = \underline{1}\underline{\otimes}\underline{B}^T$$

$$\frac{\partial R_E}{\partial \Delta \underline{E}} = \underline{\underline{1}} - (\Delta \underline{F} \cdot \underline{F}^T) \underline{\otimes} \underline{1} + \underline{1} \underline{\otimes} \left(\sum_s \Delta \nu^s \underline{m}^s sign(\tau^s) + \sum_\chi \Delta \nu^\chi \underline{m}^\chi sign(\tau^\chi) \right)$$

- Partial derivative: $\Delta \nu^s$

$$\frac{\partial R_E}{\partial \Delta \nu^r} = \underline{E} \cdot \left(\underline{m}^s sign(\tau^s) + \sum_\chi K_B \phi_\chi \underline{m}^\chi sign(\tau^\chi) \right)$$

- Partial derivative: $\Delta \rho^r$

$$\frac{\partial R_E}{\partial \Delta \rho^r} = 0$$

- Partial derivative: $\Delta \chi^r$

$$\frac{\partial R_E}{\partial \Delta \chi^r} = \underline{E} \cdot (\underline{m}^\chi sign(\tau^\chi))$$

- Partial derivative: $\Delta r^{r\chi}$

$$\frac{\partial R_E}{\partial \Delta r^{r\chi}} = 0$$

B.2.0.2 R_{ν_s} Terms

$$R_{\nu^s} = \Delta \nu^s - \left(\frac{|\tau^s| - r^s - \tau_y}{K} \right)^n \Delta t$$

- Partial derivative: $\Delta \underline{E}$ (Mandel stress)

$$\frac{\partial R_{\nu^s}}{\partial \Delta \underline{E}} = \frac{\partial R_{\nu^s}}{\partial \underline{M}} : \frac{\partial \underline{M}}{\partial \underline{C}^e} : \frac{\partial \underline{C}^e}{\partial \underline{E}} : \frac{\partial \underline{E}}{\partial \Delta \underline{E}}$$

$$\frac{\partial R_{\nu^s}}{\partial \underline{M}} = -\Delta t \frac{\partial \phi}{\partial x} \frac{\partial x}{\partial \tau^s} \frac{\partial \tau^s}{\partial \underline{M}} = -\Delta t \phi' sign(\tau^s) \underline{m^s} = -\Delta t \phi' \underline{m^s} sign(\tau^s)$$

where $\phi(x) = \left\langle \frac{x}{K} \right\rangle^n$, $\phi(x)' = \frac{n}{K} \left\langle \frac{x}{K} \right\rangle^{n-1}$, and $x = |\tau^s| - r^s - \tau_y$

$$\frac{\partial \underline{M}}{\partial \underline{C}^e} = \frac{\partial \left[\underline{C}^e \cdot \left(\underline{\underline{\Lambda}} : \frac{1}{2} (\underline{C}^e - \underline{1}) \right) \right]}{\partial \underline{C}^e} = (\underline{1} \underline{\otimes} \underline{S}^e) + \frac{1}{2} (\underline{C}^e \underline{\otimes} \underline{1}) : \underline{\underline{\Lambda}}$$

$$\frac{\partial \underline{C}^e}{\partial \underline{E}} = \frac{\partial \underline{E}^T \underline{E}}{\partial \underline{E}} = \frac{\partial E_{ni}}{\partial E_{kl}} E_{nj} + E_{ni} \frac{\partial E_{nj}}{\partial E_{kl}} =$$
$$\delta_{nk}\delta_{il}E_{nj} + E_{ni}\delta_{nk}\delta_{jl} = \delta_{il}E^T_{jk} + E^T_{ik}\delta_{jl} = (\underline{1}\overline{\otimes}\underline{E}^T + \underline{E}^T\underline{\otimes}\underline{1})$$

$$\frac{\partial R_{\nu^s}}{\partial \Delta \underline{E}} = (-\Delta t \phi' \underline{m^s} sign(\tau^s)) : \left((\underline{1}\underline{\otimes}\underline{S^e}) + \frac{1}{2}(\underline{C}^e\underline{\otimes}\underline{1}) : \underline{\underline{\Lambda}} \right) : \left((\underline{1}\overline{\otimes}\underline{E}^T + \underline{E}^T\underline{\otimes}\underline{1}) \right)$$

- Partial derivative: $\Delta\nu^r$

$$\frac{\partial R_{\nu_s}}{\partial \Delta \nu^r} = \frac{\partial \phi}{\partial x}\frac{\partial x}{\partial r^s}\frac{\partial r^s}{\partial \nu}$$

$$\frac{\partial \phi}{\partial x}\frac{\partial x}{\partial r^s} = -\phi(x)'\Delta t(-1)$$

$$\frac{\partial r^s}{\partial \nu} = (bQH_{rs}exp(-b\nu^r))$$

$$\frac{\partial R_{\nu_s}}{\partial \Delta \nu^r} = \delta_{rs} + \phi'(x)\Delta t(bQH_{rs}exp(-b\nu^r))$$

- Partial derivative: $\Delta\rho^r$

$$\frac{\partial R_{\nu_s}}{\partial \Delta \rho^r} = \frac{\partial \phi}{\partial x}\frac{\partial x}{\partial r^s}\frac{\partial r^s}{\partial \Delta \rho^r} = \Delta t \phi'(x)(bQH_{rs})$$

- Partial derivative: $\Delta\chi^r$

$$\frac{\partial R_{\nu_s}}{\partial \Delta \chi^r} = 0$$

- Partial derivative: $\Delta r^{\chi r}$

$$\frac{\partial R_{\nu_s}}{\partial \Delta r^{\chi r}} = 0$$

B.2.0.3 R_{ρ_s} Terms

$$R_{\rho^s} = \Delta\rho^s - (1 - b\rho^s)\Delta\nu^s$$

- Partial derivative: $\Delta\underline{E}$

$$\frac{\partial R_{\rho^s}}{\partial \Delta\underline{E}} = 0$$

- Partial derivative: $\Delta\nu^r$

$$\frac{\partial R_{\rho^s}}{\partial \Delta\nu^r} = -(1 - b^s\rho^s)\delta_{rs}$$

- Partial derivative: $\Delta\rho^r$

$$\frac{\partial R_{\rho^s}}{\partial \Delta\rho^r} = \delta_{rs} + b\Delta\nu_s\delta_{rs}$$

- Partial derivative: $\Delta\chi^r$

$$\frac{\partial R_{\rho^s}}{\partial \Delta\chi^r} = 0$$

- Partial derivative: $\Delta r^{\chi r}$

$$\frac{\partial R_{\rho^s}}{\partial \Delta r^{\chi r}} = 0$$

B.2.0.4 R_{χ_r} Terms

$$R_{\chi^r} = \Delta\chi^r - K_B\left(\frac{|\tau^r| - r^{\chi r} - \tau_{\chi y}}{K_\chi}\right)^n \sum_s \Delta\nu^s$$

- Partial derivative: $\Delta\underline{E}$

$$\frac{\partial R_{\chi^r}}{\partial \Delta\underline{E}} = \frac{\partial R_{\chi^r}}{\partial \underline{M}} : \frac{\partial \underline{M}}{\partial \underline{C}^e} : \frac{\partial \underline{C}^e}{\partial \underline{E}} : \frac{\partial \underline{E}}{\partial \Delta\underline{E}}$$

$$\frac{\partial R_{\chi^r}}{\partial \underline{M}} = -K_B\frac{\partial\phi}{\partial x}\frac{\partial x}{\partial \tau^r}\frac{\partial \tau^r}{\partial \underline{M}}\sum_s \Delta\nu^s = -K_B\phi'_\chi sign(\tau^r)\underline{m^\chi}\sum_s \Delta\nu^s = -K_B\phi'_\chi\underline{m^\chi}sign(\tau^r)\sum_s \Delta\nu^s$$

where $\phi_\chi(x) = \left\langle \frac{x}{K} \right\rangle^n$, $\phi_\chi(x)' = \frac{n}{K} \left\langle \frac{x}{K} \right\rangle^{n-1}$, and $x = |\tau^r| - r^{\chi r} - \tau_{y\chi}$

$$\frac{\partial \underline{M}}{\partial \underline{C}^e} = \frac{\partial \left[\underline{C}^e \cdot \left(\underline{\underline{\Lambda}} : \frac{1}{2}(\underline{C}^e - \underline{1}) \right) \right]}{\partial \underline{C}^e} = (\underline{1} \underline{\otimes} \underline{S}^e) + \frac{1}{2}(\underline{C}^e \underline{\otimes} \underline{1}) : \underline{\underline{\Lambda}}$$

$$\frac{\partial \underline{C}^e}{\partial \underline{E}} = \frac{\partial \underline{E}^T \underline{E}}{\partial \underline{E}} = \frac{\partial E_{ni}}{\partial E_{kl}} E_{nj} + E_{ni} \frac{\partial E_{nj}}{\partial E_{kl}} =$$
$$\delta_{nk}\delta_{il}E_{nj} + E_{ni}\delta_{nk}\delta_{jl} = \delta_{il}E^T_{jk} + E^T_{ik}\delta_{jl} = (\underline{1} \overline{\otimes} \underline{E}^T + \underline{E}^T \underline{\otimes} \underline{1})$$

$$\frac{\partial R_{\chi^r}}{\partial \Delta \underline{E}} = \left(-K_B \phi'_\chi sign(\tau^r) \underline{m^\chi} \sum_s \Delta \nu^s \right) : \left((\underline{1} \underline{\otimes} \underline{S}^e) + \frac{1}{2}(\underline{C}^e \underline{\otimes} \underline{1}) : \underline{\underline{\Lambda}} \right) : \left((\underline{1} \overline{\otimes} \underline{E}^T + \underline{E}^T \underline{\otimes} \underline{1}) \right)$$

- Partial derivative: $\Delta \nu^s$

$$\frac{\partial R_{\chi^r}}{\partial \Delta \nu^s} = -K_B \phi_\chi(x)$$

- Partial derivative: $\Delta \rho^s$

$$\frac{\partial R_{\chi^r}}{\partial \Delta \rho^s} = 0$$

- Partial derivative: $\Delta \chi^s$

$$\frac{\partial R_{\chi^r}}{\partial \Delta \chi^s} = \delta_{rs} \left(1 + \phi'_\chi(x) b_\chi (Q_\chi H_{rs} exp(-b_\chi \chi^r)) \right)$$

- Partial derivative: $\Delta r^{\chi r}$

$$\frac{\partial R_{\chi^r}}{\partial \Delta r^{\chi r}} = -K_B \phi'_\chi (-1) \sum_s \Delta \nu^s = K_B \phi'_\chi \sum_s \Delta \nu^s$$

- Partial derivative: $\Delta \rho^s_\chi$

$$\frac{\partial R_{\chi_s}}{\partial \Delta \rho^r_\chi} = \frac{\partial \phi}{\partial x} \frac{\partial x}{\partial r^s} \frac{\partial r^s}{\partial \Delta \rho^s_\chi} = \phi'_\chi(x)(b_\chi Q_\chi H^{rs}_\chi)\delta_{rs}$$

B.2.0.5 $R_{r\chi r}$ Terms

$$R_{r\chi r} = \Delta r^{\chi r} - H_{slsb}(\sum_s \nu^s)^d \sum_s \Delta\nu^s - H_{sbnd}(\sum_{r\neq s} \chi^s)^f \sum_{r\neq s} \Delta\chi^r$$

- Partial derivative: ΔE

$$\frac{\partial R_{r\chi r}}{\partial \Delta E} = 0$$

- Partial derivative: $\Delta\nu^s$

$$\frac{\partial R_{r\chi r}}{\partial \Delta\nu^s} = -H_{slsb}\left(d(\sum_s \nu^s)^{d-1} \sum_s \Delta\nu^s + (\sum_s \nu^s)^d\right)$$

- Partial derivative: $\Delta\rho^s$

$$\frac{\partial R_{r\chi r}}{\partial \Delta\rho^s} = 0$$

- Partial derivative: $\Delta\chi^s$

$$\frac{\partial R_{r\chi r}}{\partial \Delta\chi^s} = -H_{sbnd}\left(f(\sum_{s\neq r} \chi^s)^{f-1}(\sum_{s\neq r} \Delta\chi^s) + (\sum_{s\neq r} \chi^s)^f\right)$$

- Partial derivative: $\Delta r^{\chi s}$

$$\frac{\partial R_{r\chi r}}{\partial \Delta r^{\chi s}} = \delta_{rs}$$

B.2.0.6 $R_{\rho\chi}$ Terms

$$R_{\rho^s_\chi} = \Delta\rho^s_\chi - (1 - b_\chi \rho^s_\chi)\Delta\chi^s$$

$$\frac{\partial R_{\rho^s_\chi}}{\partial \Delta\chi^r} = -(1 - b_\chi \rho^s_\chi)\delta_{rs}$$

$$\frac{\partial R_{\rho^s_\chi}}{\partial \Delta\rho^r_\chi} = \delta_{rs}(1 + b_\chi \Delta\chi^r)$$

Tampereen teknillinen yliopisto
PL 527
33101 Tampere

Tampere University of Technology
P.O.B. 527
FI-33101 Tampere, Finland

ISBN 978-952-15-3814-8
ISSN 1459-2045